

https://dspace.org/

Accelerating two-dimensional supersonic wedge flow

Missing, Timothy

2020
https://hdl.handle.net/10539/31279

Downloaded from a DSpace repository. https://dspace.org/

Accelerating Two-Dimensional Supersonic Wedge Flow

Timothy Missing

A dissertation submitted to the Faculty of Engineering and the Built Environment, University of the Witwatersrand, Johannesburg, in fulfilment of the requirements for the degree of Master of Science in Engineering.

Johannesburg, July 2020

Declaration

I declare that this dissertation is my own, unaided work, except where otherwise acknowledged. It is being submitted for the degree of Master of Science in Engineering in the University of the Witwatersrand, Johannesburg. It has not been submitted before for any degree or examination at any other university.

Signed this 28th day of July 2020



Timothy Missing

To my parents Peter and Paula, and my brother Daniel, for their unyielding support.

Acknowledgements

I would like to thank the following people:

Professor B. W. Skews, my supervisor for his guidance and insight throughout this project, as well as my co-supervisor Doctor H. Roohani. Additionally, I am grateful for the help and guidance I received from Doctor R. T. Paton, research officer for the Flow Research Unit.

Mr. S. Riekert and all the technical staff in the North West Engineering Laboratory, without whom the development of the experimental test rig would not have been possible.

My colleagues in the Flow Research Unit, in particular Irshaad Mohamed, for their assistance and invaluable discussions about all manor of fluid dynamics problems.

Abstract

An experimental and numerical investigation was performed to study the effects of accelerating a wedge with an attached shock wave. In particular, the experiment aimed to capture possible curvature of shock waves, which could validate CFD (Computational Fluid Dynamics) results, so that dynamic flow fields could be studied in greater detail. A test rig was designed to rapidly pitch a wedge about a fixed pivot inside a supersonic wind tunnel. A shadowgraph flow visualisation setup was used to capture high speed footage of the shock waves during the motion. Digital image processing techniques were then used to extract the shape of the shock waves, as well as the motion of the wedge. It was found that the experimental setup was unable to provide sufficient resolution of the shock shape to make significant conclusions about the dynamic effects (shock curvature) caused by the rotation. However, the shock wave angles did deviate from the angles predicted for a stationary wedge, beyond the bounds of uncertainty. These deviations could not be correlated clearly with rotational derivatives. However, independent CFD results showed that the shock wave curvature was actually significant on this scale and must be partly responsible for these deviations. Fitting the CFD results to the experiment indicated that there was noise in the experimental results. Possible sources of noise were identified, including vibration of the wedge mounts during rapid actuation.

In addition to a commercial Finite Volume (FV) CFD code used in this study, a new Unsteady Method of Characteristics (MoC) code was developed, based on the modified tetrahedral network by Sauerwein [1]. It is capable of simulating arbitrary motions of an attached shock domain with a flat line surface. Specific modifications to the previous method included a factorisation of the dicretised compatibility equations, which resulted in faster and more robust convergence; a more natural parameterisation of shock point properties which improved the convergence rates and robustness of the shock point solutions; and development of an attached shock tip boundary for the purposes of this study. These codes were

applied to match the Experimental rotations and used for a parametric study of transverse accelerations of attached shock domains. They showed strong agreement in all aspects, on the scale of the dynamic flow features (primarily shock wave curvature) being studied. Additionally, the MoC code was shown to provide smoother results, with less computational effort - largely due to the advantages of a shock fitting approach for this shock bound problem.

Application of these codes to rotating experimental rotation profiles showed how shock waves curve as they lag the motion of the wedge surface. For these relatively slow rotating cases, the angular velocity was the most significant cause of shock curvature, due to the rapid change in surface angle with respect to the upstream flow. It was demonstrated that the shock curvature causes pressure and other flow property gradients to propagate into the bound shock domain, due to its varying tangential angle of incidence with respect to the upstream flow. In the linearly accelerating parametric study, extreme transverse accelerations were applied to an attached shock, oblique wedge domain - producing significant shock wave curvature and pressure gradients in the domain. This curvature was caused by compression and expansion waves generated by the accelerating wedge surface which interact with the incident shock wave to strengthen or weaken it. Once again, the curvature presents as a lagging of the shock wave as it follows the accelerated motion of the wedge. Varying the acceleration resulted in proportionally increased shock curvature. Whereas the curvature was relatively insensitive to varying Mach numbers. Additionally, the relative velocity of the wedge with respect to the upstream flow was shown to produce an initial deviation of the shock angle compared to the static angle for a stationary wedge - which then curved in the opposite direction under the influence of the surface pressure waves.

These numerical results have some significance since they were verified by independent numerical methods. However, it is crucial that a new experiment be designed to provide direct validation for future work - which may also involve curved or three-dimensional geometries.

Contribution

- An experimental test rig was developed which is capable of producing high rotation rates of an oblique wedge in supersonic flow conditions, faster than has been achieved previously in experiments.
- Novel data processing techniques were developed for semi-automatically extracting the shock waves and wedge angles from high speed flow visualisation images, with quantified uncertainties.
- A novel unsteady two-dimensional method of characteristics code was developed based on the Modified Tetrahedral Network by Sauerwein [1]. A factorised form of the compatibility equations was implemented to improve stability and convergence rates. A more natural parameterisation of the shock wave points was implemented, and the non-linear shock wave solutions were solved with a third order method to improve robustness. The code was verified by comparison with a commercial Finite Volume code for rapid wedge rotations and transverse accelerations.

Contents

Declaration **i**

Acknowledgements **iii**

Abstract **iv**

Contribution **vi**

Contents **vii**

List of Figures **xii**

List of Tables **xviii**

List of Acronyms **xix**

List of Symbols **xx**

1 Introduction **1**

1.1 Background and Motivation 1

1.2 Scope and Overview 3

2 Literature Survey **4**

2.1 Supersonic Flow 4
2.1.1 Oblique Wedges 4
2.1.2 Isentropic Flow and Supersonic Wind Tunnels 7
2.2 Acceleration Effects 8
2.3 The Governing Equations 10
2.4 Computational Fluid Dynamics (CFD) 11
2.4.1 Shock Fitting Verses Shock Capturing 12
2.4.2 Finite Volume Methods 13
2.4.3 Method of Characteristics 15
2.4.3.1 Steady Two-Dimensional Method of Characteristics 16
2.4.3.2 Unsteady Two-Dimensional Method of Characteristics 17
2.4.3.3 Method of Characteristics - Conclusions 22
2.5 Flow Visualisation 22
2.6 Three-Dimensional Edge Effects 24

3 Experimental Investigation **27**

3.1 Objectives 27
3.2 Facilities and Apparatus 27
3.2.1 Supersonic Wind Tunnel 27
3.2.2 Optical Setup 31
3.2.3 Test Rig 32
3.2.3.1 Rig Specification 33
3.2.3.2 Wedge Specification 37

3.3 Data Processing 37
3.3.1 Image Scaling 37
3.3.2 Angle Measurement 41
3.3.3 Tip Measurement 44
3.3.4 Angular Velocity and Acceleration 45
3.3.4.1 Angular Velocity and Acceleration - Results 48
3.3.5 Dynamic Oblique Shock Analysis 52
3.3.6 Shock Extraction 55
3.4 Experimental Results 60
3.4.1 Captured Shock Waves 61
3.5 Matching CFD to Experiment 73
3.6 Experiment vs CFD - Results 77
3.6.1 Discrepancies Between Experiment and CFD 82
3.7 CFD Results In Detail 85
3.7.1 Time Series Results 85
3.7.1.1 Shock Waves 85
3.7.1.2 Surface pressures 87
3.7.1.3 Pressure Contours 89
3.7.2 Varying Angular Velocity 92
3.7.3 Varying Mach Number 96
3.8 Conclusions 99
3.8.1 Recommendations 101

4 Method Of Characteristics **103**

4.1 The Characteristic and Compatibility Equations 103

4.2 Notation 105

4.3 Richmond's Iteration Procedure 106

4.4 Field Points 107

4.4.1 Factorising the Cone Compatibility Equation 113

4.4.2 Streamline Characteristic 114

4.4.3 Stability - Domain of Dependence 115

4.4.4 The Field Procedure 117

4.5 Cone Intersections 119

4.5.1 Cone-Plane Intersections 120

4.5.2 Initial Point Estimates 121

4.6 Surface Points 123

4.6.1 Surface Boundary 124

4.6.2 Cone-Surface Intersection: Improved 127

4.6.3 Surface Streamline Characteristic 128

4.6.4 Domain of Dependence 128

4.6.5 The Surface Procedure 129

4.7 Shock Points 130

4.7.1 The Cone Compatibility Equations 131

4.7.2 Domain of Dependence 133

4.7.3 The Shock Procedure 135

4.8 Meshing and the Overall Program 136

4.9 Validation and Performance 140

4.10 Conclusions and Recommendations 141

5 Finite Volume CFD Setup **144**

5.1 Fluid Model 147

5.2 Wedge Motion 147

5.3 Boundary Conditions 148

5.4 Solution Formulation and Methods 149

5.5 Shock Extraction - Post Processing 149

6 Linear Acceleration - Parametric CFD Study **152**

6.1 Mesh and Solver Independence 155

6.2 Flow Field Evolution 158

6.3 Varying Acceleration 161

6.4 Varying Mach Number 163

6.5 Conclusions and Recommendations 165

References **167**

A Test Rig: Dynamic Modelling and Design **170**

B Digital Appendix Contents **173**

List of Figures

1.1 F-35 Lightning II [2] 1

1.2 Oblique shock wave. Stationary (left); rotating (right) 2

2.1 Oblique wedge flow 6

2.2 Oblique shock solutions 6

2.3 Supersonic wind tunnel schematic 7

2.4 Shock capturing vs shock fitting 13

2.5 Finite volume schematic 14

2.6 Two-dimensional steady state Method of Characteristics 17

2.7 Two-dimensional unsteady characteristics 19

2.8 Reference plane characteristic network 19

2.9 Pentahedral network 20

2.10 Modified tetrahedral network 21

2.11 Shadowgraph z-configuration 23

2.12 Finite span wedge 24

2.13 3D edge effects 26

3.1 Wind tunnel overview [3] 28

3.2 Sample stagnation pressure trace 29

3.3 Variable area nozzle 29

3.4 Veeder counter calibration curve 30

3.5 Wind tunnel optics rig [4] 31

3.6 Test rig 35

3.7 Front view - Sharp rig chamfers 36

3.8 Test wedge specification 37

3.9 Scaling grid 38

3.10 Rigid scaling 39

3.11 Least squares scaling 40

3.12 Wedge surface line queries 41

3.13 Measured wedge angles 42

3.14 Sample standard error for angle measurements 43

3.15 Measured wedge angles with error bands 43

3.16 Relative uncertainty sources 46

3.17 Error bands 47

3.18 Wedge angle, velocity and acceleration - varying stopping angle θ_f. with and without error bands. M = 3.3, C = 40mm. Test numbers 6, 7 and 8 in table 3.3 49

3.19 Wedge angle, velocity and acceleration - varying initial spring compression length. with and without error bands. M = 3.3, $\theta_f \approx -12°$. Test numbers 2, 3 and 4 in table 3.3 50

3.20 Wedge angle, velocity and acceleration - varying Mach number. With and without error bands. C = 40mm, $\theta_f \approx -12°$. Test numbers 1, 4 and 5 in table 3.3 51

3.21 Wedge rotation geometry 54

3.22 Dynamic shock theory 54

3.23 Oriented line filter kernel 56

3.24 Convolutional shock filter 56

3.25 Binary filtering 57

3.26 Smoothed line fit 57

3.27 Shock grid transform Illustration 58

3.28 Shock grid 58

3.29 Rectangular shock processing 59

3.30 Captured shock wave 59

3.31 Wedge angle sign convention reference 60

3.32 Rotation profile. Test 3 62

3.33 Oblique shock $\theta - \beta - M$ theory shock line overlay, Test 3. Wedge angle $\theta = 19.57°$, angular velocity $\omega = -99.57°/s$ 63

3.34 Shock wave coordinate transform. Test 3 63

3.35 Shock wave in the $x' - y'$ axis with static and dynamic theory lines . 64

3.36 Shock angle measurement 64

3.37 Shock capture series, Test 3. $\max|\omega| = 8.55{\times}10^3 degrees/s$, $\max|\alpha| = 1.89 \times 10^5\ rad/s^2$ 66

3.38 Captured shock waves. $M = 3$, $C = 40mm$ 70

3.39 Failed shock capturing. Frame **E**. 71

3.40 All measured shock angles. Oblique shock theory lines shown as solid lines with dashed uncertainty bands. Measured angles from experimental frames shown as scattered points, coloured by Mach number, with horizontal and vertical error bars. 72

3.41 Rotation profile extraction 74

3.42 MoC moving line geometry 74

3.43 Wedge rotation symmetry 74

3.44 Extracted FV, and MoC-top, Profile **a-d** 75

3.45 Extracted MoC-bottom profile **b-d** 75

3.46 Finite volume reference frame 76

3.47 CFD - experiment frames 78

3.48 CFD - experiment shock wave results 81

3.49 Experiment shock correction 84

3.50 MoC - shock wave results 86

3.51 CFD surface results 88

3.52 CFD pressure contours. MoC - left, FV - right 91

3.53 Matching frames : varying rotational velocity, sets 1 and 2 - $M = 3$. 94

3.54 Shock wave and surface pressures - varying angular velocity, set 1. $M = 3$, $\theta \approx -10°$ 94

3.55 Shock wave and surface pressures : Varying Angular Velocity, Set 2. $M = 3$, $\theta \approx 3.5°$ 95

3.56 Pressure contours : varying angular velocity, set 1. $M = 3$, $\theta \approx -10°$ 95

3.57 Matching frames : varying Mach number, sets 1 and 2 - $C = 40mm$ 97

3.58 Shock wave and surface pressures - varying Mach number, Set 1. $C = 40mm$, $\theta \approx -8°$ 97

3.59 Shock wave and surface pressures - Varying Mach Number, Set 2. $C = 40mm$, $\theta \approx 4°$ 98

4.1 Field cones intersection 108

4.2 Cone basis 109

4.3 Streamline characteristic 115

4.4 Solution point - domain of dependence 116

4.5 Inscribed circle geometry 116

4.6 Field iteration residuals 118

4.7 Surface cone intersection 124

4.8 Moving line geometry 125

4.9 Surface streamline 128

4.10 Surface domain of dependence 129

4.11 Shock geomtery 131

4.12 Shock domain of dependence 134

4.13 Shock line interpolation 135

4.14 Method of characteristics mesh 137

4.15 Time plane interpolation 137

4.16 Scattered solution points 138

5.1 Finite volume mesh 145

5.2 Dynamic adaption 146

5.3 Finite volume shock capturing 150

5.4 Bounding box 151

5.5 Shock point capturing 151

6.1 Finite Volume (FV) and Method of Characteristics (MoC) meshing . 154

6.2 Captured shock independence 156

6.3 Normalised pressure contours - CFD code comparison 157

6.4 Evolving pressure contours 159

6.5 Evolution of shock curvature 160

6.6 Varying acceleration 161

6.7 Pressure contours - varying acceleration 162

6.8 Varying Mach number 163

6.9 Pressure contours - varying Mach number 164

A.1 Detailed Linkage View 171

A.2 Wedge Spring Moment Variation 171

List of Tables

3.1 Wind tunnel operating conditions 28

3.2 Chronos 1.4 - high speed camera specs 31

3.3 Test matrix 60

3.4 Varying rotational velocity, set 1 - $M = 3$, $\theta \approx -10^\circ$ (top surface) . . 93

3.5 Varying rotational velocity, set 2 - $M = 3$, $\theta \approx 3.5^\circ$ (bottom surface) 93

3.6 Varying Mach number, set 1 - $C = 40mm$, $\theta \approx -8^\circ$ 96

3.7 Varying Mach number, set 2 - $C = 40mm$, $\theta \approx 4^\circ$ 96

4.1 CFD performance comparison 141

5.1 Mesh statistics 144

6.1 Mesh metrics 153

6.2 Flow conditions 155

List of Acronyms

CFD Computational Fluid Dynamics.

FV Finite Volume.

MoC Method of Characteristics.

PDEs Partial Differential Equations.

UDF User Defined Function.

List of Symbols

Q	Dimensionless acceleration parameter
α	Angular acceleration / Normal cone coordinate
β	Oblique Shock Angle / Bicharacteristic cone coordinate
C	Initial spring compression length
ρ	Static density
e	Internal energy
f	Residual
fps	Frames per second
γ	Transverse cone coordinate / Specific heat ratio
Gpx/s	Gigapixel per second
k_s	Spring constant
$M = \frac{V}{a}$	Mach number
ω	Angular velocity
p	Static pressure
$R = 287\, J.kg^{-1}.K^{-1}$	Air gas constant
a	Sound speed
T	Static temperature
$M_\omega = \frac{\omega R_t}{a_\infty}$	Tip mach number
$*_\infty$	Upstream flow condition *subscript
V	Velocity magnitude
$\vec{\mathbf{V}} = (u, v, 1)$	Velocity space-time
$\vec{V} = (u, v)$	Velocity two-dimensional
u	Velocity x-direction
v	Velocity y-direction
θ	Wedge angle / Surface Angle
R_t	Wedge tip length

1 Introduction

1.1 Background and Motivation

Since the first manned supersonic flight of the Bell X-1 (1946), supersonic aircraft have been a prominent feature of military and space aviation. Modern fighter jets such as the F-35 Lightning II, figure 1.1, are capable of maneuvering rapidly during supersonic flight. New developments in supersonic drones and missiles demand even more intense high speed maneuvering capabilities. Therefore it is necessary to develop techniques for modelling these rapid motions involving supersonic air speeds. Before complex three dimensional geometries, such as an aircraft wing, can be studied for cases of rapid manoeuvres, it is necessary to consider simpler cases which become the building blocks of the more complex cases. In particular, this study focuses on a particular type of two-dimensional flow - that of a sharp wedge immersed in supersonic flow, which is then accelerated rapidly. To introduce this, the concept of supersonic flow must first be briefly discussed.



Figure 1.1: F-35 Lightning II [2]

The term *supersonic* refers to the flow of a gas, air in this context, at a velocity V, faster than the speed of sound a of that fluid, with respect to some reference

frame. The Mach number $M = \frac{V}{a}$ characterises the compressibility of a fluid depending on its velocity. When the velocity is supersonic $M > 1$, the gas is able to compress as it interacts with a boundary, such as a wing. In particular, when a supersonic flow encounters a sharp wedge, an oblique shock wave forms, as shown in figure 1.2. The shock wave discontinuously deflects the flow parallel to the wedge surface and simultaneously compresses the gas. This is an elementary supersonic flow phenomenon which is critical to understanding more complex cases. However, it has been observed in previous numerical Computational Fluid Dynamics (CFD) studies [5; 6] that if the wedge is rotated rapidly, the incident shock wave may curve as illustrated. This observation was not critical to these studies and, as yet, this phenomenon has not been studied in detail or observed experimentally. This investigation aims to study the phenomenon in detail using numerical and experimental methods.

Once this simplified geometry has been studied, it is the goal that future work can extend the ideas presented here to more complex cases - such as curved wedge surfaces and three dimensional geometries. It should be noted that this work is quite theoretical. It intends to add to the body of theoretical knowledge, at least in some small way, but does not immediately have direct practical application for specific aerospace engineering practises.

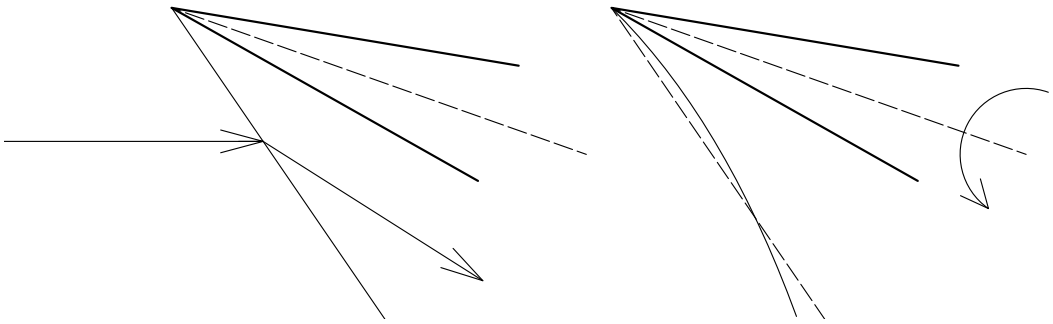


Figure 1.2: Oblique shock wave. Stationary (left); rotating (right)

1.2 Scope and Overview

The scope of this investigation is quite broad. It involves novel experimental and computational approaches which had to be developed largely without a clear guide from previous investigations, since no previous studies have investigated extreme accelerations (sufficient to produce clear shock wave curvature) of oblique wedges with attached shock waves - at least not in a direct, detailed manner. Furthermore, there are many types of accelerations and configurations that could be studied under the heading of this investigation. Ultimately two types of acceleration were considered: Firstly, rapidly rotating cases were investigated experimentally, and in further detail by Computational Fluid Dynamics (CFD) methods. Secondly, more extreme linear transverse (perpendicular to the flow direction) accelerations were studied only numerically. The layout of the investigation is broadly divided into two sections:

1. Experimental: the experimental process is described in detail in section 3. It covers the design of the experiment; the data processing methods employed; the process of matching the CFD models to the experiment; and the final experimental and matching numerical results.

2. Numerical: two CFD codes were used for computational analysis to provide independently verified results. Primarily, this section describes the development of a novel Method of Characteristics (MoC) code developed for this investigation, in section 4. The development and verification of this method is one of the primary outcomes of the overall investigation. The second CFD code is a commercial Finite Volume code, which is briefly described in section 5.

   This section also includes the numerical investigation of transverse linear wedge accelerations.

But firstly, a review of the relevant literature is presented in the following section.

2 Literature Survey

2.1 Supersonic Flow

Information propagates through gases primarily through pressure waves - which have finite velocity (the sound speed a). For an ideal gas, this is given by $a = \sqrt{\gamma RT}$, where $R = 287\ J.kg^{-1}.K^{-1}$ and $\gamma = 1.4$ are the gas constant and specific heat ratio for air. The Mach number $M = \frac{V}{a}$, the ratio of fluid velocity to the sound speed is a key characterisation of fluid flow. When the velocity is greater than the sound speed ($M > 1$) in some reference frame, the flow is said to be supersonic. In which case information cannot pass back into the upstream direction. This has powerful implications for the nature of supersonic flow. For instance, when it encounters a stationary boundary, information about the boundary cannot propagate upstream into the air flow. Whereas subsonic flow might gently curve around a boundary as pressure waves from the surface are sent upstream to turn the flow away; in a supersonic flow, this adjustment of direction occurs instantaneously through shock waves which discontinuously adjust the flow to accommodate the boundary.

Another interpretation of the Mach number, is as a characterisation of the effective compressibility of a moving gas which encounters a boundary. For sufficiently high Mach numbers (approximately $M > 0.3$), the gas will tend to compress significantly - its density will vary greatly. In the supersonic case, shock waves demonstrate this compressibility in an extreme way, as the gas density changes dramatically and discontinuously through the shock wave.

2.1.1 Oblique Wedges

When a supersonic flow encounters an oblique surface, such as the bottom surface of the wedge in figure 2.1a, the flow direction is adjusted abruptly through an oblique shock wave. The shock wave compresses the flow, increasing the density, pressure

and temperature. In reality the shock has finite width, across which these changes occur but for most cases this width may be assumed to be zero.

At the top surface, the flow is turned more gently through an expansion fan, centred at the tip - which reduces the density, pressure and temperature of the flow as it turns towards the surface.

The oblique shock wave and expansion fan always act to turn the flow parallel to the respective surfaces. Equations governing these processes can be derived by asserting the conservation laws which govern compressible fluid flow, as well as this surface boundary condition, across appropriately constructed control volumes. The oblique shock equation implicitly relating the shock angle β to the surface angle θ and the upstream Mach number M_1, is shown in equation 2.1. Where $\gamma = 1.4$ is the the heat capacity ratio for air. Solutions to this relation are shown for a range of Mach numbers in figure 2.2. For each Mach number and surface angle, there are two valid solutions - corresponding to strong and weak solutions, which respectively produce subsonic or supersonic downstream flow. Additionally, notice that there is a maximum surface angle for each Mach number, at which a solution exists. Beyond this angle, the shock wave becomes a bow shock, detached from the wedge as shown in figure 2.1b.

The change of flow properties across the shock wave may be calculated by applying the Rankine-Hugoniot relations (for flow passing perpendicularly through a shock wave) to the normal component of the Mach number $M_{1n} = M_1 \sin\beta$. The normal component of the downstream Mach number and the downstream flow properties are then given by equations 2.2-2.4.

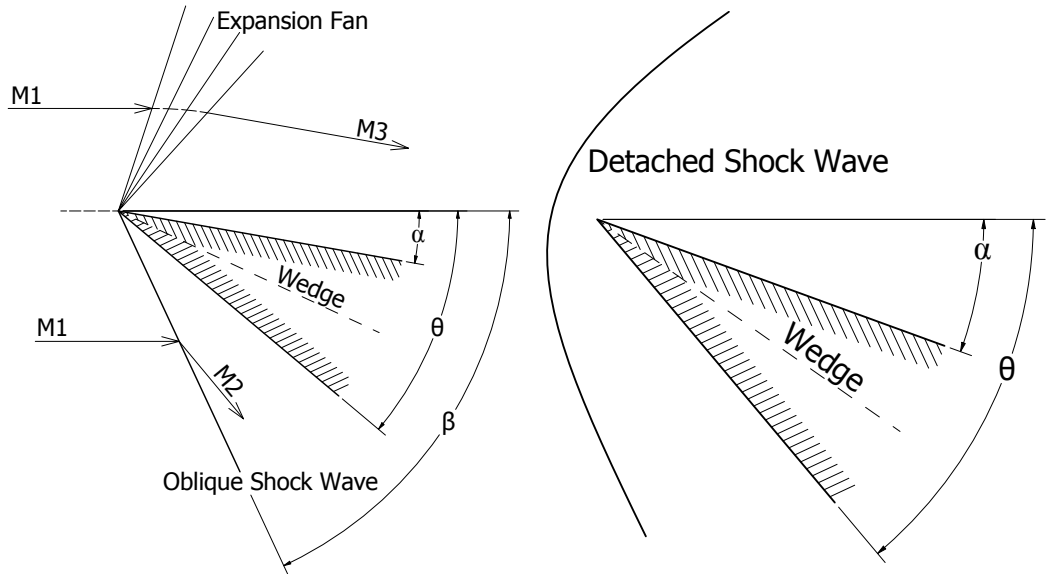
Further details may be found in any standard text book involving high speed aerodynamics, such as Anderson's Fundamentals of Aerodynamics [7].

$$\tan\theta = 2\cot\beta \frac{M_1^2 \sin^2\beta - 1}{M_1^2\left(\gamma + \cos 2\beta\right) + 2} \tag{2.1}$$

$$M_{2n} = \frac{1 + \left[(\gamma-1)/2\right] M_{1n}^2}{\gamma M_{1n}^2 - (\gamma-1)/2} \tag{2.2}$$

$$\frac{p_2}{p_1} = 1 + \frac{2\gamma}{\gamma+1}\left(M_{1n}^2 - 1\right) \tag{2.3}$$

$$\frac{\rho_2}{\rho_1} = \frac{(\gamma+1) M_{1n}^2}{2 + (\gamma-1) M_{1n}^2} \tag{2.4}$$



(a) Attached shock wave

(b) Detached shock wave

Figure 2.1: Oblique wedge flow

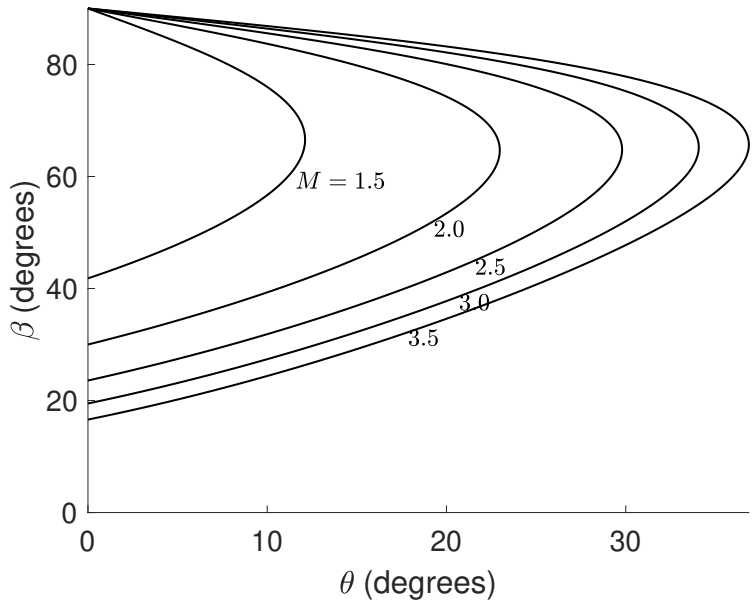


Figure 2.2: Oblique shock solutions

2.1.2 Isentropic Flow and Supersonic Wind Tunnels

Supersonic flow can be generated in a wind tunnel in the following way: when a sufficient pressure difference exists across a nozzle, in figure 2.3, airflow coming from a high pressure reservoir accelerates to Mach 1 at the nozzle throat (minimum cross section), and continues to accelerate and expand to supersonic speeds as it exits the nozzle and enters the test section. Simultaneously, the air density, pressure and temperature decrease.

The Mach number in the test section can be varied by changing the area of the nozzle throat. In the test section, supersonic flow impinges on a test model. The resulting flow field may be observed using visualisation techniques such as schlieren. The airflow is then decelerated at a diffuser to subsonic speeds as it exits the tunnel. It is critical that the test model does not constrict the airflow too much. If the constriction is smaller than the diffuser throat, or produces large pressure losses (due to viscous effects - friction), the tunnel will not be able to start properly and supersonic flow will not be achieved.

If the nozzle is designed correctly, the airflow through the tunnel, up to the test model, can be modelled as isentropic (constant entropy), and equations can be derived to relate the flow properties in the test section to the reservoir stagnation conditions via the test Mach number (M), as shown in equation 2.5 and 2.6 for the static pressure and temperature respectively. The Mach number at any cross-section of the tunnel can be related to the area of that A section compared to the area of the nozzle throat A^*, in equation 2.7.

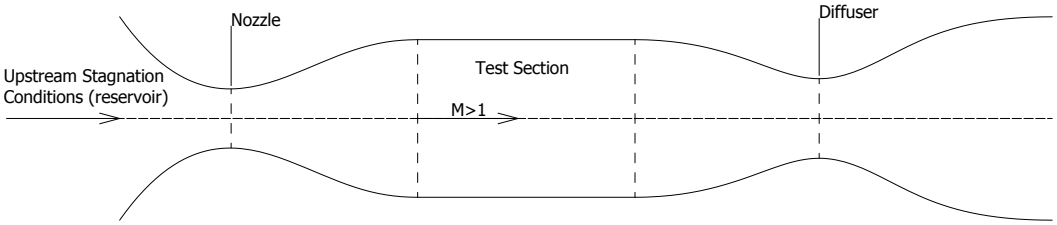


Figure 2.3: Supersonic wind tunnel schematic

$$\frac{P}{P_t} = \left(1 + \frac{\gamma - 1}{2} M^2\right)^{-\frac{\gamma}{\gamma+1}} \tag{2.5}$$

$$\frac{T}{T_t} = \left(1 + \frac{\gamma - 1}{2} M^2\right)^{-1} \tag{2.6}$$

$$\frac{A}{A^*} = \left(\frac{\gamma+1}{2}\right)^{-\frac{\gamma+1}{2(\gamma-1)}} \frac{\left(1+\frac{\gamma-1}{2}M^2\right)^{\frac{\gamma+1}{2(\gamma-1)}}}{M} \tag{2.7}$$

2.2 Acceleration Effects

This investigation involves acceleration of a wedge in supersonic flow. However, relatively few previous investigations have considered effects of acceleration on high speed flow fields, several of which will now be summarised:

Some relatively early studies come from investigations of transition between regular and Mach reflections (types of shock wave reflections). These studies dynamically pitched a wedge shock generator (a wedge which creates an oblique shock wave) to study the effects on this reflection transition. This transition phenomenon is not directly relevant here, but it has been observed in several of these studies that the shock wave may become curved under extreme rotation rates. In particular, Felthun and Skews [5] simulated rapid rotations of a shock generating wedge about its leading edge, using an Arbitrary Lagrangian Eulerian finite volume scheme, with trailing edge Mach numbers (the ratio of the trailing edge velocity to the upstream sound speed $M_T = \frac{V_T}{a_\infty}$ - this is a non-dimensional characterisation of the rotation rate) up to $M_T = 0.1$, and found significant shock wave curvature. This shock curvature was also observed by Khotyanovsky et al. [6] in numerical simulations in which a wedge was rotated about its trailing edge. In that case a leading edge Mach number $M_E = \frac{V_E}{a_\infty}$ was used to non-dimensionalise the rotation rate. Leading edge Mach numbers up to 0.1 were simulated and once again curvature of the incident shock wave was observed.

Naidoo and Skews [8] experimentally studied rapid symmetrical rotations of a pair of shock generating wedges about their trailing edges. Where the tip velocity $V_E = \omega R$ is given in terms of the rotational velocity ω and the tip length from the rotation pivot R. A maximum experimental rotation rate of $M_E = 0.033$ ($\omega = 11,000°/s$) was achieved, but shock curvature was not observed experimentally. Thus far it appears that no shock wave curvature caused by rapid motions have been observed experimentally.

Roohani and Skews [9] investigated linear (unidirectional) accelerations of a two-dimensional biconvex aerofoil in a free-stream air flow with upstream Mach numbers between $0.1 < M_\infty < 1.6$ and linear positive and negative accelerations along the

flow direction of up to $1041m/s^2$. It was found that the accelerated cases resulted in significant changes to drag and lift coefficients compared to steady cases.

Gledhill et al. [10; 11] presented the Navier-Stokes equations (the general governing equations of fluid dynamics) transformed to a generalised non-inertial reference frame (accelerating reference frame) so that Computational Fluid Dynamics (CFD) simulations could be solved for arbitrary motions of surface bodies. By non-dimensionalising flow variables using upstream flow conditions (e.g. pressure: $\hat{p} = \frac{p}{p_\infty}$), non-dimensional similarity parameters can be derived which help to characterise the influence of various effects on the flow field. In particular, by this process, the non-inertial terms (source terms) provide relative acceleration and velocity similarity parameters which help to characterise the influence of acceleration and relative velocity on the flow field. Additionally, the full set of similarity parameters provide a basis for achieving dynamic similarity: if flow fields on different scales have the same similarity parameters and the geometry is rigidly scaled, then the non-dimensional flow variables (e.g $\hat{p}$) will be identical at all corresponding points. This property is often used to simulate full scale aircraft using scaled down models in a wind tunnel. The inviscid non-dimensional terms relevant to this study, which are discussed by Gledhill et al. [11], will be described briefly:

1. Firstly the standard inertial frame dimensionless terms applicable to inertial or non-inertial frames are: the Mach number $M = \frac{V_\infty}{a_\infty}$; the Strouhal number $S_t = \frac{V_\infty t_0}{L}$, where L and t_0 are length and timescales respectively; and the Euler number $E_u = \frac{\rho_\infty V_\infty^2}{p_\infty}$. However, for Ideal gases, the Euler number is not independent from the Mach number: $E_u = \frac{\rho_\infty V_\infty^2}{p_\infty} = \gamma M^2$, since the sound speed $a_\infty = \sqrt{\gamma \frac{p_\infty}{\rho_\infty}}$. So the inertial frame similarity parameters are the Mach number and Strouhal number. The Strouhal number has been used to characterise oscillating flow mechanisms, but that usage is not relevant in this study, so in this context it is just another term needed to achieve dynamic similarity.

2. The acceleration terms are the linear (unidirectional) acceleration parameter $Q = \frac{La_c}{V_\infty^2}$, where a_c is the linear acceleration magnitude; and the Rossby number $R_o = \frac{V_\infty}{2\omega L}$, which characterises rotational velocity effects. However, only the linear acceleration parameter Q will be used in this study.

Gledhill et al. additionally applied the transformed equations to simulate an accelerating axisymmetric missile flare in a non-inertial reference frame. The flare was accelerated from transonic Mach numbers ($0.8 < M < 1.2$) with a linear acceleration

of up to $4,500m/s^2$. Wave drag was found to reduce by up to 20% compared to the steady case.

The term 'flow history' was used in several of these studies to refer to the dependence of flow fields on disturbances from earlier times, which have not yet dissipated. This is a fundamental character of unsteady fluid dynamics. In particular, any acceleration of a body in a fluid will produce a flow field that differs from the corresponding steady case at the same velocity, because at each increment of time, the change in velocity produces disturbances which propagate at finite speed (limited by the sound speed) through the domain. These disturbances will still be present at future times, until they have dissipated or left the domain of interest. Therefore, it is necessary to consider the time period required for such disturbances to leave the domain when considering a particular flow field - any disturbance which occurred during that *flow history* period must be considered when interpreting the current flow field.

2.3 The Governing Equations

Particular flow phenomena, such as oblique shock waves and acceleration effects have been discussed. Now the full set of governing equations will be presented, with simplifying assumptions. Application of these equations to simulating the relevant phenomena will follow.

In this study air will be modelled as an inviscid, ideal gas. Additionally, the flow will be assumed to be adiabatic (no heat transfer). The effects of air viscosity are generally insignificant in the flow field away from boundaries. Near wall surfaces, viscous effects become significant. Wall boundary layers - regions of slow moving air near to walls - have the potential to significantly effect regions away from the surface, particularly when separation occurs - when the free stream separates from regions of stagnated (or slower moving) air which form particularly in the wake of bodies. However in the case of an oblique wedge, the boundary layer growth begins at the wedge tip, and grows along the surface, but is not likely to have enough distance to grow to any significant size. Consider, the turbulent boundary layer growth on a flat plate in equation 2.8 [7], where $Re_x = \frac{Vx}{\nu}$ is the Reynolds number, which helps to characterise viscous effects, in terms of the fluid velocity V, characteristic length x (in this case, the surface distance measured from the wedge tip), and the kinematic viscosity ν. For a supersonic flow at Mach 3 and a wedge surface length of $50mm$, the boundary layer height δ would be expected grow to a height on the

order of about $0.5 - 1mm$. The displacement of the flow would be even smaller. Additionally, any form of flow separation is very unlikely over this short, flat surface facing the upstream flow.

$$\delta = \frac{0.37x}{Re_x^{1/5}} \tag{2.8}$$

The equations governing inviscid, adiabatic compressible flow are the Euler equations, shown in differential form in equations 2.9-2.12, [12]. In order, these represent mass continuity; conservation of momentum in the x- and y-directions (with velocity components u and v); and the conservation of energy. The internal energy e is related to the static temperature by $e = c_v T$ (assuming constant specific heat), and the equation of state for ideal gases $p = \rho RT$ relates the pressure p, density ρ and temperature, with the gas constant for air $R = 287 J.kg^{-1}.K^{-1}$.

$$\frac{\partial \rho}{\partial t} + \bigtriangledown \cdot \left(\rho \vec{V}\right) = 0,\ \vec{V} = (u, v) \tag{2.9}$$

$$\frac{\partial \rho u}{\partial t} + \bigtriangledown \cdot \left(\rho u \vec{V}\right) = -\frac{\partial p}{\partial x} \tag{2.10}$$

$$\frac{\partial \rho v}{\partial t} + \bigtriangledown \cdot \left(\rho v \vec{V}\right) = -\frac{\partial p}{\partial y} \tag{2.11}$$

$$\frac{\partial \rho E}{\partial t} + \bigtriangledown \cdot \left(\rho E \vec{V}\right) = - \bigtriangledown \cdot \left(p \vec{V}\right),\ E = e + \frac{V^2}{2} \tag{2.12}$$

2.4 Computational Fluid Dynamics (CFD)

Not all fluid dynamics phenomena can be studied in sufficient detail by experiment. Therefore it has been a staple of fluid dynamics research to model phenomena using computer simulations, which generally can provide far greater detail. These computer simulations rely on solving forms of the Navier-Stokes equations which model general continuum fluid dynamics. These equations generally do not have analytical solutions. Therefore, the general philosophy of fluid dynamics is to dicretise (break into small elements) fluid domains in various ways so that the partial deviates in the equations can be replaced by some form of finite difference. The finite approximations to all discretised elements then form a set of algebraic equations which may be solved using linear or non-linear solution methods. Usually this involves integrating a fluid domain forward in time, based on the discretised time derivatives.

A critical aspect of the CFD approach is validating results. CFD models are not perfect; they often do not accurately model particular physical flow phenomena. Therefore it is generally desirable to obtain some validation by matching results with experiment. Once a CFD model is validated for a particular case, it can provide greater detail and insight into the phenomenon than could be obtained from experiment. Additionally, the model may then be applied to similar cases to study a greater range of variables, which potentially could not easily or rapidly be setup experimentally. In cases where direct experimental validation is not available, results from a CFD model may instead be compared to the results of an independent CFD calculation (ideally using a vastly different CFD method): if two independent CFD models agree to a sufficient level of accuracy on a particular prediction about some flow phenomenon, then the researcher can at least have some confidence in the accuracy of the results with respect to the physical problem being modelled; at least in the sense that the results appear to represent accurate and repeatable solutions to the relevant governing equations.

Two CFD approaches will now be described as they will both be applied in this investigation. But first the shock fitting and shock capturing methods of simulating shock waves will be discussed briefly.

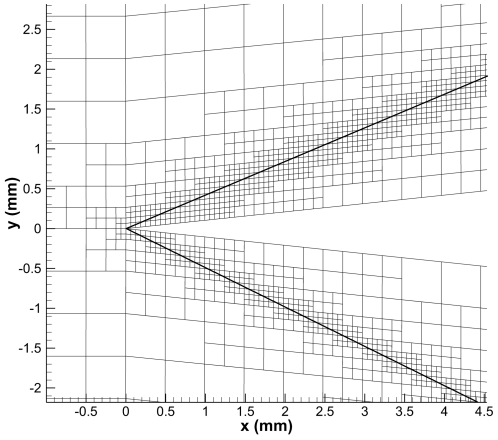
2.4.1 Shock Fitting Verses Shock Capturing

An important aspect of simulating supersonic flows is handling shock waves. Strategies for simulating shock waves may be broadly classified in two categories: shock capturing, and shock fitting schemes. Shock capturing schemes rely on the spatial discretisation scheme to naturally capture shock waves, as illustrated in figure 2.4a, for a Finite Volume (FV) scheme, where the solid line indicates the approximate location of the shock wave. The shock wave exists as a rapid change in flow properties, but spread over a finite span of cells. Cells with steep gradients in flow properties are refined - split into smaller cells to improve shock resolution. But the exact location of shock points is not part of the solution process.

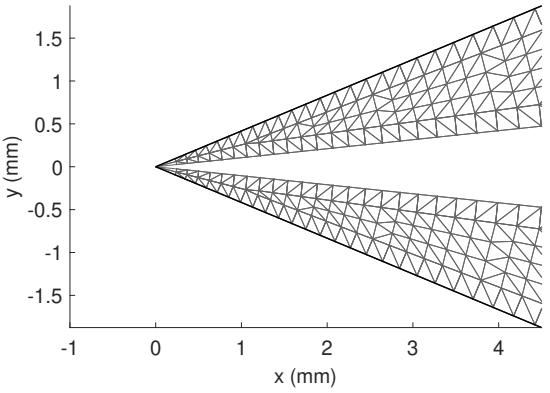
Whereas, shock fitting schemes treat shock waves as dicrete line (2D) or surface (3D) boundaries in the flow field, as shown in figure 2.4b for the Method of Characteristics (MoC) scheme. These schemes use the Rankine-Hugoniot shock relations to calculate the change of flow properties across the shock wave and determine how shock points evolve in time.

Shock capturing schemes have the advantage of simplicity in handling complex shock configurations - they are naturally resolved without having to explicitly define shock boundary intersections. Therefore shock capturing schemes are generally more common for studying complex flow configurations. However, in order to obtain sufficient resolution of shock waves, these schemes often require extremely fine cells along the shock waves, which leads to large cell counts and high computational loads. Whereas shock fitting schemes resolve shock waves as precise boundaries and do not require fine cells [12].

Most finite volume schemes (and other methods) use shock capturing. However it is possible to apply shock fitting methods to these schemes. For example, Paciorri and Bonfiglioli [13] applied mixed shock fitting and shock capturing schemes to a complex shock reflection configuration, with multiple shock interfaces. They demonstrated that there is potential for shock fitting schemes to improve shock resolution even for complex flow fields.



(a) FV - shock capturing



(b) MoC - shock capturing

Figure 2.4: Shock capturing vs shock fitting

2.4.2 Finite Volume Methods

Finite Volume (FV) methods are commonplace in the fluid dynamics community and exist in many variations. This section aims to provide a brief introduction to the basic concept. For further details see the following references, [14; 15].

Finite volume methods are termed by the fact that they conserve mass, momentum and energy at a discrete level - within individual cells. These methods have the additional advantage of being applicable to unstructured meshes, as illustrated

in figure 2.5. The two-dimensional Euler equations, from section 2.3, written in integral, vector form - for an enclosed cell volume V - are shown in equation 2.13.

Consider the cell with center Q_0 in figure 2.5 - where Q_0 represents the primitive flow variables ρ, u, v, e at this point. The conserved variables $\boldsymbol{W}$ (derived from Q_0) are integrated over the cell volume (with unit depth) - the first term in equation 2.13 - by taking W_0 as an average at the cell center: $\int_V \boldsymbol{W} dV = VW_0$. Where V is the cell volume (area $\times$ unit depth). The second term is the surface integral of the flux vector $\boldsymbol{F}$ over the cell boundary. Once the components of the flux vector are calculated at the midpoints of the cell faces, the surface integration is given by the sum of the flux vector components, normal to the cell faces: $\sum \vec{f_i} \cdot \vec{A_i}$. Finally, the source terms $\boldsymbol{H}$ are replaced with the cell average at the center $\int_V \boldsymbol{H} dV = VH_0$. Now, equation 2.15 can be discretised in time by taking finite differences of the conserved variables $\boldsymbol{W}$ with respect to time. These equations applied to each cell in a fluid domain can now be solved to step forward in time. In order to properly resolve shock waves, the flux vectors at the cell faces must be calculated using an upwind scheme, which extrapolates variables from the directions in which flow information travels (characteristic directions). The choice of upwind scheme and time discretisation results in different orders of spatial and temporal accuracy of the solution.

This general process may be applied to complex fluid dynamics problems to resolve steady state and time dependent flow fields which predict real world flow phenomena.

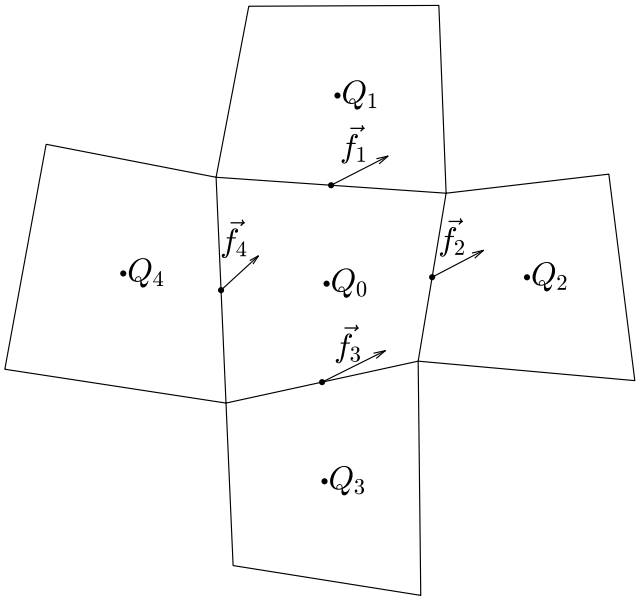


Figure 2.5: Finite volume schematic

$$\frac{\partial}{\partial t}\int_V \boldsymbol{W} dV + \oint \boldsymbol{F}\cdot dA = \int_V \boldsymbol{H} dV \tag{2.13}$$

$$\boldsymbol{W} = \begin{bmatrix} \rho \\ u\rho \\ v\rho \\ E\rho \end{bmatrix}, \quad \boldsymbol{F} = \begin{bmatrix} \rho\vec{V} \\ \rho\vec{V}u + p\vec{i} \\ \rho\vec{V}v + p\vec{j} \\ \rho\vec{V}E + p\vec{V} \end{bmatrix}, \quad E = e + \frac{1}{2}|\vec{V}|^2 \tag{2.14}$$

$$\vec{V} = \begin{bmatrix} u & v \end{bmatrix}, \quad \begin{bmatrix} \vec{i} \\ \vec{j} \end{bmatrix} = \begin{bmatrix} 1 & 0 \\ 0 & 1 \end{bmatrix}$$

$$V\frac{\partial}{\partial t}\boldsymbol{W_0} + \sum \vec{f_i}\cdot\vec{A_i} = V\boldsymbol{H_0} \tag{2.15}$$

2.4.3 Method of Characteristics

In this section, the Method of Characteristics (MoC) approach will be introduced to provide the theoretical grounds for the specific formulation of this method in section 4, and its application in sections 3 and 6.

Method of Characteristics techniques are a family of methods applicable to hyperbolic Partial Differential Equations (PDEs). Roughly speaking, hyperbolic PDEs produce wave-like solutions, in which disturbances do not propagate to all regions of the coordinate space (there is a limited domain of influence). For example, supersonic flow is hyperbolic in space: a small disturbance at a point in the supersonic flow travels at the speed of sound. But since the fluid moves faster than this speed, information from the disturbance cannot travel upstream. The downstream region which may be influenced by the point disturbance is a cone with its apex at the point, and a cone angle given in terms of the Mach number: $\sin\mu = \frac{1}{M_\infty}$ - referred to as a Mach cone [12].

Hyperbolic PDEs have a property that derivates of independent variables with respect to the coordinate space may be discontinuous along specific directions. Hypersufaces (with one fewer dimension than the coordinate space) whose normals correspond to these indeterminate derivative directions at every point are called characteristic surfaces. For a two- or three- dimensional supersonic flow, the characteristic surfaces are Mach cones. Flow derivatives normal to these cones may be discontinuous.

If the coordinate system is transformed so that one of the new coordinates is aligned normal to a characteristic surface, and the hyperbolic equations are transformed

to these coordinates, then it is possible to take combinations of the transformed equations such that partial derivatives along the characteristic surface normals are eliminated. This is necessary since these derivatives may be undefined (discontinuous). However, this process also yields hyperbolic PDEs in one fewer independent coordinate than the original space - called the compatibility equations, which are specific to particular characteristic surfaces. These compatibility equations can then be discretised along the characteristic surfaces and solved simultaneously with equations from other characteristic surfaces intersecting at common points to obtain new solution points, which advance along the characteristic directions.

2.4.3.1 Steady Two-Dimensional Method of Characteristics

To introduce these concepts, consider the case of a steady two-dimensional supersonic flow, in figure 2.6. Where flow variables are known along an initial line $1-2$. The characteristics emanating from these points are Mach cone-lines (the projection of Mach cones in two-dimensions), with cone angles corresponding to the local Mach number; counter clock wise C_+ and clock wise C_- from the fluid velocity vectors. The governing equation is the steady state two dimensional Euler equation which has two independent coordinates (x, y). Therefore, compatibility equations derived along the characteristic lines become differential equations in one coordinate (the length coordinate along the characteristic lines) - which is an ordinary differential equation (ODE). If, additionally, the flow is assumed to be isentropic, it turns out that the ODEs for the line characteristics have analytical solutions. Therefore solving the compatibility equations for the characteristic lines reduces to solving a set of algebraic, but non-linear equations. Which also happen to have an analytical solution. Therefore, the solution proceeds as follows: determine the cone angles μ_1 and μ_2; approximate the C_- line from 1 and the C_+ line from 2 as being straight, and find their intersection at 3 - for a sufficiently fine mesh, the straight-line approximation becomes sufficiently accurate. Now obtain the non-linear equations along $1-3$ and $2-3$. Solve these simultaneously for the state at 3. This process is applied to all sets of points along an initial data line so that a new set of points are obtained, stepped forward in space.

Points which lie along a surface or shock boundary may also be handled. In the case of a surface boundary: a characteristic line from a point in the flow field is projected to the surface. Now, for the surface point, the wall boundary condition (the velocity component normal to the wall is zero) replaces the compatibility equation which would have come from a second field point. The compatibility-boundary condition

equations are solved simultaneously for the new wall point. Similarly, for a shock wave boundary (particularly a weak oblique shock - with supersonic downstream conditions), a field point line characteristic is projected to the shock wave. If the conditions upstream of the shock wave are known, the Rankine-Hugoniot shock relations can be applied to find the downstream flow state. However, the shock will generally be curved and the angle and position of the characteristic line-shock intersection, and the shock angle at this point, are variable. In fact the solution here aims to solve for the changing shape of the shock wave (along the downstream direction): the new shock point and angle are found such that the characteristic line intersects the shock at this point and the compatibility equation is satisfied by the downstream shock state. This solution is relatively complex, generally requiring an iterative solution. Further details on the steady two-dimensional MoC may be found in most standard fluid dynamics text books, for example [7].

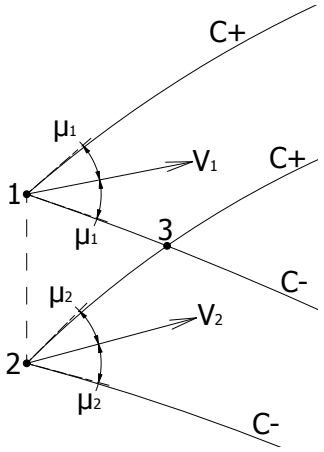


Figure 2.6: Two-dimensional steady state Method of Characteristics

2.4.3.2 Unsteady Two-Dimensional Method of Characteristics

The two-dimensional steady state form of the Method of Characteristics is perhaps the most widely known form of the method in the fluid dynamics community. However, the general Method of Characteristics is equally applicable to hyperbolic PDEs with more than two independent variables. This includes steady supersonic flow in three dimensions as well as any unsteady flow (subsonic or supersonic): the transient Euler equations, for two or three spacial dimensions, are always hyperbolic in time, in the sense that disturbances have limited domains of influence in space-time (disturbances propagate at a finite rate).

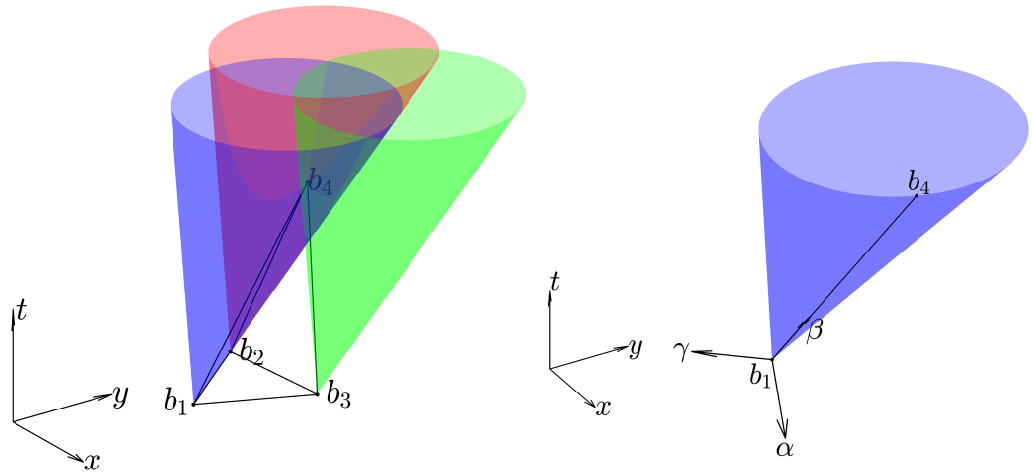
The Method of Characteristics appears to have been applied to three independent variables first by Thornhill [16]. In the two-dimensional unsteady case, applied in

this investigation, time is seen as a third coordinate, on equal footing with the spatial coordinates. The characteristic surfaces become cones in this x, y, t space, as shown for the tetrahedral network, presented by Thornhill, in figure 2.7a - which intersect at the solution point b_4. These are the domains of influence from base points b_1, b_2, b_3 all at the same initial time plane. According to the general Method of Characteristics, compatibility equations must then be derived from the unsteady Euler equations by transforming the x, y, t coordinates to a new set of coordinates $\alpha_i, \beta_i, \gamma_i$, shown in figure 2.7b, for each cone $i = 1, 2, 3$, so that one of these coordinates α_i is normal to the cone along a given bicharacteristic line (joining base point i to the solution point b_4 - tangent to the cone); and another direction β_i is aligned with the bicharacteristic line. The third direction γ_i is commonly taken perpendicularly to α_i and β_i. The compatibility equations are then taken as combinations of the unsteady Euler equations in these new coordinates such that flow derivatives along the α_i direction are eliminated. Simultaneously, one of the dependent variables - usually from the energy equation - will no longer be included in terms of its partial derivatives. The partial derivatives in the compatibility equation must then be disretised by taking finite differences in the cell. Differences in the β direction are taken between the solution point and base points, while γ differences must be obtained from differences involving neighboring cell points.

The discrete compatibility equations for each base point are then solved simultaneously for solution point at b_4 - thereby stepping forward in time. However, these equations are in terms of three dependent flow variables at the solution point, so an additional equation is needed for the final flow property. This comes from another characteristic: the streamline passing through the solution point from the initial solution plane. The corresponding compatibility equation is the energy equation along a streamline, which for inviscid, adiabatic, unsteady flow is the entropy equation $\frac{Ds}{Dt} = 0$ or $s = const.$ along the streamline.

Surface boundary points are solved by intersecting two characteristic cones with the surface boundary and using the surface boundary condition as the third equation, along with the compatibility equations for the two cones, to solve for the solution state on the surface. This process permits arbitrary surface motions. Motions of two-dimensional surfaces (lines) trace out three-dimensional hypersurfaces in space-time, whose normals are used for the boundary conditions in unsteady calculations.

Several developments of the unsteady Method of Characteristics will now be discussed. Subsequent to Thornhill, Sauer [17] and Ferrari [18] proposed a reference plane network, shown in figure 2.8, which computes compatibility equations along



(a) Characteristic cones - tetrahedral network

(b) Transformed coordinates

Figure 2.7: Two-dimensional unsteady characteristics

characteristics intersecting reference planes $y = const.$ and $t = const.$ Compatibility equations along these lines $(1-5,\ 3-5,\ 2-6,\ 4-6)$ may then be solved in combination with an additional equation along $5-6$. In general, the intersection of characteristic lines from 1 and 3 at 5 will not be at the same time coordinate as 6. Therefore an additional step involves extrapolating 5 back to 7 and finding a new base point 8 whose characterisic line intersects at 7. This network has the advantage of potentially simplified geometry and intersection calculations (it avoids 3-dimensional cone intersections). However, it is potentially less accurate than the bicharacterstic method described previously, because it does not take differences along the true characteristic directions.

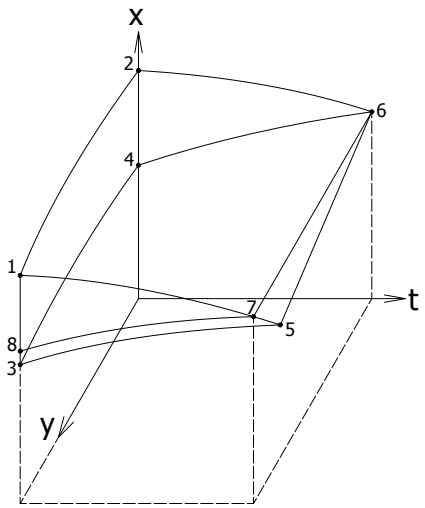


Figure 2.8: Reference plane characteristic network

Holt [19] extended a form of the reference plane network to handle shock wave boundary points. A point along a shock boundary is determined by solving for a new shock point which intersects with two adjacent field point cones, such that the space-time normal vector (of the shock surface) produces a downstream flow state (using the Rankine-Hugoniot equations) which satisfies the two cone compatibility equations. The shock space-time normal represents the orientation of the shock normal in x, y space as well as its velocity along its normal direction - as the third coordinate.

One issue with the networks presented thus far is that the cone compatibility equations contain partial derivatives along a direction tangential to bicharacteristic lines. For the tetrahedral network, this is the γ direction. Recall that the α derivatives are eliminated from the compatibility equations, while β derivatives may be discretised by finite differences between the base points and solution point. The γ derivatives must be discretised in terms of neighboring cell points and require finite difference approximations in all three space-time coordinates. Therefore the accuracy of the overall solution depends on the accuracy of these finite differences. Butler [20] suggests a method for eliminating these cross derivatives by introducing an additional base point, in figure 2.9. Where the cone of dependence from the solution point b_5 is shown - which is tangent to the characteristic cones from the base points. The compatibility equation for this additional bicharacteristic is used to eliminate the γ derivatives. Using this approach Butler was able to achieve third order accuracy in time and space.

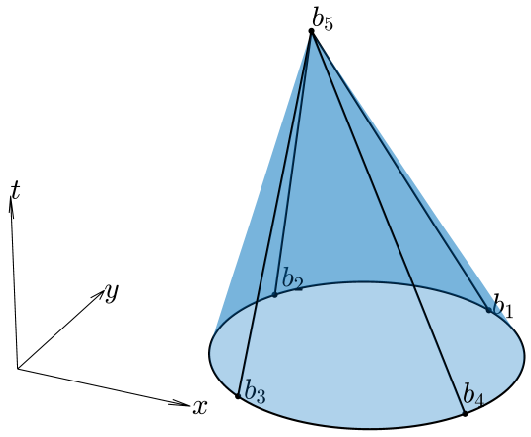


Figure 2.9: Pentahedral network

Sauerwein [1; 21] modified Thornhill's original tetrahedral network, noting that it did not satisfy the Courant-Friedrichs-Lewy (CFL) stability condition for hyperbolic PDEs [22]. Consider figure 2.10. The domain of dependence of b_4 is shown. This is the region from which disturbances in the flow field may reach the solution point -

it is the counterpart of the domain of influence. In the original network (b_1, b_2, b_3, b_4), the domain of influence includes points in the initial solution plane which are outside of the convex hull of the base points (the base point triangle). This violates the CFL stability condition (which places this limit on the domain of influence), and Thornhill's original network is found to become unstable after sufficiently many time steps.

Sauerwein's modified method starts with the outer points B_1, B_2, B_3 in the initial solution plane. The inner triangle is then constructed inside an inscribed circle. This ensures that the CFL condition is satisfied. Additionally, Sauerwein extended the Method of Characteristics to problems with four independent variables x, y, z, t so that unsteady three-dimensional problems could be solved; and applied a multi-step time integration procedure, using average flow variables along the bicharacteristics at each step, to achieve higher order accuracy. The method seems to be second order in space and time. However this accuracy was not rigorously analysed, due to the inherent complexity of the procedure.

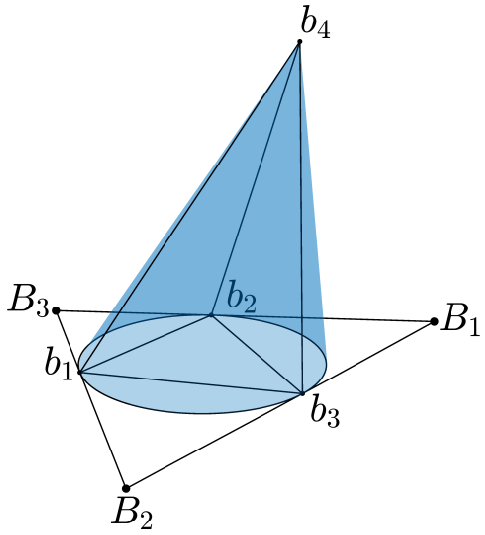


Figure 2.10: Modified tetrahedral network

These developments in the MoC method took place before sufficiently powerful computing capabilities were available to run large scale simulations over many time steps. Therefore, there have not been many applications of these methods. To mention a few: Sauerwein [21] applied the modified tetrahedral network to the problem of a detached bow shock ahead of a blunt two-dimensional accelerating body; Rakich [23] applied the reference plane method to steady supersonic flow with inclined bodies of revolution; Delaney [24] applied a method similar to the pentahedral network by Butler [20] to turbo machinery cascades.

2.4.3.3 Method of Characteristics - Conclusions

More detailed reviews of developments in the Method of Characteristics approach can be found in the following references [1; 21; 24]. Several authors claim that these methods have the potential to be more accurate than other CFD methods due to the direct treatment of characteristic directions. However, these methods seem to have fallen out of favour in recent years. This is likely due in part to the relative complexity in setting up the characteristic networks. Additionally, MoC schemes require careful treatment and definition of shock and surface boundaries; whereas FV schemes are more amenable to general setups - allowing fluid dynamics problems with complex geometries and governing equations to be modelled with relative ease.

The Method of Characteristics approach is applied in this investigation because the accelerating oblique shock wave problem involves a simple fluid domain geometry, between surface and shock wave boundaries. Since MoC methods treat these boundaries explicitly (they are shock fitting schemes) and potentially provide high accuracy, they should offer high accuracy and precision in terms of shock wave curvature effects. Additionally, since only the surface-shock bound region needs to be simulated, the MoC approach avoids the high cell count from the extended domain and adapted shock capturing cells required by the FV method - thereby potentially reducing the required computational effort. Specifically, a method is developed based on Sauerwein's modified tetrahedral network. Which is relatively simple, compared to Bulter's method, while still offering accuracy and stability.

2.5 Flow Visualisation

In this investigation, experimental measurement of shock waves will come from high speed images obtained during rotations of a wedge in supersonic flow. However, shock waves cannot readily be seen without techniques which emphasise their optical properties. In particular, a Shadowgraph technique is applied.

Consider the Z-Configuarion in figure 2.11. A point light source is reflected off a parabolic mirror, creating a parallel beam which is passed through the test section. This beam is focused by a second parabolic mirror onto the image sensor of a camera. The refractive index of air varies with its density, and air density changes rapidly through shock waves. So the rapid change in refractive index through shock waves causes light rays to refract. The parallel light rays which would have passed to the camera are diverted, presenting as darker regions on the image plane. In this

way, rapid changes in density caused by shock waves, and other flow features, are visualised as shadows on the image.

In fact the change in light intensity at point on the image plane is proportional to the magnitude of the second order spatial derivatives of the density $\sqrt{\left(\frac{\partial^2\rho}{\partial x^2}\right)^2 + \left(\frac{\partial^2\rho}{\partial y^2}\right)^2}$ [25].

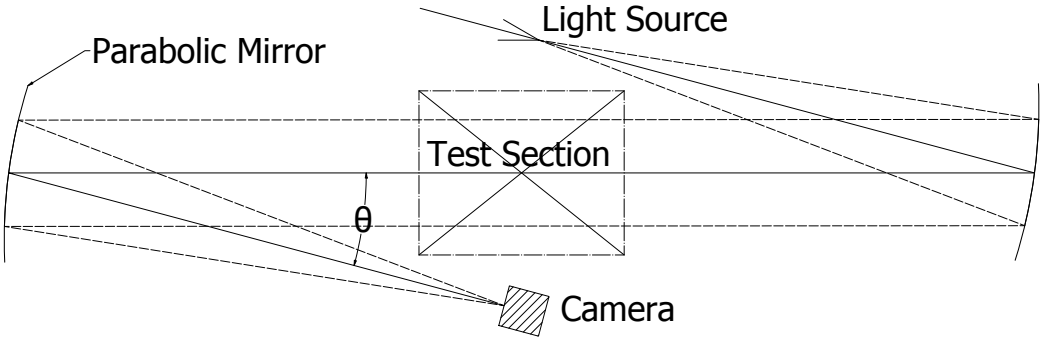


Figure 2.11: Shadowgraph z-configuration

2.6 Three-Dimensional Edge Effects

Investigations of two dimensional flow phenomena, e.g. in an $x-y$ plane, are studied experimentally in three dimensions (the real world) by ensuring that changes in the flow field along the z direction are insignificant. Two-dimensional oblique shock problems must be studied in the real world using a wedge of finite span. Such a wedge is used in this investigation, as shown in figure 2.12. In these cases, the two-dimensional flow being considered occurs along the vertical symmetry plane dividing the wedge along its width. Skews [26] showed that disturbances at the leading corners and along the sides of the wedge propagate towards the symmetry plane (along Mach cones) until, after some length, the flow in the symmetry plane is effected by these corner signals, and the assumption of two-dimensional flow becomes invalid beyond this point.

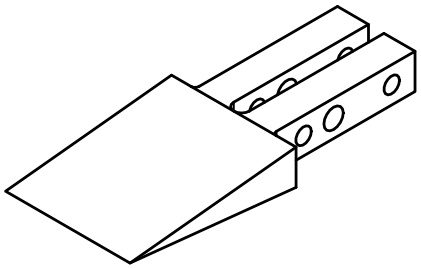


Figure 2.12: Finite span wedge

Skews derived an expression for the distance along the wedge at which an attached shock wave becomes influenced by these three-dimensional effects. A similar analysis will now be shown, but the shock wave along the symmetry plane will be treated as a general curved line defined by a set of discrete points (rather than a straight continuous line), so that it may be applied to the discrete shock points captured in the experimental investigation.

Consider the view from just downstream of the wedge in figure 2.13. Half the wedge is shown, split by the vertical symmetry plane. The incident shock is shown to curve around the edge of the wedge due to expansion of the air flow around the wedge edges (these are three-dimensional effects). A Mach cone is centered at the wedge corner, with a cone angle deriving from the flow Mach number just behind the incident shock wave. A full cone is shown for clarity but is really only valid behind the shock wave. Where this cone intersects the symmetry plane, three-dimensional effects begin to alter the assumed two-dimensional flow. A slightly lesser restriction can be taken at the intersection of the cone with the shock line along the symmetry plane. This analysis assumes that the flow properties behind the shock wave (between the

shock and the surface) are uniform, which is not true for accelerating cases, but is expected to be a good approximation unless the acceleration becomes sufficiently large. For the accelerations achieved in the experimental tests in chapter 3, the matching CFD results demonstrate only relatively small variations in flow properties within the domain bound between the shock wave and wedge surface. Therefore, this approximation is assumed to be appropriate.

Consider the coordinates x', y', z' centered at the wedge corner, with the x'-axis aligned along the upper surface. The corner Mach cone is aligned with the x'-axis and is defined by the locus of points along a circle, in the $z' - y'$ plane, growing along this axis, starting from the origin. The radius grows linearly along this axis according to the Mach cone angle, in equation 2.16. The discrete shock points (x_i, y_i) captured from the experiment are transformed to the (x', y') coordinates and shifted (by half the wedge width w) to the symmetry plane as shown in equation 2.17. The distance from the x'-axis to the shock line along the symmetry plane, at a given x' coordinate, is given by equation 2.18. Finally, the two-dimensional limit (after which, three-dimensional edge effects alter the shock wave) is given by equation 2.19. This limit is evaluated for each discrete shock point until the limit is reached. This limit then defines the valid region in the symmetry plane which can be assumed to behave two-dimensionally.

$$R_{cone} = x' \tan(\mu) \tag{2.16}$$

$$\vec{r_i'} = \begin{bmatrix} x_i' \\ y_i' \\ -\frac{w}{2} \end{bmatrix} \tag{2.17}$$

$$R_{shock} = \left| \begin{bmatrix} x_i' \\ y_i' \\ -\frac{w}{2} \end{bmatrix} - \begin{bmatrix} x_i' \\ 0 \\ 0 \end{bmatrix} \right| = \sqrt{y_i'^2 + \left(\frac{w}{2}\right)^2} \tag{2.18}$$

$$R_{cone} \leq R_{shock} \tag{2.19}$$

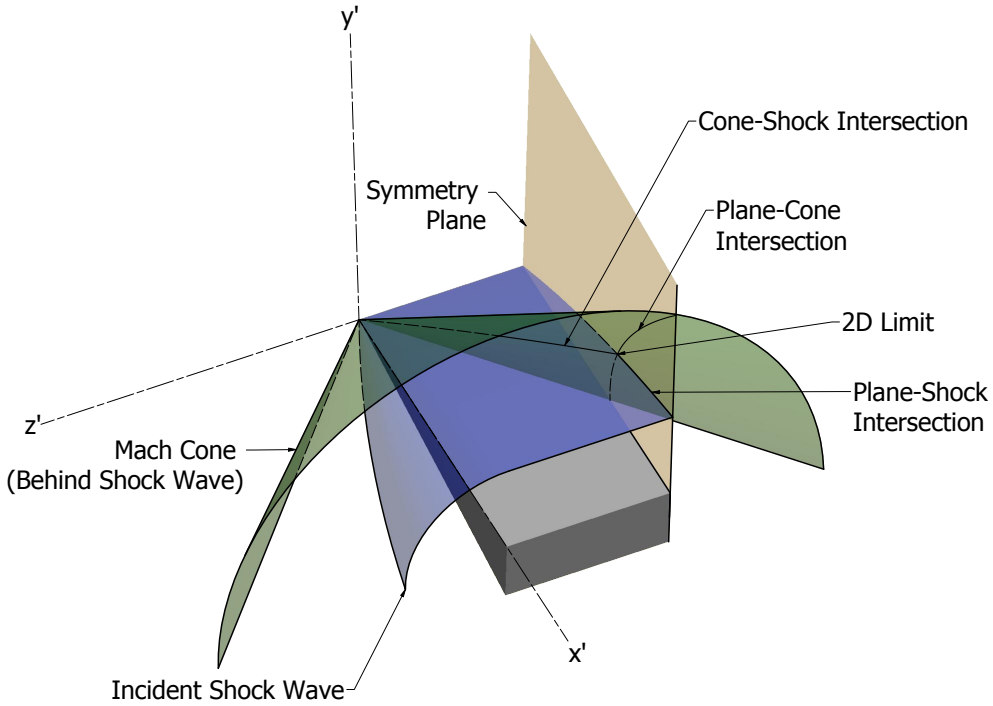


Figure 2.13: 3D edge effects

3 Experimental Investigation

This experimental investigation aims to test a rapid motion of a wedge with an attached oblique shock wave. Similar to Naidoo and Skews [8], this is achieved by rotating a wedge about a fixed pivot in a supersonic wind tunnel.

3.1 Objectives

1. Develop a test rig capable of producing rapid rotations with rotation rates at least comparable to those achieved previously.
2. Capture a series of test rotations for a range of rotation rates and Mach numbers.
3. Develop data processing methods for capturing potential shock wave curvature from high speed flow visualisation images. Additionally, the wedge rotation angle and its time derivatives must be extracted from these images.
4. Examine potential shock wave curvature to compare with CFD results for validation.
5. Examine the effects of acceleration and rotation speed on the flow field in terms of experimental and CFD results.

3.2 Facilities and Apparatus

3.2.1 Supersonic Wind Tunnel

The blow-down type supersonic wind tunnel in the Flow Research Unit is capable of operating at Mach numbers in the range 2.5-3.5. The operating conditions are given in Table 3.1. The layout of the tunnel is shown in figure 3.1. A storage tank,

pressurised up to 15 bar, supplies dried air through the pressure relief valve, which maintains a constant stagnation pressure. The air flows through the honeycomb settling chamber, which 'straightens' the air (reducing turbulence and increasing uniformity). A variable area nozzle contracts the flow to a desired area ratio, before expanding to supersonic conditions. Supersonic airflow is directed through the test section, which houses the test piece. Resulting flow features are visualised through adjacent view-windows, via a shadowgraph optical setup. Finally the airflow is diffused to subsonic speeds through the diffuser, which vents to the roof of the laboratory. The stagnation pressure at the pressure relief valve is measured by a digital pressure transducer and stored on a computer, via a data acquisition system. A sample trace of stagnation pressures are shown in figure 3.2. During the test period, when steady supersonic flow is achieved in the test section, the stagnation pressure tends to vary by $\pm 20\, kPa$ from the set point. The stagnation temperature is the temperature in the pressure supply vessel, assumed equal the ambient temperature, which fluctuated around $17 - 25\, ^{\circ}C$.

Table 3.1: Wind tunnel operating conditions

Mach Number	2-3.5
Stagnation pressure (gauge)	$250 \pm 20\, kPa$
Stagnation temperature	$295 \pm 4\, K$
Run Time	2-10 s
Test Cross-Section	101.6 mm x 118 mm

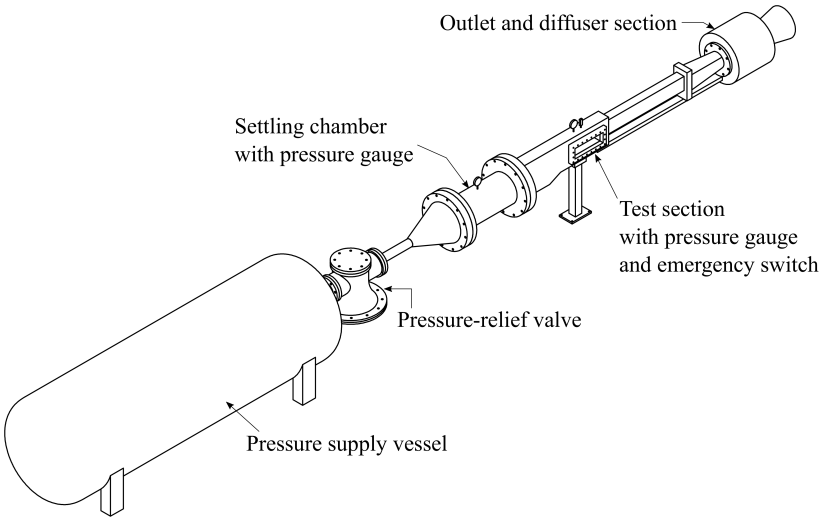


Figure 3.1: Wind tunnel overview [3]

The supersonic wind tunnel nozzle area is varied by shifting the lower half of a set of curved sections comprising the nozzle, shown in figure 3.3. The position is set by

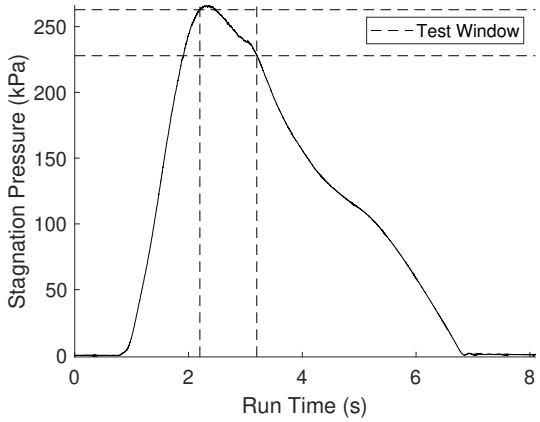


Figure 3.2: Sample stagnation pressure trace

a control wheel equiped with a veeder counter used to accurately set the position. This veeder count corresponds to the Mach number which will be produced in the test section by the calibration curve in figure 3.4. The uncertainty in the Mach number is given by taking the numerical gradient of the Mach number with respect to veeder count from this calibration curve: $\delta M = \frac{dM}{dV}\delta V$. The uncertainty in the veeder count is $\delta V = \pm 0.5 units$. For $M = 3$, the uncertainty is calculated to be $\delta M = \pm 0.0011$.

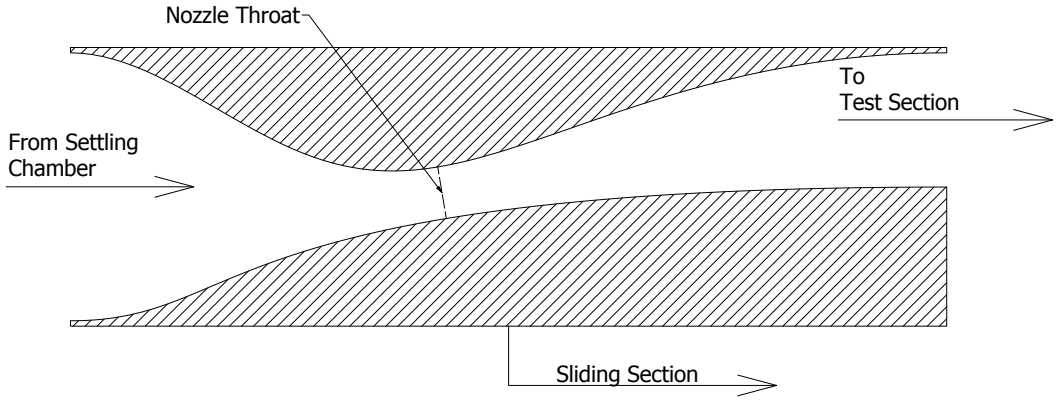


Figure 3.3: Variable area nozzle

The static pressure p and temperature T in the test section were calculated using the isentropic flow relations, equations 2.5-2.6. These depend on the stagnation conditions and the Mach number. Associated uncertainties are calculated using the lineaised propagation of error method [27], illustrated for the static pressure in equation 3.2.

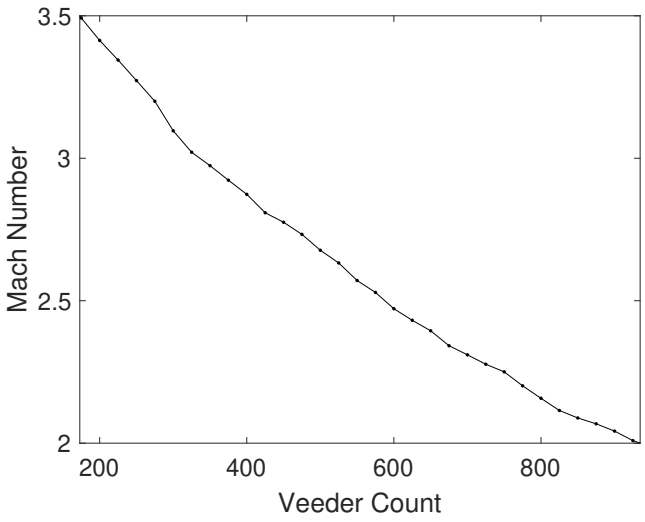


Figure 3.4: Veeder counter calibration curve

$$p = f\left(P_0, M\right) \tag{3.1}$$

$$\delta p \approx \sqrt{\left(\frac{\partial f}{\partial P_0}\delta P_0\right)^2 + \left(\frac{\partial f}{\partial M}\delta M\right)^2} \tag{3.2}$$

3.2.2 Optical Setup

A shadowgraph optics rig, shown in figure 3.5, is suspended by a rail from the ceiling of the Laboratory. It can slide along the tunnel axis, and rotate as necessary - allowing variable positions along the view area and variable view angles to be captured. However, for this investigation, the view will always be perpendicular to the tunnel axis (normal to the test section windows).

The optical setup is slightly more complex than the z-configuration shown in section 2.5, but the working principle is the same. A light source is passed through a slit, in order to approximate a point-source - centered at the focal length of the parabolic mirror above it. The parallel beam reflects off a 45° planar mirror (1), through the test section, to the opposite 45° mirror (2), to a second overhead parabolic mirror. Near the focal length of this second mirror, a small 45° planar mirror directs the narrowed beam through a converging lens and to the high speed camera.

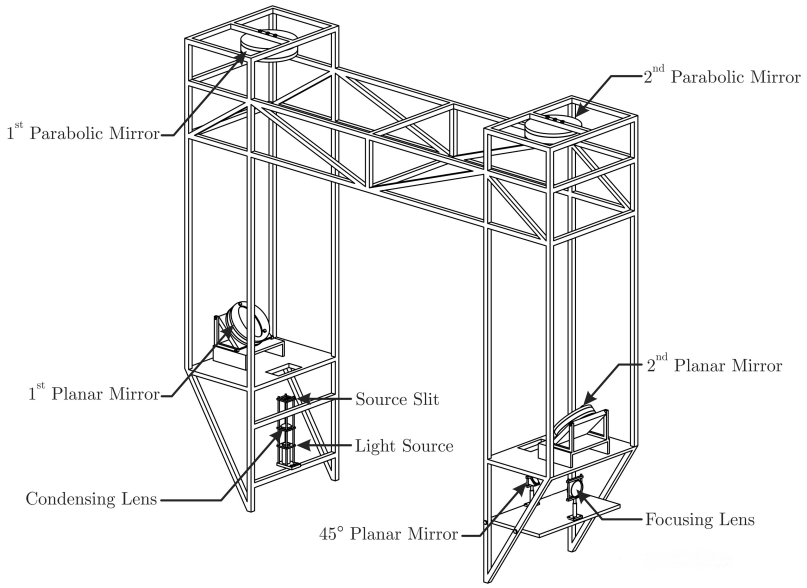


Figure 3.5: Wind tunnel optics rig [4]

The high speed camera used for this investigation was the Chronos 1.4 (1.4 Gigapixel/s) camera, with specs shown in table 3.2.

Table 3.2: Chronos 1.4 - high speed camera specs

Maximum Pixel Rate	1.4Gpx/s
Buffer Length At Max Pixel Rate	4s
Maximum Resolution	1280x1024 @ 1047 fps
Maximum Frame Rate	38,500 fps @ 336x96

3.2.3 Test Rig

In the previous study by Naidoo and Skews [8], a compression spring system, housed fully inside a supersonic wind tunnel, was used to rapidly rotate a pair of symmetrically opposite wedges. A maximum speed of 11,000 degrees/s was achieved, with a chord length of 40 mm.

To ensure the supersonic wind tunnel can start properly, the maximum effective reduction in cross-sectional area in the tunnel caused by the addition of the test piece and its housing must be kept at least below the throat area of the diffuser - refer to section 2.1.2. The blockage ratio - the maximum cross-section of the test piece and housing compared to the tunnel cross-sectional area - for the wind tunnel used in this investigation was 8%. This is similar to the allowable ratio for for the wind tunnel used by Naidoo and Skews. However, that tunnel was approximately four times the dimension (in terms of cross-section). Therefore area ratio and general size constraints were far less strict in that case. With this in mind, even matching those rotational velocities was a difficult task. A conservative goal of approximately 15,000 degrees/s was set, for a minimum chord length of 40 mm. A further requirement was for the rig to allow for a range of speeds, starting, and stopping angles to be set.

Several rig designs were considered. It was clear that the actuation mechanism must be housed outside the tunnel, given the area constraints. Ultimately a compression spring system was chosen for actuation, similar to the previous study, because: high stiffness springs offer high energy densities; are predictable; can be manufactured cheaply to specification; and can be housed compactly.

Two additional actuation methods were initially considered, which are briefly described:

1. An impact type system was considered, in which a spring driven weight would accelerate and impact an intermediate spring/damper. This would then transfer an impulsive load to the output arm. This would allow kinetic energy to be dumped rapidly into the output. However, initial calculations with an impact load applied to a discretized spring model indicated that excessive and rapidly varying loads could be transferred to the output, which may compromise the strength of components and make prediction and measurement of the wedge response very difficult. Even if some kind of rubber damper is used, accurate prediction of viscoelastic materials, particularly under impact loading is very difficult.

2. A gas cylinder system was also considered, in which high pressure gas is separated from a driving piston by a diaphragm (similar to a shock tube setup). When the diaphragm ruptures at sufficiently high pressures, or when pricked by a secondary system, the output piston would be rapidly exposed to high pressures - producing an impulsive driving force. This would rely on the short time scale of the gas interaction compared to the response of the relatively heavy output load. It would also be relatively compact and simple to setup. Unfortunately, since the energy density of air is so much lower than for an equivalent steel spring, the piston cylinder diameter would have to be impractically large.

3.2.3.1 Rig Specification

Detailed views of the final test rig and images of the rig assembled, and mounted in the wind tunnel are shown in figure 3.6. A set of compression springs with a combined stiffness of 180 kN/m drive the wedge rotation through a linkage in the tunnel as follows:

1. The compression springs are compressed by a jacking nut to the desired compression length, up to $45mm$. These springs push downwards on the drive head, which is held up by the release pin.

2. Once the wind tunnel is running at the desired Mach number, a ball valve is manually actuated, supplying pressure to the pneumatic cylinder, pulling upwards on the release arm.

3. The release arm provides a large lever ratio so that the friction between itself and the release trigger can be overcome. As the arm lifts, the release trigger is released.

4. A steel pin joined to the drive head is held up by the release trigger. As the trigger rotates, the pin and drive head are released.

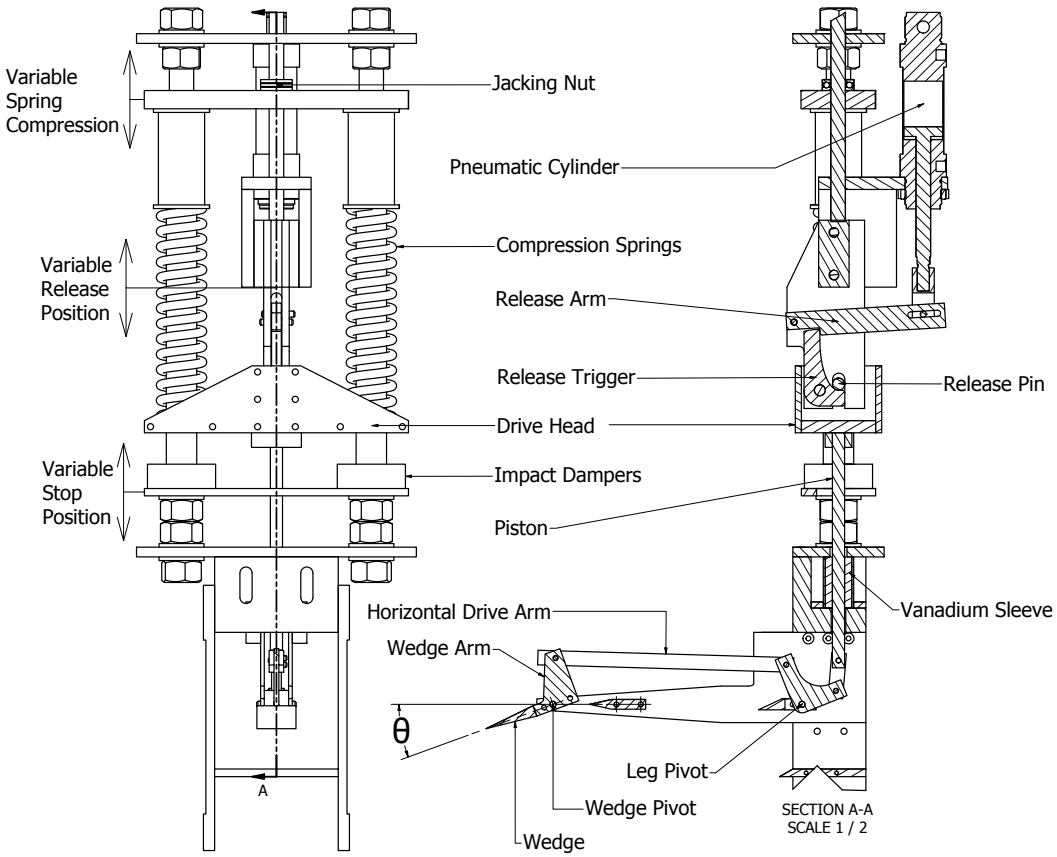
5. The drive head pushes a piston, through a low friction vanadium sleeve, joined to a pinned leg which rotates clock wise, pulling on the horizontal drive arm.

6. The drive arm is attached to the pinned wedge arm. As the drive arm pulls backwards on the wedge arm, the wedge rotates clock wise from some initial angle θ measured counter clock wise from the negative x-axis.

7. After some angle of rotation, the drive head is decelerated by a set of impact dampers comprising of four layers of expanded polyethylene rubber each of thickness $4mm$. This rubber has an elastic modulus of approximately $348kPa$ at 25% compression. Stacking more layers results in a more gradual deceleration. The stopping postion can also be varied by changing the height of the stopping platform, using a set of nuts.

This rig allows a range of initial wedge angles to be set, between $-20°$ and $20°$. As per the tunnel blockage ratio restriction, the maximum cross-sectional area of the wedge and in-tunnel components was kept below 8% of the tunnel cross section $101.6 \times 118 \times 8\% \approx 960mm^2$. However these blockage ratio calculations assume that the rig restricts the flow isentropically. In reality there will be pressure losses (losses in stagnation pressure $\Leftrightarrow$ increase in entropy) due in part to the viscous skin friction of the airflow over the rig surfaces. A more important source of potential pressure losses would be due to detached shock waves on blunt leading surfaces. Therefore, the leading edges of the rig were all designed with sharp $20°$ chamfers, as shown in figure 3.7. These sharp edges will produce oblique shock waves which produce significantly lower pressure loss and less hindrance to effective starting of supersonic flow in the tunnel.

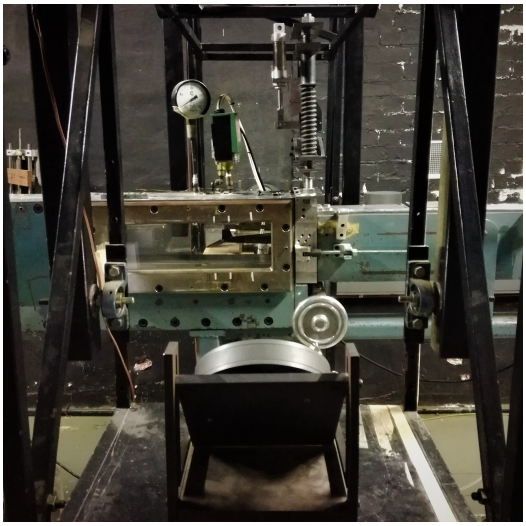
The complete manufacturing drawings for the test rig are too long to include in this dissertation. They may be found in the *Digital Appendix*. Further details regarding the modelling and design of the rig are given in Appendix A.



(a) Detail view



(b) Assembled



(c) Mounted

Figure 3.6: Test rig

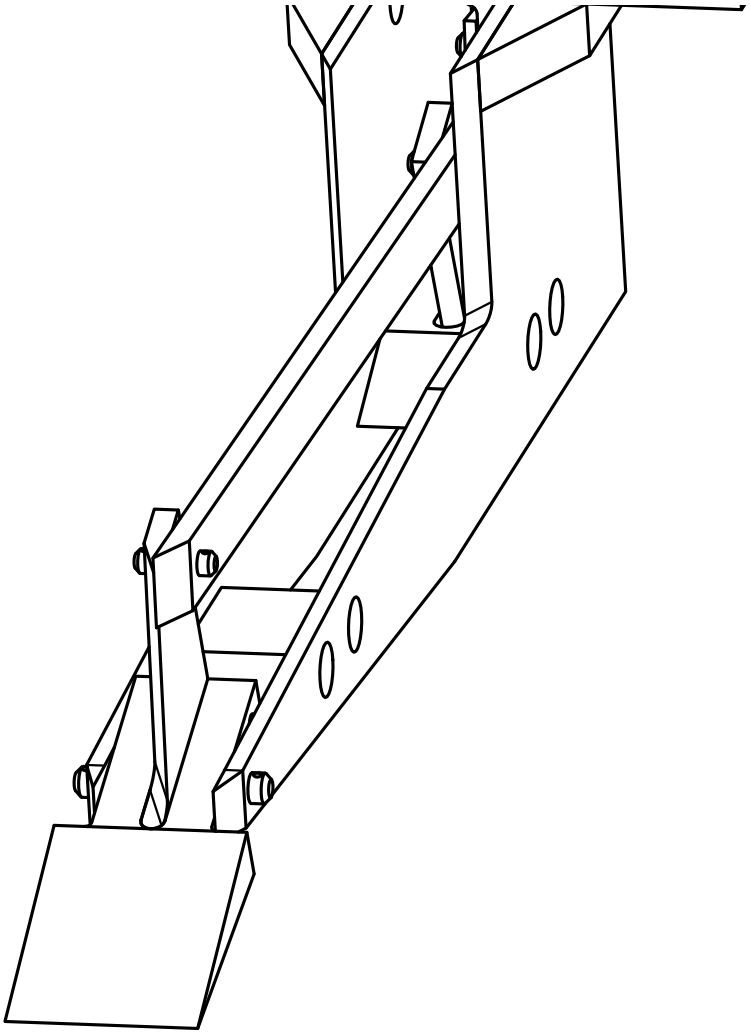


Figure 3.7: Front view - Sharp rig chamfers

3.2.3.2 Wedge Specification

A 12° wedge, with a pivot length of 58.6 mm was used for all tests. The specifications are shown in figure 3.8. The dimensions were chosen on the basis of reducing tunnel blockage; maximising tip speeds; ensuring structural integrity; while maximising the wedge span (width) to delay the chord wise onset of three-dimensional edge effects on the symmetry plane.

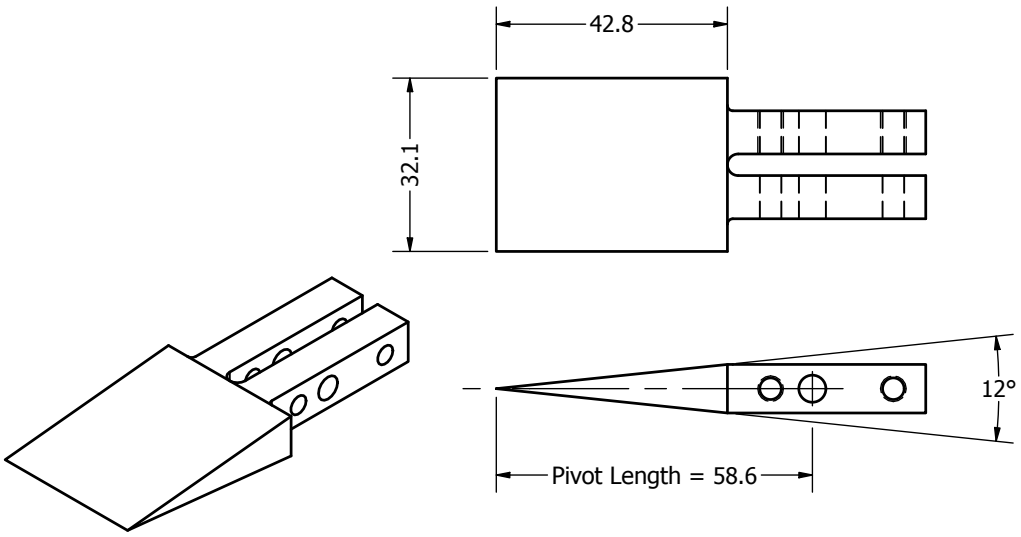


Figure 3.8: Test wedge specification

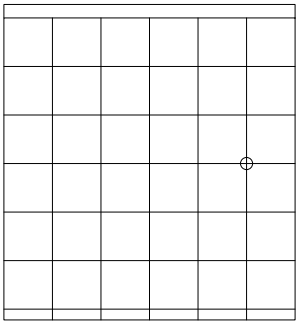
3.3 Data Processing

The only direct data captured from the experiments were the high speed Shadowgraph images. From this, the rotation profiles (angle, angular velocity and angular acceleration) and the shock wave shape (at each frame) were extracted. The steps involved in extracting these rotation profiles and the shock wave shapes are detailed in the following sections.

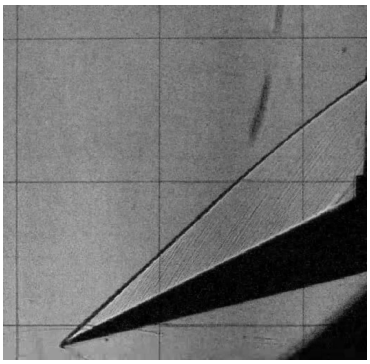
3.3.1 Image Scaling

A background grid with 20 mm divisions was printed on transparent film and placed on the test window to provide an accurate physical scale for data processing - shown in figure 3.9. The grid is also shown as used for a test at Mach 3.3, with a starting angle of approximately 20° (recall that the wedge angle is measured positive counter

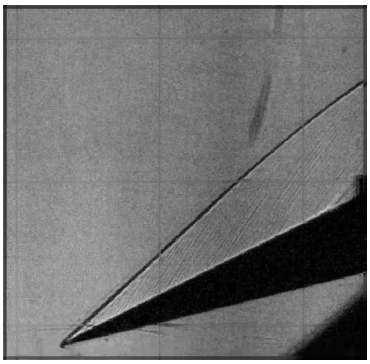
clock wise from the negative x-axis). The grid was positioned such the grid circle was centered at the pivot point. The grid was (partially) removed in post processing using convolutional image filters designed to highlight vertical and horizontal lines (separately) and blur these regions using neighboring pixels.



(a) Template



(b) Image with grid



(c) Grid removed

Figure 3.9: Scaling grid

In order to scale the test images, four grid points (the widest available selection within the frame) are manually extracted using a simple script in Matlab (points are selected using the mouse cursor, from a zoomed view, with a precision within 2-3 pixels in any direction). These four points are then mapped to their physical locations using a transformation. At first, a rigid rotation, enlargement and shift was used to map the image square onto the corresponding physical positions, the result of which is shown in figure 3.10. It is seems that a degree of distortion - a degree of vertical stretching - is present in the optical setup (a perfect square does not map perfectly onto the image). Therefore a second, more general transformation, with a generalised scaling matrix $[A]$ (between image pixel coordinates x', y' and physical coordinates x, y, centered at the pivot) was used to account for distortion, as shown in equation 3.3. The scaling matrix is determined from a least squares solution to equation 3.4, matching the four points in pixel co-ordinate (image) space to the

corresponding physical co-ordinate space. This results in a far better scaling, as shown in figure 3.11.

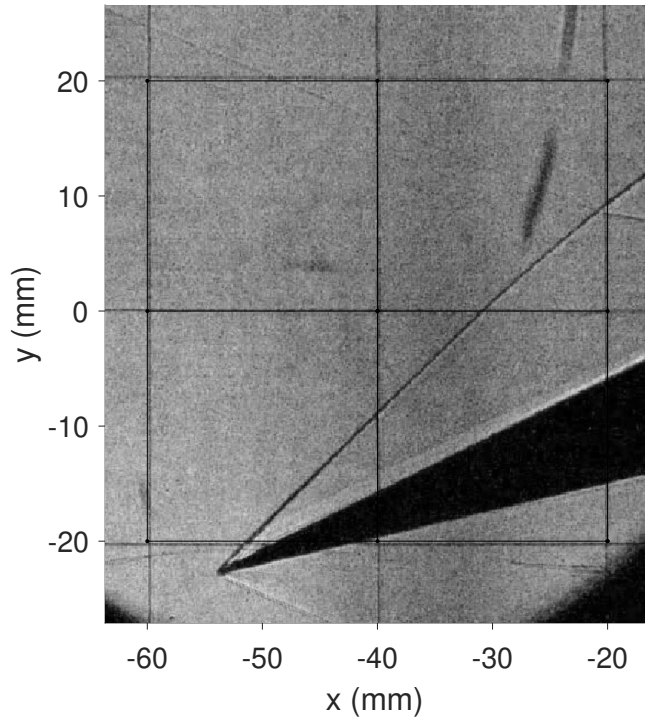


Figure 3.10: Rigid scaling

$$\begin{bmatrix} x \\ y \end{bmatrix} = \begin{bmatrix} a_{11} & a_{12} \\ a_{21} & a_{22} \end{bmatrix} \begin{bmatrix} x' \\ y' \end{bmatrix} + \begin{bmatrix} a_{13} \\ a_{23} \end{bmatrix} = \begin{bmatrix} a_{11} & a_{12} & a_{13} \\ a_{21} & a_{22} & a_{23} \end{bmatrix} \begin{bmatrix} x' \\ y' \\ 1 \end{bmatrix} \tag{3.3}$$

$$\begin{bmatrix} x_1 & x_2 & x_3 & x_4 \\ y_1 & y_2 & y_3 & y_4 \end{bmatrix} = [A] \begin{bmatrix} x'_1 & x'_2 & x'_3 & x'_4 \\ y'_1 & y'_2 & y'_3 & y'_4 \\ 1 & 1 & 1 & 1 \end{bmatrix} \tag{3.4}$$

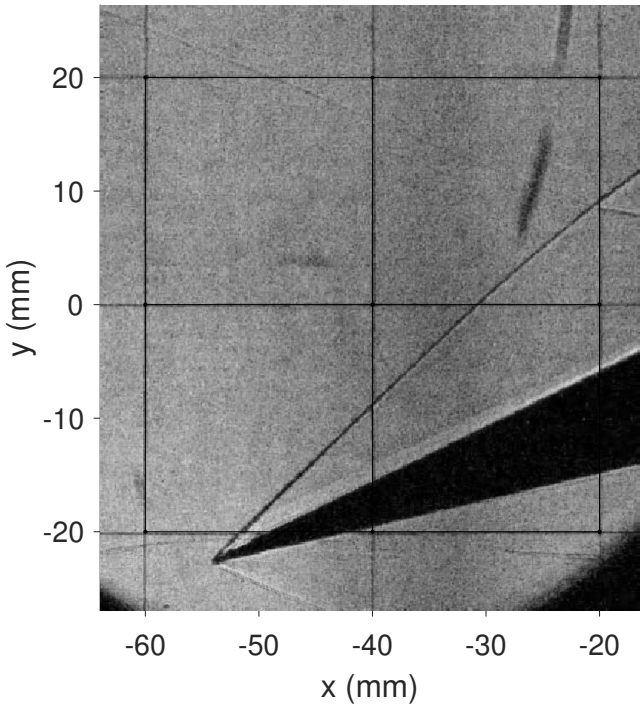


Figure 3.11: Least squares scaling

3.3.2 Angle Measurement

A critical aspect of this experimental investigation was measuring the wedge angle at each photographed frame. The wedge angles are measured by fitting lines through the top and bottom surfaces of the wedge image in the following way: Firstly, an initial wedge angle is estimated from a manually captured tip point. Based on this angle estimate, line queries are captured along the top and bottom surfaces, each with sufficient length to ensure full coverage along the surfaces, as illustrated in figure 3.12. The surface edges are found at a falling edge (in pixel intensity). Lines are fit though these edge points along the surfaces using a least squares regression. The top and bottom line angles, calculated from the gradients, are averaged to give the wedge angle θ, measured counter clockwise from the negative x-axis. This angle is then used as the estimate for the next frame and the solution proceeds through all image frames, extracting angles corresponding to times given by $time = \frac{frame\ number}{framerate}$. Angles measured for a sample test with a spring compression of 40mm and a Mach number of 3.3 are shown in figure 3.13.

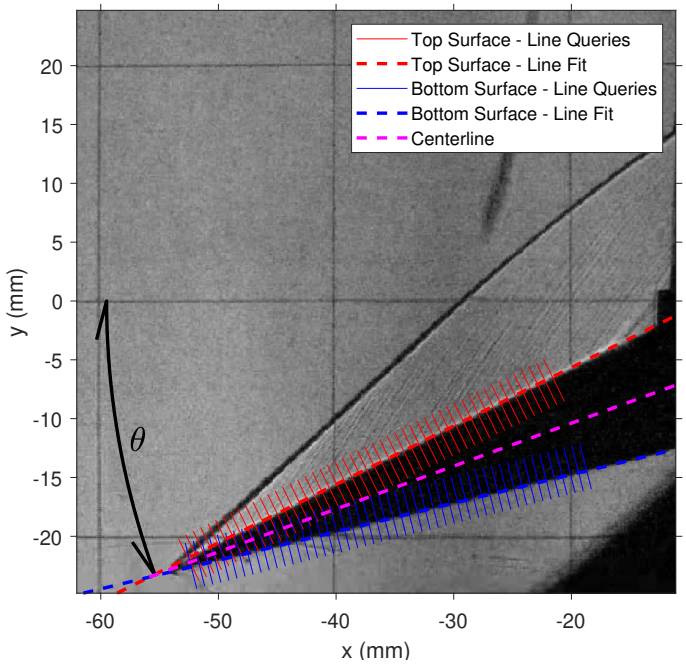


Figure 3.12: Wedge surface line queries

The uncertainty in the wedge angle may be obtained from the line regressions: Assuming the errors are normally distributed, the standard error σ_m in each line gradient m_{top}, m_{bot} is given by equation 3.5 [28]. The center line angle is the average of the two line angles. Its standard error may be estimated by the linearised propagation of error method [27], which estimates the contribution of independent variable uncertainties to a derived variable, in equation 3.6.

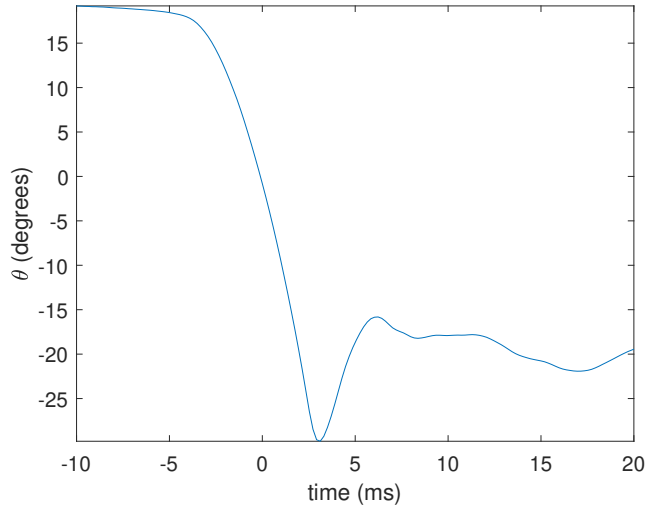


Figure 3.13: Measured wedge angles

$$\sigma_m = \sqrt{\frac{\frac{1}{n-2}\sum_{i=1}^{n}\epsilon_i^2}{\sum_{i=1}^{n}(x_i-\overline{x})^2}}, \epsilon_i = y_i - (mx_i + c) \tag{3.5}$$

$$\sigma_\theta = \sqrt{\left(\frac{\partial\theta}{\partial m_{top}}\right)^2 \sigma_{m_{top}}^2 + \left(\frac{\partial\theta}{\partial m_{bot}}\right)^2 \sigma_{m_{bot}}^2} \tag{3.6}$$

The standard error in the angle for the sample test, calculated at each image frame, is shown in figure 3.14. The 95th percentile (0.033°) of these errors was taken as the standard error for all frames in this set of images. This value is relatively invariant across each set of test images. Therefore, an uncertainty band of $\theta \pm \delta\theta$, where $\delta\theta = 2 \times 0.033° = 0.066°$, was used for all measured angles, for all tests - representing a 95% confidence interval (2 standard deviations above and below). The sample measured wedge angles are shown with uncertainty bands in figure 3.15.

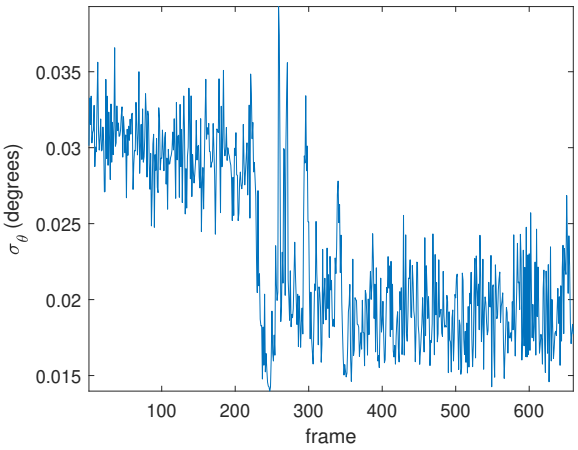


Figure 3.14: Sample standard error for angle measurements

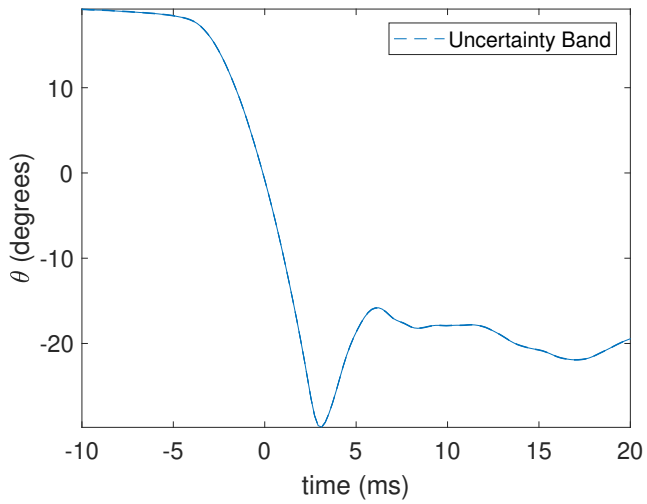


Figure 3.15: Measured wedge angles with error bands

3.3.3 Tip Measurement

The position of the wedge tip must also be obtained for the purposes of shock wave capturing, since the tip is the start point of the incident shock waves. Following from the angle measurement (section 3.3.2), the tip is found at the intersection of the top and bottom surface fit lines. The intersection is given by equation 3.7. The uncertainty in this measurement depends on the uncertainties in the line coefficients m and c, and is given by equation 3.8 using the linearised propagation of errors approach. Here it has been assumed that the coefficient uncertainties for both lines are approximately equal (i.e $\delta m = \delta m_1 = \delta m_2$ and $\delta c = \delta c_1 = \delta c_2$). Observe the $\frac{1}{m_2 - m_1}$ factor present in this equation. It implies that if the gradients of the two surface lines are similar (as is the case for the wedge, which has a relatively small tip angle of 12°), then the uncertainty in the tip position becomes large. A sample tip uncertainty is given in equation 3.9, which does not vary greatly between tests and image frames.

$$y_1 = m_1 x + c_1$$

$$y_2 = m_2 x + c_2$$

$$\vec{r_{tip}} = \frac{1}{m_2 - m_1} \begin{bmatrix} 1 & -1 \\ m_2 & -m_1 \end{bmatrix} \begin{bmatrix} c_1 \\ c_2 \end{bmatrix} \tag{3.7}$$

$$\delta \vec{r_{tip}} = \begin{bmatrix} \delta x \\ \delta y \end{bmatrix}$$

$$= \frac{1}{m_2 - m_1} \begin{bmatrix} \sqrt{2\delta c^2 + 2\left(\frac{c_2 - c_1}{m_2 - m_1}\right)^2 \delta m^2} \\ \sqrt{\left(m_1^2 + m_2^2\right)\delta c^2 + \left(\frac{c_2 - c_1}{m_2 - m_1}\right)^2 \left(m_1^2 + m_2^2\right)\delta m^2} \end{bmatrix} \tag{3.8}$$

$$\delta \vec{r_{tip}} = \frac{1}{0.2573} \begin{bmatrix} 0.1422 \\ 0.0618 \end{bmatrix} = \begin{bmatrix} 0.55 \\ 0.24 \end{bmatrix} mm \tag{3.9}$$

3.3.4 Angular Velocity and Acceleration

The angular velocity and acceleration of the wedge was estimated at each frame by differentiating the wedge angles with respect to time using central finite differencing. The measured angle θ will be assumed to be the sum of the true wedge angle $\hat{\theta}$ in the experiment plus a random variable θ^*, representing the measurement uncertainty. The random variable θ^* is assumed to be normally distributed. Additionally it is assumed that the uncertainties of consecutive measurements are independent.

The error in the numerical differentiation may now be split, as shown in equation 3.10, into a truncation error and a propagation error. The truncation error arises due to the finite difference approximation to the true time derivative (angular velocity : $\hat{\omega}$) of the true angle ($\hat{\theta}$), whilst the propagation error arises from the uncertainties in the measured angles. The truncation error, estimated as the leading term truncated from the Taylor expansion of the first derivative is given by equation 3.11. This depends on the third derivative of the angle with respect to time, which is estimated by repeated central differencing of the angle time series. Note that this derivative has its own associated truncation error, but will be of order $\mathcal{O}((\Delta t)^4)$, and will be neglected.

The propagation error of the angular velocity is derived from the uncertainties in consecutive angle measurements appearing in the numerical differentiation, $\theta^*_{t+\Delta t}$ and $\theta^*_{t-\Delta t}$. The difference of these independent normally distributed random variables is also normally distributed, with a standard error $\sigma_{difference} = \sqrt{(\sigma_{t+\Delta t})^2 + (\sigma_{t-\Delta t})^2} = \sqrt{2}\sigma_\theta$. The propagation error is finally given by dividing the difference error term by the time interval $2\Delta t$ in equation 3.12. Similar formulae are derived for the angular acceleration α, based on a 2nd order central difference scheme, equation 3.13. The corresponding truncation and propagation errors are given in equations 3.14 and 3.15 respectively.

The truncation and propagation errors are compared in figure 3.16a and 3.16b for a sample test. The errors are normalized by the absolute maximum angular velocity and acceleration respectively. The truncation errors are generally insignificant compared to the propagation errors. The ω propagation error is approximately 1% of $\max(|\omega|)$, while the relative α propagation error is approximately 10%. The propagation errors are magnified for higher order derivatives due to the dependence on a greater number of measured angle uncertainties, as well as the higher order time differences in the denominator. The combined uncertainties for angular velocity and acceleration were taken as the root square sum of the constant propagation error

and the maximum truncation error ($\delta\omega_{total} = \sqrt{\delta\omega^2_{propagation} + \delta\omega^2_{truncation}}$). These final errors are shown as error bands for the derivatives in figure 3.17.

$$\omega = \frac{\theta_{t+\Delta t} - \theta_{t-\Delta t}}{2\Delta t} = \frac{\hat{\theta}_{t+\Delta t} - \hat{\theta}_{t-\Delta t}}{2\Delta t} + \frac{\theta^*_{t+\Delta t} - \theta^*_{t-\Delta t}}{2\Delta t} \tag{3.10}$$

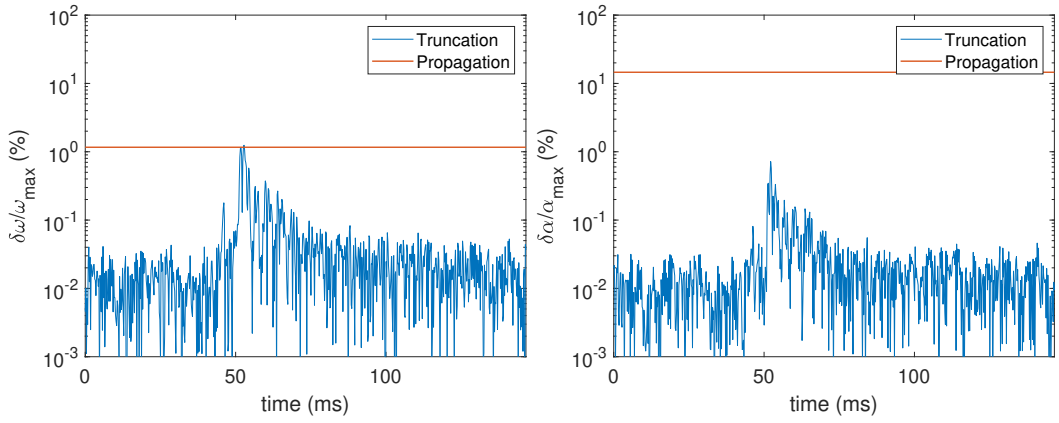
$$\delta\omega_{truncation} \approx \frac{(\Delta t)^2}{6}\frac{d^3\theta}{dt^3} \tag{3.11}$$

$$\delta\omega_{propagation} = \frac{\sqrt{2}}{2}\frac{\delta\theta}{\Delta t} \tag{3.12}$$

$$\alpha = \frac{\theta_{t+\Delta t} - 2\theta_t + \theta_{t-\Delta t}}{\Delta t^2} = \frac{\hat{\theta}_{t+\Delta t} - 2\hat{\theta}_t + \hat{\theta}_{t-\Delta t}}{\Delta t^2} + \frac{\theta^*_{t+\Delta t} - 2\theta^*_t + \theta^*_{t-\Delta t}}{\Delta t^2} \tag{3.13}$$

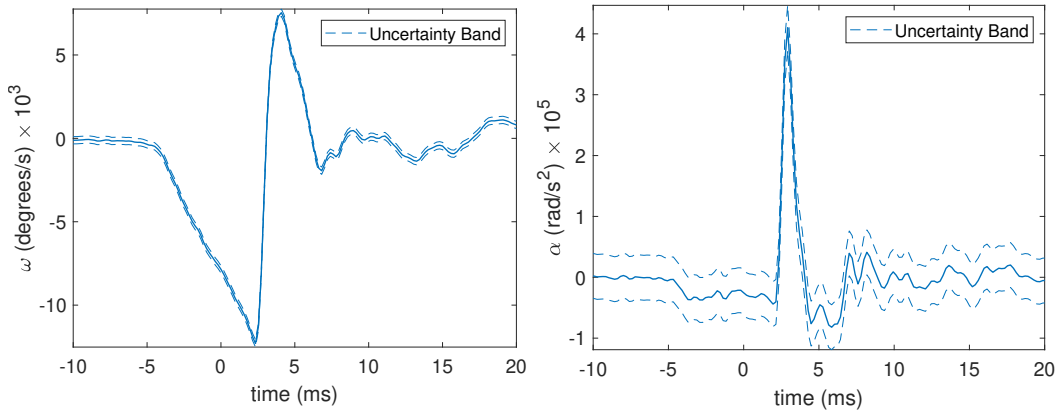
$$\delta\alpha_{truncation} \approx \frac{(\Delta t)^2}{12}\frac{d^4\theta}{dt^4} \tag{3.14}$$

$$\delta\alpha_{propagation} = \sqrt{6}\frac{\delta\theta}{(\Delta t)^2} \tag{3.15}$$



(a) Angular velocity (b) Angular acceleration

Figure 3.16: Relative uncertainty sources



(a) Angular velocity

(b) Angular acceleration

Figure 3.17: Error bands

3.3.4.1 Angular Velocity and Acceleration - Results

Angular derivatives are demonstrated in figures 3.18, 3.19 and 3.20 - showing the effects of changing the wedge stopping angle, spring compression length and test Mach number respectively. The test numbers correspond to the test matrix in table 3.3. Key features of these results will be briefly discussed:

1. Varying Stopping Angle θ_f. If the Mach number and spring compression length are held constant and the wedge stopping angle is varied - so that, before the deceleration begins, the setup is approximately identical - the angular derivative profiles are very similar in all respects. Of course it is observed that later stopping positions result in greater angular velocities and accelerations. Once deceleration begins, at each set stopping angle, the profiles appear similar in their pattern.

2. Varying Initial Spring Compression Length C. If the Mach number and stopping angle are held constant and the initial spring compression length is varied - so that the initial actuation force $F = k_s C$ is varied - the resulting excitation varies accordingly. Recall that the total spring constant $k_s \approx 180kN/m$. The angular velocities and accelerations appear to increase approximately in proportion to the applied force.

3. Varying Mach Number M. If only the Mach number is varied, the resulting derivatives appear relatively similar. However it does appear that lower Mach numbers result in slightly higher maximum velocities and accelerations. This may be attributed to the effect of aerodynamic loads on the actuation of the wedge. If the aerodynamic loads on the primary surfaces (top and bottom) of the wedge are estimated (assuming 2-dimensional flow, and applying oblique shock and expansion fan relations) it can be shown that, within this range of Mach numbers, a positive feedback force results on the actuation system which increases with decreasing Mach number. It is positive in the sense that it pushes the system away from $\theta = 0°$ due to the lift on the wedge. The force increases (within this range) at lower Mach numbers essentially due to increased air density outweighing the decreased air velocity in terms of momentum. The positive feedback force will slow the rotation while $\theta < 0°$ but accelerate the rotation speed once $\theta > 0°$ - such that the latter outweighs the former.

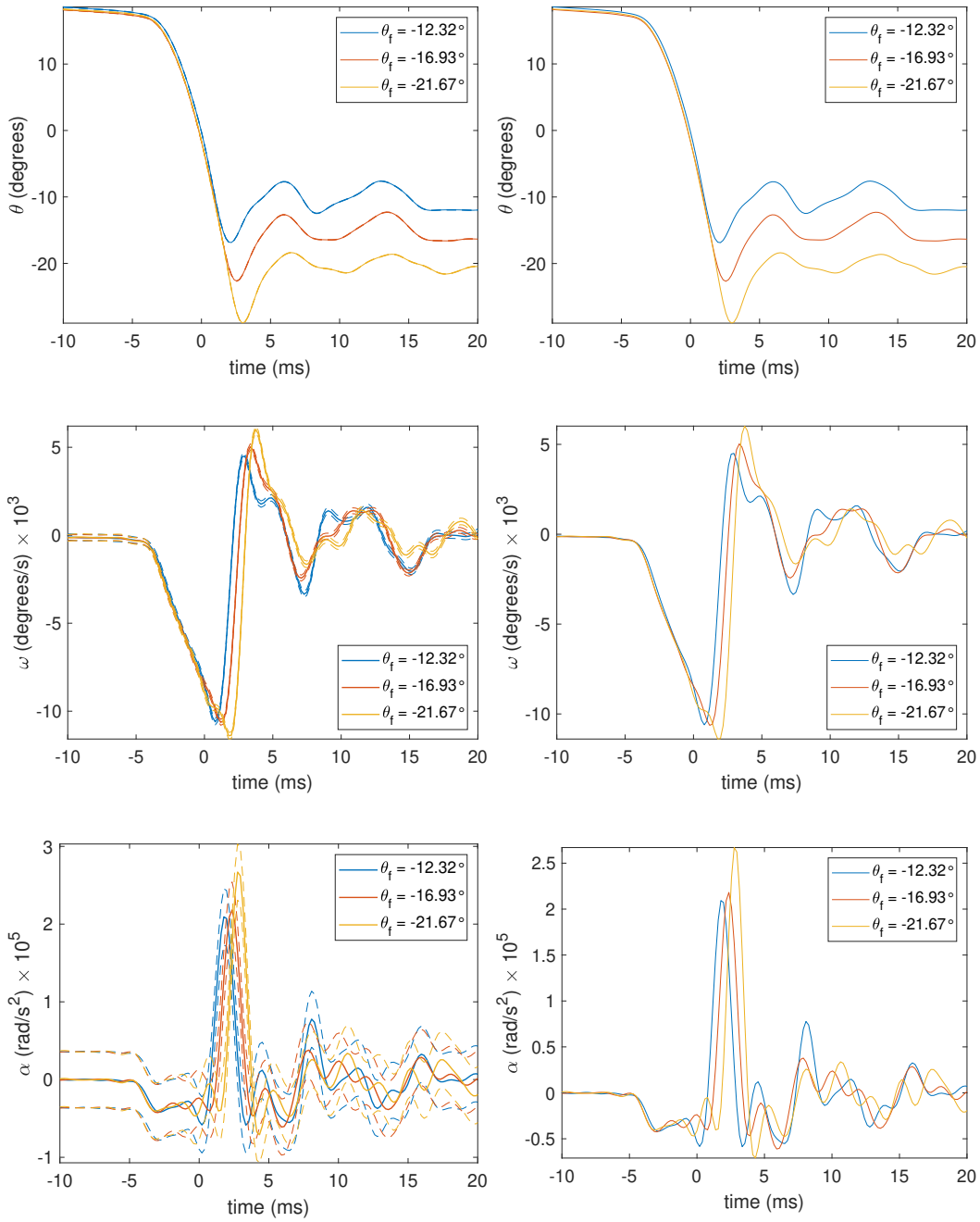


Figure 3.18: Wedge angle, velocity and acceleration - varying stopping angle θ_f. with and without error bands. M = 3.3, C = 40mm. Test numbers 6, 7 and 8 in table 3.3

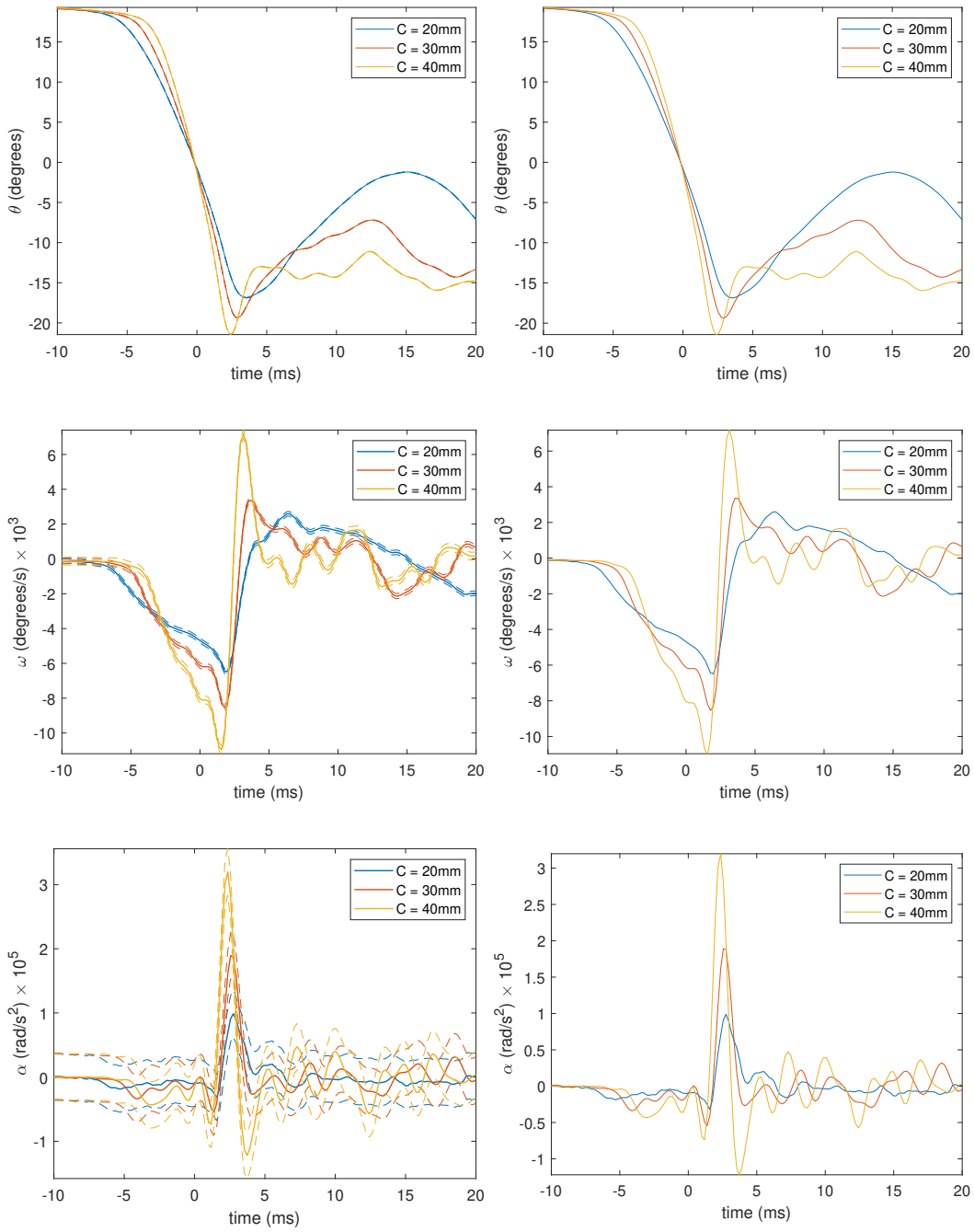


Figure 3.19: Wedge angle, velocity and acceleration - varying initial spring compression length. with and without error bands. M = 3.3, $\theta_f \approx -12°$. Test numbers 2, 3 and 4 in table 3.3

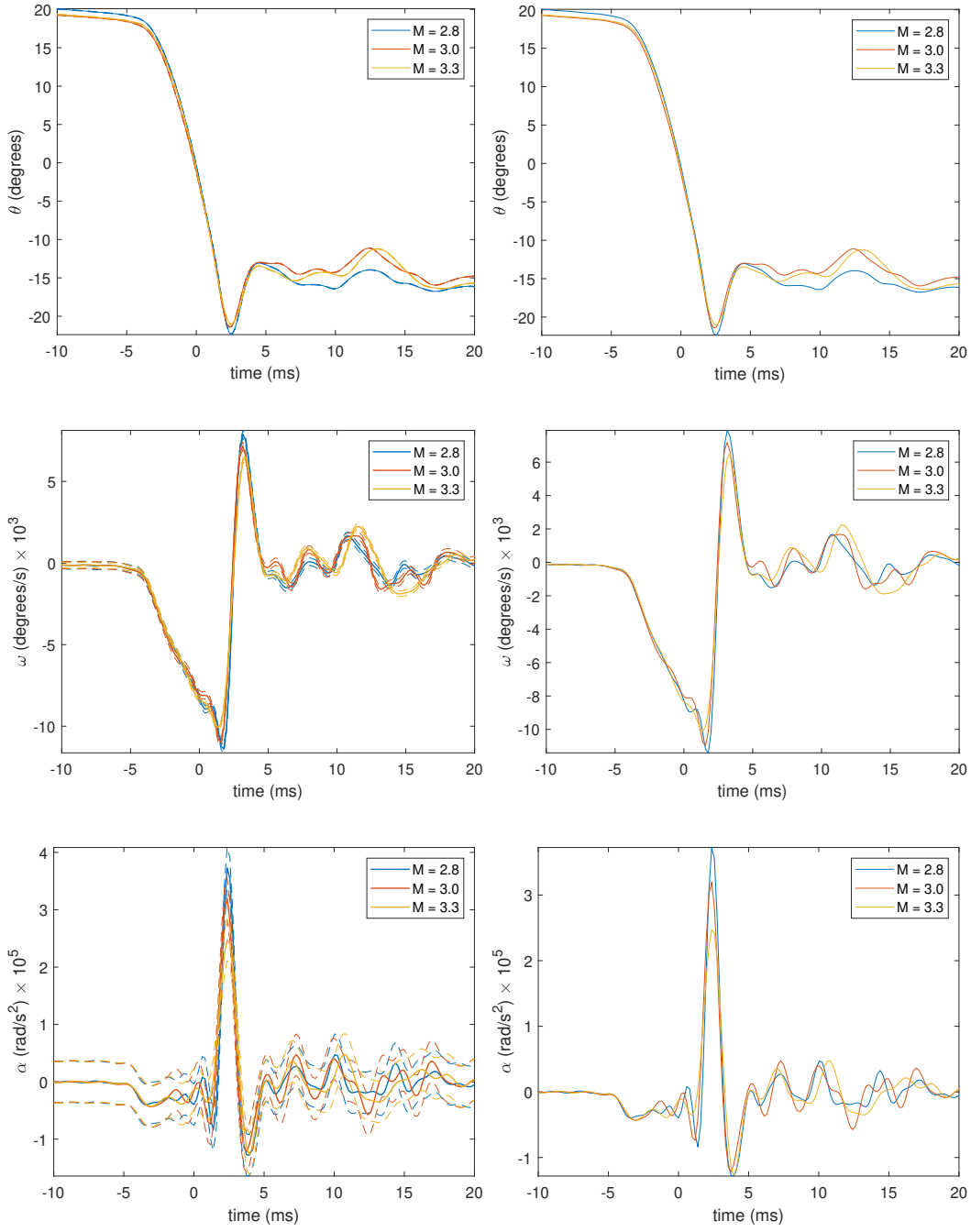


Figure 3.20: Wedge angle, velocity and acceleration - varying Mach number. With and without error bands. C = 40mm, $\theta_f \approx -12°$. Test numbers 1, 4 and 5 in table 3.3

3.3.5 Dynamic Oblique Shock Analysis

The $\theta - \beta - M$ relation applied to oblique shock waves incident on a surface inclined to a supersonic flow may be applied to a moving wedge surface through a change in reference frame. Consider the supersonic flow with Mach number M_∞ incident on the wedge rotating about the origin in figure 3.21. The tip velocity is given by equation 3.16. The relative flow velocity at the tip is the difference between the upstream flow velocity ($\vec{v}_\infty$) and the tip velocity, shown in equation 3.17. Dividing this by the upstream sound speed (a_∞), yields a relative Mach number vector ($\vec{M}_{rel}$) in equation 3.18. Where a tip speed Mach number (M_ω) has been defined, as described in section 2.2. This relative Mach number vector provides the Mach number magnitude and flow direction experienced at the tip. The standard $\theta - \beta - M$ shock wave relation (or expansion fan relation) can now be applied. This approach will only give accurate results in the limit of proximity to the wedge tip. However it provides a useful boundary value along the wedge surface and helps characterise the significance of dynamic rotation effects.

For example, consider a case where $\theta = 10°$ and $\omega = 12,000°/s$, with an upstream Mach number $M_\infty = 3$ and sound speed $a_\infty = 207.5m/s$ - realistic conditions for the available wind tunnel. The tip speed Mach number is $M_\omega = 0.060$. The relative Mach number magnitude and direction are $|\vec{M_{rel}}| = 2.990$ and $\angle\vec{M_{rel}} = 1.124°$. To find the shock angle β: the effective surface angle is the difference between the absolute surface angle and the flow direction angle. The surface angle ($\theta_s = 16°$) is $6°$ (half the wedge tip angle) higher than the central angle θ. The effective surface angle is then $\theta'_s = \theta_s - \angle\vec{M_{rel}} = 14.88°$. This effective angle and Mach number give a shock angle $\beta' = 32.19°$. This must be rotated back to the original axis: $\beta = \beta' + \angle\vec{M_{rel}} = 33.31°$. Compare this with the shock angle predicted by the static analysis ($\omega = 0$): $\beta_{static} = 33.29°$, which is only $0.02°$ lower. The shock angle is relatively insensitive to the rotational velocity for this geometry and these upstream conditions. At this angle at the given upstream conditions, an angular velocity of $110,000°/s$ would produce a difference of approximately $1°$ between the static and dynamic theory shock angles.

Applying this analysis to a range of Mach numbers and wedge surface angles, corresponding shock angles are shown in figure 3.22 - showing the static case ($\omega = 0$) and dynamic cases with equal positive and negative rotational velocities - with a tip Mach number of $M_\omega = 0.15$. This is about 3 times the maximum rotational velocity achieved in the experimental tests but is chosen to show trends more clearly. Note that this is valid for shock waves on the top and bottom surfaces, with the

surface angle θ_s defined separately: top surface: $\theta_s = \theta + 6°, \omega_s = \omega$; bottom surface $\theta_s = -\theta + 6°, \omega_s = -\omega$. This ensures that a positive surface angle corresponds to an oblique shock wave, and negative to an expansion fan (at least for the static case $\omega_s = 0$).

The effect of rotating clockwise ($\omega < 0$) for high surface angles results in larger shock angles. Below some threshold, this effect is reversed (for sufficiently large Mach numbers) - the opposite behaviour occurs for counter-clockwise rotations. Therefore, for sufficiently large Mach numbers, there is some surface angle at which the dynamic shock angle is the same as the static case (the static and dynamic lines cross). This is due to the counter effect of the shock angle decreasing with increasing relative Mach number, and increasing with increasing relative deflection angle. Critically, this means that even at high rotation rates, the angle of the incident shock wave near the tip may be relatively unchanged, depending on the surface angle.

A final feature: the minimum deflection angle (at which point, any decrease in the surface angle results in an expansion fan at the tip), and the maximum deflection angle (beyond which the shock wave becomes detached), for each Mach number, are seen to vary markedly with the rotational speed.

The uncertainty in the tip Mach number δM_ω, which depends on the upstream static temperature T and angular velocity ω, is given by the linear propagation of uncertainty method [27], in equation 3.20. Where the sound speed equation has been used to relate the upstream sound speed to the static temperature.

$$\vec{v}_{tip} = \vec{\omega} \times \vec{r}_{tip} = \omega \begin{bmatrix} 0 \\ 0 \\ 1 \end{bmatrix} \times R \begin{bmatrix} -\cos\theta \\ -\sin\theta \\ 0 \end{bmatrix} = \omega R \begin{bmatrix} \sin\theta \\ -\cos\theta \end{bmatrix} \tag{3.16}$$

$$\vec{v}_{rel} = \vec{v}_\infty - \vec{v}_{tip} = v_\infty \begin{bmatrix} 1 \\ 0 \end{bmatrix} - \omega R \begin{bmatrix} \sin\theta \\ -\cos\theta \end{bmatrix} \tag{3.17}$$

$$\vec{M}_{rel} = M_\infty \begin{bmatrix} 1 \\ 0 \end{bmatrix} - \frac{\omega R}{a_\infty} \begin{bmatrix} \sin\theta \\ -\cos\theta \end{bmatrix} = \begin{bmatrix} M_\infty - M_\omega \sin\theta \\ M_\omega \cos\theta \end{bmatrix} \tag{3.18}$$

$$M_\omega \equiv \frac{\omega R}{a_\infty} \tag{3.19}$$

$$\frac{\delta M_\omega}{M_\omega} \approx \sqrt{\left(\frac{\delta\omega}{\omega}\right)^2 + \left(-\frac{1}{2}\frac{\delta T}{T}\right)^2} \tag{3.20}$$

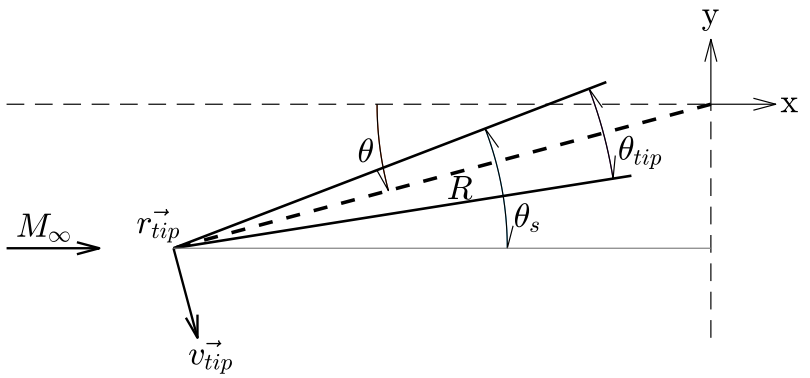


Figure 3.21: Wedge rotation geometry

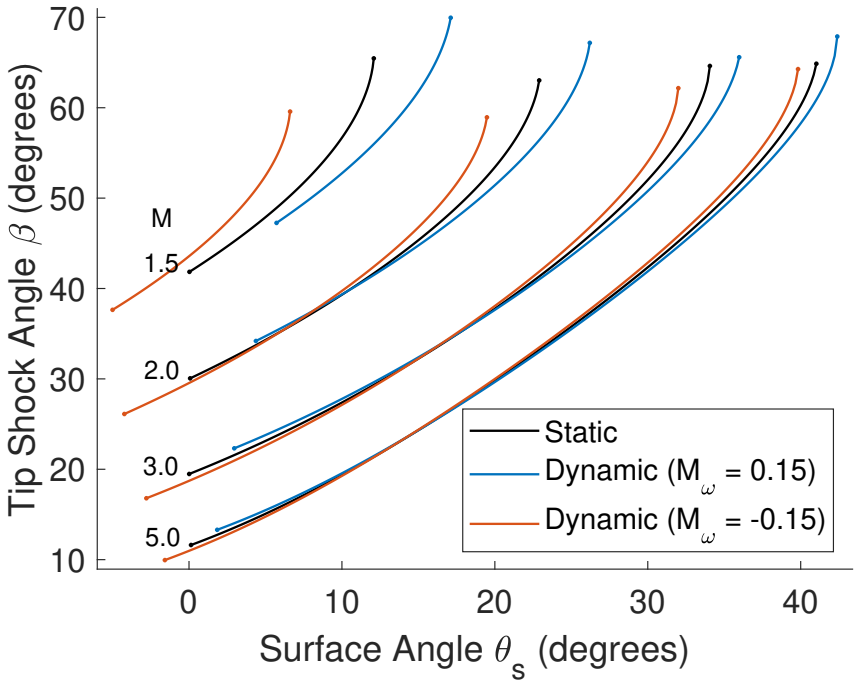


Figure 3.22: Dynamic shock theory

3.3.6 Shock Extraction

In order to study dynamic effects on the incident shock waves, data points along the shock waves were captured from captured test images. Firstly, a convolutional image filter was used to highlight the shock wave. The kernel used is illustrated in figure 3.23. The image is filtered by convoluting the kernel over each pixel - calculating the dot product of overlapping pixel values between the image and the kernel, with the kernel centered successively at each image pixel. This kernel is oriented to match the theoretical shock angle β for the given surface angle and Mach number in the corresponding image frame. Although the filter highlights lines aligned with the kernel angle most intensely, it will capture a range of line angles above and below this (this range can be increased by modifying the kernel shape). Therefore, it is not necessary to predict the exact shock angle at each point - providing a reasonable estimate simply improves the extraction process. The resulting image is shown in figure 3.24.

A binary filter then selects pixels above a specified brightness, producing a set of highlighted points along the shock wave, as in shown in figure 3.25. A convex hull is also used to eliminate spurious points accidentally included by the filter (such as the wedge surface). A two step curve fitting process then yields a smooth curve through these points, as shown in figure 3.26: 1) a 3rd order polynomial was fit to the scattered points to remove major outliers so that 2) a low-pass filter could be applied to fit a smooth curve through the shock wave. This curve was used to transform the curved shock wave to a rectangular grid in the following way: a rectangular grid with coordinates (s, h) = (curve length, perpendicular height) is transformed to a curved grid by equations 3.21 to 3.24, as illustrated in figure 3.27. The initial shock curve $\vec{r}_0$ is parameterised by the curve length. The unit normal $\vec{n}_0$ to the curve is expressed as a 90° counter clock-wise rotation of the unit derivative of the curve vector with respect to length. The central curve and normal vectors provide the basis for the transformation. This transformation is shown overlaid on a shock image in 3.28. The transformed points are used to read corresponding pixel values, which can then be shown in the rectangular grid, figure 3.29a.

This grid provides a basis for final shock detection and uncertainty analysis. For each vertical strip along the s-axis, the height h corresponding to the minimum (darkest) pixel value (the position of the shock) is found. Joining these points creates a jagged line (of pixel brightness minima) representing the measured shock wave line, in figure 3.29b. This line contains noise - a moving average smoothing is applied to obtain a smoother shock wave line. This smoothed line also provides

a basis for quantifying uncertainty. The uncertainty band is descried by statistical analysis of the difference between the smoothed shock line and the original, noisy pixel minima. Two standard deviations above and below the smoothed shock line define the uncertainty (95° confidence interval). Note that the smoothed line appears to be jagged only in this rectangular scaling, due to disproportionate scale of the h-axis. Finally, the shock line and uncertainty band are transformed back to (x, y) coordinates. They are shown overlaid on the original shock image in figure 3.30.

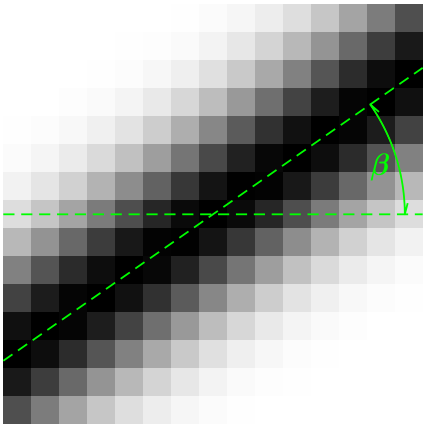
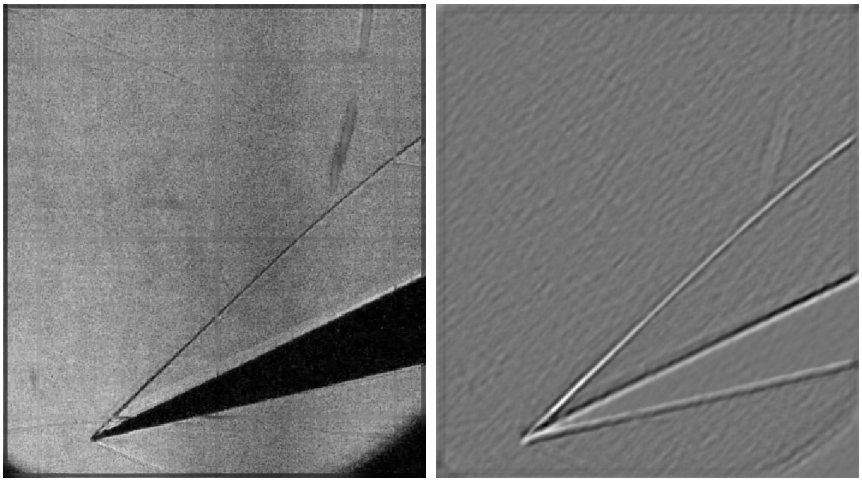
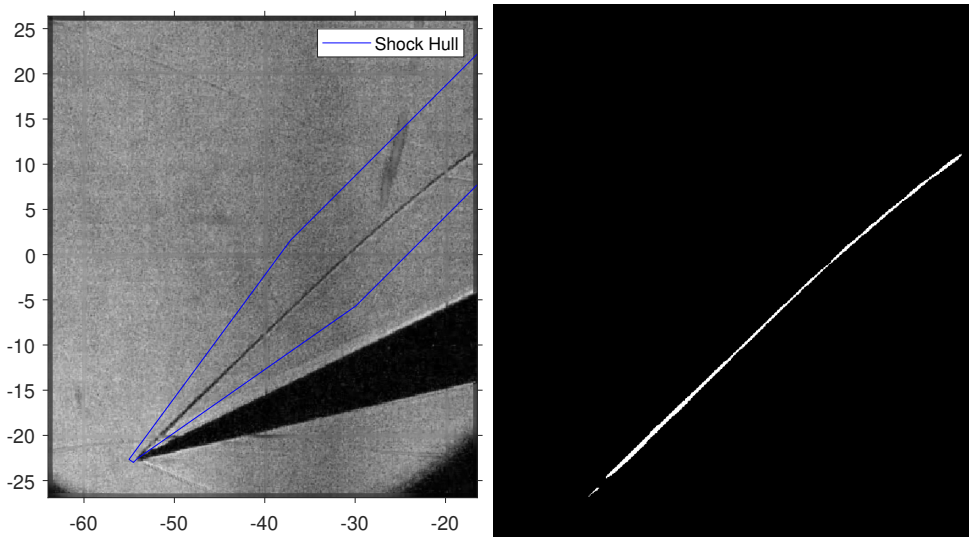


Figure 3.23: Oriented line filter kernel



(a) Original (b) Filtered

Figure 3.24: Convolutional shock filter



(a) Shock hull

(b) Threshold filter

Figure 3.25: Binary filtering

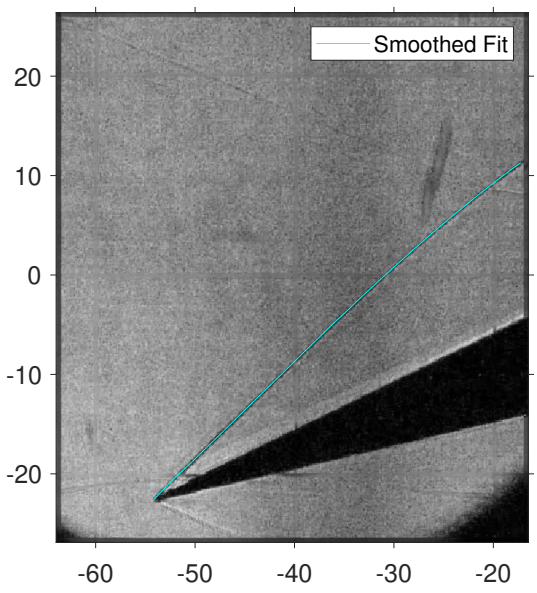


Figure 3.26: Smoothed line fit

$$\vec{r_0} = \vec{r_0}(s) \tag{3.21}$$

$$\vec{u_0} = \frac{\frac{d\vec{r_0}}{ds}}{\left|\frac{d\vec{r_0}}{ds}\right|} \tag{3.22}$$

$$\vec{n_0} = \begin{bmatrix} 0 & -1 \\ 1 & 0 \end{bmatrix} \vec{u_0} \tag{3.23}$$

$$\vec{r} = \vec{r_0}(s) + \vec{n_0}(s)h \tag{3.24}$$

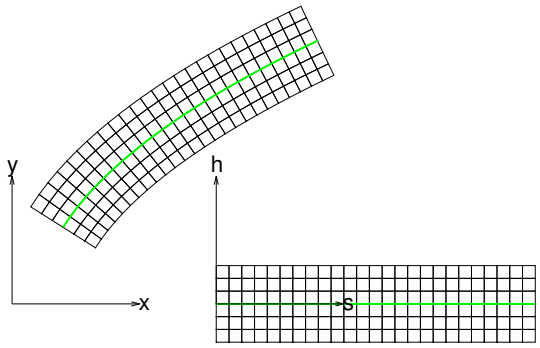
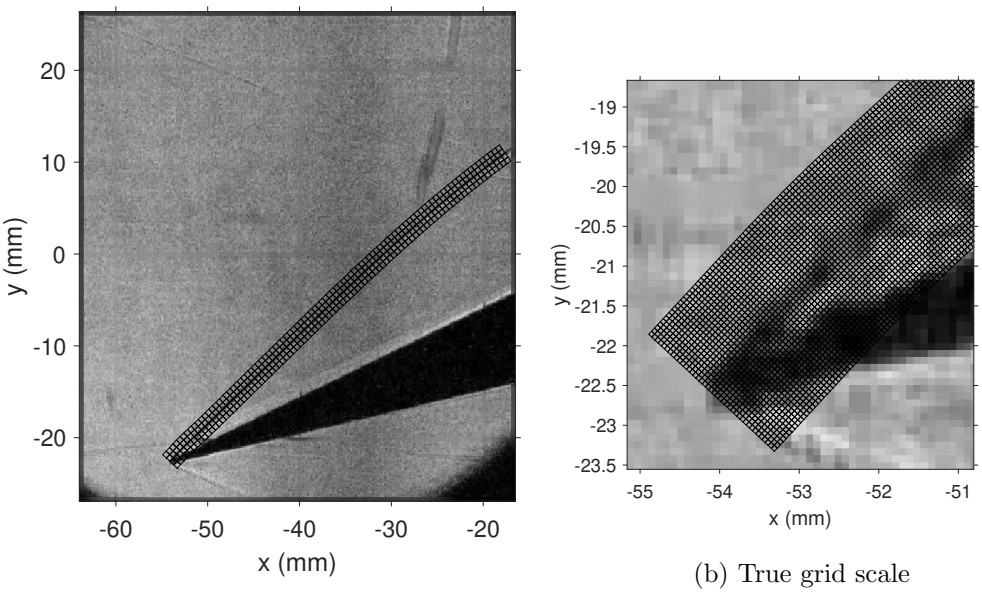


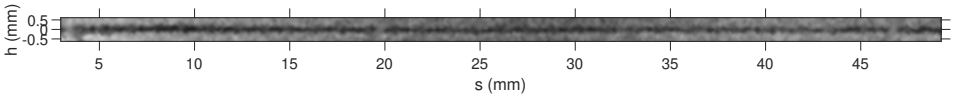
Figure 3.27: Shock grid transform Illustration



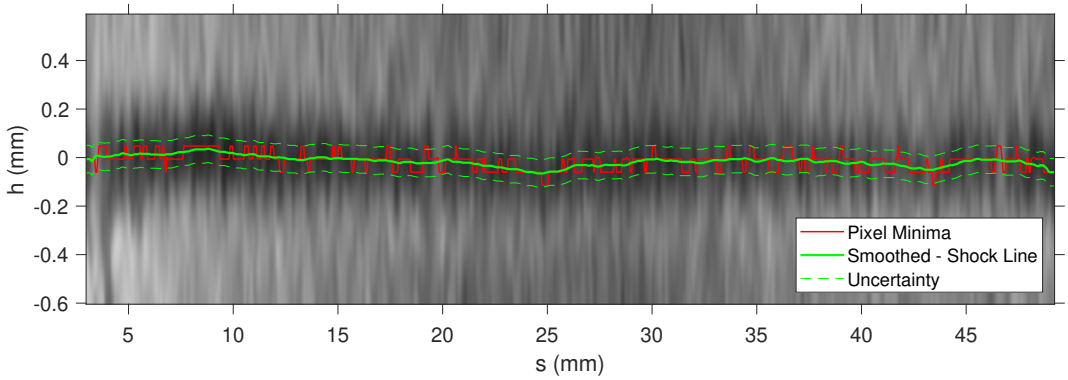
(a) Grid overlaid

(b) True grid scale

Figure 3.28: Shock grid



(a) Rectangular shock image



(b) Shock line detection

Figure 3.29: Rectangular shock processing

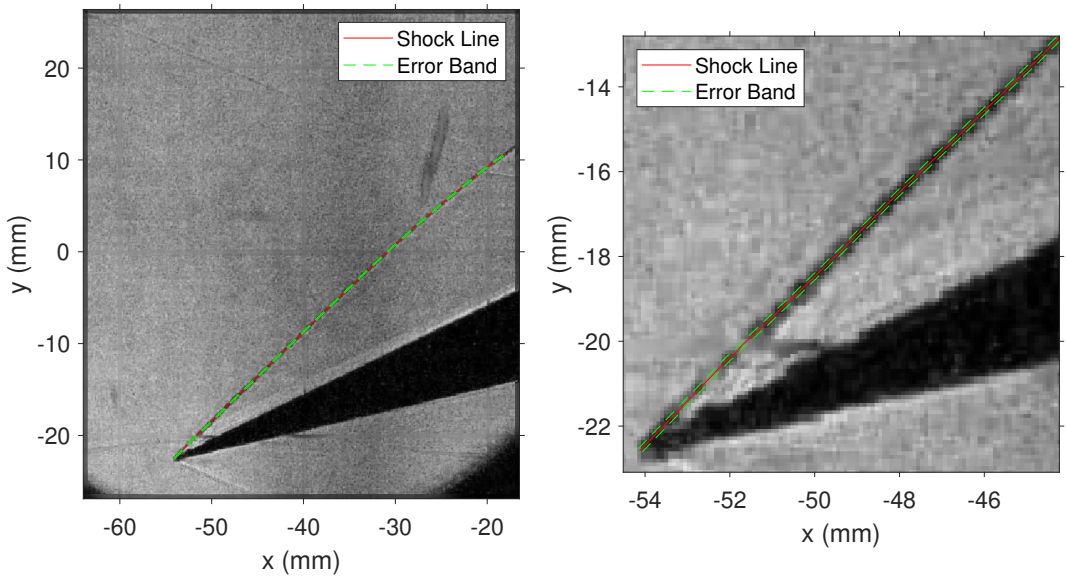


Figure 3.30: Captured shock wave

3.4 Experimental Results

For the purpose of demonstrating results, the following tests in table 3.3 are highlighted. Corresponding rotation profiles were presented in section 3.3.4.1. The wedge angle sign convention is illustrated for reference in figure 3.31. Flow visualisation videos are available in the *Digital Appendix*. Additional tests were used for collecting extra single data points in specific cases. The test number, e.g Test 1, will be used to refer to the tests in this table. The stop angle technically refers to the steady state angle after the wedge oscillations die down. It is approximately equal to the angular position at which the rubber foam dampers come into contact with the sliding drive head, to decelerate the rotation. The peak conditions are the maximum magnitude, with sign, of the wedge angle and its derivatives. The static conditions are the static pressure and temperature in the test section during the test. Note the maximum angular velocity achieved $\omega = 11.4 \times 10^3 degrees/s$. This is approximately the same as was achieved in the previous study [8] - though this is somewhat lower than the original goal of $15 \times 10^3 degrees/s$. The tip Mach number $M_\omega = \frac{\omega R_{tip}}{a_\infty}$, section 3.3.5, is used to non-dimensionalise the rotational velocity. The maximum tip Mach number achieved was $M_\omega = 0.06$. This is actually approximately double what was achieved in the previous study $M_\omega \approx 0.033$, since additionally, the tip length from the pivot was longer in this study ($60mm$ compared to $40mm$).

Table 3.3: Test matrix

Test Number			1	2	3	4	5	6	7	8
Mach Number M		± 0.001	2.8	3.0	3.0	3.0	3.3	3.3	3.3	3.3
Spring Compression C	mm	± 0.5	40	20	30	40	40	40	40	40
Initial Angle θ_f	$^\circ$	$\pm 0.07^\circ$	20.67	20.26	20.08	19.95	19.88	19.15	18.67	18.91
Stop Angle θ_f	$^\circ$	$\pm 0.07^\circ$	-17.03	-9.00	-12.51	-15.46	-15.89	-12.32	-16.93	-21.67
Peak Angle	$^\circ$	$\pm 0.07^\circ$	-22.67	-17.06	-19.44	-21.79	-21.37	-16.91	-22.81	-29.11
Peak Velocity	$^\circ/s \times 10^3$	± 0.2	-11.3	-6.7	-8.5	-11.0	-10.1	-10.6	-10.6	-11.4
Peak Tip Mach Number M_ω		± 0.005	-0.054	-0.032	-0.042	-0.054	-0.053	-0.056	-0.056	-0.060
Peak Acceleration	$rad/s^2 \times 10^4$	± 4	32	11	19	32	25	21	22	27
Static pressure p	kPa	± 0.3	12.2	9.0	9.0	9.0	5.8	5.8	5.8	5.8
Static temperature T	K	± 2	117	107	107	107	94	94	94	94
Frame Rate	kHz		5.077	5.077	5.077	5.077	5.077	5.077	5.077	5.077

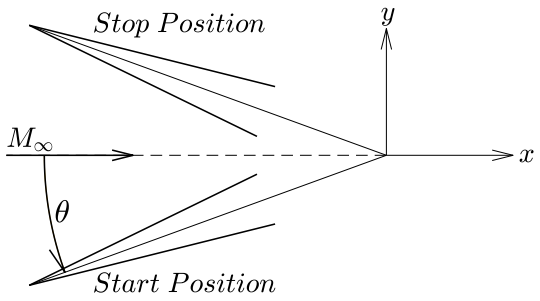


Figure 3.31: Wedge angle sign convention reference

3.4.1 Captured Shock Waves

In this section, the captured shock waves are transformed to coordinates more suitable for analysis and compared to theoretical predictions. Consider Test 3. Its rotation profile is shown in figure 3.32. Applying the two-dimensional oblique shock ($\theta-\beta-M$) relation to the top surface shock wave taken from an image frame shortly after the wedge rotation has begun, the theoretical shock line is shown on the shock image in figure 3.33. The captured shock wave may appear curved here compared to the theory line but this is due to 3-dimensional edge effects weakening the shock wave, which occurs at shorter distances due to the lower Mach number behind the shock wave for steeper surface angles, which results in a wider Mach cone (representing the domain influenced by the corner signals) which intersects with the symmetry plane sooner. The shock uncertainty band appears to overlap the shock line because it is narrow. If the captured shock wave is transformed to a new axis (x', y') oriented along the theoretical shock line, as shown in figure 3.34a, the perpendicular y' variations can be enhanced and experimental results and theory can be compared more clearly. The transformed coordinates are plotted in figure 3.34b with error bands for the captured shock and the theory line. The theoretical 2-dimensional flow limit (before edge effects begin to weaken the shock wave), as defined in section 2.6, is shown at its corresponding x' coordinate - after this point, the shock line is seen to curve significantly as the wedge lateral-edge expansions weaken the shock wave. The shock line angle is notably different compared to the theory line for a stationary oblique surface at the same angle. It may be that this is due to dynamic effects of the rotation, but the wedge velocity is relatively low here. If the relative tip theory, in section 3.3.5 is applied, as shown in figure 3.35, it does not account for the difference between the theory and measured shock. This dynamic theory line is only valid in the limit of the wedge tip - so it is only valid if the shock is assumed not to curve along its length.

The $\theta - \beta - M$ theory line uncertainties result from the uncertainties in the Mach number and surface angle, and are derived by the linearised propagation of error method, shown in equation 3.26. The shock angle β depends implicitly on θ and M - so it is solved numerically, represented by function f. The partial derivatives of f are also calculated numerically using central finite differencing. The same approach is applied for the dynamic tip theory line, except that there is an additional dependence on the rotational velocity ω and its associated uncertainty.

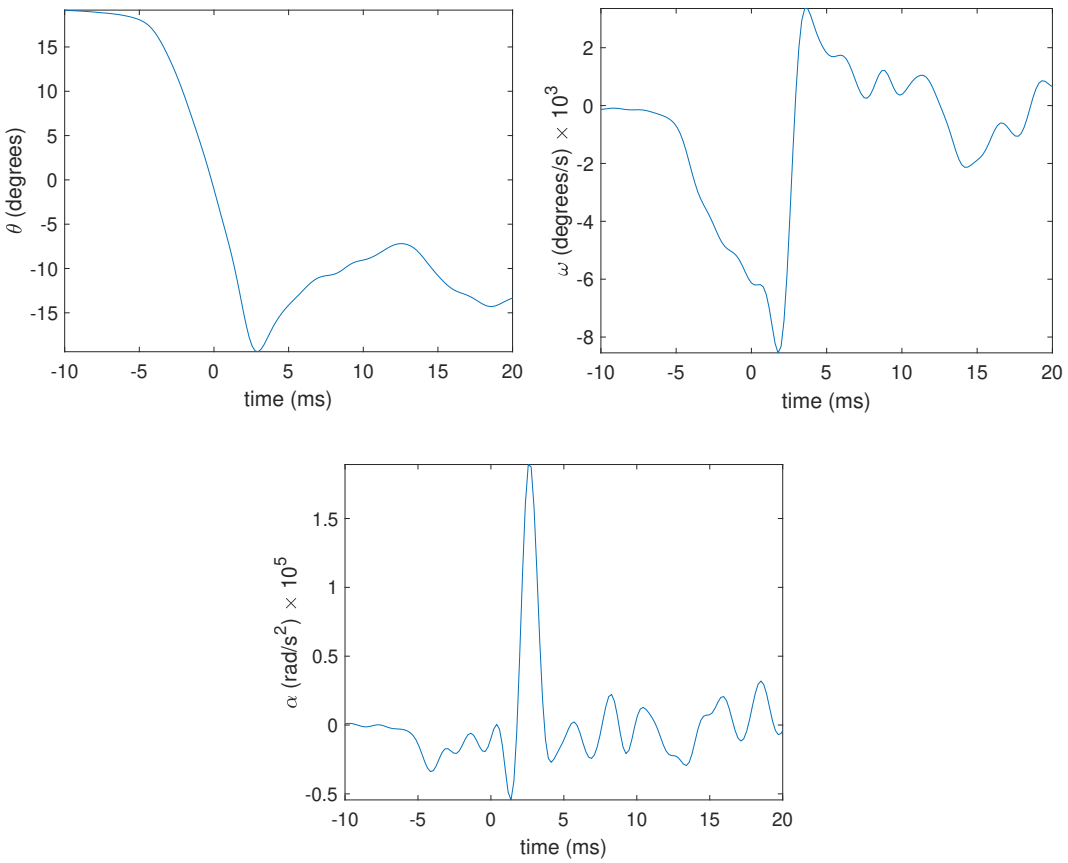


Figure 3.32: Rotation profile. Test 3

$$\beta = f(\theta, M) \tag{3.25}$$

$$\delta\beta = \sqrt{\left(\frac{\partial f}{\partial \theta}\delta\theta\right)^2 + \left(\frac{\partial f}{\partial M}\delta M\right)^2} \tag{3.26}$$

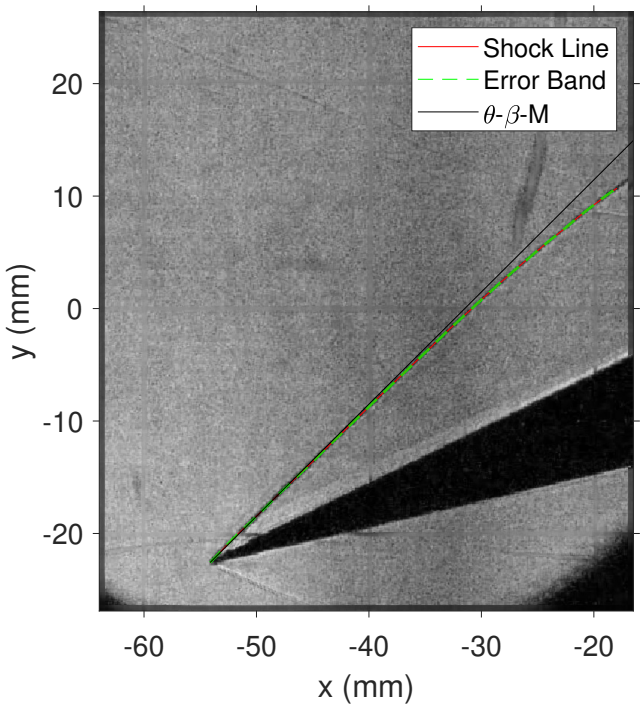
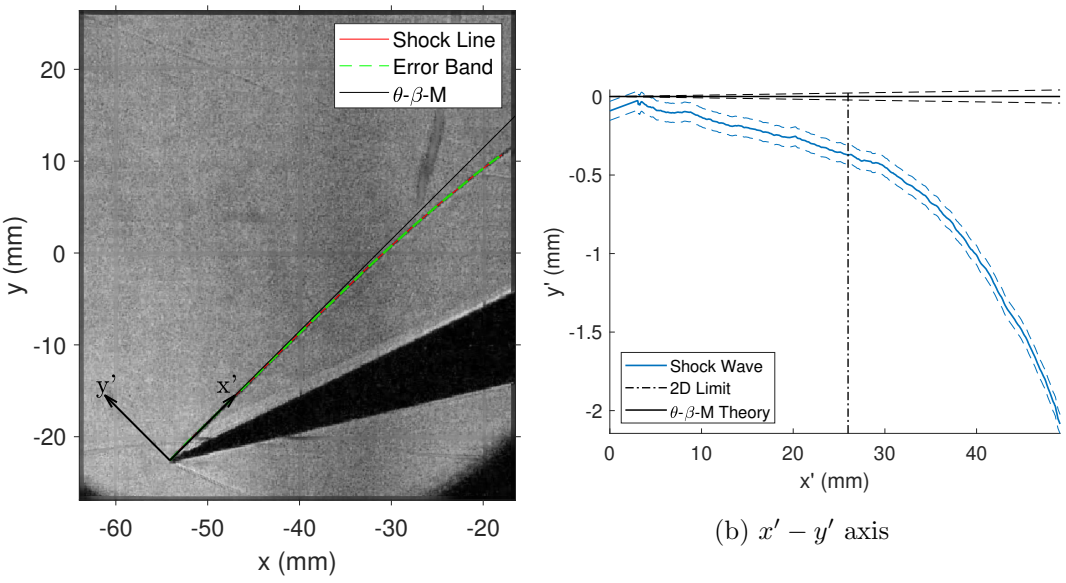


Figure 3.33: Oblique shock $\theta - \beta - M$ theory shock line overlay, Test 3. Wedge angle $\theta = 19.57°$, angular velocity $\omega = -99.57°/s$



(a) Axis geometry

(b) $x' - y'$ axis

Figure 3.34: Shock wave coordinate transform. Test 3

Generally, the 2-dimensional portion of the captured shock waves (before edge effects) appears to be relatively straight. Assuming that it can be represented by a straight line, a shock angle measurement is performed by fitting a line through this section, and obtaining the angle from the line gradient. It will be shown later that the assumption of a straight shock wave is flawed - but, this process is heuristic. Since the points along the shock line were smoothed during the capturing process, the original (unsmoothed) points are used for this linear regression, as described in section 3.3.2 for the wedge angle measurement. This line fit is illustrated in figure 3.36. The first few millimeters of the shock tend to deviate sharply from this line fit. This occurs for most captured shock lines. It is likely a consequence of the relatively large uncertainty of the measured tip position as motivated in section 3.3.3.

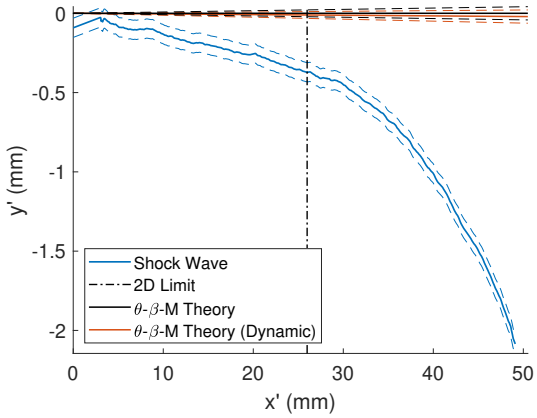


Figure 3.35: Shock wave in the $x' - y'$ axis with static and dynamic theory lines

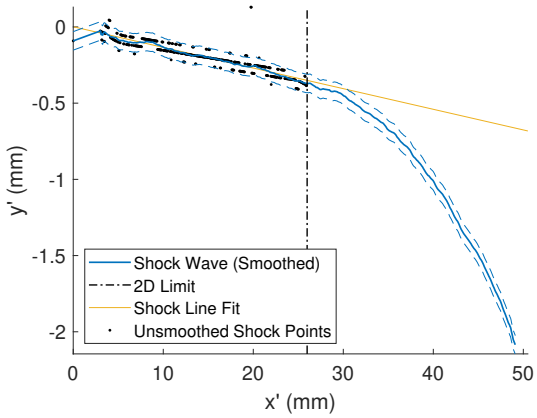


Figure 3.36: Shock angle measurement

A series of frames from Test 3 are taken to show a range of captured shock waves. These frames **A-J** are shown on the rotation profile in figure 3.37. The rotational velocity and acceleration are shown on the same axis, but scaled by their absolute maximum values throughout the domain. These frames give a range of wedge angles and include the maximum positive and negative velocities and accelerations. The captured shock waves are shown overlaid on the shock images and plotted on the

scaled shock theory axes for this series of frames in figure 3.38. Several features will now be discussed:

1. When the wedge incidence to the flow falls below approximately 5° in magnitude (consider frames **D** and **E**), the shock capturing process begins to fail as the optical setup fails to capture the relatively weak incident shock waves. In figure 3.39 a magnified view of frame **E** shows how the bottom shock wave becomes poorly defined. In general, with this optical setup, this problem is encountered for most low incidence angles, and the corresponding captured shocks are not reliable.

2. At the maximum rotational velocity for this test, frame **H**, (Tip Mach number $M_\omega = -0.042$), the dynamic tip theory line angle is relatively higher than the static line, compared to other frames, but still far from the measured shock line. The portion of the shock before the 2D limit appears straight. Similarly, for the maximum angular acceleration, frame **I**, the captured shock appears straight.

3. The 2-dimensional limit becomes larger for smaller angles of incidence, due to the higher Mach numbers produced behind the incident shock wave. Indeed, this limit is not even shown for frames **D** to **F**, as it falls after the end of the portion of the shock captured. At high angles of incidence, this limit becomes as short at about 27mm, for frame **I**. This presents a serious limitation in terms of studying 2-dimensional effects. Whereas, two-dimensional regions would facilitate better measurement of dynamic effects - curvature of the shock wave.

4. The error in the wedge tip position is apparent in all frames - presenting as a sharp deviation from the straight line fit at start of the shock wave.

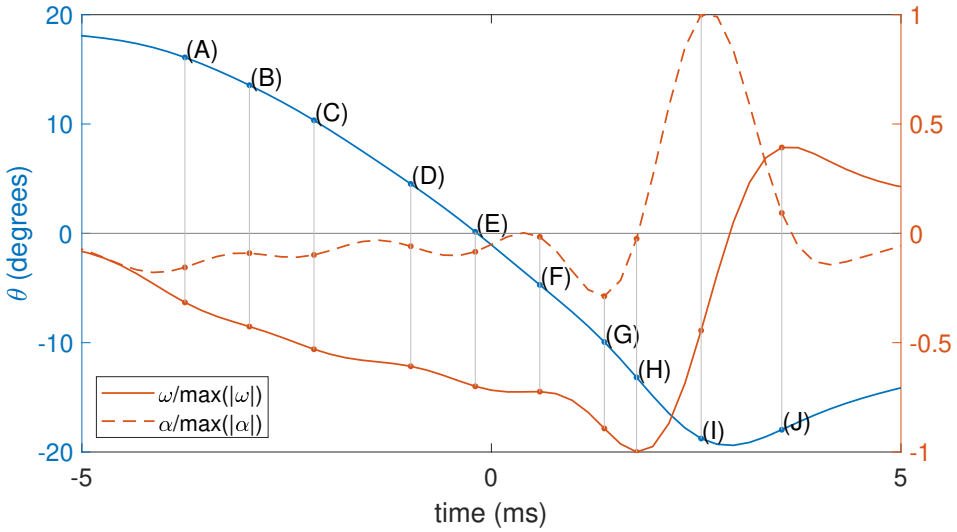
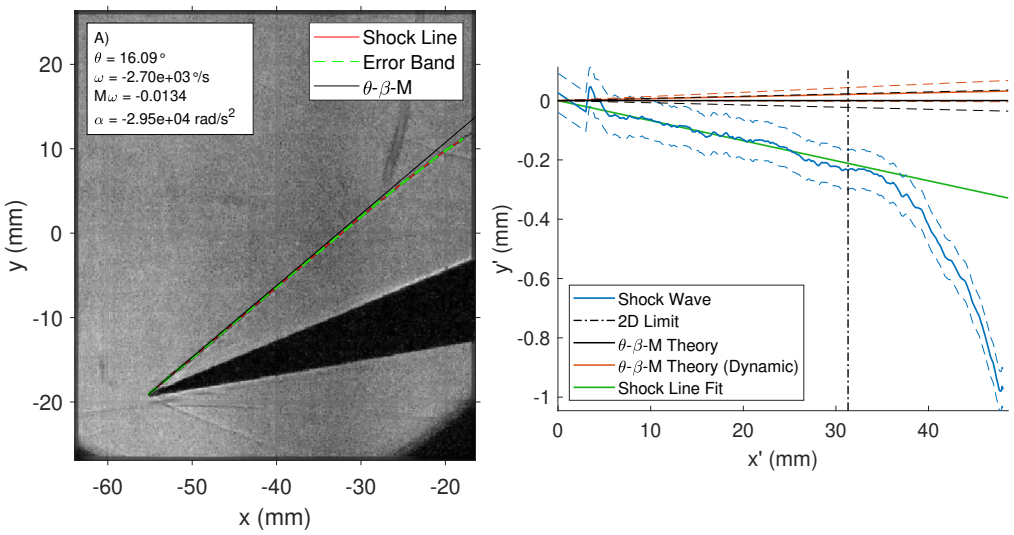
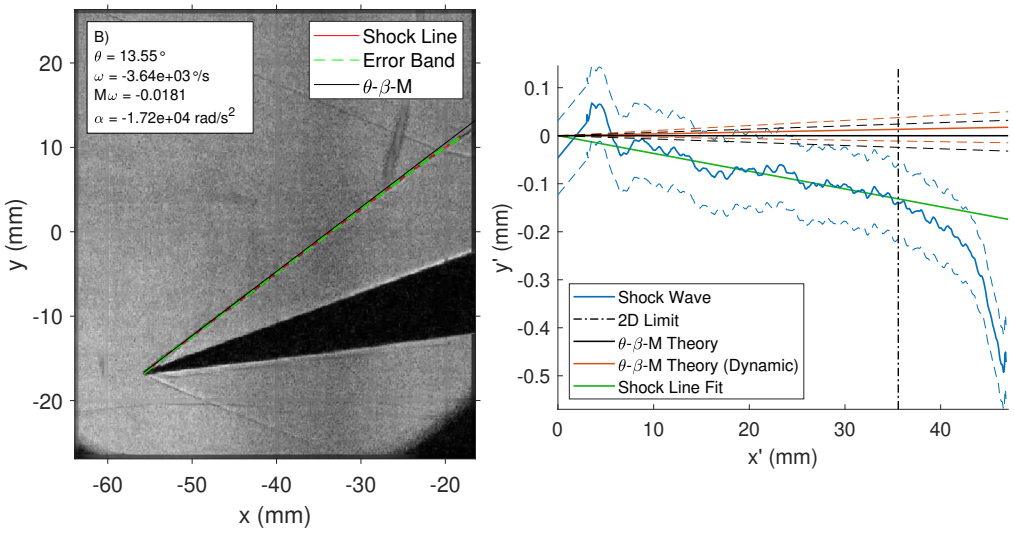
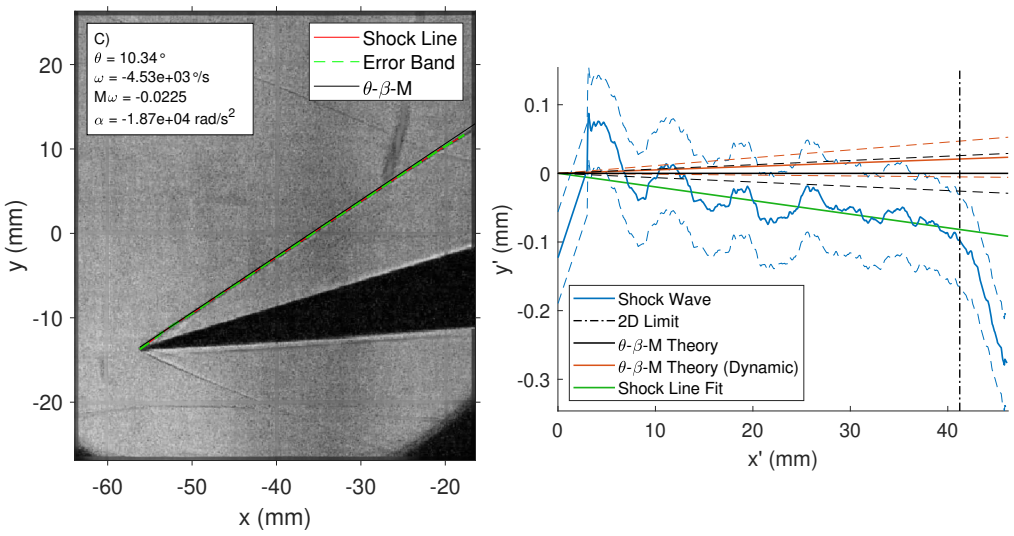
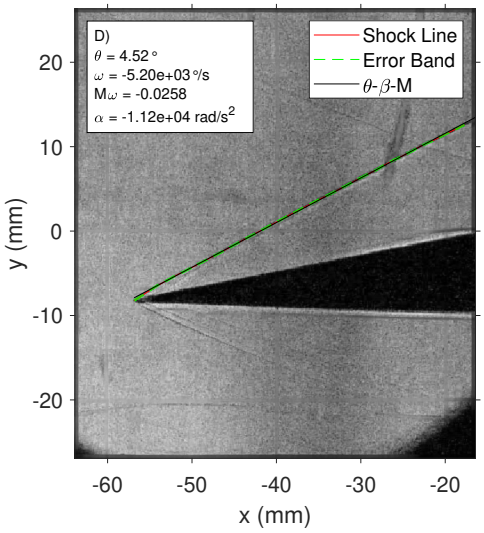


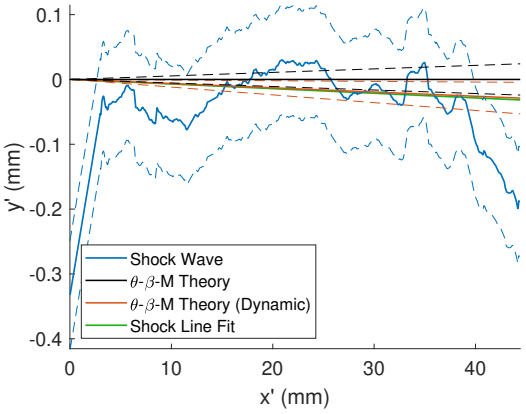
Figure 3.37: Shock capture series, Test 3. $\max|\omega| = 8.55 \times 10^3\, degrees/s$, $\max|\alpha| = 1.89 \times 10^5\, rad/s^2$

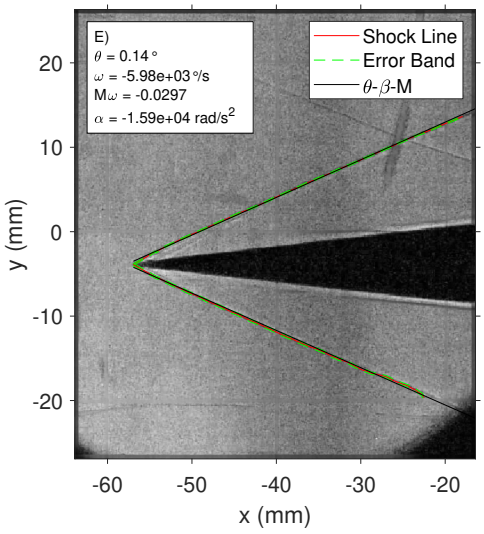

A)
θ = 16.09°
ω = -2.70e+03°/s
Mω = -0.0134
α = -2.95e+04 rad/s²
Shock Line
Error Band
θ-β-M
y (mm)
x (mm)
Shock Wave
2D Limit
θ-β-M Theory
θ-β-M Theory (Dynamic)
Shock Line Fit
y' (mm)
x' (mm)

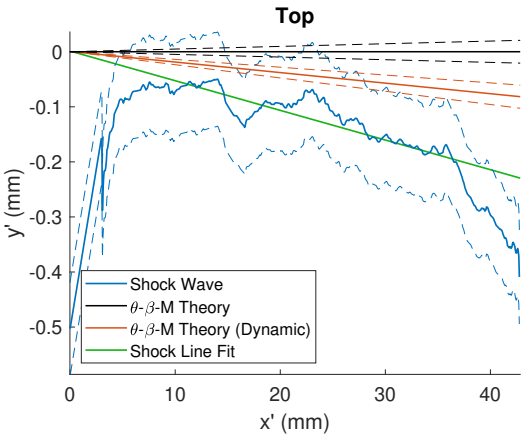

B)
θ = 13.55°
ω = -3.64e+03°/s
Mω = -0.0181
α = -1.72e+04 rad/s²
Shock Line
Error Band
θ-β-M
y (mm)
x (mm)
Shock Wave
2D Limit
θ-β-M Theory
θ-β-M Theory (Dynamic)
Shock Line Fit
y' (mm)
x' (mm)

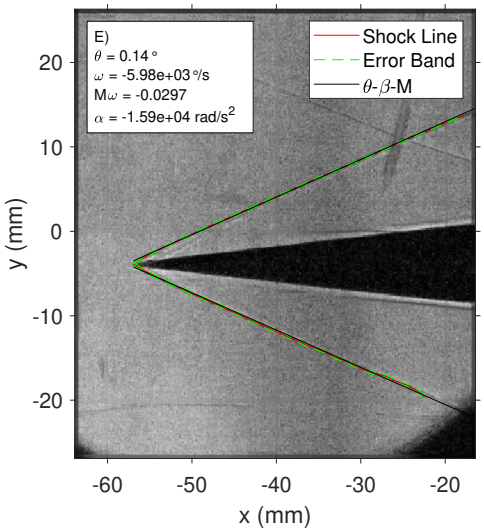

C)
θ = 10.34°
ω = -4.53e+03°/s
Mω = -0.0225
α = -1.87e+04 rad/s²
Shock Line
Error Band
θ-β-M
y (mm)
x (mm)
Shock Wave
2D Limit
θ-β-M Theory
θ-β-M Theory (Dynamic)
Shock Line Fit
y' (mm)
x' (mm)

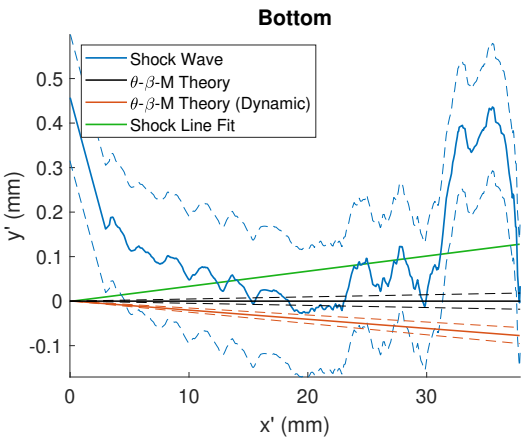

D)
θ = 4.52 °
ω = -5.20e+03 °/s
Mω = -0.0258
α = -1.12e+04 rad/s²
Shock Line
Error Band
θ-β-M
y (mm)
x (mm)

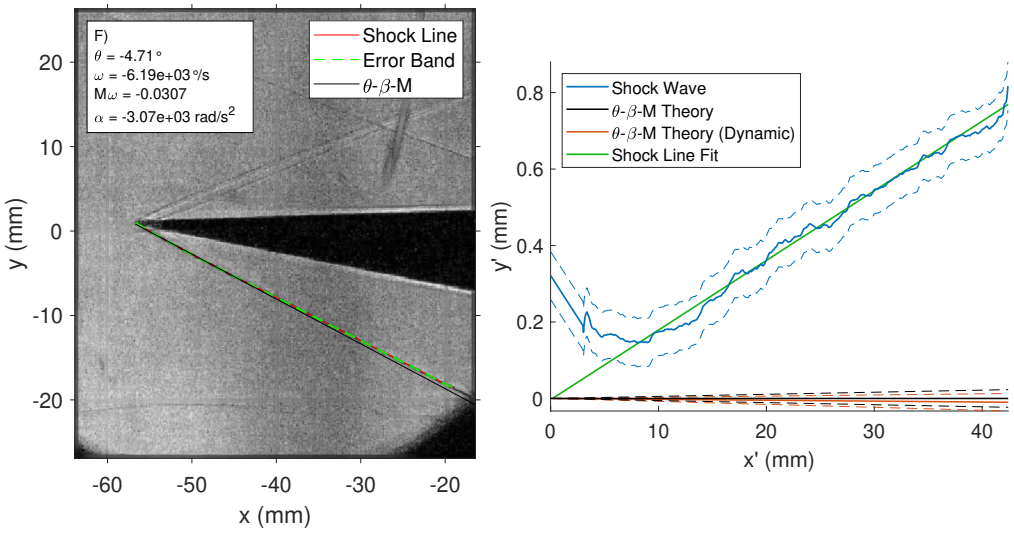

Shock Wave
θ-β-M Theory
θ-β-M Theory (Dynamic)
Shock Line Fit
y' (mm)
x' (mm)

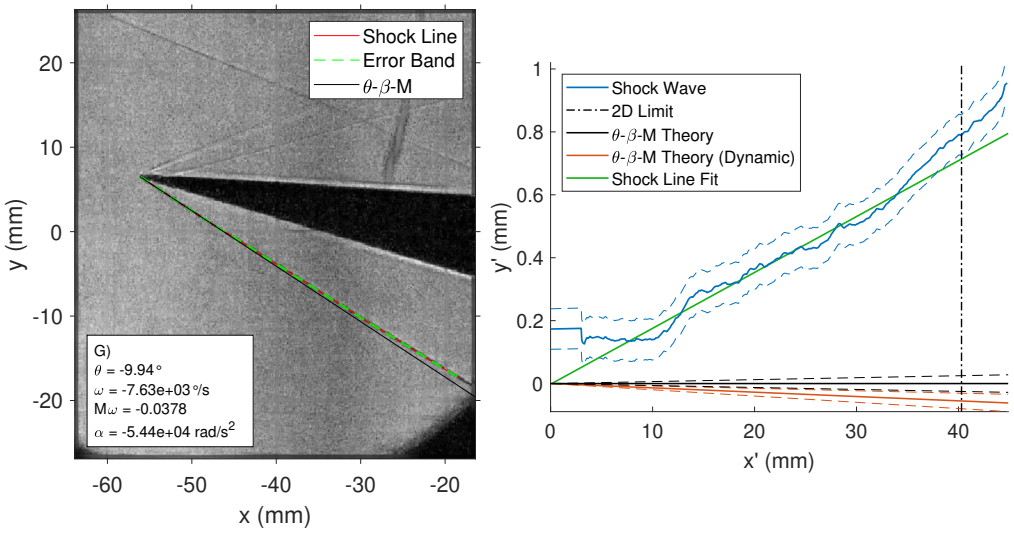

E)
θ = 0.14 °
ω = -5.98e+03 °/s
Mω = -0.0297
α = -1.59e+04 rad/s²
Shock Line
Error Band
θ-β-M
y (mm)
x (mm)

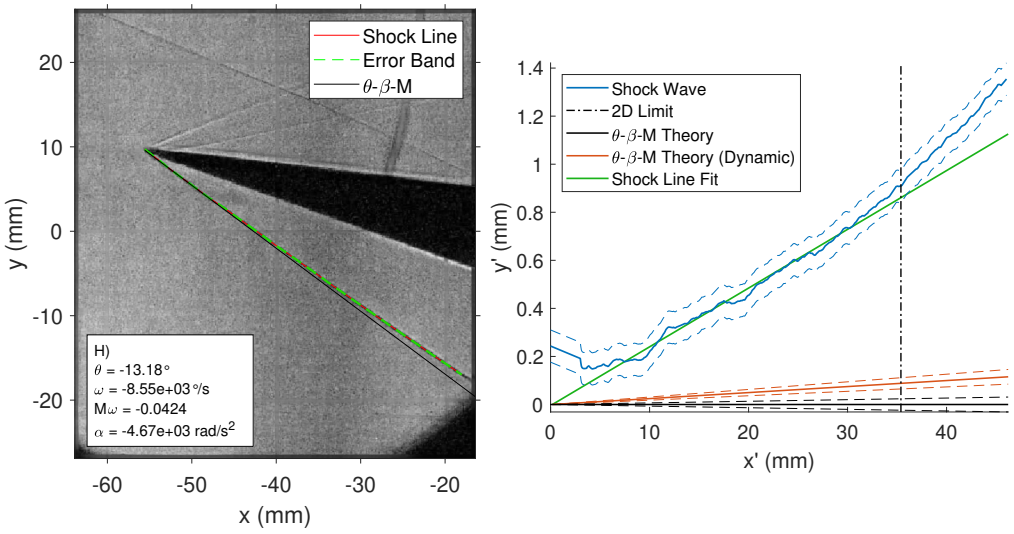

Top
Shock Wave
θ-β-M Theory
θ-β-M Theory (Dynamic)
Shock Line Fit
y' (mm)
x' (mm)


E)
θ = 0.14 °
ω = -5.98e+03 °/s
Mω = -0.0297
α = -1.59e+04 rad/s²
Shock Line
Error Band
θ-β-M
y (mm)
x (mm)


Bottom
Shock Wave
θ-β-M Theory
θ-β-M Theory (Dynamic)
Shock Line Fit
y' (mm)
x' (mm)


F)
θ = -4.71°
ω = -6.19e+03 °/s
Mω = -0.0307
α = -3.07e+03 rad/s²
Shock Line
Error Band
θ-β-M
y (mm)
x (mm)
Shock Wave
θ-β-M Theory
θ-β-M Theory (Dynamic)
Shock Line Fit
y' (mm)
x' (mm)


G)
θ = -9.94°
ω = -7.63e+03 °/s
Mω = -0.0378
α = -5.44e+04 rad/s²
Shock Line
Error Band
θ-β-M
y (mm)
x (mm)
Shock Wave
2D Limit
θ-β-M Theory
θ-β-M Theory (Dynamic)
Shock Line Fit
y' (mm)
x' (mm)


H)
θ = -13.18°
ω = -8.55e+03 °/s
Mω = -0.0424
α = -4.67e+03 rad/s²
Shock Line
Error Band
θ-β-M
y (mm)
x (mm)
Shock Wave
2D Limit
θ-β-M Theory
θ-β-M Theory (Dynamic)
Shock Line Fit
y' (mm)
x' (mm)

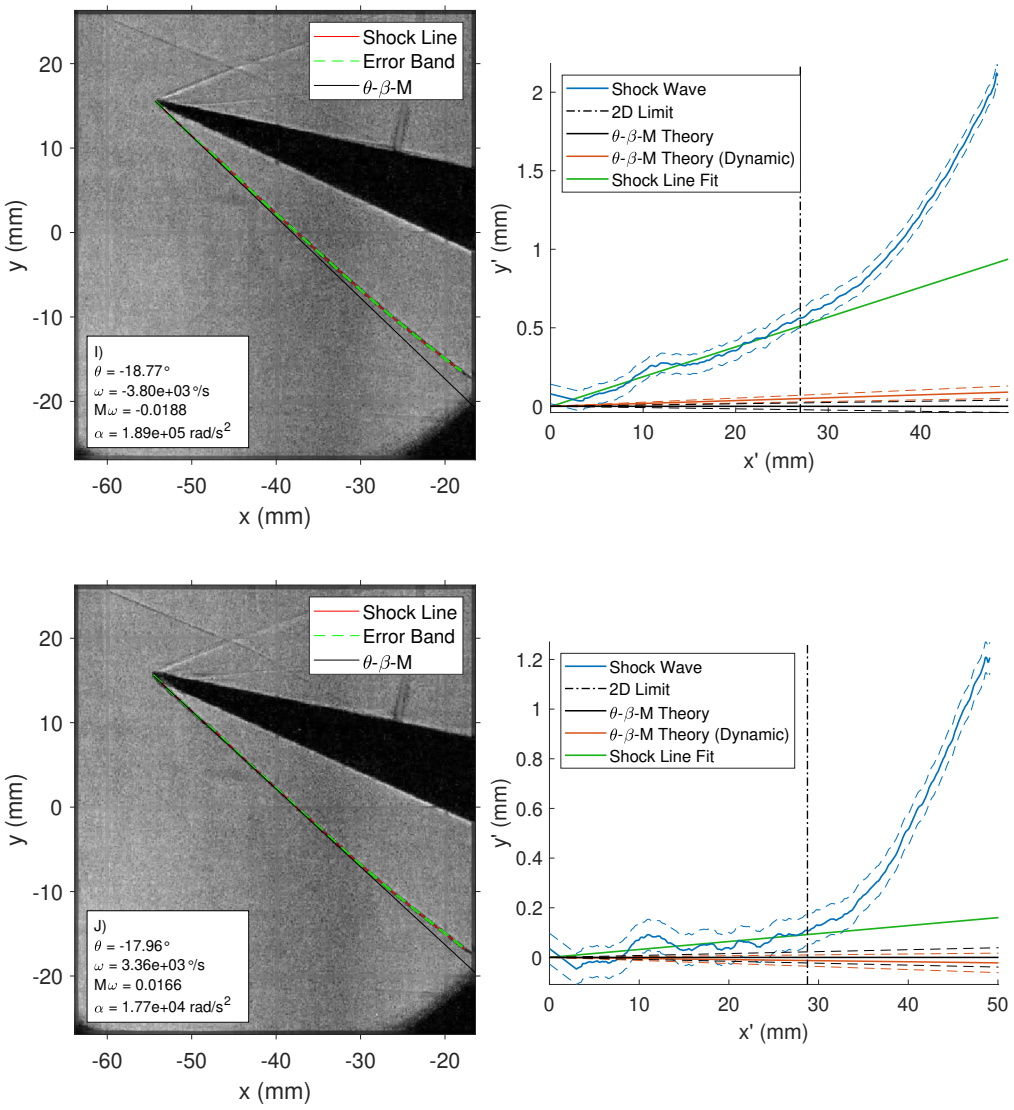


Figure 3.38: Captured shock waves. $M = 3$, $C = 40mm$

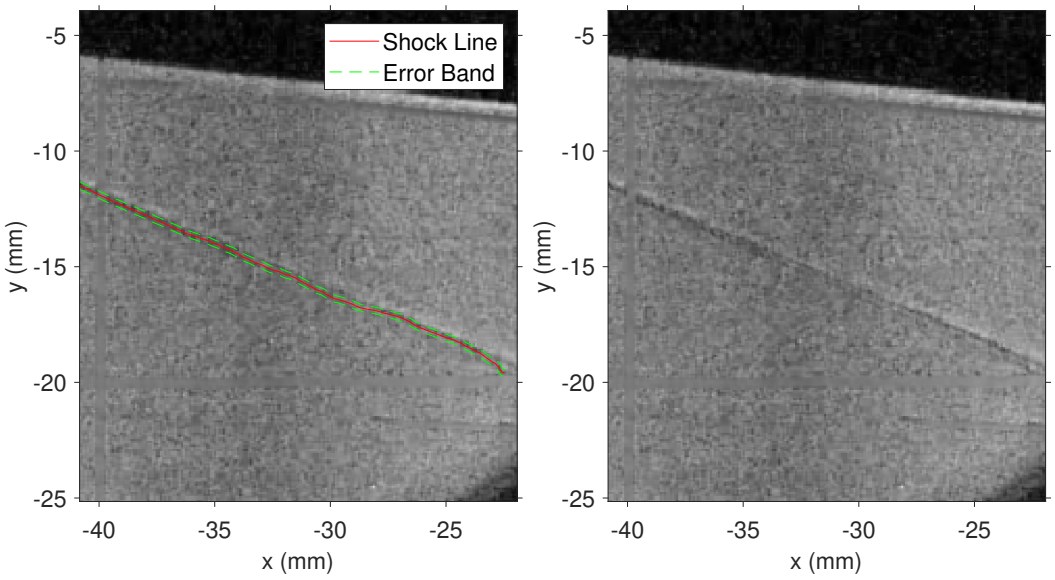


Figure 3.39: Failed shock capturing. Frame **E**.

The shock angles measured from the captured shock waves for all tests (in table 3.3, plus additional tests) are shown compared to the surface angles (absolute angles of incidence of top and bottom surfaces measured from the horizontal) in figure 3.40, along with the static shock angle theory lines for each Mach number. To avoid the poor shock resolution issues at small incidence angles, only frames with incidence $|\theta| > 5°$ were included. This still represents a total of 491 data points (from 21 tests). The theory line uncertainty bands result from the uncertainty in the test Mach number. While the measured shock angle uncertainties result from the linear regression fit.

The measured angles correlate with the static oblique shock theory, but disagree beyond the bounds of uncertainty. In the following sections, CFD results will show that the curvature of the shock waves for these cases is actually expected to be significant on this scale - enough to shift points along the shock wave away from the theory line to an extent comparable to the discrepancy seen here between experiment and static theory (the shift of experimentally measured angles from the theory lines beyond the uncertainty bounds in figure 3.40) - but not large enough to clearly show as a curved line within the uncertainty bands of captured shock waves. However, noise in the experimental results was identified and is also a major factor in the disparity seen here. This will be discussed with comparison to CFD results.

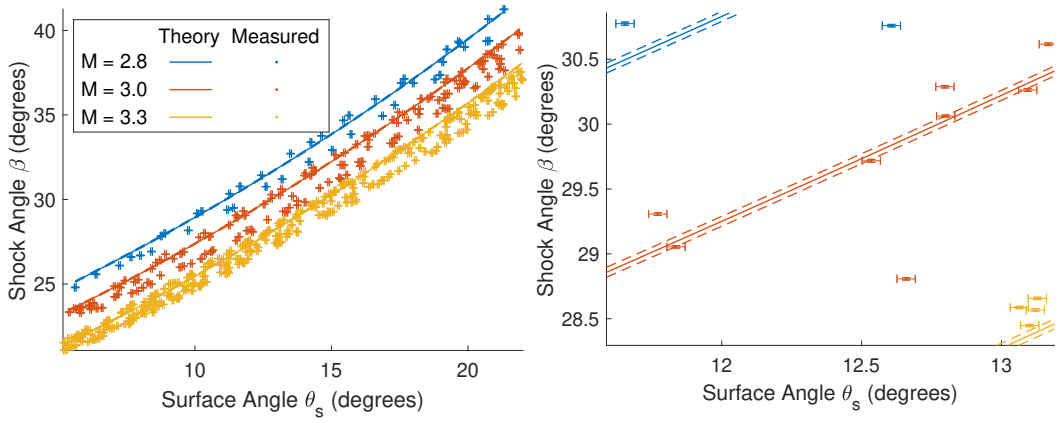


Figure 3.40: All measured shock angles. Oblique shock theory lines shown as solid lines with dashed uncertainty bands. Measured angles from experimental frames shown as scattered points, coloured by Mach number, with horizontal and vertical error bars.

3.5 Matching CFD to Experiment

Since the experimental setup does not provide sufficient resolution of potential shock wave curvature, it cannot be used to validate CFD. One approach to overcome this issue (until a new experiment can be designed) is to apply different numerical methods and discretisations to the problem and compare results, so that if there is agreement, we can be more confident in the results (as discussed in section 2.4). Therefore, a finite volume (FV) code and Method of Characteristics (MoC) code was applied to this problem. These codes are described in sections 5 and 4 respectively. The setup of these codes to match the experimental results is discussed this section.

In order to match CFD to the experimental results, the rotation profiles extracted for each test were used to define the motions in each code. Consider the rotation profile in figure 3.41. To reduce the computational load required, only part of the motion was simulated. For the finite volume code which can continuously handle positive and negative wedge angles, the profile section **a** to **d** was taken, which includes the maximum negative and positive rotational velocities and accelerations. A constant acceleration section, starting from rest was appended to the beginning of this section to avoid potential numerical issues and spurious flow features which could result from a large instantaneous change in velocity. The acceleration of this section was chosen to be equal to the maximum instantaneous acceleration in the test rotation profile.

The MoC code handles attached shock-bound regions (top and bottom surfaces) separately. In fact, it is setup to only handle a 'top' surface - counter clock wise from the line surface, as shown in figure 3.42 - refer to section 4.6.1 for details. However, a region below the line (counter clock wise) can always be transformed to an equivalent clock wise case, by reflecting the flow problem (geometry and field vectors) about the x-axis, solving and then reflecting the results back - since the physics will not change for a mirror image flow field. For the experimental case - rotation about a fixed axis - this symmetry is illustrated in figure 3.43: if the bottom surface is exposed ($\theta < 0$), it is equivalent to the reflected problem with the opposite angle and rotational derivatives. One drawback of this method, for the MoC scheme, is that the experimental rotation profile must be divided into separate sections for the top and bottom surfaces - the periods during which an oblique shock, rather than an expansion fan exists on these surfaces (The MoC code only handles attached shock regions). Referring again to figure 3.41. Section **a-c** is used for the top surface MoC simulation and the section **b-d** is used for the bottom.

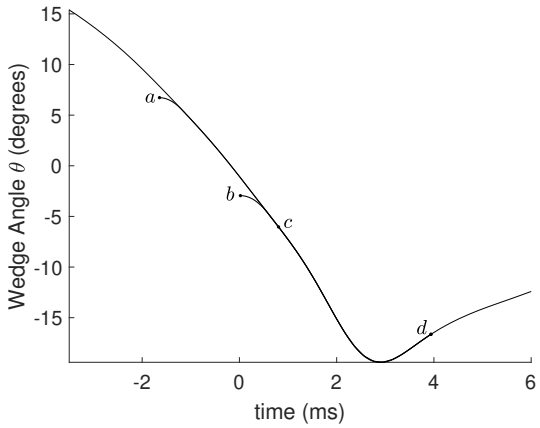


Figure 3.41: Rotation profile extraction

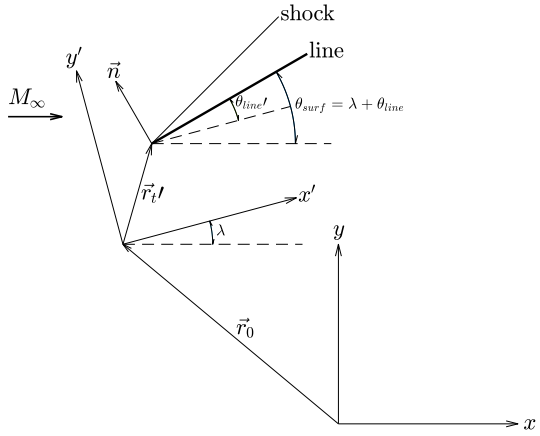


Figure 3.42: MoC moving line geometry

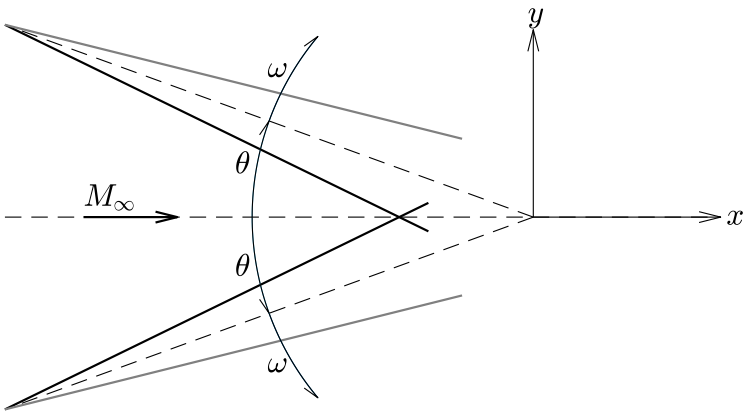


Figure 3.43: Wedge rotation symmetry

The profile section (**a-d**) extracted for the finite volume model is shown in figure 3.44. This profile is also used for the top surface MoC simulation (since it also starts at **a**), but is cut off at point **c**. The bottom surface MoC profile is shown in figure 3.45. Of course for the bottom surface, the sign of these angles and derivatives will be switched ($\theta_{bottom} = -\theta,\ \omega_{bottom} = -\omega,\ \alpha_{bottom} = -\alpha$).

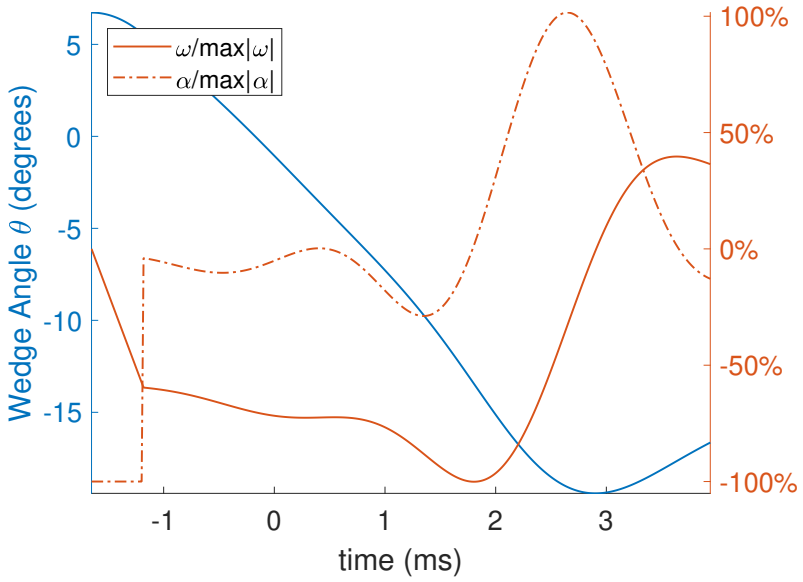


Figure 3.44: Extracted FV, and MoC-top, Profile **a-d**

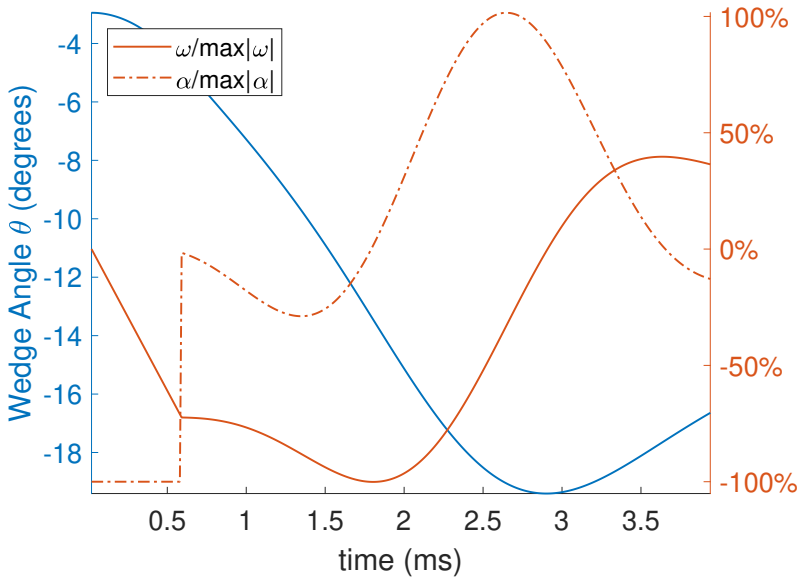


Figure 3.45: Extracted MoC-bottom profile **b-d**

The finite volume rotation profile is applied to the finite volume model described in section 5 in the following way: in figure 3.46 the wedge is shown with the x-axis aligned with the flow direction and the origin centered at the wedge pivot. The approach used by the finite volume model is to solve the Euler equations in the non-inertial reference frame, the $x' - y'$ axis, which in this case executes a rotation about the $x - y$ axis origin according to the time dependent rotation profile obtained from the experiment. In Fluent, this is achieved by defining a rotation axis at $(x', y') = (R, 0)$ and varying the angular velocity about this axis, according to the rotation profile, via a User Defined Function (UDF). The UDF reads the wedge angle and rotational velocity time series from a text file and interpolates linearly from this time series to obtain the angle and angular velocity at each time step. Initially, the far field boundary (box surrounding the wedge) condition is set such that the steady supersonic flow, with conditions matching the wind tunnel test conditions, enters aligned with the absolute frame x-axis which is angled downwards by the angle θ when viewed from the relative reference frame. In addition to varying the angular velocity of the relative frame about the pivot, it is necessary to vary the fluid velocity inlet angle at the far field boundary as the orientation of the relative frame changes with respect to the oncoming air flow - since Fluent does not automatically update the inlet angle, as described in section 5.3. An example Fluent V19.2 case is included in the *Digital Appendix* for Test 3.

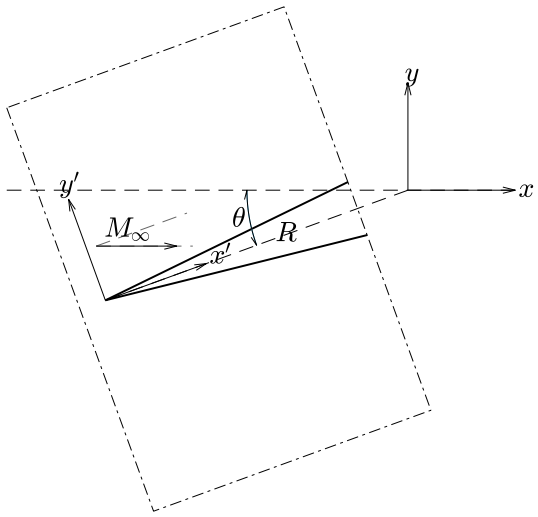


Figure 3.46: Finite volume reference frame

The Method of Characteristics rotation profile was implemented as follows: consider again the generalised line motion available to the solver in figure 3.42. The relative reference frame $x' - y'$ is kept at the origin $\vec{r}_0 = \vec{0}$; the relative frame tip position is set at $\vec{r}_t' = (-R, 0)$ (were R is the distance to the wedge tip from the rotational axis); and the line angle is set to the wedge half angle $\theta'_{line} = 6°$. Finally, the frame

axis angle λ and its derivatives are equivalent to the wedge angle and its derivatives - which are similarly interpolated from the time series at each time step.

3.6 Experiment vs CFD - Results

Firstly results for Test 3 will be compared. A series of frames **A**-**G**, shown in figure 3.47 are selected to compare experimental and CFD results. These include two frames with the top surface exposed **A** and **B**; the maximum negative and positive angular velocities **D** and **G**; the maximum negative and positive angular accelerations **C** and **E**. At frame **F**, there is a high angular acceleration, with low angular velocity. For each frame, the dynamic tip oblique shock theory gives the corresponding flow conditions behind the shock wave, in the limit of the tip. Using these properties, the slowest characteristic speed along the surface was determined as the convective velocity minus the sound speed: $C_- = |\vec{V}| - a$. Using this, and the surface length (L_s) the longest time taken for information from the tip to leave the domain was approximated: $T_- = \frac{L_s}{C_-}$. This characterises the period of time before any given frame which may affect the frame flow field (approximately) - this will be referred to as the flow history, as discussed in section 2.2. The flow history periods are shown immediately behind each selected frame in figure 3.47. Theoretically, the changes in wedge rotation derivatives during these periods could effect the frame results - rather than just the wedge motion at the exact frame. However, the rotation derivatives generally do not change greatly during there periods, so the results will usually be discussed in terms of the rotation derivatives exactly at a given frame.

Captured experimental shock waves are compared with the CFD results in the horizontal $x - y$ (wind tunnel) axis, and in the static $\theta - \beta - M$ line theory axis $x' - y'$, in figure 3.48. The wedge angles and time derivatives are shown. Again, the wedge angles (θ) are measured counter clock wise from the horizontal axis. Due to the relatively large uncertainty in the wedge tip measurement, the first 3 mm of each experimental shock was trimmed and set to zero for all theory axis plots, since including this initial section only obscures results.

Consider the first two (top surface) frames **A** and **B**. The CFD shock lines show good agreement and show a significant degree of curvature, compared to the dynamic tip theory line - which assumes the shock angle in the limit of the tip remains constant along the wedge. This line appears opposed to the CFD curvature; however, in the limit of the tip, they are tangential - in fact this is guaranteed for the MoC results, since the dynamic tip theory is used to define the tip properties in this code. Similar

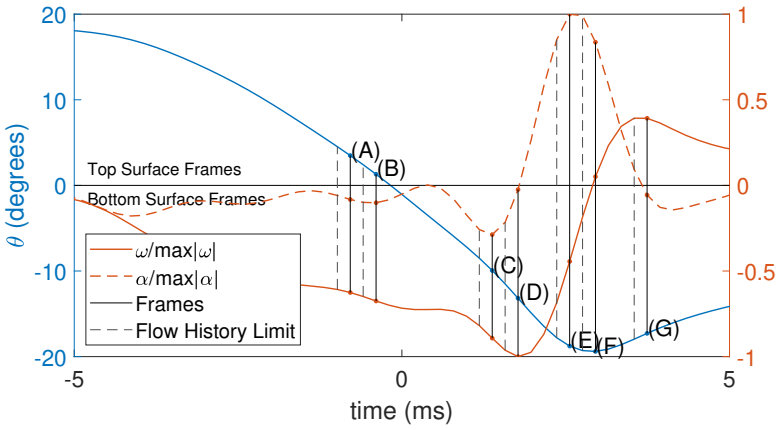


Figure 3.47: CFD - experiment frames

departure from the tip limit is seen throughout. This clearly demonstrates that the tip limit shock angle is not a good characterisation of the overall flow field.

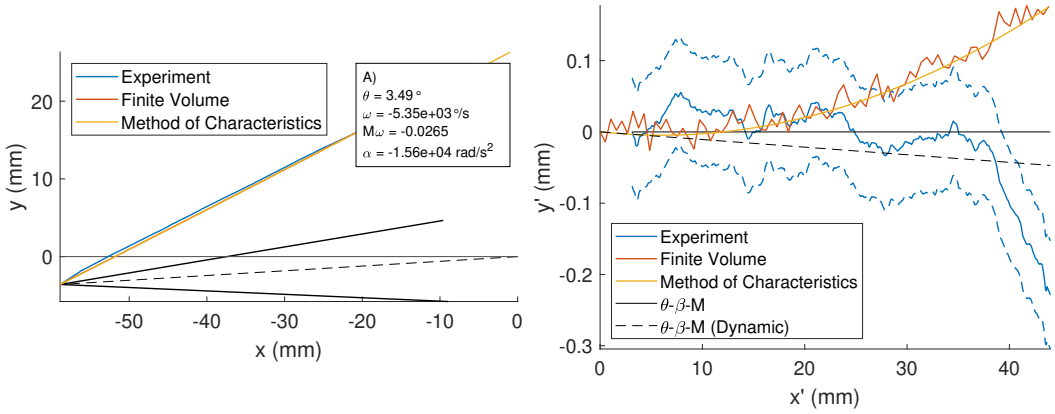
In these two frames, the wedge is rotating and accelerating clock wise. The shock wave is seen to lag the movement of the tip (instantaneously in the y' direction) - the tip moves faster than the rest of the surface, and is closer to the shock wave, therefore the surface signals reach parts of the shock nearer the tip first, and parts further along the shock later, thus curving the shock upwards. The experimental shock wave appears to agree with the theory line here, but this behaviour is not observed in general.

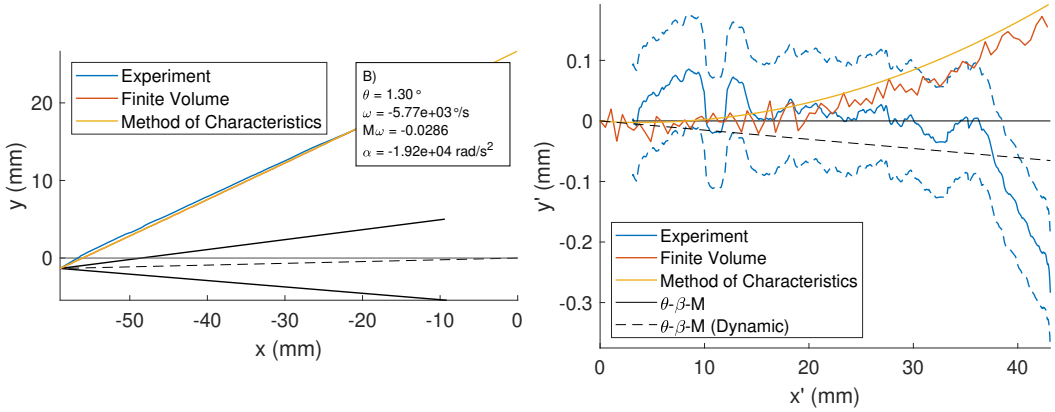
Consider the first two bottom surface frames **C** and **D**. It becomes apparent that the shock curvature is very significant compared to the tip limit theory. The deviation of the experimental shock from the static shock theory appears to agree partially with the CFD shock lines; though outside of the uncertainty bounds. At these frames, the angular velocities are similar, but **D** has a relatively small acceleration and **C** has the maximum negative acceleration; however, the shock lines are quite similar - which may indicate that in this regime, the curvature is more strongly a function of angular velocity than acceleration.

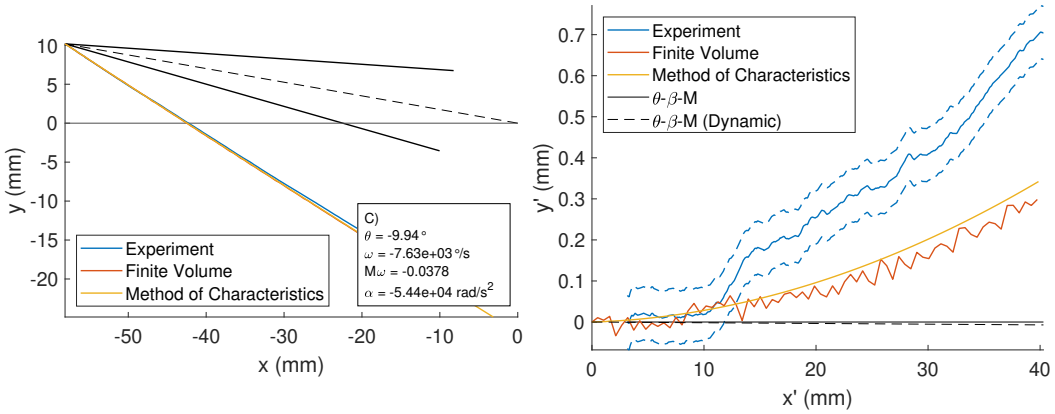
Consider frames **E** and **F**. These frames have large positive angular accelerations, but the velocity at **F** is relatively small. The curvature of the CFD shock at **F** is far smaller than at **E**, once again indicating that the angular velocity has a stronger effect on the curvature. The experimental shock wave once again does not agree with the CFD shock lines. However, note that the shift of experiment from static theory is larger in frame **E** than in frame **F** (by approximately $0.2\,mm$ at $x' = 25\,mm$. This might be a result of the larger curvature of the shock wave predicted by the CFD

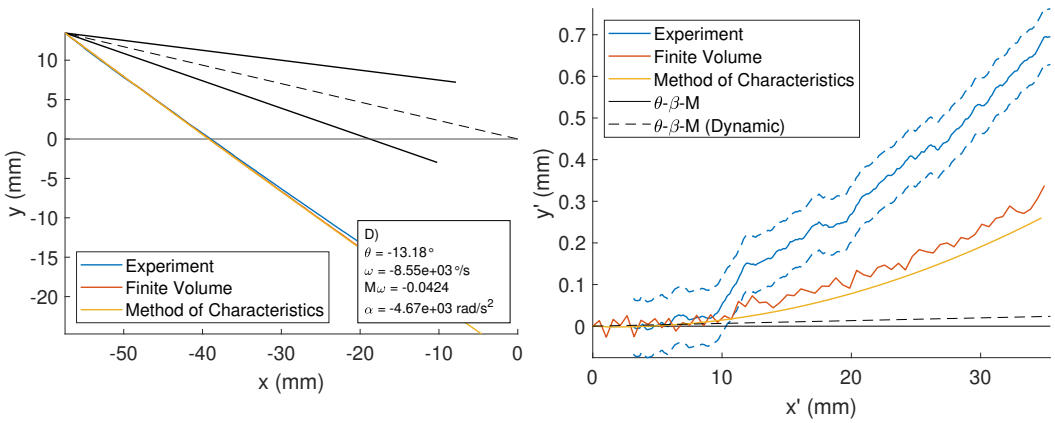
for frame **E**. Observe that the y' height of the CFD shock line at $x' = 25\,mm$ for frame **E** is approximately $0.15\,mm$ higher than in frame **F**.

At frame **G**, the wedge has begun to rotate counter clock wise, after its deceleration. The shock now curves downwards - lagging the motion of the wedge. In this frame in particular the experimental shock wave is jagged - a result of errors in the shock capturing process. Finally, notice that in the horizontal $x - y$ coordinates, the experimental shock curves upwards (counter clock wise) at the end. This is due to the three-dimensional edge effects weakening the shock wave. The shock curves downwards in the two-dimensional region (visible in the $x' - y'$ axis), before the three-dimensional edge effects begin, and then upwards towards the end (in the experiment), due to these edge effects. Of course the CFD results will not show these three-dimensional effects as they are two-dimensional models.


Experiment
Finite Volume
Method of Characteristics
A)
θ = 3.49 °
ω = -5.35e+03 °/s
Mω = -0.0265
α = -1.56e+04 rad/s²
y (mm)
x (mm)
Experiment
Finite Volume
Method of Characteristics
θ-β-M
θ-β-M (Dynamic)
y' (mm)
x' (mm)


Experiment
Finite Volume
Method of Characteristics
B)
θ = 1.30 °
ω = -5.77e+03 °/s
Mω = -0.0286
α = -1.92e+04 rad/s²
y (mm)
x (mm)
Experiment
Finite Volume
Method of Characteristics
θ-β-M
θ-β-M (Dynamic)
y' (mm)
x' (mm)


Experiment
Finite Volume
Method of Characteristics
C)
θ = -9.94 °
ω = -7.63e+03 °/s
Mω = -0.0378
α = -5.44e+04 rad/s²
y (mm)
x (mm)
Experiment
Finite Volume
Method of Characteristics
θ-β-M
θ-β-M (Dynamic)
y' (mm)
x' (mm)


Experiment
Finite Volume
Method of Characteristics
D)
θ = -13.18 °
ω = -8.55e+03 °/s
Mω = -0.0424
α = -4.67e+03 rad/s²
y (mm)
x (mm)
Experiment
Finite Volume
Method of Characteristics
θ-β-M
θ-β-M (Dynamic)
y' (mm)
x' (mm)

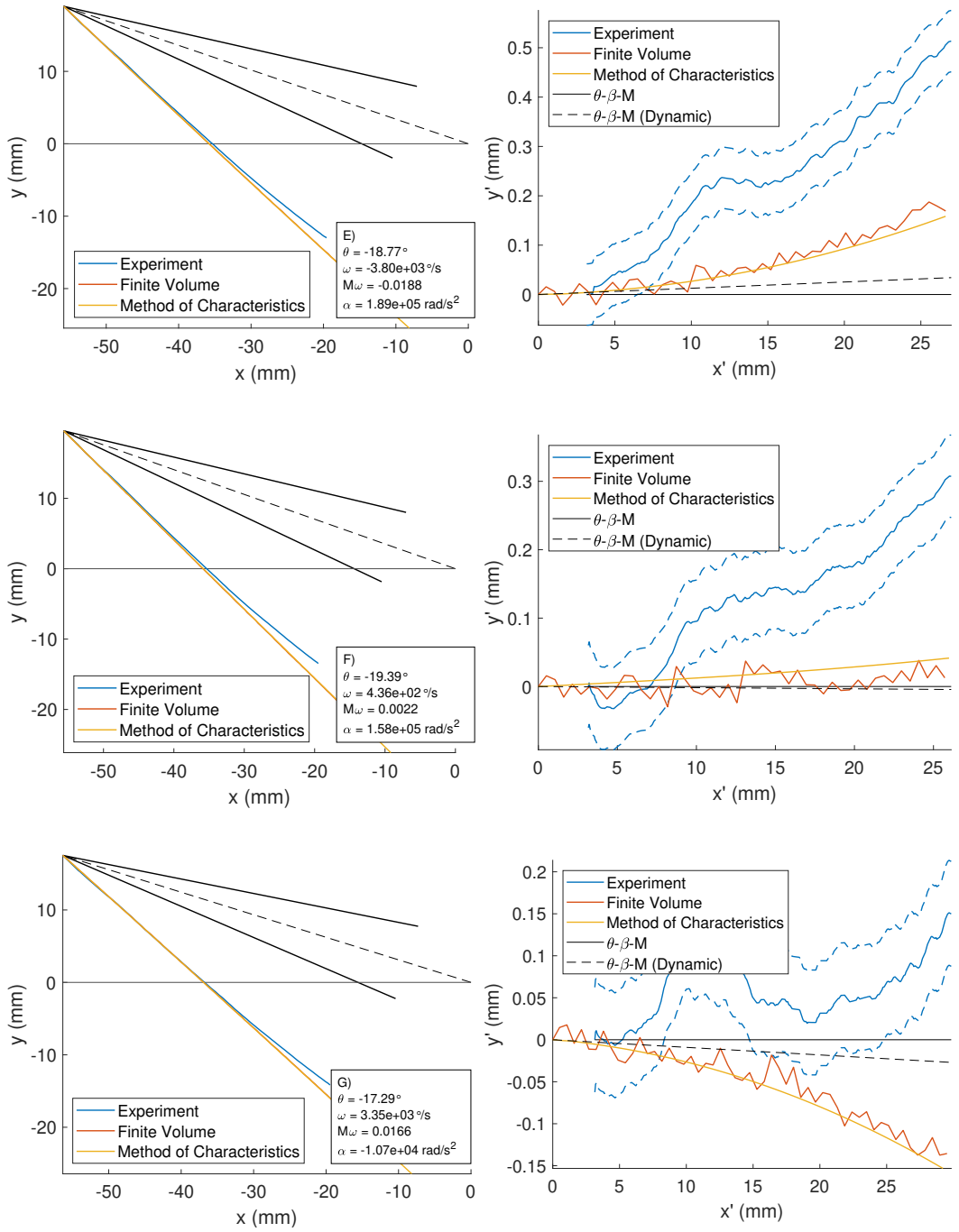


Figure 3.48: CFD - experiment shock wave results

3.6.1 Discrepancies Between Experiment and CFD

Based on CFD results, the curvature of the shock wave is relatively significant compared to the scale of the difference between the experiment and static theory lines, and therefore is expected to contribute significantly, on this scale, to the departure of experiment from the static shock theory. However, the CFD and experiment shock lines generally tend to disagree, beyond the bounds of the experimental uncertainty. This disagreement is generally of the order of about 0.5°. Since the CFD results are independently verified it is not unreasonable to assume that they are valid - at least in terms of the order of these curvature effects. Of course, viscous effects - the boundary layer - which are not accounted for by these CFD models may contribute to a slight shift in angle, compared to the Experiment. At this time no direct viscous CFD results are available for comparison to quantify this effect. However, if this were due to the boundary layer, we might expect to see a more consistent difference between CFD and experiment. There are other potential sources of error in the experiment which could account for these discrepancies. Particular potential error sources will now be discussed:

1. Matching of CFD with experiment relies on the measured wedge angle and its time derivatives - as inputs. The uncertainty in these variables has been quantified. However, determining the propagation of these uncertainties in CFD results would be extremely challenging, since it would require determining changes in the full time dependent CFD solutions with respect to small changes in the wedge angle and angular velocity; which also evolve in time. This was not attempted in this study. The problem could be mitigated by reducing the angular measurement uncertainties, by improving the resolution of the images with a higher resolution camera, since the angular measurements are obtained from image analysis. Alternatively, it may be possible to measure the angular rotation of the wedge in some other, more direct way. For example, an accelerometer could be attached to the wedge. The acceleration signal could be integrated to obtain the velocity and angle - this process would produce far less noise than the current differentiation scheme. A combination of image based angle measurement and acceleration measurement might further improve the accuracy.

2. It was observed that during the rapid motion of the wedge, the arm supports (which hold the wedge pivot) tend to vibrate vertically under the high inertial and aerodynamic loads. The wedge angle measurement is performed at each frame and does not depend on the pivot position. However, it still assumes

that the wedge motion is perfectly rotational about a fixed pivot. The added motion of the pivot, modifying the wedge motion could effect the flow fields and shock waves. It is recommended that the supports be made more rigid for future rigs.

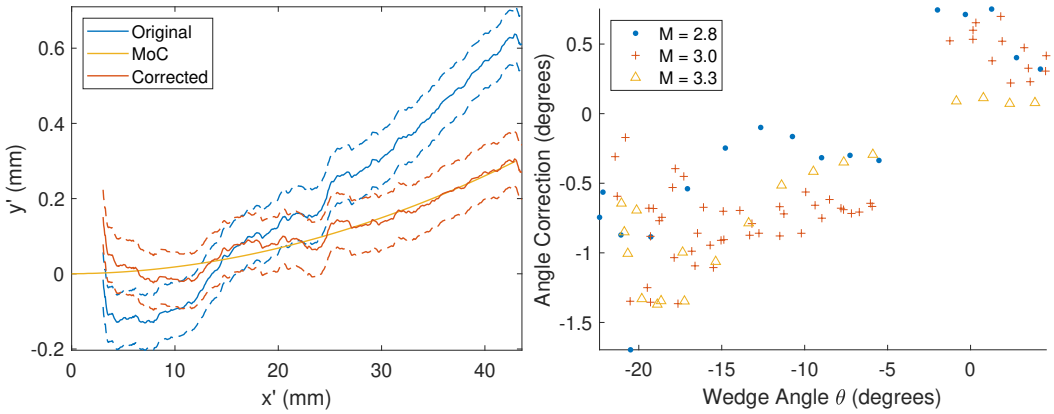
3. It was observed that the optics rig, mounted from the ceiling, tends to shake slightly under the vibrations caused by the supersonic tunnel in the building. This vibration presents as a slow shift of the optical view horizontally and vertically. The grid used to transform the image coordinates to tunnel coordinates for data extraction, in section 3.3.1, therefore also shifts with respect to the image view and must be graphically re-extracted (ideally at each frame). Instead, since this process was not automated, the grid was captured at intervals, and the grid transform used for particular frames was interpolated linearly between them. Manual extraction at each frame was infeasible because there are hundreds of frames for each test - all necessary for extracting the rotation profile. Therefore it may be necessary to automate this process, and reacquire the grid transform at every frame - this is recommended for future work.

4. The experimental shock extraction process is limited by the resolution of the optical setup, which is limited at high frame rates. It was shown that the shock extraction fails in certain cases, due to these low resolution issues. Although these cases were excluded from consideration, some of the results shown here may still be negatively effected. Once again, a higher resolution camera is recommended.

Previously, a straight line fit was applied to the two-dimensional section of the captured shock waves, and compared to theory. But the assumption of a (relatively) straight shock wave was shown to be invalid - based on the CFD results. If it is the case that the discrepancy between experiment and CFD is a rigid, but possibly changing, shift in angle (due to, for example, rotation of the optical view due to vibrations; or boundary layer effects), then it may be useful to define a correction angle - as a rigid rotation of the captured shock to match the CFD, in a least squares sense. This is illustrated in figure 3.49a. It actually appears that there may be some small degree of curvature visible in the experimental results, matching with CFD. However, this cannot be stated with any confidence in light of the scale of the uncertainty bands, and the need to rotate the results to achieve this.

The correction angles are shown across all available data as a function of the wedge angular position in figure 3.49b. The angular differences between experiment and

CFD, defined in this way, are generally on the order of about 0.5°. This angle seems to be shifted in the same direction with an opposite sense for shocks on the top surface (approximately $\theta > 0$) and bottom surface (approximately $\theta < 0$). This is very possibly a result of the boundary layer shifting the angle of the shock wave - since on the top surface, the boundary layer would increase the flow deflection and therefore the shock angle clock wise, and vise versa for the bottom surface. It is therefore recommended that CFD models which include viscous effects be run to match these cases and confirm this theory. However, these boundary layer effects (which should be relatively consistent) would not account for the relatively large variation in the correction angle observed. It is likely that other error sources, including those listed, contribute significantly to the discrepancy between experiment and CFD results (in addition to potential boundary layer effects).



(a) Least squares rotation correction

(b) Correction angle vs wedge angle

Figure 3.49: Experiment shock correction

3.7 CFD Results In Detail

The errors in the experimental process prohibit any significant conclusions being made about the dynamic effects of rapid wedge rotation on an experimental basis. Until the experiment can be redesigned, the CFD results, which already appear to be verified (the FV and MoC results appear to agree), will be examined in greater detail in terms of dynamic effects on the shock wave and overall flow field.

3.7.1 Time Series Results

In this section, a series of frames from Test 3 are selected to show how the flow field varies throughout the rotation profile for this particular test.

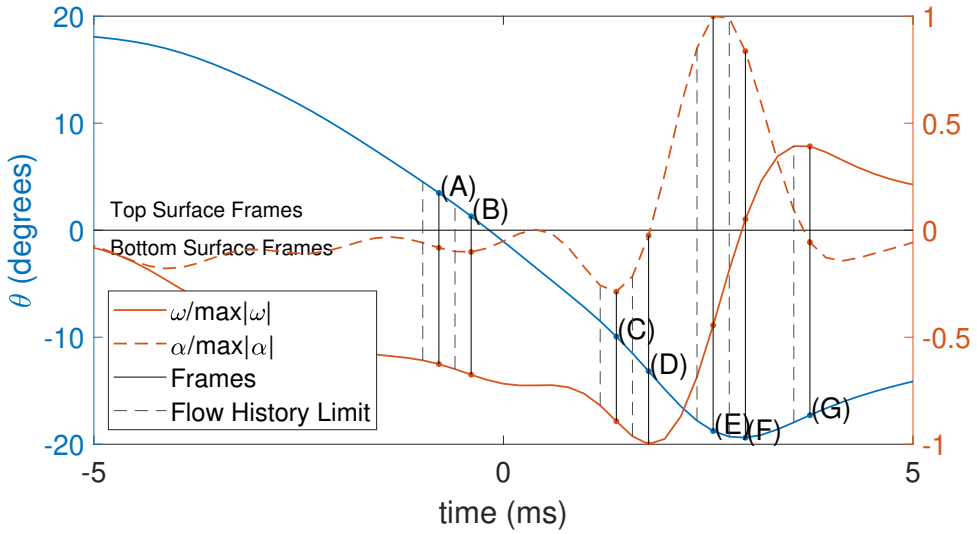
3.7.1.1 Shock Waves

Consider again the test frames in figure 3.50a. All the shock waves from the MoC results are shown, in the static theory line coordinates $x' - y'$, in figure 3.50b. Note that the static shock angles are different for each frame ($x' - y'$ is orientated differently for each frame), but they are all compared here on the same axis. The trend of increasing shock curvature with respect to angular velocity (magnitude) is shown clearly through frames **A**-**D**. However, notice that frame **E** has a greater curvature than frames **A**-**C**, even though its angular velocity is smaller in magnitude. Its acceleration is strongly positive (in fact maximum), compared to these other frames. Therefore it might be that the curvature is also function of angular acceleration. However, these frames have different surface angles, and although the shock wave coordinates were transformed so their static angles align, the sensitivity of shock curvature to angular velocity and acceleration should still be effected by the absolute surface angles. Therefore it is difficult to make a conclusion about the effect of acceleration on shock wave curvature from this comparison.

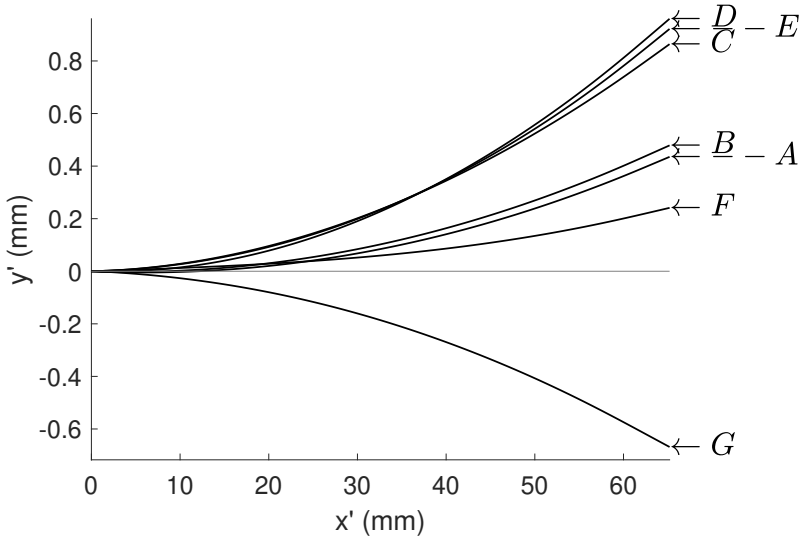
Now consider frame **F**. The shock wave has positive curvature (upwards) even though its tip velocity is down ($\omega > 0$) - as opposed to frames **A**-**E** which also curve up but have an upward tip velocity ($\omega < 0$). However, **F** has a large positive acceleration (counter clock wise - downward tip acceleration) - which may counteract the effect of the velocity on the shock curvature. Now observe that the angular velocity of the wedge changes within the flow history of frame **F**. It was rotating clock wise and decelerating, came to rest, and then began to rotate counter clock wise. The

disturbances of this whole motion on the fluid domain have not yet had time to exit the domain. Therefore, the positive curvature at **F** should be considered with regard to this changing motion during its flow history period. In fact the curvature may be due to the initial clock wise rotation. Only at **G**, with positive angular velocity and negative acceleration, does the shock curve downwards.

Generally it is observed that the shock wave curvature lags the motion of the tip as delayed disturbances from the motion of the wedge reach further along the shock wave.



(a) CFD - experiment frames



(b) Frame shock waves

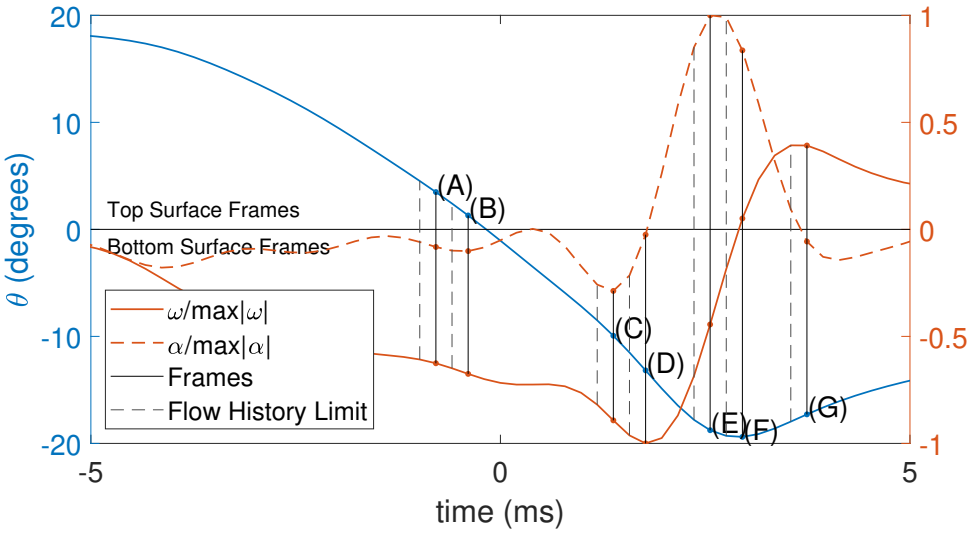
Figure 3.50: MoC - shock wave results

3.7.1.2 Surface pressures

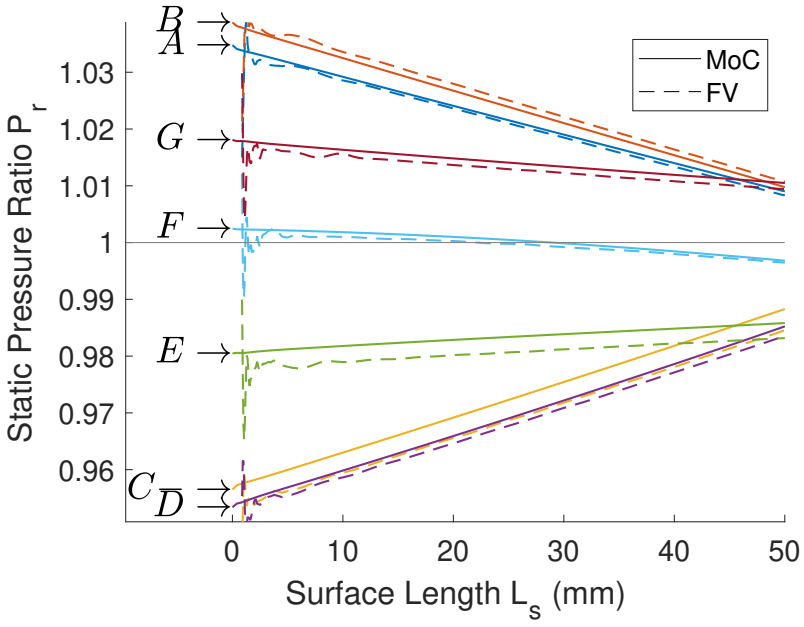
In figure 3.51b, the wedge surface pressures are shown for all frames. These pressures are shown as a ratio P_r between the surface pressure and the theoretical pressure from the static oblique shock solution for the same surface angle. The static wedge case is therefore represented by the horizontal line $P_r = 1$. In the limit of the tip (surface length $L_s = 0$), the surface pressures approach the tip pressures, which are governed by the dynamic tip oblique shock theory - this is once again guaranteed for the MoC results, since it is used as a boundary condition for that code; and the FV surface pressures show agreement.

The deviation of surface pressures from the static case can be best explained in terms of the rotational velocity, causing the surfaces to rotate into or away from the flow: In frames **A** and **B**, the tip velocity is upwards, in the positive normal direction of the top surface. This additional normal velocity increases the surface pressure as the flow stagnates (is brought to rest with respect to the surface) in the normal direction. Since the normal velocity caused by the rotation is proportional to the distance from the pivot, the surface pressure is seen to increase approximately linearly towards the tip. In frames **C**-**E**, the wedge is still rotating clock wise (upwards), but this is opposite to the normal direction of the bottom surface. Therefore the stagnation pressure along the bottom surface with respect to the normal direction decreases (the surface is moving away from the flow). In frame **G**, the wedge is now rotating counter clock wise, so the bottom surface is rotating into the flow. Therefore, the surface pressures are increased compared the static case. In frame **F**, the rotational velocity is low and the surface pressures are similar to the static case. However, observe that the pressure is slightly greater near the tip, and less than the static case towards the end of the surface. This could be understood in terms of the flow history. During the early part of the flow history of **F**, the wedge rotation was clock wise, so the bottom surface was moving in the negative normal direction. This would have produced weaker pressures ($P_r < 1$). However, towards the end of the flow history of **F**, the wedge begun to rotate counter clock wise, reversing this effect. Consider that the initial history pressures ($P_r < 1$) have not had time to leave the domain (at $L_s = 50mm$) - so we observe these weak pressures towards the end of the surface, and higher pressures ($P_r > 1$) near the tip which is now rotating into the flow.

Once again, the MoC and FV results agree quite well. The FV results do however suffer from overshoots just behind the shock wave ($L_s = 0$) due to the shock capturing scheme.



(a) CFD - experiment frames



(b) Frame surface pressures

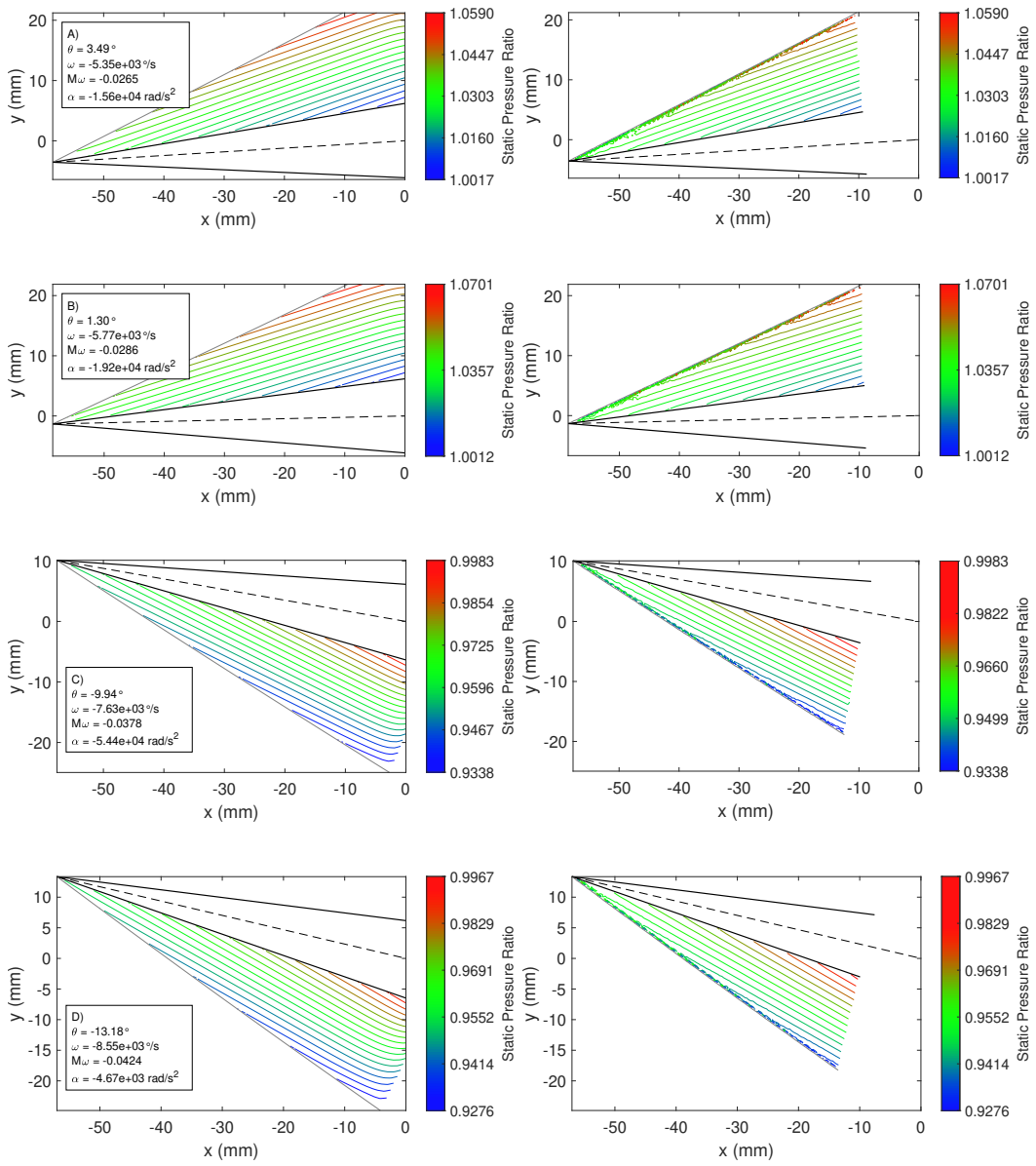
Figure 3.51: CFD surface results

3.7.1.3 Pressure Contours

Pressure contours for each frame are compared for MoC and FV CFD results in figure 3.52. The pressures are once again shown as the ratio of static pressure to the theoretical pressure behind the corresponding oblique shock solution. The MoC and FV results show good agreement throughout. Notice that the MoC domain is set larger than the FV domain. This is to reduce the possibility of spurious features from the exit boundary affecting the domain of interest, as described in section 4.

The pressure contours show how pressure waves caused by the rapid rotation propagate through the domain. In frames **A** and **B**, the pressure is seen to increase in the domain along the shock wave. This corresponds to the upwards curvature of the shock waves at these frames, as shown in figure 3.50b: as the shock tangent angle increases along its length, the shock angle with respect to the upstream flow increases, resulting in greater pressure rises across the shock. These pressures propagate into the domain producing pressure gradients throughout. In frames **C**-**E**, the pressure decreases along the shock wave. In these frames the shock still curves upwards but these shocks are attached to the bottom surface (they are angled downwards), and so curving upwards reduces the shock angle, thus reducing the pressure rise along its length. In frame **G** the shock is also angled downwards, but now also curves downwards. Therefore the pressure gradient increases along its length.

Now consider frame **F**. The pressure gradient is clearly and unusually orientated along the surface direction. Note also that the shock wave curvature is particularly small in this frame (figure 3.50b) - so the change in pressure along the surface and shock wave cannot clearly be attributed to the change in shock angle along its length. In this frame there are regions with pressure ratios greater than and less than unity. It seems that this is a sort of transitional period - consider that within the flow history of frame f, the wedge velocity changes direction. In the proceeding and subsequent frames, the direction of the pressure gradients has switched, apparently due to the change in sign of the wedge velocity.


A)
θ = 3.49°
ω = -5.35e+03 °/s
Mω = -0.0265
α = -1.56e+04 rad/s²
B)
θ = 1.30°
ω = -5.77e+03 °/s
Mω = -0.0286
α = -1.92e+04 rad/s²
C)
θ = -9.94°
ω = -7.63e+03 °/s
Mω = -0.0378
α = -5.44e+04 rad/s²
D)
θ = -13.18°
ω = -8.55e+03 °/s
Mω = -0.0424
α = -4.67e+03 rad/s²
y (mm)
x (mm)
Static Pressure Ratio
1.0590
1.0447
1.0303
1.0160
1.0017
1.0701
1.0357
1.0012
0.9983
0.9854
0.9725
0.9596
0.9467
0.9338
0.9822
0.9660
0.9499
0.9967
0.9829
0.9691
0.9552
0.9414
0.9276

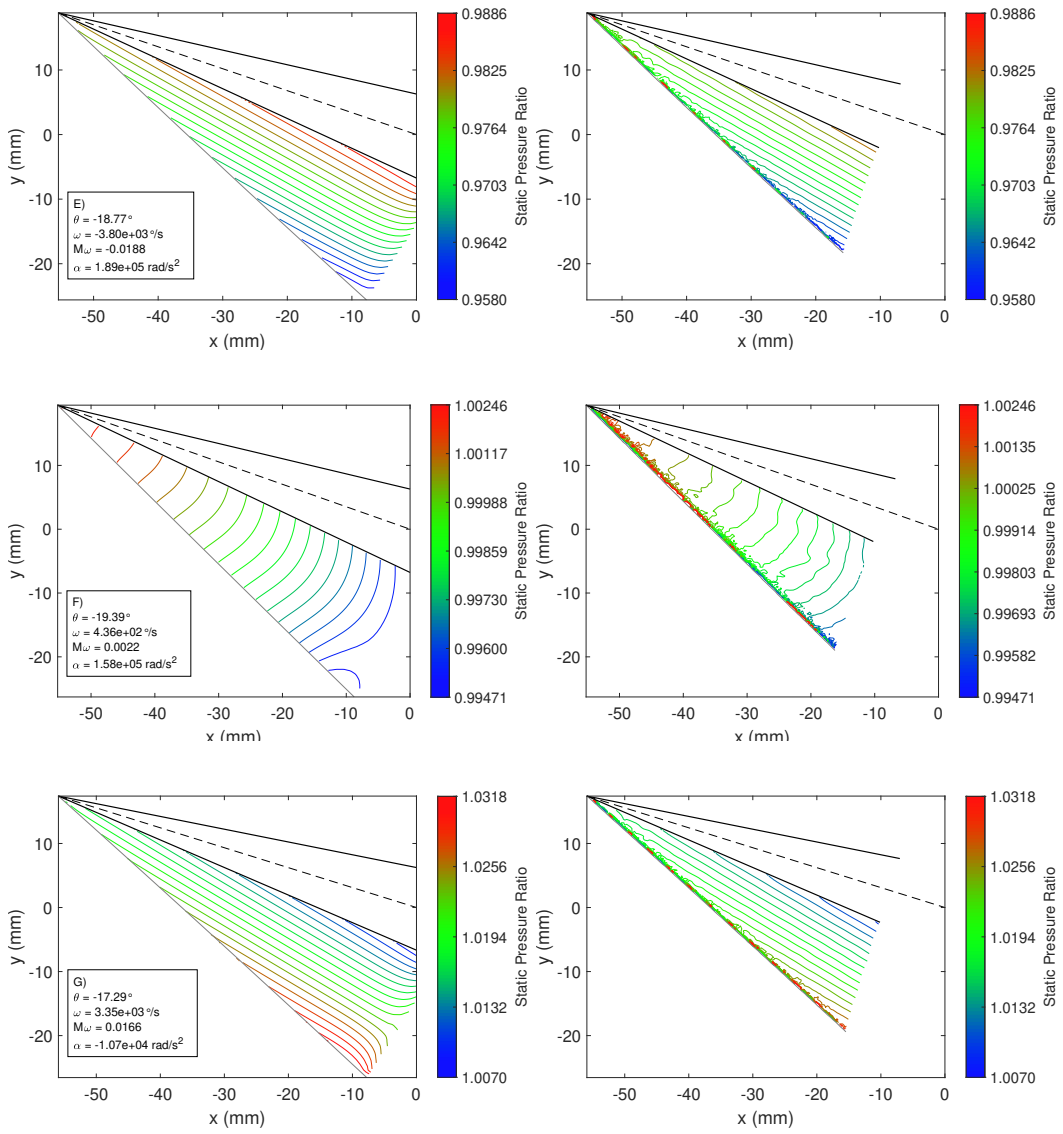


Figure 3.52: CFD pressure contours. MoC - left, FV - right

3.7.2 Varying Angular Velocity

Thus far, only results from a single test rotation have been discussed. Presenting further test runs separately will not clearly reveal any new features, as their results are generally qualitatively similar. Instead, frames from separate tests will be matched in terms of wedge angle, so that the effect of varying the rotation rate can be studied for the same wedge angles - varying Mach numbers are examined in the following section. Unfortunately the velocities and accelerations are not independent, since they come from particular experimental rotation profiles. This means that it is not possible to independently study the effects of rotational velocity and acceleration using these CFD results which were setup for the experimental study. Note that these CFD results will be compared for completeness, but ideally, a separate numerical rotational study should be performed so that rotation parameters can be studied in depth. Such a study is not presented here. Instead, a linear acceleration study, in section 6, investigates linear acceleration parameters for attached shock wave domain acceleration. Future work should include a similar study focusing on rotational motions.

Consider the test point sets in table 3.4 and 3.5 table for wedge angles of $\theta \approx -10^{\circ}$ and $\theta \approx 3.5^{\circ}$ respectively. In the first Set, the bottom surface is facing the upstream flow and the results shown are from this bottom shock-surface domain; whereas in Set 2, the shock-surface domain is on the top surface. The angles were not matched exactly, since these points represent discrete CFD data sets with finite time intervals between time steps. The frame-matching between tests is illustrated in figure 3.53. Notice how there is no reliable way to match any two of the angular derivatives (θ, ω, α) simultaneously. The corresponding shock and surface pressure results are compared in figure 3.54 and 3.55. The shock results are again shown in the theory line coordinates - where $y' = 0$ corresponds to the static shock solution. While the surface pressures are shown as the ratio ($P_r = p/p_{theory}$) of surface pressure to the theoretical surface pressure from the static oblique shock solution. In Set 1, the MoC and FV results do not show as clear agreement as seen previously in terms of the shock wave and surface pressure profiles. However, they agree qualitatively in terms of the increasing shock curvature and pressure gradients with increasing rotation rates (loosely referring to the combined effect of angular velocity and acceleration). The corresponding results for Set 2 show far better agreement between the MoC and FV results. Likewise, the effect of increasing the rotation rate is demonstrated. In both sets, the shock waves curve upwards as they lag the clock wise rotation of the wedge tip.

in Set 2, the surface pressures increase approximately linearly toward the wedge tip. The opposite occurs for Set 1. This effect was described in section 3.7.1.2 in terms of the stagnation pressure in the normal direction of the surfaces.

Pressure contours in the bound shock domain are compared for Set 1 in figure 3.56. These do not show clear differences - except that the pressure contours appear to be closer together at higher rotation rates - indicating a steeper pressure gradient.

Table 3.4: Varying rotational velocity, set 1 - $M = 3$, $\theta \approx -10°$ (top surface)

Test Number		2	3	4
Wedge Angle θ	$^\circ$	-10.20	-9.94	-9.37
Angular Velocity ω	$^\circ/s \times 10^3$	-6.44	-7.63	-9.13
Tip Mach Number M_ω		-0.0320	-0.0378	-0.0453
Angular Acceleration α	$rad/s^2 \times 10^4$	-1.86	-5.44	-6.89

Table 3.5: Varying rotational velocity, set 2 - $M = 3$, $\theta \approx 3.5°$ (bottom surface)

Test Number		2	3	4
Wedge Angle θ	$^\circ$	3.59	3.49	3.23
Angular Velocity ω	$^\circ/s \times 10^3$	-4.23	-5.35	-6.97
Tip Mach Number M_ω		-0.0210	-0.0265	-0.0346
Angular Acceleration α	$rad/s^2 \times 10^4$	-0.54	-1.56	-3.52

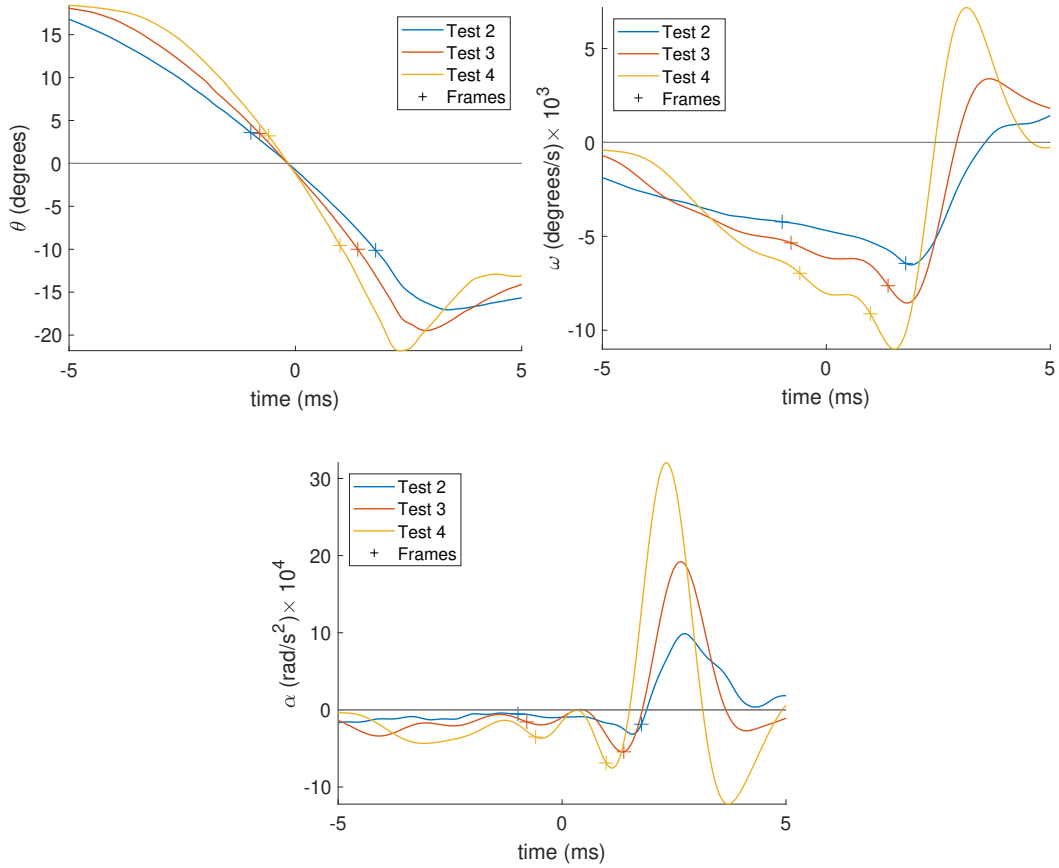


Figure 3.53: Matching frames : varying rotational velocity, sets 1 and 2 - $M = 3$

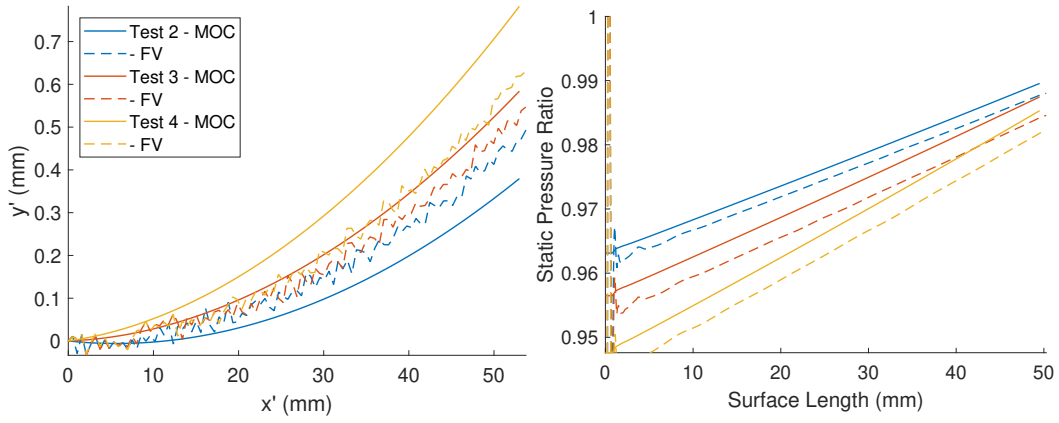


Figure 3.54: Shock wave and surface pressures - varying angular velocity, set 1. $M = 3$, $\theta \approx -10°$

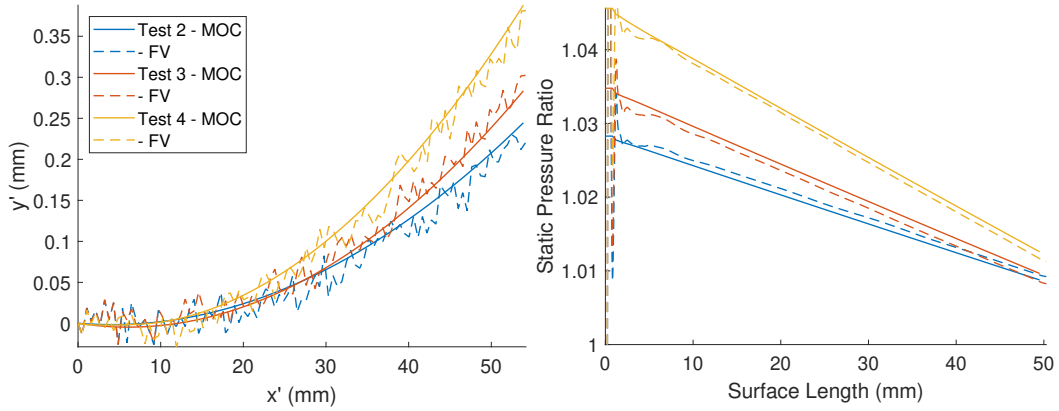
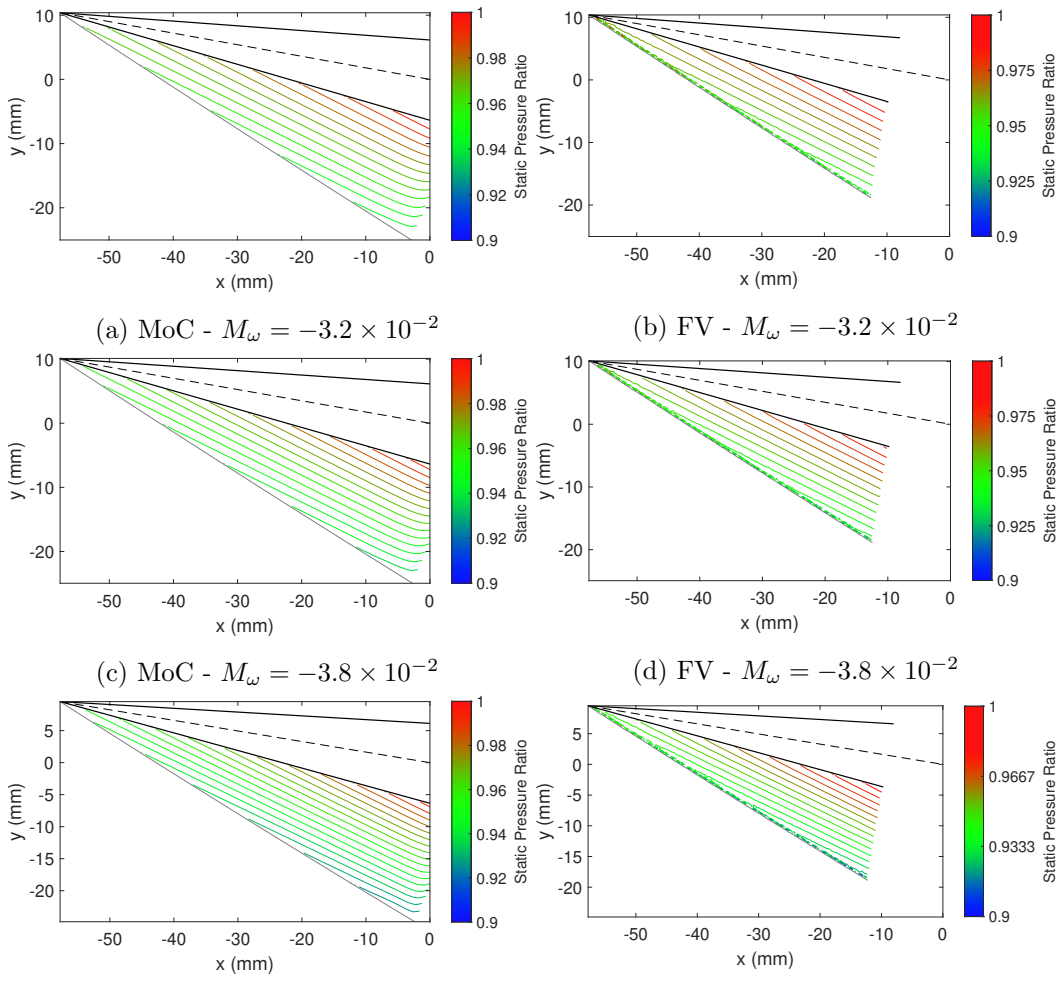


Figure 3.55: Shock wave and surface pressures : Varying Angular Velocity, Set 2. $M = 3$, $\theta \approx 3.5°$



(a) MoC - $M_\omega = -3.2 \times 10^{-2}$

(b) FV - $M_\omega = -3.2 \times 10^{-2}$

(c) MoC - $M_\omega = -3.8 \times 10^{-2}$

(d) FV - $M_\omega = -3.8 \times 10^{-2}$

(e) MoC - $M_\omega = -4.5 \times 10^{-2}$

(f) FV - $M_\omega = -4.5 \times 10^{-2}$

Figure 3.56: Pressure contours : varying angular velocity, set 1. $M = 3$, $\theta \approx -10°$

3.7.3 Varying Mach Number

Similarly, sets of frames are matched for varying Mach numbers. Tests were run with the same spring compression length and initial/stop angles, but with a varying Mach number. Matching frames are shown in tables 3.6 and 3.7, and in figure 3.57. In this case it was possible to simultaneously match the angular derivatives ω, α (approximately). The rotation profiles are somewhat different, as discussed in section 3.3.4.1, due to the aerodynamic lift moment (which varies with upstream Mach number) on the wedge, effecting the rotation.

The corresponding shock and surface profiles are shown in figure 3.58 and 3.59. There does appear to be some variation in these profiles across the varying Mach numbers. However, there is no clear pattern, and no significant conclusion can be made, on the basis of these results, about the effect of Mach number - particularly since the surface angle and angular derivatives could not be matched to a high degree of accuracy.

Table 3.6: Varying Mach number, set 1 - $C = 40mm$, $\theta \approx -8°$

Test Number		1	4	5
Wedge Angle θ	$^\circ$	-7.27	-7.66	-7.64
Mach Number M		2.8	3.0	3.3
Angular Velocity ω	$^\circ/s \times 10^3$	-8.78	-8.46	-9.10
Tip Mach Number M_ω		-0.0417	-0.0420	-0.0481
Angular Acceleration α	$rad/s^2 \times 10^4$	0.52	-4.32	-3.27

Table 3.7: Varying Mach number, set 2 - $C = 40mm$, $\theta \approx 4°$

Test Number		1	4	5
Wedge Angle θ	$^\circ$	4.21	4.56	3.88
Mach Number M		2.8	3.0	3.3
Angular Velocity ω	$^\circ/s \times 10^3$	-7.21	-6.60	-7.52
Tip Mach Number M_ω		-0.0343	-0.0328	-0.0398
Angular Acceleration α	$rad/s^2 \times 10^4$	-2.15	-2.78	-3.55

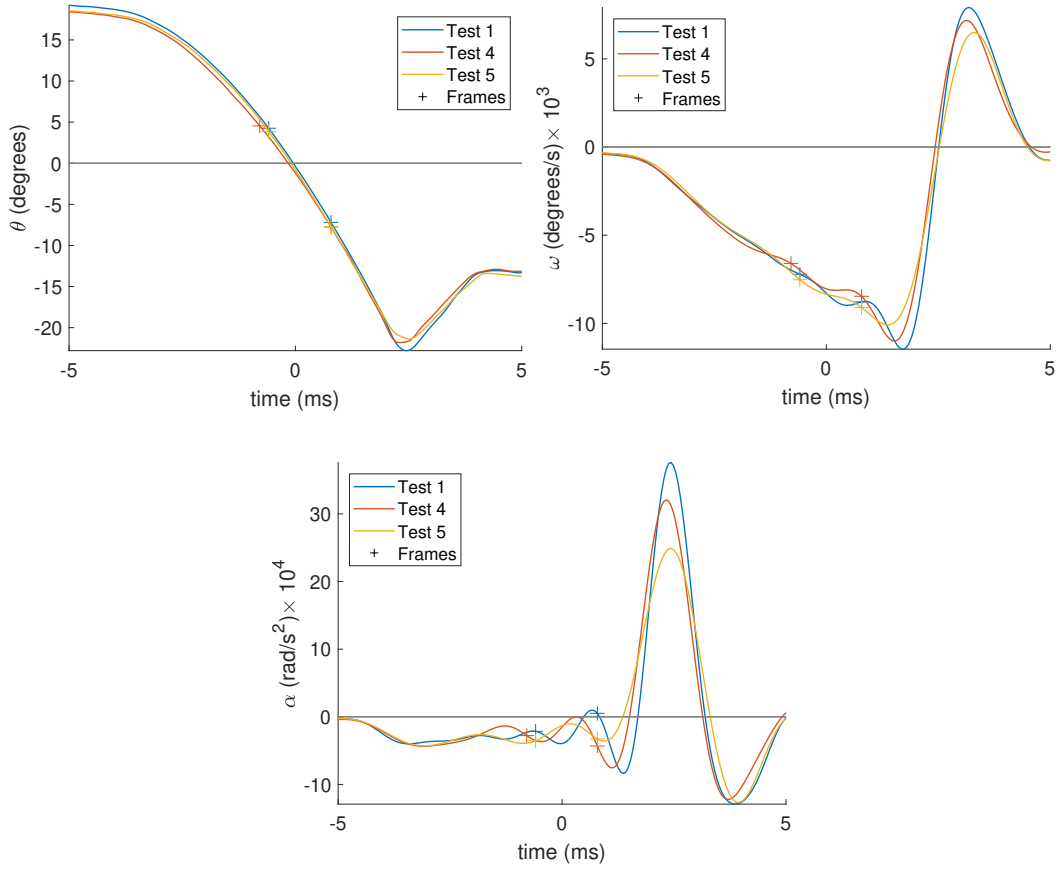


Figure 3.57: Matching frames : varying Mach number, sets 1 and 2 - $C = 40mm$

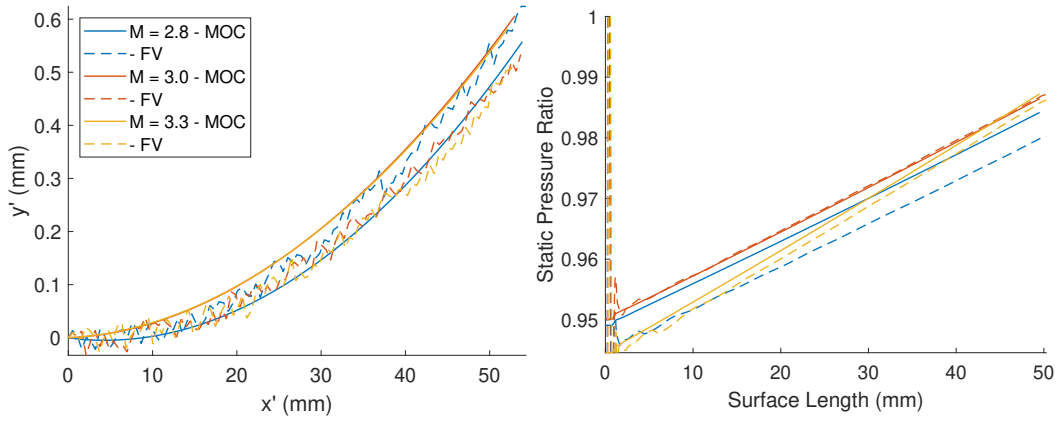


Figure 3.58: Shock wave and surface pressures - varying Mach number, Set 1. $C = 40mm$, $\theta \approx -8°$

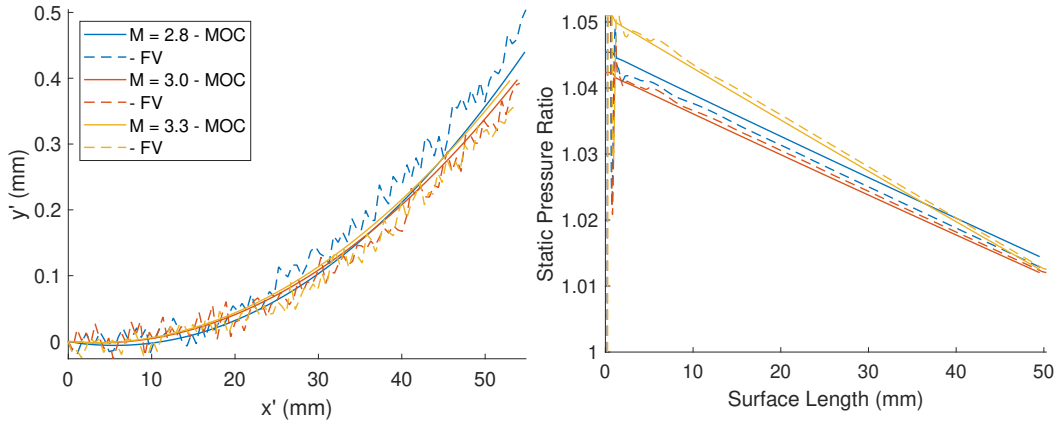


Figure 3.59: Shock wave and surface pressures - Varying Mach Number, Set 2. $C = 40mm$, $\theta \approx 4°$

3.8 Conclusions

1. A test rig was developed, using a similar approach to Naidoo and Skews [8], which uses a compression spring system to actuate a rapid wedge rotation inside a supersonic wind tunnel. The maximum angular velocities achieved were slightly larger than in the previous study - $(11.4 \pm 0.2) \times 10^3$ $degrees/s$ compared to $\approx 11 \times 10^3$ $degrees/s$. However, the maximum tip Mach number achieved $M_\omega = \frac{\omega R_{tip}}{a_\infty}$ was significanly higher in this investigation: 0.06 ± 0.005, compared to ≈ 0.033, due to the longer wedge chord. Significantly greater rotation rates will not easily be achieved in this tunnel, due to area restrictions. The portion of the rig housed inside the tunnel - including the wedge and its mounts - was limited to 8% of the cross sectional area of the tunnel ($101.6\ mm \times 118\ mm \times 8\% = 960\ mm^2$) to ensure proper supersonic operation of the tunnel. This meant that the wedge could not be too long or wide, and the housing had to have minimal width - limiting the actuation rates and tip speeds possible in terms of the wedge pivot length and the structural integrity of the inner components.

2. A series of tests were successfully captured over a range of Mach numbers $M = 2.8, 3.0, 3.3$ and initial spring compression lengths $C = 20, 30, 40\ mm$ - producing a range of rotation rates, approximately in proportion. A high speed Shadowgraph flow visualisation setup captured the attached shock waves and wedge motion at $5,000$ fps.

3. Digital image processing techniques were developed to automatically compute the wedge angles (measured counter clock wise from the negative x-axis to the wedge center line) at each image frame, with associated uncertainties, for each test: calculated to within $\pm 0.07°$. The angular velocity ω and acceleration α, with associated uncertainties, were computed using finite differencing of the angle time series, with uncertainties, approximately: $\omega : \pm 2\%, \alpha : \pm 10\%$, compared to the maximum velocity and acceleration. The acceleration uncertainties were particularly high due to the higher order numerical differencing of the measured angle. However, the general rotation profiles were shown to be repeatable and relatively smooth. The maximum velocity and acceleration were shown to vary approximately linearly with respect to the initial spring compression length. Additionally, it was shown that decreasing the Mach number $M = 3.3, 3.0, 2.8$ resulted in higher rotation rates due to the increased aerodynamic lift on the wedge - since lower Mach numbers (in this range) produced denser flows which outweighed the decreased velocities in terms of momentum.

Techniques were developed to capture the shock waves from the high speed Shadowgraph images. Uncertainty bands for the shock waves were approximately 0.1 mm in width - varying with the effective optical resolution of stronger or weaker shock waves. At small wedge angles (approximatly $|\theta| < 5°$), the optical setup was sometimes unable to sufficiently resolve shock edges, and the digital shock capturing process failed. Therefore, cases of interest were generally limited to larger wedge angles.

4. It was found that, although the shock wave angles did deviate from the static oblique shock theory - by up to approximately 0.5° (beyond the quantified uncertainty bounds), the resolution of shock waves captured from the experiment was not sufficient to demonstrate clear shock wave curvature for these rotation rates. Therefore, direct validation of CFD was not possible. Instead, independent MoC and FV numerical codes were used to at least provide some verification, and some level of confidence in CFD results. These models showed clear agreement on the scale of the shock wave curvature and other dynamic flow features. These models actually predicted quite significant curvature of shock waves for the experimental rotation profiles - deviating from the static oblique shock solution by amounts on the order of 1 to 3 times the width of the experimental shock wave uncertainty bands. It was shown that the level of curvature predicted would be enough to account for some of deviation of experimental shock waves from the static theory; but not wide enough to actually present as clear curvature within the bands of experimental uncertainty. Rotational errors between experimental and CFD shock waves were calculated to help identify patterns in the discrepancies. It was concluded that a shift in angle due to the viscous boundary layer on the wedge surfaces was a likely contribution. Additionally, sources of experimental error were identified which may have contributed to the remaining noisy component of the discrepancies. These included: vibration of the wedge mount during rapid actuation; shaking of the optical rig caused by the wind tunnel operation; and uncertainties in rotation derivatives with regards to matching these profiles with CFD.

5. Since the experimental results could not directly assess dynamic shock wave features, the verified CFD results were relied upon to study the dynamic flow fields in detail. It was demonstrated that shock curvature can be understood in terms of a lagging of the shock wave behind rapid perturbations of the wedge tip - as delayed information propagates further along the shock wave. Increasing the rate of rotation resulted in steeper curvature. However, based on the available results, it was not possible to draw a clear distinction between the effects of rotational velocity vs acceleration on shock wave curvature - though

it does appear that it is more strongly a function of velocity. Wedge surface pressures were shown to vary approximately linearly along the surface, and approximately in proportion to the rotational velocity. This variation is likely due to the changing stagnation pressure along the surface with respect to local normal surface velocities - which vary linearly with distance from the pivot. The surface pressures near the tip are predicted by the dynamic tip shock theory. This theory was useful for characterising the surface pressures. However, it was not a good characterisation of the shape of the shock waves, since it only predicts the limiting shock angle and not the curvature. Contours of pressure in the surface-shock bound domain demonstrated the pressure waves resulting from the rapid motion which propagate though the field and interact with the shock wave. The pressure gradients are partially a result of the downstream pressures, produced by the curved shock waves, convecting into the domain. In terms of varying Mach number, no clear distinction could be made between the shock wave curves or surface pressures based on these results. Finally, it was demonstrated that dynamic effects, such as shock wave curvature and unsteady pressure gradients can be understood in terms of the flow history. The flow history was characterised for the surface-shock bound domain by the period required for the slowest characteristic information to pass from the tip to the exit boundary of the domain. It was shown that the historical wedge motion that occurred within the flow history period of a particular solution time-frame effects that solution flow field because those disturbances have not had time to dissipate or leave the domain.

3.8.1 Recommendations

- It is recommended that a larger supersonic wind tunnel be used for future work. This would facilitate the development of a test rig capable of far more rapid actuation. The corresponding wedge should be designed with as long a chord as possible, to maximise the tip velocity; and a relatively wide aspect ratio to delay the onset of three-dimensional edge effects.

- A higher resolution camera would improve the resolution of shock waves so that dynamic curvature effects becomes more apparent. It would also improve the wedge angle measurements - reducing the uncertainty in angle and angular time derivatives.

- Alternative angular measurement methods should be considered. One approach would be to attach a high frequency accelerometer to the wedge to measure acceleration. This would help solve the issue of the large error in the

acceleration measurements due to the second order numerical differentiation of the angular time series. Additionally, integrating to obtain the angular velocity should produce far less error in the angular velocity.

- Although the boundary layer is expected to have little effect on the flow field, it would be useful to run viscous CFD models, matching the inviscid simulations run in this investigation, to confirm this assumption and quantify the extent of boundary layer effects on these rotating attached shock domains.

- Future studies might involve curved wedges and three dimensional phenomena with rapid body rotations. Blunt body problems and cases involving flow separation involve low frequency viscous effects, with relatively large time scales. Therefore even relatively slow rotations might result in notable dynamic effects.

4 Method Of Characteristics

This section describes the development of an unsteady two-dimensional Method of Characteristics (MoC) code, based on the modified tetrahedral network proposed by Sauerwein [1], and developed in MatLab (R2019b). Note that in general, the method is applicable to any unsteady two-dimensional inviscid adiabatic flow - there is no restriction to supersonic or irrotational conditions. At present, the code is setup to simulate arbitrary motions of attached shock domains with flat surfaces. However, the methods described here may be extended to more general cases, including curved surfaces and detached shock waves. This code, along with a separate Finite Volume code, provides CFD results for the experimental study, section 3, which involves rapid rotations of wedges in supersonic flow. Furthermore, it is used in a parametric study, section 6, involving transverse linear acceleration of an attached shock domain. By comparing the results produced by this code to the FV code (which has been validated for many flow phenomena), it will be demonstrated that these substantially different CFD models produce similar results, providing a degree of validation for this code. Theoretical and practical aspects will now be described, and particular modifications to Sauerwein's method will be highlighted.

4.1 The Characteristic and Compatibility Equations

Starting with the Euler equations, for two-dimensional inviscid, adiabatic flow, the (x, y, t) coordinates are transformed to a new set of coordinates (α, β, γ) which align with characteristic surfaces, by an orthogonal transformation $[Q]$, in equation 4.1. Note that this transformation only applies locally as it will depend on flow properties at each point in space-time. The partial derivatives of flow variables in the Euler equations are also transformed using the chain rule for partial derivatives, as illustrated in equation 4.2. The characteristic surfaces are then found by the property that flow derivatives normal to these surfaces are indeterminate. Defining the surfaces by the coordinate $\alpha = 0$, the determinate of the Euler equations with

respect to the $\frac{\partial q}{\partial \alpha}$ derivatives is set to zero (where q represents the flow variables u, v and p). This results in two sets of characteristic surfaces in equations 4.3 and 4.4. These correspond respectively to curved cones in x, y, t space representing the envelope of sound waves emanating from the given point in the flow field (curved because the flow properties vary in space and time); and the streamline (in x, y, t space) passing through the same point. The β coordinate is chosen to align with the bicharacteristic line joining the given base point (at which the characteristic surfaces are centered) to a new solution point along the characteristic cone. The remaining coordinate γ may be defined arbitrarily, but is chosen in this method to be orthogonal to α (which is the direction normal to the characteristic cone surface) and β. This defines the transformation $[Q]$. This transformation is illustrated in figure 4.2. Finally, linear combinations of the transformed Euler equations are chosen so that the $\frac{\partial q}{\partial \alpha}$ derivatives are excluded. These are the compatibility equations which may be applied along the characteristic surfaces. The compatibility equation corresponding to the cone, is given in equation 4.5. Where the gradient operator $\bigtriangledown = (\frac{\partial}{\partial x}, \frac{\partial}{\partial y}, \frac{\partial}{\partial t})$ and space-time velocity vector $\vec{\mathbf{V}} = (u, v, 1)$ are defined in space-time coordinates. This equation may appear unwieldy but can be simplified as will be shown. The compatibility equation corresponding to the streamline is the energy equation, which can be taken as (entropy $s = const.$ along the streamline). This is not a limiting assumption except that it is not valid through shock discontinuities. The discretisation and application of these equations to advancing a given two-dimensional flow field in time is described in the following sections.

$$\begin{bmatrix} \alpha \\ \beta \\ \gamma \end{bmatrix} = [Q] \begin{bmatrix} x \\ y \\ t \end{bmatrix} \tag{4.1}$$

$$\frac{\partial u}{\partial x} = \frac{\partial u}{\partial \alpha}\frac{\partial \alpha}{\partial x} + \frac{\partial u}{\partial \beta}\frac{\partial \beta}{\partial x} + \frac{\partial u}{\partial \gamma}\frac{\partial \gamma}{\partial x} \tag{4.2}$$

$$\left(\frac{D\alpha}{Dt}\right)^2 - a^2\left[\left(\frac{\partial \alpha}{\partial x}\right)^2 + \left(\frac{\partial \alpha}{\partial y}\right)^2\right] = 0 \tag{4.3}$$

$$\left(\frac{D\alpha}{Dt}\right)^2 = 0 \tag{4.4}$$

$$\frac{\partial u}{\partial \beta}\left[\frac{\partial \beta}{\partial x}\left(\vec{V}\cdot\bigtriangledown\alpha\right)-\frac{\partial \alpha}{\partial x}\left(\vec{V}\cdot\bigtriangledown\beta\right)\right]+$$
$$\frac{\partial v}{\partial \beta}\left[\frac{\partial \beta}{\partial y}\left(\vec{V}\cdot\bigtriangledown\alpha\right)-\frac{\partial \alpha}{\partial y}\left(\vec{V}\cdot\bigtriangledown\beta\right)\right]+$$
$$\frac{\partial p}{\partial \beta}\frac{1}{\rho}\left[\frac{1}{a^2}\left(\vec{V}\cdot\bigtriangledown\beta\right)\left(\vec{V}\cdot\bigtriangledown\alpha\right)-\left(\frac{\partial \beta}{\partial x}\frac{\partial \alpha}{\partial x}+\frac{\partial \beta}{\partial y}\frac{\partial \alpha}{\partial y}\right)\right]+$$

$$\frac{\partial u}{\partial \gamma}\left[\frac{\partial \gamma}{\partial x}\left(\vec{V}\cdot\bigtriangledown\alpha\right)-\frac{\partial \alpha}{\partial x}\left(\vec{V}\cdot\bigtriangledown\gamma\right)\right]+$$
$$\frac{\partial v}{\partial \gamma}\left[\frac{\partial \gamma}{\partial y}\left(\vec{V}\cdot\bigtriangledown\alpha\right)-\frac{\partial \alpha}{\partial y}\left(\vec{V}\cdot\bigtriangledown\gamma\right)\right]+$$
$$\frac{\partial p}{\partial \gamma}\frac{1}{\rho}\left[\frac{1}{a^2}\left(\vec{V}\cdot\bigtriangledown\gamma\right)\left(\vec{V}\cdot\bigtriangledown\alpha\right)-\left(\frac{\partial \gamma}{\partial x}\frac{\partial \alpha}{\partial x}+\frac{\partial \gamma}{\partial y}\frac{\partial \alpha}{\partial y}\right)\right]=0 \tag{4.5}$$

4.2 Notation

The following notation and conventions apply throughout the following sections. The symbolic vector $\vec{b}=(x,y,t)$ will generally refer to space-time coordinates, where $\vec{r}=(x,y)$ will refer only to space coordinates. The bold face symbol $\vec{\mathbf{V}}$ will refer to the space-time velocity $(u,v,1)$, while $\vec{v}$ will refer to the two dimensional velocity vector (u,v). Generally, the absolute value function $|x|$ will refer to the L_2 norm when applied to vectors. The scripts i, j and q will generally refer to base point indices $(1,2..n)$ (corresponding to base points in the cell networks), space-time coordinates (x,y,t) and fluid properties (u,v,p) respectively. For example, a matrix $[A]$ whose rows correspond to equation numbers and columns correspond to fluid properties would be written as shown in equation 4.6. A general, e.g. 2 by 3 matrix may also be written as in equation 4.7. Column and row vectors with spatial and flow property elements are illustrated respectively in 4.8. Matrix multiplication is performed in the usual way, written as in equation 4.10. A matrix dot product is defined, as illustrated in equation 4.11, in which the resulting column vector elements consists of the standard dot product of the matrix row vectors. An array-wise product is defined between a matrix and column vector, as illustrated in equation 4.12, in which the elements in each row of the matrix are multiplied by the corresponding row element of the column vector. These two product definitions are commutative. Finally, a lemma involving these products is defined in equation 4.13, which is easily verified.

$$[A]_i^q = \begin{bmatrix} a_{1u} & a_{1v} & a_{1p} \\ a_{2u} & a_{2v} & a_{2p} \\ a_{3u} & a_{3v} & a_{3p} \end{bmatrix} \tag{4.6}$$

$$[A]_2^3 = \begin{bmatrix} a_{11} & a_{12} & a_{13} \\ a_{21} & a_{22} & a_{23} \end{bmatrix} \tag{4.7}$$

$$[a]_j = \begin{bmatrix} a_x \\ a_y \\ a_t \end{bmatrix}$$
$$[a]^q = \begin{bmatrix} a_u & a_v & a_p \end{bmatrix} \tag{4.8}$$

$$[A]_i^q = \begin{bmatrix} a_{1u} & a_{1v} & a_{1p} \\ a_{2u} & a_{2v} & a_{2p} \\ a_{3u} & a_{3v} & a_{3p} \end{bmatrix} \tag{4.9}$$

$$[C]_i^q = [A]_i^j [B]_j^q \tag{4.10}$$

$$[A]_3^2 \bullet [B]_3^2 = \begin{bmatrix} a_{11} & a_{12} \\ a_{21} & a_{22} \\ a_{31} & a_{32} \end{bmatrix} \bullet \begin{bmatrix} b_{11} & b_{12} \\ b_{21} & b_{22} \\ b_{31} & b_{32} \end{bmatrix} = \begin{bmatrix} a_{11}b_{11} + a_{12}b_{12} \\ a_{21}b_{21} + a_{22}b_{22} \\ a_{31}b_{31} + a_{32}b_{32} \end{bmatrix} = \begin{bmatrix} c_1 \\ c_2 \\ c_3 \end{bmatrix} = [c]_3 \tag{4.11}$$

$$[a]_3 \odot [B]_3^3 = \begin{bmatrix} a_1 \\ a_2 \\ a_3 \end{bmatrix} \odot \begin{bmatrix} b_{11} & b_{12} & b_{13} \\ b_{21} & b_{22} & b_{23} \\ b_{31} & b_{32} & b_{33} \end{bmatrix} = \begin{bmatrix} a_1 b_{11} & a_1 b_{12} & a_1 b_{13} \\ a_2 b_{21} & a_2 b_{22} & a_2 b_{23} \\ a_3 b_{31} & a_3 b_{32} & a_3 b_{33} \end{bmatrix} \tag{4.12}$$

$$[A]_3^3 \bullet \left([b]_3 [c]^3\right) = \left([b]_3 [c]^3\right) \bullet [A]_3^3 = \left([A]_3^3 \odot [b]_3\right) [c]_3 \tag{4.13}$$

4.3 Richmond's Iteration Procedure

In several instances in this MoC code, it is required that sets of non-linear algebraic equations are solved simultaneously. For these cases, a 3rd order Richmond iteration

procedure was used, as suggested by Sauerwein [21], for its stability and high rate of convergence. Consider a truncated 2nd order Taylor expansion of a set of functions f_i of a set of independent variables x_j, equated to zero, as shown in equation 4.14, in tensor notation. Note that repeated indices indicate summation. An inner iteration process proceeds as follows: the inner differences (Δx_k) are initially set to zero; the outer differences are then solved for and used for the inner difference in the next iteration, as shown in 4.15. This proceeds until the change in corrections diminishes below a convergence condition, equation 4.16; where the correction components are each normalised by a reference scale. In the outer iteration, these corrections (Δx_j) are added to the state x_j. The outer iteration continues until the residual of the set of equations ($f_i = 0$) is reduced to some error, equation 4.17.

$$f_i + \left[\frac{\partial f_i}{\partial x_j} + \frac{1}{2}\frac{\partial^2 f_i}{\partial x_j \partial x_k}\Delta x_k\right]\Delta x_j = 0 \tag{4.14}$$

$$\Delta x_j^{n+1} = -\left[\frac{\partial f_i}{\partial x_j} + \frac{1}{2}\frac{\partial^2 f_i}{\partial x_j \partial x_k}\Delta x_k^n\right]^{-1} f_i \tag{4.15}$$

$$\left|\left(\frac{\Delta x^{n+1} - \Delta x^n}{x_{ref}}\right)_j\right| < \epsilon \tag{4.16}$$

$$|f_i| < \epsilon \tag{4.17}$$

4.4 Field Points

Given a point i in an initial flow field, the characteristic cone emanating from this point - representing the space-time envelope of sound waves from an infinitesimal disturbance - may be approximated as an oblique circular cone, defined by equation 4.18. It is an approximation because realistically, this cone may curve as the field varies in space and time. The approximation becomes exact as the size of the cone approaches zero - a standard property of discretisation schemes. Along this cone, a point at a time Δt later may be obtained. Since it lies on the characteristic surface, the corresponding compatibility equation may be discretised and used to relate flow properties between these two points. Consider the compatibility equation, 4.5. There are unknown space-time derivatives for three flow variables (u, v and p). Therefore, three instances of the discretised compatibility equation must be solved

simultaneously. A fourth flow property will come from the streamline compatibility equation. In order to apply three cone compatibility equations simultaneously, the cones from three points (b_1, b_2, b_3) in the initial flow field must intersect at a single point (b_4), as illustrated in figure 4.1. Unfortunately, there is no analytical solution for obtaining this point, so it must be found numerically, as discussed in section 4.5.

$$[(x - x_i) - u_i (t - t_i)]^2 + [(y - y_i) - v_i (t - t_i)]^2 - a_i^2 (t - t_i)^2 = 0 \tag{4.18}$$

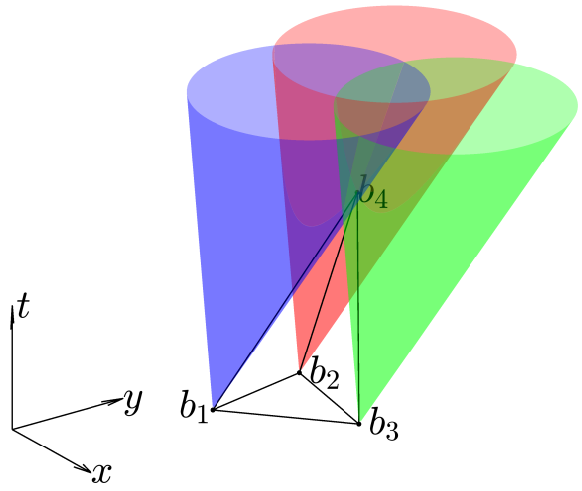


Figure 4.1: Field cones intersection

Once the intersection point is found, the transformed bases $(\alpha_i, \beta_i, \gamma_i)$ for each base point must be determined. Consider the point b_1 with its cone, connected to the intersection point b_4 in figure 4.2. The basis is centered at b_1 with the β-axis parallel to the bicharacteristic line b_{1-4}. The α-axis is normal to the cone along b_{1-4}. Its basis vector can be derived from a parameterised form of the cone, shown in equation 4.19 - with the time difference Δt measured from the base point apex; and ϕ measuring the angular position at given circle cross-section of the cone. The cone normal can be found by taking the cross-product of the partial derivatives with respect to each parameter, as shown in equation 4.20. Notice that this normal does not depend on Δt, and so is constant along b_{1-4}. The particular ϕ coordinate may be obtained from the parameterised equation, as shown in 4.21. Finally the γ-axis is taken perpendicular to the α and β-axes to form an orthonormal basis. These basis vectors must of course be normalised first. Basis vectors function as the gradient of the corresponding basis coordinate with respect to, in this case, the x, y, t coordinates. e.g. The basis vector for the α coordinate may be written as $\bigtriangledown\alpha$, since a change in α produced by moving by $\Delta\vec{b}$ in x, y, t space can be written as $\Delta\alpha = \bigtriangledown\alpha \cdot \Delta\vec{b}$. The basis vectors $\bigtriangledown\alpha_i, \bigtriangledown\beta_i, \bigtriangledown\gamma_i$ can now be substituted into the

compatibility equations directly. Also note that the remaining partial derivatives in the square brackets in equation 4.5, for example $\frac{\partial \beta}{\partial x}$, are just elements of the basis vectors. Also, the flow properties in the square brackets may be taken at the corresponding base points i (later these will be taken as an appropriate average, to achieve higher accuracy). Therefore, the coefficients for each field variable derivative (e.g $\frac{\partial u}{\partial \beta}$) are now known, and discretisation of these derivatives may proceed.

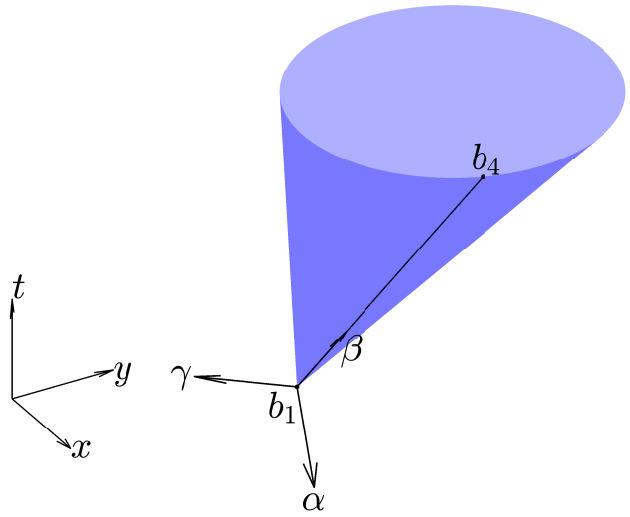


Figure 4.2: Cone basis

$$\vec{b_{cone}}\left(\Delta t, \phi\right) = \vec{b_i} + \Delta t \left(\begin{bmatrix} u_i \\ v_i \\ 1 \end{bmatrix} + a_i \begin{bmatrix} \cos(\phi) \\ \sin(\phi) \\ 0 \end{bmatrix} \right) \tag{4.19}$$

$$\begin{aligned} \frac{\partial \vec{b_{cone}}}{\partial t} \times \frac{\partial \vec{b_{cone}}}{\partial \phi} &= \begin{bmatrix} u_i + a_i \cos(\phi) \\ v_i + a_i \sin(\phi) \\ 1 \end{bmatrix} \times \begin{bmatrix} -\sin(\phi) \\ \cos(\phi) \\ 0 \end{bmatrix} \\ &= \begin{bmatrix} \cos(\phi) \\ \sin(\phi) \\ -\left(u_i \cos(\phi) + v_i \sin(\phi) + a_i\right) \end{bmatrix} \end{aligned} \tag{4.20}$$

$$\begin{bmatrix} \cos(\phi_{i-4}) \\ \sin(\phi_{i-4}) \\ 0 \end{bmatrix} = \left[\frac{\vec{b_4} - \vec{b_i}}{t_4 - t_i} - \begin{bmatrix} u_i \\ v_i \\ 1 \end{bmatrix} \right] / a_i \tag{4.21}$$

The coefficients of the flow derivatives in the compatibility equation are now written compactly in equation 4.22. The set of compatibility equations are then written in matrix form, in equation 4.23. Expanded forms are shown for illustration.

$$\frac{\partial u}{\partial \beta} B_u + \frac{\partial v}{\partial \beta} B_v + \frac{\partial p}{\partial \beta} B_p +$$
$$\frac{\partial u}{\partial \gamma} C_u + \frac{\partial v}{\partial \gamma} C_v + \frac{\partial p}{\partial \gamma} C_p = 0 \tag{4.22}$$

$$\left[\frac{\partial S}{\partial \beta}\right]_i^q \bullet [B]_i^q + \left[\frac{\partial S}{\partial \gamma}\right]_i^q \bullet [C]_i^q = 0 \tag{4.23}$$

$$\left[\frac{\partial S}{\partial \beta}\right]_i^q = \begin{bmatrix} \frac{\partial u}{\partial \beta_1} & \frac{\partial v}{\partial \beta_1} & \frac{\partial p}{\partial \beta_1} \\ \frac{\partial u}{\partial \beta_2} & \frac{\partial v}{\partial \beta_2} & \frac{\partial p}{\partial \beta_2} \\ \frac{\partial u}{\partial \beta_3} & \frac{\partial v}{\partial \beta_3} & \frac{\partial p}{\partial \beta_3} \end{bmatrix}$$

$$[B]_i^q = \begin{bmatrix} B_{1u} & B_{1v} & B_{1p} \\ B_{2u} & B_{2v} & B_{2p} \\ B_{3u} & B_{3v} & B_{3p} \end{bmatrix}$$

Flow derivatives in the β direction are given by first order finite differences along each line b_{i-4}, from base point to solution point, as shown in equation 4.26. The β differences $\Delta\beta_{i-4} = \beta_4 - \beta_i$ are aligned with the bicharacteristic line directions, as shown in figure 4.2. Therefore basis vector $\bigtriangledown\beta$ is given by equation 4.24. The β differences now become the L_2 (Euclidean) norm of the space-time vector differences $\Delta\vec{b}_{i-4} = (x_4 - x_i, y_4 - y_i, t_4 - t_i)$ - illustrated in equation 4.25. This is shown in matrix form in equation 4.27. Refer to section 4.2 for the relevant notation.

$$\frac{\partial u}{\partial \beta} \approx \frac{\Delta u_{i-4}}{\Delta \beta_{i-4}} = \frac{u_4 - u_i}{\Delta \beta_{i-4}}$$

$$\Delta\beta_{i-4} = \frac{\Delta\vec{b}_{i-4}}{\left|\Delta\vec{b}_{i-4}\right|} \tag{4.24}$$

$$\Delta\beta_{i-4} = \bigtriangledown\beta \cdot \Delta\vec{b}_{i-4} = \frac{\Delta\vec{b}_{i-4}}{\left|\Delta\vec{b}_{i-4}\right|} \cdot \Delta\vec{b}_{i-4} = \frac{\left|\Delta\vec{b}_{i-4}\right|^2}{\left|\Delta\vec{b}_{i-4}\right|} = \left|\Delta\vec{b}_{i-4}\right| \equiv L_i \tag{4.25}$$

$$\left(\frac{\partial u}{\partial \beta}\right)_i \approx \frac{u_4 - u_i}{L_i} \tag{4.26}$$

$$\left[\frac{\partial S}{\partial \beta}\right]_i^q \approx \begin{bmatrix} \frac{u_4-u_1}{L_1} & \frac{v_4-v_1}{L_1} & \frac{v_4-v_1}{L_1} \\ \frac{u_4-u_2}{L_2} & \frac{v_4-v_2}{L_2} & \frac{v_4-v_2}{L_2} \\ \frac{u_4-u_3}{L_3} & \frac{v_4-v_3}{L_3} & \frac{v_4-v_3}{L_3} \end{bmatrix} = \begin{bmatrix} 1/L_1 \\ 1/L_2 \\ 1/L_3 \end{bmatrix} \odot \begin{bmatrix} u_4-u_1 & v_4-v_1 & p_4-p_1 \\ u_4-u_2 & v_4-v_2 & p_4-p_2 \\ u_4-u_3 & v_4-v_3 & p_4-p_3 \end{bmatrix}$$

$$= [1/L]_i \odot \left(\begin{bmatrix} 1 \\ 1 \\ 1 \end{bmatrix} \begin{bmatrix} u_4 & v_4 & p_4 \end{bmatrix} - \begin{bmatrix} u_1 & v_1 & p_1 \\ u_2 & v_2 & p_2 \\ u_3 & v_3 & p_3 \end{bmatrix} \right) = [1/L]_i \odot ([1]_3 [S_4]^q - [S]_i^q) \tag{4.27}$$

The β flow differences are then substituted into equation 4.23. Array-wise multiplying this equation by $[L]_i$ and applying the lemma 4.13, results in a matrix equation 4.28, which may be solved for $[S_4]_q$ - the solution point flow properties. However, the γ flow differences $\left[\frac{\partial S}{\partial \gamma}\right]_i^q$ are required first.

$$\begin{aligned} [1/L]_i \odot ([1]_3 [S_4]^q - [S]_i^q) \bullet [B]_i^q + \left[\frac{\partial S}{\partial \gamma}\right]_i^q \bullet [C]_i^q = 0 \\ [B]_i^q \bullet ([1]_3 [S_4]^q) - [S]_i^q \bullet [B]_i^q + [L]_i \odot \left[\frac{\partial S}{\partial \gamma}\right]_i^q \bullet [C]_i^q = 0 \\ [B]_i^q [S_4]_q = \left([S]_i^q \bullet [B]_i^q - [L]_i \odot \left[\frac{\partial S}{\partial \gamma}\right]_i^q \bullet [C]_i^q \right) \end{aligned} \tag{4.28}$$

The γ flow derivatives $\left[\frac{\partial S}{\partial \gamma}\right]_i^q$ must are approximated using finite differences in the cell ($i = 1..4$, figure 4.1): In equation 4.29, finite differences in x, y, t coordinates ($\left[\frac{\partial S}{\partial b}\right]_j^q$) are solved simultaneously and transformed to the *gamma*-axis. For these finite differences $[\Delta S]_i^q$, Sauerwein suggests initially taking the flow properties at $i = 4$ to be taken as the average of the base point flow properties. When the solution is iterated, previous solution values are used instead, and these differences converge. However, it was found that instead, the solution state S_4 may be factorised from the γ derivatives so that the solution may be obtained immediately. This is shown in section 4.4.1.

$$\left[\frac{\partial S}{\partial \gamma}\right]_i^q = \left[\frac{\partial b}{\partial \gamma}\right]_i^j \left[\frac{\partial S}{\partial b}\right]_j^q$$

$$\left[\frac{\partial b}{\partial \gamma}\right]_i^j = \begin{bmatrix} \frac{\partial x}{\partial \gamma_1} & \frac{\partial y}{\partial \gamma_1} & \frac{\partial t}{\partial \gamma_1} \\ \frac{\partial x}{\partial \gamma_2} & \frac{\partial y}{\partial \gamma_2} & \frac{\partial t}{\partial \gamma_2} \\ \frac{\partial x}{\partial \gamma_3} & \frac{\partial y}{\partial \gamma_3} & \frac{\partial t}{\partial \gamma_3} \end{bmatrix}$$

$$\left[\frac{\partial S}{\partial b}\right]_j^q = \begin{bmatrix} \frac{\partial u}{\partial x} & \frac{\partial v}{\partial x} & \frac{\partial p}{\partial x} \\ \frac{\partial u}{\partial y} & \frac{\partial v}{\partial y} & \frac{\partial p}{\partial y} \\ \frac{\partial u}{\partial t} & \frac{\partial v}{\partial t} & \frac{\partial p}{\partial t} \end{bmatrix} \approx \left([\Delta b]_i^j\right)^{-1} [\Delta S]_i^q =$$

$$\begin{bmatrix} x_4 - x_1 & y_4 - y_1 & t_4 - t_1 \\ x_4 - x_2 & y_4 - y_2 & t_4 - t_2 \\ x_4 - x_3 & y_4 - y_3 & t_4 - t_3 \end{bmatrix}^{-1} \begin{bmatrix} u_4 - u_1 & v_4 - v_1 & p_4 - p_1 \\ u_4 - u_2 & v_4 - v_2 & p_4 - p_2 \\ u_4 - u_3 & v_4 - v_3 & p_4 - p_3 \end{bmatrix} \tag{4.29}$$

The transformation $\left[\frac{\partial b}{\partial \gamma}\right]_i^j$ required in equation 4.29 are obtained from the (inverse) coordinate transformations from each base point. Due to the orthogonality of the transformation matrices $[Q_i]$, the inverses are simply equal to the transposes. This implies that $\frac{\partial \beta}{\partial x} = \frac{\partial x}{\partial \beta}$ for all pairs of transform derivatives, as shown in equation 4.30. Therefore, the γ-transforms $\left[\frac{\partial b}{\partial \gamma}\right]_i^j$ are given by the γ basis vectors for each base point, in equation 4.31.

$$\begin{bmatrix} \Delta\alpha \\ \Delta\beta \\ \Delta\gamma \end{bmatrix} = [Q]_i^j \begin{bmatrix} \Delta x \\ \Delta y \\ \Delta t \end{bmatrix} = \begin{bmatrix} \frac{\partial \alpha}{\partial x} & \frac{\partial \alpha}{\partial y} & \frac{\partial \alpha}{\partial t} \\ \frac{\partial \beta}{\partial x} & \frac{\partial \beta}{\partial y} & \frac{\partial \beta}{\partial t} \\ \frac{\partial \gamma}{\partial x} & \frac{\partial \gamma}{\partial y} & \frac{\partial \gamma}{\partial t} \end{bmatrix} \begin{bmatrix} \Delta x \\ \Delta y \\ \Delta t \end{bmatrix}$$

$$\begin{bmatrix} \Delta x \\ \Delta y \\ \Delta t \end{bmatrix} = \left([Q]_i^j\right)^{-1} \begin{bmatrix} \Delta\alpha \\ \Delta\beta \\ \Delta\gamma \end{bmatrix} = \begin{bmatrix} \frac{\partial x}{\partial \alpha} & \frac{\partial x}{\partial \beta} & \frac{\partial x}{\partial \gamma} \\ \frac{\partial y}{\partial \alpha} & \frac{\partial y}{\partial \beta} & \frac{\partial y}{\partial \gamma} \\ \frac{\partial t}{\partial \alpha} & \frac{\partial t}{\partial \beta} & \frac{\partial t}{\partial \gamma} \end{bmatrix} \begin{bmatrix} \Delta\alpha \\ \Delta\beta \\ \Delta\gamma \end{bmatrix}$$

$$\left([Q]_i^j\right)^{-1} = \left([Q]_i^j\right)^T (orthonormal)$$

$$\implies \begin{bmatrix} \frac{\partial x}{\partial \alpha} & \frac{\partial x}{\partial \beta} & \frac{\partial x}{\partial \gamma} \\ \frac{\partial y}{\partial \alpha} & \frac{\partial y}{\partial \beta} & \frac{\partial y}{\partial \gamma} \\ \frac{\partial t}{\partial \alpha} & \frac{\partial t}{\partial \beta} & \frac{\partial t}{\partial \gamma} \end{bmatrix} = \begin{bmatrix} \frac{\partial \alpha}{\partial x} & \frac{\partial \beta}{\partial x} & \frac{\partial \gamma}{\partial x} \\ \frac{\partial \alpha}{\partial y} & \frac{\partial \beta}{\partial y} & \frac{\partial \gamma}{\partial y} \\ \frac{\partial \alpha}{\partial t} & \frac{\partial \beta}{\partial t} & \frac{\partial \gamma}{\partial t} \end{bmatrix} = \begin{bmatrix} \bigtriangledown\alpha & \bigtriangledown\beta & \bigtriangledown\gamma \end{bmatrix} \tag{4.30}$$

$$\left[\frac{\partial b}{\partial \gamma}\right]_i^j = \begin{bmatrix} \frac{\partial x}{\partial \gamma_1} & \frac{\partial y}{\partial \gamma_1} & \frac{\partial t}{\partial \gamma_1} \\ \frac{\partial x}{\partial \gamma_2} & \frac{\partial y}{\partial \gamma_2} & \frac{\partial t}{\partial \gamma_2} \\ \frac{\partial x}{\partial \gamma_3} & \frac{\partial y}{\partial \gamma_3} & \frac{\partial t}{\partial \gamma_3} \end{bmatrix} = \begin{bmatrix} \bigtriangledown\gamma_1 \\ \bigtriangledown\gamma_2 \\ \bigtriangledown\gamma_3 \end{bmatrix} \tag{4.31}$$

4.4.1 Factorising the Cone Compatibility Equation

The γ flow derivatives in the cone equation may be expanded from equation 4.29, as shown for the β derivatives in equation 4.27, to give equation 4.32. Where two new matrices $[M]_i^i$ and $[m]_i$ have been defined. Substituting this into the compact form of the compatibility equation 4.28 and using the dot product lemma 4.13 for the underlined term, yields equation 4.33. From here, the $[S_4]_q$ term is factorised from both sides, yielding a final factorised equation 4.34, which may be solved for the solution state $[S_4]_q$. The coefficients matrices of this equation are written as $[G]_i^q$ and $[H]_i$, as shown. These matrices now depend only on the cone bases and flow properties $[S]_i^q$ at the base points. This is the final dicretised form of the cone compatibility equations used for all field points, and modified accordingly for surface and shock points. By factorising out the γ derivatives, the solution is found to converge significantly faster and more robustly, compared to the method proposed by Sauerwein.

$$\begin{gathered}\left[\frac{\partial S}{\partial \gamma}\right]_i^q = \left[\frac{\partial b}{\partial \gamma}\right]_i^j \left([\Delta b]_i^j\right)^{-1} [\Delta S]_i^q = [M]_i^i \left([1]_3 [S_4]^q - [S]_i^q\right) = \\ [M]_i^i [1]_3 [S_4]^q - [M]_i^i [S]_i^q = [m]_i [S_4]^q - [M]_i^i [S]_i^q \\ [M]_i^i \equiv \left[\frac{\partial b}{\partial \gamma}\right]_i^j \left([\Delta b]_i^j\right)^{-1} \\ [m]_i \equiv [M]_i^i [1]_3\end{gathered} \tag{4.32}$$

$$\begin{gathered}[B]_i^q [S_4]_q = \left([S]_i^q \bullet [B]_i^q - [L]_i \odot \left[\frac{\partial S}{\partial \gamma}\right]_i^q \bullet [C]_i^q\right) = \\ \left([S]_i^q \bullet [B]_i^q - [L]_i \odot \left([m]_i [S_4]^q - [M]_i^i [S]_i^q\right) \bullet [C]_i^q\right) = \\ \left([S]_i^q \bullet [B]_i^q - [L]_i \odot \underline{([m]_i [S_4]^q) \bullet [C]_i^q} - [L]_i \odot \left([M]_i^i [S]_i^q\right) \bullet [C]_i^q\right) = \\ [S]_i^q \bullet [B]_i^q - [L]_i \odot [m]_i \odot [C]_i^q [S_4]_q - [L]_i \odot \left([M]_i^i [S]_i^q\right) \bullet [C]_i^q\end{gathered} \tag{4.33}$$

$$\begin{gathered}([B]_i^q + [L]_i \odot [m]_i \odot [C]_i^q) [S_4]_q = \left([S]_i^q \bullet [B]_i^q - [L]_i \odot \left([M]_i^i [S]_i^q\right) \bullet [C]_i^q\right) \\ [G]_i^q [S_4]_q = [H]_i\end{gathered} \tag{4.34}$$

4.4.2 Streamline Characteristic

Once the states u_4, v_4 and p_4 have been determined from the cone compatibility equations, there remains one state variable to solve for ρ_4 or T_4, which will come from the compatibility equation for the streamline characteristic. Consider figure 4.3. The streamline passes through the solution point, but may be traced back to the base plane, at point b_5. Initially, this line may be assumed to have a constant flow velocity $V_4 = (u_4, v_4, 1)$, implying that it is straight. In reality it will curve as the flow velocity varies through the cell. A better approximation may be obtained by using the average velocity between b_4 and b_5 - in an iterative process:

Point b_5 may initially be given by $b_5 = b_4 - \vec{\mathbf{V}}_4 \Delta t$, where Δt is the time step between the base plane and b_4. The flow properties u_5, v_5, T_5 can be found by linearly interpolating between the base points, as shown in equation 4.35: the differences between base point properties (arbitrarily choosing b_1 as a datum) are assumed to vary linearly, with constant partial gradients (e.g u_x). The velocity components obtained (u_5, v_5) may now be used to provide an improved convection velocity for the streamline: $\vec{\mathbf{V}}_{5-4} = (\frac{u_5+u_5}{2}, \frac{v_5+v_5}{2}, 1)$. This process is iterated to improve accuracy.

Now a suitable compatibility equation must be chosen. For inviscid, adiabatic flow, the entropy equation 4.36 [12] may be used, which implies that the entropy of a point convecting through the flow field is constant. The only exception in this context would be when this point moves through a shock wave. Therefore the isentropic relation, equation 4.37, may be used to obtain the final flow property T_4.

$$\Delta q = q_x(x - x_1) + q_y(y - y_1)$$

$$\begin{bmatrix} x_2 - x_1 & y_2 - y_1 \\ x_3 - x_1 & y_3 - y_1 \end{bmatrix} \begin{bmatrix} u_x & v_x & T_x \\ u_y & v_y & T_y \end{bmatrix} = \begin{bmatrix} u_2 - u_1 & v_2 - v_1 & T_2 - T_1 \\ u_3 - u_1 & v_3 - v_1 & T_3 - T_1 \end{bmatrix}$$

$$\begin{bmatrix} u_x & v_x & T_x \\ u_y & v_y & T_y \end{bmatrix} = \begin{bmatrix} x_2 - x_1 & y_2 - y_1 \\ x_3 - x_1 & y_3 - y_1 \end{bmatrix}^{-1} \begin{bmatrix} u_2 - u_1 & v_2 - v_1 & T_2 - T_1 \\ u_3 - u_1 & v_3 - v_1 & T_3 - T_1 \end{bmatrix}$$

$$\begin{bmatrix} u_5 & v_5 & T_5 \end{bmatrix} = \begin{bmatrix} x_5 - x_1 & y_5 - y_1 \end{bmatrix} \begin{bmatrix} u_x & v_x & T_x \\ u_y & v_y & T_y \end{bmatrix} + \begin{bmatrix} u_1 & v_1 & T_1 \end{bmatrix} \tag{4.35}$$

$$\frac{Ds}{Dt} = 0 \tag{4.36}$$

$$\frac{T_4}{T_5} = \left(\frac{p_4}{p_5}\right)^{\frac{\gamma-1}{\gamma}} \tag{4.37}$$

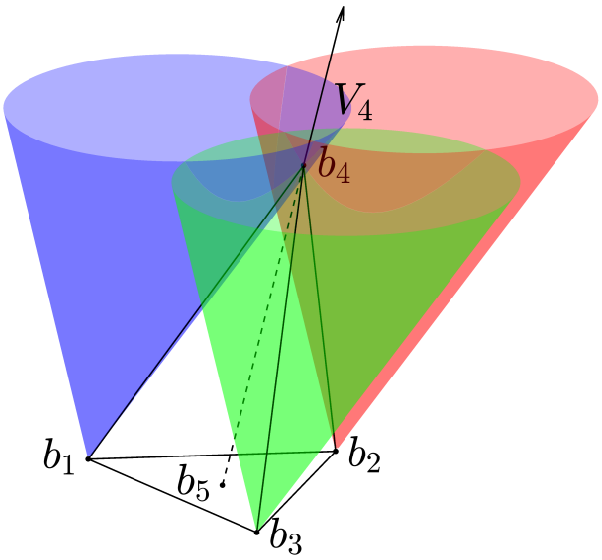


Figure 4.3: Streamline characteristic

4.4.3 Stability - Domain of Dependence

Consider the solution point in figure 4.4. Its domain of dependence may be projected back to the base plane. Notice that this domain includes points outside the base triangle. Setting up the field solution in this way leads to instabilities because the CFL condition [12] is violated. To remedy this, Sauerwein suggests inscribing a circle into the triangle formed by a triangular element B_1, B_2, B_3 in the flow field. Now the base points used in the field procedure b_1, b_2, b_3 will be taken on the edge of this circle, as shown in figure 4.5.

To find this inscribed circle, first its center may be given in barycentric coordinates, and then x, y coordinates by equation 4.38. Where for example, the length $L_{12} = |\vec{B}_2 - \vec{B}_1|$. Finally, the points b_1, b_2, b_3 are found at the tangents. For example, b_1 may be found by projecting the line from $\vec{B}_2$ to $\vec{b}_c$ onto $\vec{B}_{23}$, as shown in equation 4.39. Finally, properties at these inner points are found by linearly interpolating between the outer points. e.g. At the inner point b_1, the flow variables are a linear combination of those at B_2 and B_3.

$$\hat{C} = \frac{(L_{23}, L_{12}, L_{12})}{L_{23} + L_{12} + L_{12}}$$
$$\vec{b}_c = \vec{b}_1\hat{C}(1) + \vec{b}_2\hat{C}(2) + \vec{b}_3\hat{C}(3) \tag{4.38}$$

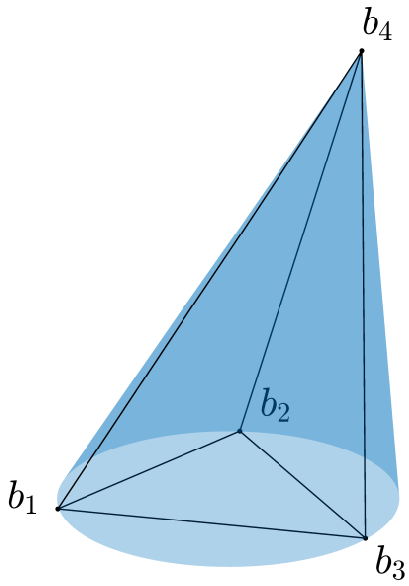


Figure 4.4: Solution point - domain of dependence

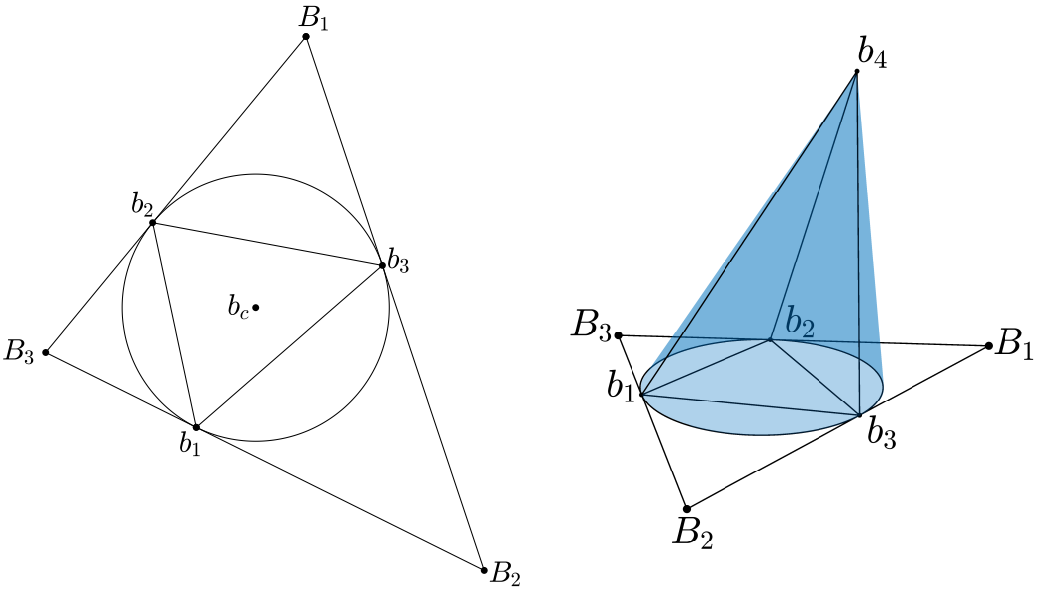


Figure 4.5: Inscribed circle geometry

$$\vec{b}_1 - \vec{B}_2 = \left(\vec{b}_c - \vec{B}_2\right) \circ \left(\frac{\vec{B_{23}}}{L_{23}}\right) \frac{\vec{B_{23}}}{L_{23}} \tag{4.39}$$

4.4.4 The Field Procedure

All the necessary definitions for handling triangular elements in a flow field have now been described, and the overall iteration procedure is now briefly discussed:

1. Given an element B_1, B_2, B_3 in a flow field, as shown in figure 4.5, with known flow properties u, v, p, T, an inner triangle b_1, b_2, b_3 is constructed and flow properties are linearly interpolated to the inner points.

2. The cone characteristics from each base point are approximated by oblique cones and the location of the solution point b_4 is found by their intersection, as described in section 4.5.

3. The cone basis vectors for each base point are then found and the solution matrices $[G]_i^q$ and $[H]_i$ are determined using the basis vectors and base point flow states. The solution state variables $[S_4]_q$ are found by solving the cone compatibility equations: $[G]_i^q[S_4]_q = [H]_i$.

4. The remaining flow state T_4 is then obtained from the streamline compatibility equation.

5. To improve the accuracy of the procedure, the average flow properties between the base points and the solution point - e.g. $u_1^{(n+1)} = [u_1^{(0)} + u_4^{(n)}]/2$ (where n represents the iteration number) - are used to re-evaluate: the solution point location from the cone intersections; and the flow derivative coefficients $[B]_i^q$ and $[C]_i^q$ in equation 4.23. In this way, steps 2 to 4 are repeated, re-averaging these states each iteration. This continues until the scaled change in each degree of freedom - the coordinates of the solution point (x_4, y_4) and its flow state (u_4, v_4, p_4) - shown in expression 4.40, all reduce below some error ϵ. A common length scale (l_{scale}) taken from some x, y length in the base cell B_1, B_2, B_3 is used for the x, y coordinates, while a time scale t_{scale} taken from the initial point estimate for b_4 ($t_{scale} = t_{40} - t_{base}$) is used for scaling the time changes. Similarly, the flow state changes are scaled by average flow properties in the cell. Combining the position and state residuals using the L_2 norm of residual components, the scaled residuals are shown per iteration for a test case in figure 4.6.

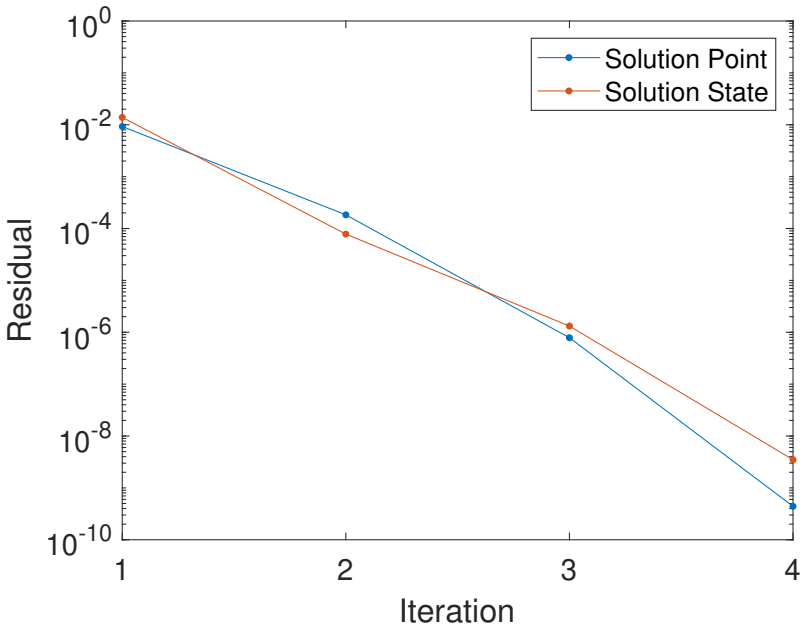


Figure 4.6: Field iteration residuals

$$\begin{matrix} \dfrac{x^{(n+1)} - x^{(n)}}{l_{scale}} & \dfrac{y^{(n+1)} - y^{(n)}}{l_{scale}} \\ \dfrac{t^{(n+1)} - t^{(n)}}{t_{scale}} & \\ \dfrac{u^{(n+1)} - u^{(n)}}{V_{scale}} & \dfrac{v^{(n+1)} - v^{(n)}}{V_{scale}} \\ \dfrac{p^{(n+1)} - p^{(n)}}{p_{scale}} & \\ \dfrac{T^{(n+1)} - T^{(n)}}{T_{scale}} & \end{matrix} \tag{4.40}$$

4.5 Cone Intersections

This section describes methods used to find intersections of combinations oblique cones and planes required for the field, surface and shock methods.

First, consider the intersection of three oblique cones shown in figure 4.1. The corresponding cone equations 4.41, for points $i = 1, 2, 3$ must be solved simultaneously for (x, y, t). After an initial approximation is obtained (section 4.5.2), Richmond's method (section 4.3) is applied to solve these equations numerically. The setup for this method will now be shown using the matrix notation defined in section 4.2. The Jacobian $\frac{\partial f}{\partial b}$ is shown in equation 4.42 along with its first row - the remaining rows are the same except the i index changes accordingly. Unfortunately, matrix notation cannot handle the 2nd order derivatives as cleanly as tensor notation. The 2nd order derivatives are broken up into three matrices, $[A]_i^j$, $[B]_i^j$ and $[C]_i^j$ shown with their first rows in equations 4.43, 4.44 and 4.45. Once again, the remaining rows are the same except for the i index. Finally, the Jacobian and 2nd order matrices are used in equation 4.46 to perform the inner iteration for Richmond's method. Convergence of the inner iteration is given by equation 4.16. Where the error may be scaled by distance and time lengths in the given cell, for example: $|(x_{40}, y_{40}) - (x_1, y_1)|$ might be used for a length scale, and $|t_{40} - t_1|$ might be used for a time scale. Where the point $b_{40} = (x_{40}, y_{40}, t_{40})$ is the initial point estimate obtained before application of the iteration procedure. After each inner iteration converges, the solution point b_4 is updated by equation 4.47. The Jacobian, which depends on b_4 is updated, and the inner iteration is performed again to obtain a new correction. This outer iteration proceeds until the residual $|f_i|$ reduces to some tolerance. The residual should be scaled, in this case by a $length^2$ scale (the units of the cone equation).

$$f_i = \left[(x - x_i) - u_i\,(t - t_i)\right]^2 + \left[(y - y_i) - v_i\,(t - t_i)\right]^2 - a_i^2\,(t - t_i)^2 = 0 \qquad (4.41)$$

$$\left[\frac{\partial f}{\partial b}\right]_i^j = \begin{bmatrix} \frac{\partial f_1}{\partial x} & \frac{\partial f_1}{\partial y} & \frac{\partial f_1}{\partial t} \\ \frac{\partial f_2}{\partial x} & \frac{\partial f_2}{\partial y} & \frac{\partial f_2}{\partial t} \\ \frac{\partial f_3}{\partial x} & \frac{\partial f_3}{\partial y} & \frac{\partial f_3}{\partial t} \end{bmatrix}$$

$$\left[\frac{\partial f}{\partial b}\right]_{i=1}^j = 2[(x - x_1) - u_1\,(t - t_1)\,,$$
$$(y - y_1) - v_1\,(t - t_1)\,,$$
$$(t - t_1)\left(u_1^2 + v_1^2 - a_1^2\right) - u_1\,(x - x_1) - v_1\,(y - y_1)] \qquad (4.42)$$

$$[A]_i^j = \frac{\partial}{\partial x}\left[\frac{\partial f}{\partial b}\right]_i^j = \begin{bmatrix} \frac{\partial^2 f_1}{\partial^2 x} & \frac{\partial^2 f_1}{\partial x \partial y} & \frac{\partial^2 f_1}{\partial x \partial t} \\ \frac{\partial^2 f_2}{\partial^2 x} & \frac{\partial^2 f_2}{\partial x \partial y} & \frac{\partial^2 f_2}{\partial x \partial t} \\ \frac{\partial^2 f_3}{\partial^2 x} & \frac{\partial^2 f_3}{\partial x \partial y} & \frac{\partial^2 f_3}{\partial x \partial t} \end{bmatrix}$$

$$[A]_{i=1}^j = 2\begin{bmatrix} 1 & 0 & -u_1 \end{bmatrix} \tag{4.43}$$

$$[B]_i^j = \frac{\partial}{\partial y}\left[\frac{\partial f}{\partial b}\right]_i^j = \begin{bmatrix} \frac{\partial^2 f_1}{\partial y \partial x} & \frac{\partial^2 f_1}{\partial y^2} & \frac{\partial^2 f_1}{\partial y \partial t} \\ \frac{\partial^2 f_2}{\partial y \partial x} & \frac{\partial^2 f_2}{\partial y^2} & \frac{\partial^2 f_2}{\partial y \partial t} \\ \frac{\partial^2 f_3}{\partial y \partial x} & \frac{\partial^2 f_3}{\partial y^2} & \frac{\partial^2 f_3}{\partial y \partial t} \end{bmatrix}$$

$$[B]_{i=1}^j = 2\begin{bmatrix} 0 & 1 & -v_1 \end{bmatrix} \tag{4.44}$$

$$[C]_i^j = \frac{\partial}{\partial t}\left[\frac{\partial f}{\partial b}\right]_i^j = \begin{bmatrix} \frac{\partial^2 f_1}{\partial t \partial x} & \frac{\partial^2 f_1}{\partial t \partial y} & \frac{\partial^2 f_1}{\partial t^2} \\ \frac{\partial^2 f_2}{\partial t \partial x} & \frac{\partial^2 f_2}{\partial t \partial y} & \frac{\partial^2 f_2}{\partial t^2} \\ \frac{\partial^2 f_3}{\partial t \partial x} & \frac{\partial^2 f_3}{\partial t \partial y} & \frac{\partial^2 f_3}{\partial t^2} \end{bmatrix}$$

$$[C]_{i=1}^j = -2\begin{bmatrix} u_1 & v_1 & a_1^2 - u_1^2 - v_1^2 \end{bmatrix} \tag{4.45}$$

$$\left[\Delta b^{(n+1)}\right]_j = -\left(\left[\frac{\partial f}{\partial b}\right]_i^j + \frac{1}{2}\left[[A]_i^j\left[\Delta b^{(n)}\right]_j \quad [B]_i^j\left[\Delta b^{(n)}\right]_j \quad [C]_i^j\left[\Delta b^{(n)}\right]_j\right]\right)^{-1}[f]_i \tag{4.46}$$

$$\left[b_4^{(s+1)}\right]_j = [b_4^s]_j + [\Delta b]_j \tag{4.47}$$

4.5.1 Cone-Plane Intersections

Intersections involving two oblique cones and a plane, required for the surface and shock procedures, are handled in the same way, except the third row of the residual, Jacobian and 2nd order matrices $[A]_i^j$, $[B]_i^j$ and $[C]_i^j$ are replaced with expressions derived for a plane in (x, y, t) space, as shown in equation 4.48. The rows for the 2nd order derivatives of the plane residual all contain zeros.

$$f_3 = ax + by + ct - d = 0$$

$$\left[\frac{\partial f}{\partial b}\right]_{i=3}^{j} = \begin{bmatrix} a & b & c \end{bmatrix} \tag{4.48}$$

4.5.2 Initial Point Estimates

In order to ensure robust and efficient convergence of the cone (or cone-plane) intersection procedure, sufficiently accurate initial estimates for the intersection point must be found. Consider again the cone equation 4.49. Initial estimates can be derived by assuming that flow properties (u_i, v_i, a_i) at each base point - b_1, b_2, and b_3 in the 3-cone case - are all equal to the mean properties across these points (u_m, v_m, a_m). Further, it is assumed that all base points are at the same time plane (which is always true for this particular code). Expanding the cone equations for each point and subtracting the third equation from the first two: two equations representing planes in (x, y, t') space are derived - shown in equation 4.50. Where t' is the time coordinate with a shifted datum $(t' = t - t_i)$ at the common time of the base points. The intersection of these planes produces a line parameterised by t', as shown in equation 4.51. The time difference t' can be solved by the intersection of this line and any of the three cones, as shown in equation 4.52. This results in a quadratic equation in t' from which the positive time difference solution is found. The point estimate is then simply given by equation 4.51.

For the case of two cones and a plane, the process is the same, except that only one plane is produced by subtraction of the cone equations; the other is the given plane.

$$\left[(x - x_i) - u_i\,(t - t_i)\right]^2 + \left[(y - y_i) - v_i\,(t - t_i)\right]^2 - a_i^2\,(t - t_i)^2 = 0 \tag{4.49}$$

$$\begin{aligned} -\left[x_1 - x_3\right] x - \left[y_1 - y_3\right] y + \left[u_m\,(x_1 - x_3) + v_m\,(y_1 - y_3)\right] t' \\ + \left[x_1^2 + y_1^2 - x_3^2 - y_3^2\right] = 0 \\ -\left[x_2 - x_3\right] x - \left[y_2 - y_3\right] y + \left[u_m\,(x_2 - x_3) + v_m\,(y_2 - y_3)\right] t' \\ + \left[x_2^2 + y_2^2 - x_3^2 - y_3^2\right] = 0 \end{aligned} \tag{4.50}$$

$$
\begin{aligned}
a_1 x + b_1 y + c_1 t' &= d_1 \\
a_2 x + b_2 y + c_2 t' &= d_2 \\
\begin{bmatrix} a_1 & b_1 \\ a_2 & b_2 \end{bmatrix} \begin{bmatrix} x \\ y \end{bmatrix} &= \begin{bmatrix} d_1 \\ d_2 \end{bmatrix} - \begin{bmatrix} c_1 \\ c_2 \end{bmatrix} t' \\
\vec{r_{line}} &= \vec{r_0} + \vec{v}_{line} t'
\end{aligned} \tag{4.51}
$$

$$
\begin{aligned}
|\vec{r_{line}} - \vec{r_i}| &= a_m t' \\
\left(u_{line} t' + x_0 - x_i\right)^2 + \left(v_{line} t' + y_0 - y_i\right)^2 &= a_m^2 t'^2
\end{aligned} \tag{4.52}
$$

4.6 Surface Points

Elements in the flow field along a surface boundary - a line in the x, y plane - can be handled using the same general approach to solving the discretised form of the compatibility equations, but must additionally include the boundary condition of the surface. Consider a point b_3 which lies along a line surface, with adjacent field points b_1 and b_2 in figure 4.7. Notice that this line becomes a surface in x, y, t space. In general, this line may be curved in the $x-y$ plane as well as in the time direction (due to arbitrary linear or rotational acceleration); whereas a constant slant in the t direction corresponds to a constant velocity of this line.

The first step is finding the new solution point b_4 at the intersection of the characteristic cones from field points b_1 and b_2, and the surface passing through b_3. This process is described in section 4.5. Next, the cone compatibility equations must be setup to solve for the flow state at b_4. However, in this case, only two cone compatibility equations are available - one for each field point b_1 and b_2. The matrix form of these equations (4.28) is still valid for two equations ($i = 1, 2$), since the matrix operations are all valid so long as the i dimension of each item is consistent; except that the finite differences required for the γ field derivatives in equation 4.29 do in fact require three sets of differences. This means that the surface base point and its flow state must be included in this step as an extra point needed for approximating field derivatives. This is shown in equation 4.53: the spatial flow deviates $\left[\frac{\partial S}{\partial b}\right]_j^q$ are approximated by finite differences in the cell involving all four points. A k index is now used to indicate where all three base points are used, while i corresponds to the cone base points, i.e. $i = (1, 2)$ and $k = (1, 2, 3)$. The matrix definitions $[M]_i^k$ and $[m]_i$ are updated accordingly in equation 4.54. Finally, these definitions may be used to obtain the factorised form of the compatibility equations, 4.55. However this cannot yet be inverted to solve for $[S_4]_q$ because it is under-constrained (not square). The surface boundary condition in equation 4.60, described in the following section, provides the third equation so that the flow state at b_4 may be solved.

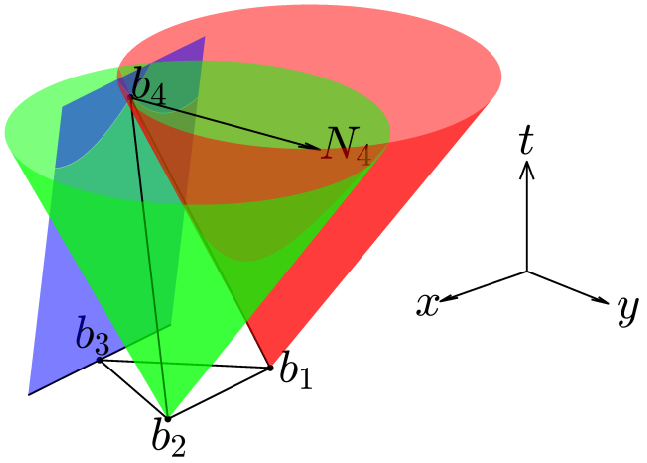


Figure 4.7: Surface cone intersection

$$\left[\frac{\partial S}{\partial \gamma}\right]_i^q = \left[\frac{\partial b}{\partial \gamma}\right]_i^j \left[\frac{\partial S}{\partial b}\right]_j^q$$

$$\left[\frac{\partial S}{\partial b}\right]_j^q \approx \left([\Delta b]_k^j\right)^{-1} [\Delta S]_k^q =$$

$$\begin{bmatrix} x_4 - x_1 & y_4 - y_1 & t_4 - t_1 \\ x_4 - x_2 & y_4 - y_2 & t_4 - t_2 \\ x_4 - x_3 & y_4 - y_3 & t_4 - t_3 \end{bmatrix}^{-1} \begin{bmatrix} u_4 - u_1 & v_4 - v_1 & p_4 - p_1 \\ u_4 - u_2 & v_4 - v_2 & p_4 - p_2 \\ u_4 - u_3 & v_4 - v_3 & p_4 - p_3 \end{bmatrix}$$

$$\left[\frac{\partial S}{\partial \gamma}\right]_i^q = \left[\frac{\partial b}{\partial \gamma}\right]_i^j \left([\Delta b]_k^j\right)^{-1} [\Delta S]_k^q = [m]_i [S_4]^q - [M]_i^k [S]_k^q \tag{4.53}$$

$$[M]_i^k \equiv \left[\frac{\partial b}{\partial \gamma}\right]_i^j \left([\Delta b]_k^j\right)^{-1}$$

$$[m]_i \equiv [M]_i^k [1]_3 \tag{4.54}$$

$$([B]_i^q + [L]_i \odot [m]_i \odot [C]_i^q) [S_4]_q = \left([S]_i^q \bullet [B]_i^q - [L]_i \odot \left([M]_i^k [S]_k^q\right) \bullet [C]_i^q\right) \tag{4.55}$$

$$[G]_i^q [S_4]_q = [H]_i$$

4.6.1 Surface Boundary

A surface boundary in the flow field, which may deform and move in arbitrary motions in time, can generally be defined by a function $\phi = \phi(x, y, t) = constant$. For this study a relatively simple geometry and motion will be defined, but the

procedures outlined may be adapted to complex geometry and motions. This setup involves a straight line surface starting at $\vec{r}_t\prime$ inclined at an angle $\theta_{line}\prime$ - in the relative frame $x' - y'$, shown in figure 4.8. This frame may then translate arbitrarily by the shift $\vec{r}_0(t)$ and rotate about the relative origin by the rotation angle $\lambda(t)$. The position of the line tip in the absolute reference frame $\vec{r}_t$, is given by equation 4.56, with a rotation matrix $R(\lambda)$. The surface function ϕ may now be given by equation 4.57, whose solution is the set of points on the surface line. Note that the normal vector $\vec{n}$, is the in-plane $(x - y)$ normal. The space-time normal vector $\vec{N}_4$ (in x, y, t space, illustrated in figure 4.7), required to define the surface boundary condition is given by equation 4.58. Finally, the surface boundary condition is given by equation 4.59, where $\vec{\mathbf{V}}_4 = (u_4, v_4, 1)$ is the space-time velocity at the solution point b_4. This may be written in matrix form in terms of the flow state at b_4, as shown in equation 4.60, so that it may appended to the set of cone compatibility equations, finally allowing the state at b_4 to be solved. The time derivatives of the line tip; relative axis origin and angle; line normal vector; and the rotation matrix, required for the boundary condition are defined in equations 4.61 to 4.65. The 2nd order derivatives will be used to improve the accuracy of the cone-surface intersection in section 4.6.2.

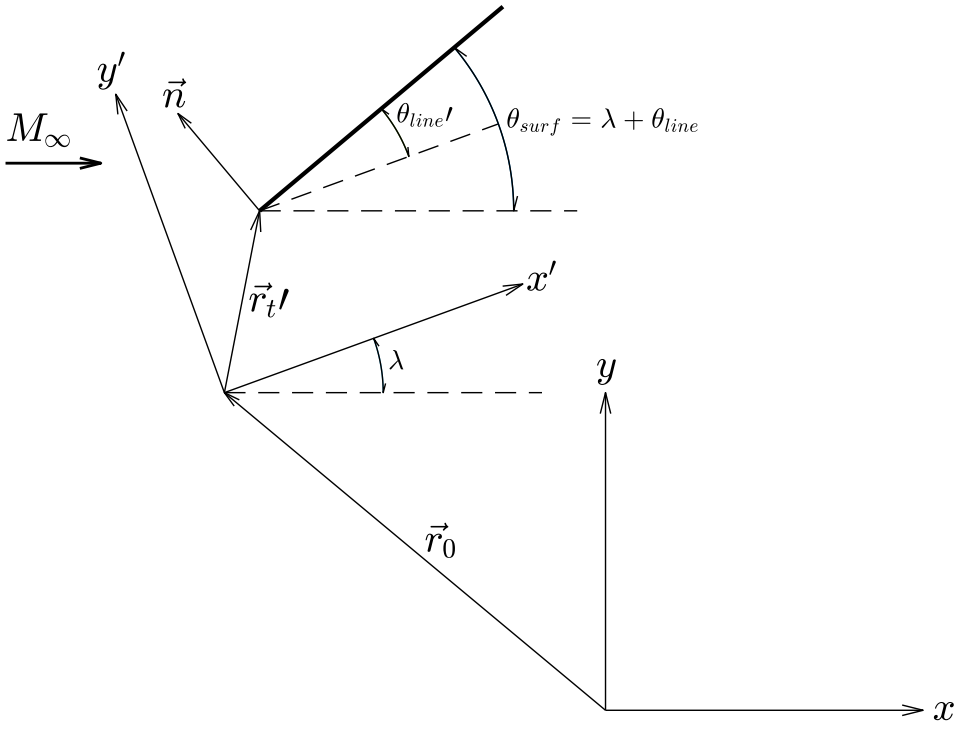


Figure 4.8: Moving line geometry

$$\vec{r}_t = \vec{r}_0(t) + R\left(\lambda(t)\right)\vec{r}_t\prime \tag{4.56}$$

$$\phi(x,y,t) = \left(\begin{bmatrix} x \\ y \end{bmatrix} - \vec{r}_t\right) \cdot \begin{bmatrix} n_1 \\ n_2 \end{bmatrix} = 0 = (\vec{r} - \vec{r}_t(t)) \cdot \vec{n}(t) = 0 \tag{4.57}$$

$$\vec{N} = \begin{bmatrix} \frac{\partial \phi}{\partial x} \\ \frac{\partial \phi}{\partial y} \\ \frac{\partial \phi}{\partial t} \end{bmatrix} = \begin{bmatrix} n_1 \\ n_2 \\ -\frac{d\vec{r}_t}{dt} \cdot \vec{n} + (\vec{r} - \vec{r}_t) \cdot \frac{d\vec{n}}{dt} \end{bmatrix}, \ (\phi = 0) \tag{4.58}$$

$$\vec{N}_4 \cdot \vec{\mathbf{V}}_4 = 0 \tag{4.59}$$

$$\begin{gathered} N_1 u_4 + N_2 v_4 + 0 p_4 = -N_3 \\ \begin{bmatrix} N_1 & N_2 & 0 \end{bmatrix} \begin{bmatrix} u_4 \\ v_4 \\ p_4 \end{bmatrix} = -N_3 \end{gathered} \tag{4.60}$$

$$\begin{aligned} \frac{d\vec{r}_t}{dt} &= \vec{v}_0 + \frac{dR}{dt}\vec{r}_t\prime \\ \frac{d^2\vec{r}_t}{dt^2} &= \vec{a}_0 + \frac{d^2R}{dt^2}\vec{r}_t\prime \end{aligned} \tag{4.61}$$

$$\vec{v}_0 \equiv \frac{d\vec{r}_0}{dt} \qquad\qquad \vec{a}_0 \equiv \frac{d^2\vec{r}_0}{dt^2} \tag{4.62}$$

$$\omega \equiv \frac{d\lambda}{dt} \qquad\qquad \alpha \equiv \frac{d^2\lambda}{dt^2} \tag{4.63}$$

$$\begin{aligned} \vec{n} &= \begin{bmatrix} -\sin\left(\lambda + \theta_{line}\right) \\ \cos\left(\lambda + \theta_{line}\right) \end{bmatrix} \\ \frac{d\vec{n}}{dt} &= \omega \begin{bmatrix} -\cos\left(\lambda + \theta_{line}\right) \\ -\sin\left(\lambda + \theta_{line}\right) \end{bmatrix} \\ \frac{d^2\vec{n}}{dt^2} &= \omega^2 \begin{bmatrix} \sin\left(\lambda + \theta_{line}\right) \\ -\cos\left(\lambda + \theta_{line}\right) \end{bmatrix} + \alpha \begin{bmatrix} -\cos\left(\lambda + \theta_{line}\right) \\ -\sin\left(\lambda + \theta_{line}\right) \end{bmatrix} \end{aligned} \tag{4.64}$$

$$
\begin{aligned}
R &= \begin{bmatrix} \cos(\lambda) & -\sin(\lambda) \\ \sin(\lambda) & \cos(\lambda) \end{bmatrix} \\
\frac{dR}{dt} &= \omega \begin{bmatrix} -\sin(\lambda) & -\cos(\lambda) \\ \cos(\lambda) & -\sin(\lambda) \end{bmatrix} \\
\frac{d^2R}{dt^2} &= \omega^2 \begin{bmatrix} -\cos(\lambda) & \sin(\lambda) \\ -\sin(\lambda) & -\cos(\lambda) \end{bmatrix} + \alpha \begin{bmatrix} -\sin(\lambda) & -\cos(\lambda) \\ \cos(\lambda) & -\sin(\lambda) \end{bmatrix}
\end{aligned} \tag{4.65}
$$

4.6.2 Cone-Surface Intersection: Improved

In section 4.5, the intersection point between two characteristic cones and a boundary surface was determined by approximating the surface locally as a plane. This approach was used by Sauerwein, but can be improved by including the higher order surface derivatives from the surface equation $\phi(x, y, t) = 0$, shown in equation 4.66. These are used to define the third rows (equation 4.67) of the 2nd order matrices in the calculation of the intersection point. This higher order method is used in this code for all surface points.

$$
\begin{aligned}
&\phi(x, y, t) = (\vec{r} - \vec{r}_t) \cdot \vec{n} = 0 \\
&\frac{\partial^2 \phi}{\partial x^2} = 0 \\
&\frac{\partial^2 \phi}{\partial y^2} = 0 \\
&\frac{\partial^2 \phi}{\partial t^2} = \vec{r} \cdot \frac{d^2\vec{n}}{dt^2} \\
&- \vec{n} \cdot \frac{d^2R}{dt^2}\vec{r}_t\prime - 2\frac{d\vec{n}}{dt} \cdot \frac{dR}{dt}\vec{r}_t\prime - \frac{d^2\vec{n}}{dt^2} \cdot R\vec{r}_t\prime \\
&- \vec{a}_0 \cdot \vec{n} - 2\vec{v}_0 \cdot \frac{d\vec{n}}{dt} - \vec{r}_0 \cdot \frac{d^2\vec{n}}{dt^2} \\
&\frac{\partial^2 \phi}{\partial x \partial y} = 0 \\
&\frac{\partial^2 \phi}{\partial x \partial t} = -\omega \cos(\lambda + \theta_{line}) \\
&\frac{\partial^2 \phi}{\partial y \partial t} = -\omega \sin(\lambda + \theta_{line})
\end{aligned} \tag{4.66}
$$

$$
\begin{aligned}
[A]^j_{i=3} &= \left[\frac{\partial^2\phi}{\partial x^2} \quad \frac{\partial^2\phi}{\partial x\partial y} \quad \frac{\partial^2\phi}{\partial x\partial t}\right] \\
[B]^j_{i=3} &= \left[\frac{\partial^2\phi}{\partial y\partial x} \quad \frac{\partial^2\phi}{\partial y^2} \quad \frac{\partial^2\phi}{\partial y\partial t}\right] \\
[C]^j_{i=3} &= \left[\frac{\partial^2\phi}{\partial t\partial x} \quad \frac{\partial^2\phi}{\partial t\partial y} \quad \frac{\partial^2\phi}{\partial t^2}\right]
\end{aligned} \tag{4.67}
$$

4.6.3 Surface Streamline Characteristic

The final flow property at the solution point once again comes from the remaining compatibility equation - the streamline. Using the velocity at b_4, a line is traced back to the time plane of the base points, as shown in figure 4.9. In general this point b_5 may not fall exactly on the surface line, due to the local curvature of the surface. Therefore the nearest point on the line passing through the outer points $B_1 - B_2$ is taken. The flow properties at this point are then linearly interpolated between the end states of this line. The flow velocity at b_5 may now be used to re-evaluate the streamline trace, now using the average velocity between b_4 and b_5, to improve accuracy. Finally, The pressure and temperature now available at b_5 are used to obtain the solution point temperature, using the isotropic relation in equation 4.37.

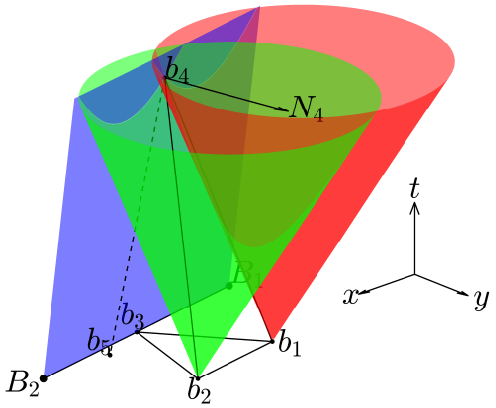


Figure 4.9: Surface streamline

4.6.4 Domain of Dependence

The inner base points used for the surface procedure are constructed from outer points B_1, B_2, B_3, B_4 as shown in figure 4.10. b_3 is taken at the midpoint between B_1 and B_2 on the line surface. Construction lines join it to B_4 and B_3. A circle of radius, less than $L_{12}/2$ is drawn around b_3. This radius must be less my some

factor, so that if the cell is skew, the lines B_{24} and B_{13} fall outside the domain of dependence of point b_4 - to theoretically satisfy the CFL condition. Points b_1 and b_2 are taken on the circle, where it intersects the construction lines. Properties at b_3 are linearly interpolated between B_1 and B_2 while properties at b_1 and b_2 are interpolated along $b_3 - B_3$ and $b_3 - B_4$ repsectively.

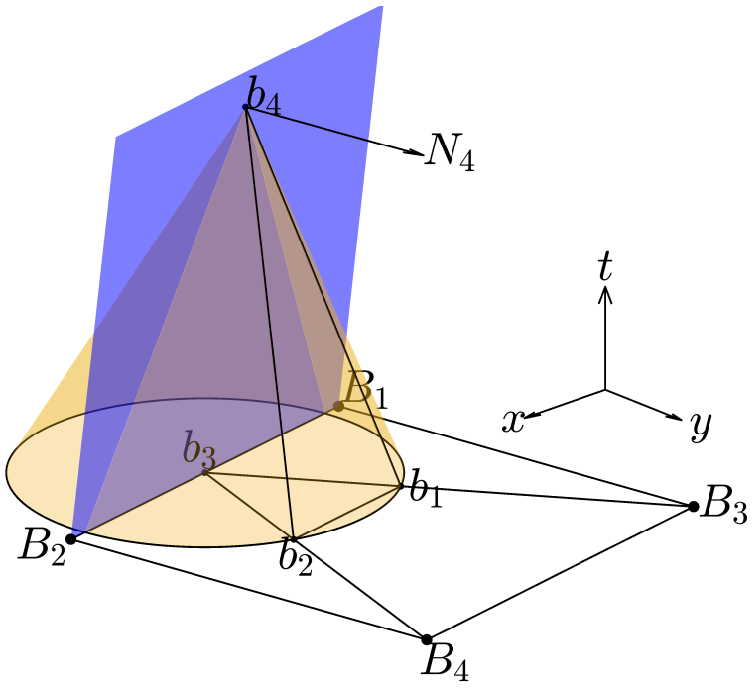


Figure 4.10: Surface domain of dependence

4.6.5 The Surface Procedure

The iteration procedure is essentially the same as the field procedure:

1. Given a rectangular element B_1, B_2, B_3, B_4, in figure 4.10, the inner base points are constructed and flow states are interpolated.

2. Cone characteristics through b_1 and b_2 are intersected with the surface passing through b_3 as described in section 4.5, including the higher order surface derivatives derived in section 4.6.2 for improved accuracy.

3. The cone basis vectors are found and compatibility coefficient matrices $[G]_i^q$ and $[H]_i^q$ are determined using these vectors and flow states at b_1 and b_2. The surface boundary condition at b_4 is then combined with the factorised compatibility equations $[G]_i^q[S_4]_q = [H]_i$, and the solution state at b_4 is determined by solving this linear set of equations.

4. The remaining flow state T_4 is determined from the streamline compatibility equation.

5. Accuracy of the procedure is improved by using average flow states along the cone lines for calculation of the intersection point and the coefficient matrices $[G]_i^q$ and $[H]_i^q$. e.g. $u_1^{(n+1)} = \left[u_1^{(0)} + u_4^{(n)}\right]/2$. Steps 2 to 4 are then repeated until the scaled changes in solution position and state become sufficiently small, as described in 4.4.4 for the field procedure.

4.7 Shock Points

The procedure for handling cells adjacent to shock boundaries is similar to the surface procedure except that instead of a boundary condition at point b_4, in figure 4.11, the Rankine-Hugoniot shock relations are used to relate flow properties behind the shock S_{4b} to the upstream flow properties S_{4a}. In the diagram, a shock wave, which is just a line in $x-y$ space, becomes a plane, or curved surface in x, y, t space. Assuming a constant, uniform upstream flow state, the strength and orientation of the shock at a given location (e.g. b_3) may be completely described by: its normal angle η_3 in the $x-y$ plane, measured counter-clockwise from the positive x-axis; and its velocity along this normal direction v_s. Equivalently, a three-dimensional normal vector ($\vec{N}_3$) in x, y, t space may describe the shock at this point: the projection of this vector onto the $x-y$ plane, gives the two-dimensional normal vector $\vec{n}_3$ with angle η_3, while the time component of this vector gives the (negative) shock velocity ($-v_s$), along the direction $\vec{n}_3$ as shown in equation 4.68. Where φ is defined as this time component of the shock normal. Now, the normal component of velocity incident on the shock wave v_a (in the reference frame of the shock) at b_4, required for the shock relations, can be given by equation 4.69. It will be negative in this case, but the shock relations are valid regardless of the sign of the incident velocity.

Note that the shock normal $\vec{N}$ changes between b_3 and b_4. In fact, the plane joining them is taken as having the averaged normal between them, which is a key aspect of finding the solution point b_4. In fact this whole procedure is really about determining the shock trajectory, rather than finding the flow state behind the shock at b_4 - since this flow state is simply given by the shock relations, once $\vec{N}_4$ is known.

The main step of the process is finding the shock normal $\vec{N}_4$ such that the flow properties behind the shock at b_4 satisfy the compatibility equations of the characteristic cones centered at field points b_1 and b_2. The average orientation of the shock plane between b_3 and b_4 is then updated, the new cone-shock intersection is found and

the process iterates until the changes in the solution point position and shock state convergence.The solution of the compatibility equations for the shock procedure is discussed in the following section. Note that for the shock procedure, the streamline characteristic is not required, since the temperature behind the solution point is also given by the shock relations.

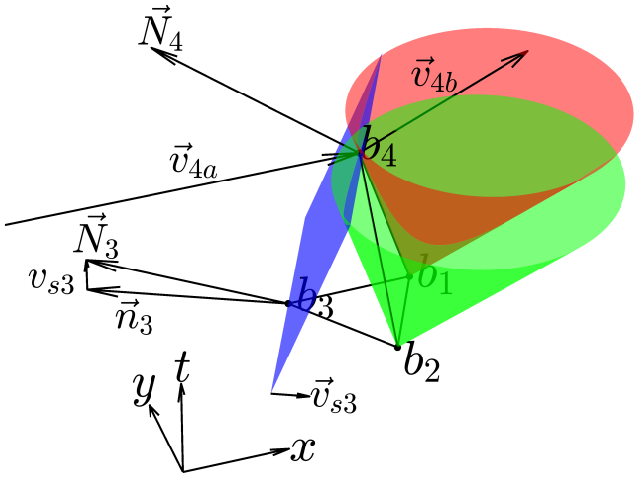


Figure 4.11: Shock geomtery

$$\vec{N} = \begin{bmatrix} \cos(\eta) \\ \sin(\eta) \\ -v_s \end{bmatrix} = \begin{bmatrix} \cos(\eta) \\ \sin(\eta) \\ \varphi \end{bmatrix}, (\varphi \equiv -v_s) \tag{4.68}$$

$$v_a = \vec{v}_{4a} \cdot \vec{n}_4 - v_s = \vec{v}_{4a} \cdot \vec{n}_4 + \varphi = u_\infty \cos(\eta) + v_\infty \sin(\eta) + \varphi = \vec{v}_\infty \cdot \vec{N}_4 \tag{4.69}$$

$$\vec{v}_{4a} = \vec{v}_\infty (upstream)$$

4.7.1 The Cone Compatibility Equations

As in the surface procedure, a set of two equations in terms of three flow state unknowns (u_4, v_4, p_4) can be obtained from the factorised form of the compatibility equations for the two field cones at b_1 and b_2 (figure 4.11): $[G]_i^q[S_4]_q = [H]_i, (i = 1, 2)$. In the surface procedure it was necessary to include an additional equation from the boundary condition in order to close these equations. However, in this case, the flow states u_4, v_4 and p_4 are not in fact independent: they depend on the shock normal $\vec{N}_4$, which only has two degrees of freedom (η and φ). Therefore, these are in fact two equations in two unknowns (η_4, φ_4). However, due to the non-linearity of the shock relations, this system is non-linear and thus cannot be simply inverted. Rather, the first and second order derivatives of these equations must be obtained

in terms of η and φ and will be used in Richmond's procedure to solve the system numerically.

The residual $[F]_i$ is defined in equation 4.70. The Jacobian and higher order derivative matrices are shown in equations 4.71 to 4.73. The derivatives of the residual with respect to the variables η, φ are simply transformed from the flow variable derivatives, using equation 4.70, as illustrated in equation 4.74. Richmond's procedure (section 4.3) may now be applied - shown in equation 4.75. Where the vector $[\chi]_i$ represents the two independent shock variables. To check convergence, the residual rows may be scaled by rows $[H]_i$, and compared independently to some error $\epsilon \approx 10^{-6}$.

$$[F]_i = [G]_i^q [S_4]_q - [H]_i \tag{4.70}$$

$$[J]_i^m = \begin{bmatrix} \frac{\partial F_1}{\partial \eta} & \frac{\partial F_1}{\partial \varphi} \\ \frac{\partial F_2}{\partial \eta} & \frac{\partial F_2}{\partial \varphi} \end{bmatrix} = \begin{bmatrix} \frac{\partial}{\partial \eta}[F]_i & \frac{\partial}{\partial \varphi}[F]_i \end{bmatrix} \tag{4.71}$$

$$[A]_i^m = \frac{\partial}{\partial \eta}[J]_i^m = \begin{bmatrix} \frac{\partial^2}{\partial \eta^2}[F]_i & \frac{\partial^2}{\partial \eta \partial \varphi}[F]_i \end{bmatrix} \tag{4.72}$$

$$[B]_i^m = \frac{\partial}{\partial \varphi}[J]_i^m = \begin{bmatrix} \frac{\partial^2}{\partial \varphi \eta}[F]_i & \frac{\partial^2}{\partial \varphi^2}[F]_i \end{bmatrix} \tag{4.73}$$

$$\frac{\partial}{\partial \eta}[F]_i = [G]_i^q \frac{\partial}{\partial \eta}[S_4]_q = [G]_i^q \begin{bmatrix} \frac{\partial u_4}{\partial \eta} \\ \frac{\partial v_4}{\partial \eta} \\ \frac{\partial p_4}{\partial \eta} \end{bmatrix} \tag{4.74}$$

$$\left[\Delta\chi^{(n+1)}\right]_m = -\left([J]_i^m + \frac{1}{2}\begin{bmatrix}[A]_i^m \left[\Delta\chi^{(n)}\right]_m & [B]_i^m \left[\Delta\chi^{(n)}\right]_m\end{bmatrix}\right)^{-1}[F]_i \tag{4.75}$$

$$[\chi]_m \equiv \begin{bmatrix} \eta \\ \varphi \end{bmatrix} \tag{4.76}$$

The derivatives of the flow variables u_4, v_4, p_4 with respect to η and φ are derived from the shock relations shown in equation 4.77, and finally equation 4.79. Where the subscripts a and b refer to flow states upstream and downstream of the shock wave respectively. An expression was derived for the downstream velocity vector $\vec{v}_{4b}$ (refer to figure 4.11) in the absolute reference frame in equation 4.78, by combining the downstream normal velocity vector (which is transformed via the shock equations) and the downstream tangential velocity ($\vec{v}_T$) (which is unchanged through the shock). Analytical expressions were developed for the derivatives of these equations with respect to the independent variables (η, φ), by successive application of the chain rule to these expressions; but they will not be shown here. Alternatively, these may be obtained by numerical differentiation.

$$
\begin{aligned}
p_b &= \frac{2\gamma M_a^2 - (\gamma - 1)}{\gamma + 1} p_\infty \\
T_b &= \frac{\left[2\gamma M_a^2 - (\gamma - 1)\right]\left[(\gamma - 1) M_a^2 + 2\right]}{(\gamma + 1)^2 M_a^2} T_\infty \\
v_b &= \frac{(\gamma - 1) M_a^2 + 2}{(\gamma + 1) M_a} a_\infty \\
M_a &= \frac{v_a}{a_\infty} \\
v_a &= u_\infty \cos(\eta) + v_\infty \sin(\eta) + \varphi
\end{aligned} \tag{4.77}
$$

$$
\vec{v}_{4b} = (v_b - \varphi)\,\vec{n}_4 + \vec{v}_T = \begin{bmatrix} (v_b - \varphi)\cos(\eta) + \sin(\eta)^2 u_\infty - \cos(\eta)\sin(\eta) v_\infty \\ (v_b - \varphi)\sin(\eta) - \cos(\eta)\sin(\eta) u_\infty + \cos(\eta)^2 v_\infty \end{bmatrix} \tag{4.78}
$$

$$
\begin{aligned}
\begin{bmatrix} u_4 \\ v_4 \end{bmatrix} &= \vec{v}_{4b} \\
p_4 &= p_b
\end{aligned} \tag{4.79}
$$

This method of solving the shock point state is modified from the approach used in the previous study. In Sauerwein's method, the compatibility equations were linearised and solved in terms of the x, y components of the solution shock normal $\vec{N}_4$. Implicitly it was assumed that these x, y components are independent, which is not actually true, since they can be parameterised in terms of the shock angle η in the x, y plane. The solution proceeded by linearising the compatibility equations in terms of these two components and solving them using a first order iteration scheme similar to Newton's method. The third shock normal component was updated at each iteration by enforcing that the shock normal has unit length. Although this method was does work, it has only first order convergence, and assumes an unrealistic independence of the normal vector components. Whereas, in this method, the shock normals are parameterised more naturally and the numerical solution scheme - Richmod's method - is theoretically third order in step size. This method is more stable and converges faster than the previous method.

4.7.2 Domain of Dependence

The shock element is defined by a rectangular element adjacent to the shock line, as shown in figure 4.12. The geometry and interpolations are the same as for the surface

element. However, since the shock line is generally curved, and the in-plane shock normals are known at the end points of the line B_{1-2}, a cubic spline interpolation is a more appropriate choice for obtaining b_3 and its normal, as shown in figure 4.13. The end normals $\vec{n}_1$ and $\vec{n}_2$ can be rotated 90° clockwise to obtain the tangents $\vec{u}_1$ and $\vec{u}_2$ (not shown), which give gradients for the spline boundary conditions. The spline may be defined in x, y coordinates, but better scaling is achieved by first transforming to the x', y' axis as shown. The cubic spline in equation 4.80 can now be solved for the x', y' coordinates of b_3 and its gradient, in equation 4.81, in terms of the length L and line gradients at the end points m'_1, m'_2 - which are transformed back to the x, y axis to obtain b_3 and its normal $\vec{n}_3$.

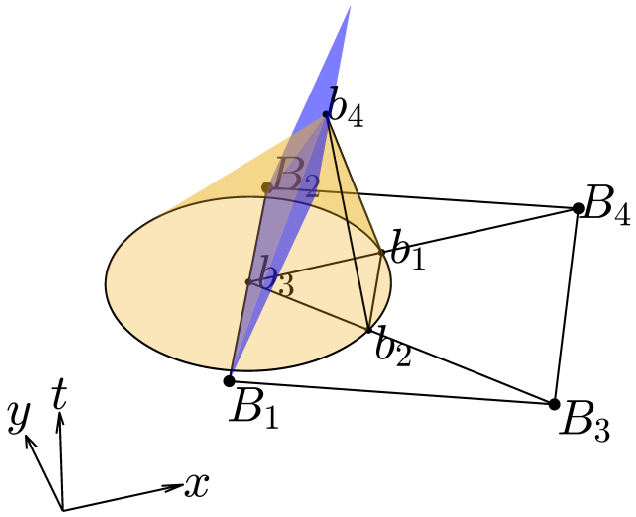


Figure 4.12: Shock domain of dependence

$$
\begin{aligned}
y' &= ax'^3 + bx'^2 + cx' \\
\frac{dy'}{dx'} &= 3ax'^2 + 2bx' + c \\
\begin{bmatrix} L^3 & L^2 & L \\ 0 & 0 & 1 \\ 3L^2 & 2L & 1 \end{bmatrix} \begin{bmatrix} a \\ b \\ c \end{bmatrix} &= \begin{bmatrix} 0 \\ m'_1 \\ m'_2 \end{bmatrix} \qquad (4.80) \\
L &= |\vec{B}_2 - \vec{B}_1| \\
x'_3 &= L/2 \\
y'_3 &= \frac{L}{8}\left(m'_1 - m'_2\right) \\
\left(\frac{dy'}{dx'}\right)_3 &= -\frac{1}{4}\left(m'_1 + m'_2\right) \qquad (4.81)
\end{aligned}
$$

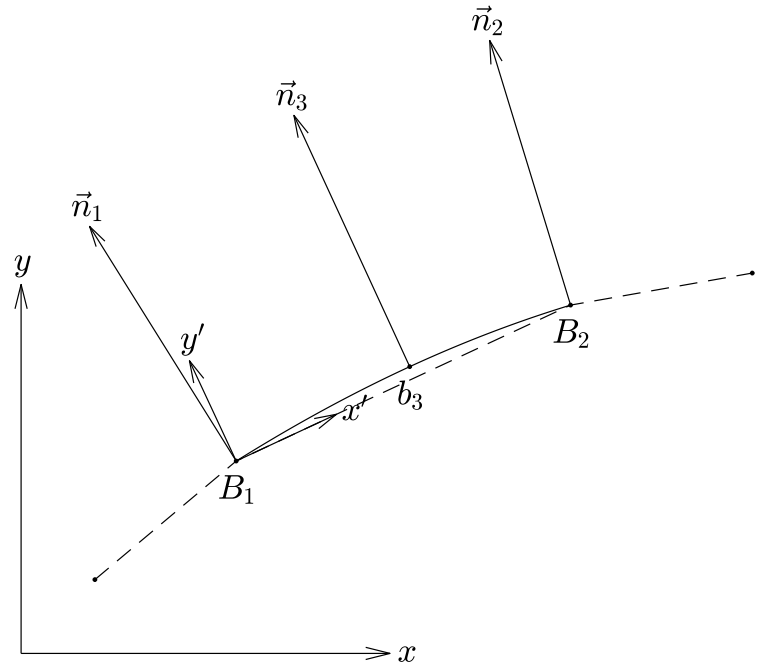


Figure 4.13: Shock line interpolation

4.7.3 The Shock Procedure

1. Given a rectangular element B_1, B_2, B_3, B_4 adjacent to a shock line in figure 4.12, inner points are constructed and corresponding flow properties are interpolated.

2. Cone characteristics through b_1 and b_2 are intersected with the shock plane through b_3 to obtain the solution point b_4.

3. The cone basis vectors are found and the derivative coefficient matrices $[G]_i^q$ and $[H]_i$ are determined using these vectors and the flow states at the cone base points. The factorised compatibility equation is then obtained. The first and second order derivatives of the residual $[F]_i$ are then obtained using the shock relations. Richmond's procedure is then used to solve the non-linear system for the shock state at b_4.

4. A new shock plane is defined, having the average normal between the shock base point b_3 and the solution point. i.e. $\vec{N}^{(n+1)} = \left[\vec{N_3} + \vec{N_4}^{(n)}\right]/2$. This new plane is used to re-evaluate the cone-shock intersection and the end shock state $\vec{N_4}$. Additionally, the derivative coefficient matrices are re-evaluated using the average flow properties along the bicharacterstic lines to improve the accuracy. This process is iterated until the changes in the shock solution state converge. In the limit, the shock plane joining the base and end shock points takes the average shock state between them.

4.8 Meshing and the Overall Program

The procedures required to obtain solution points stepped forward in time from the field, surface and shock elements have been described in detail. The code for these methods can be found in the *Digital Appendix*. The setup and meshing of the flow field domain, and the overall program flow will now be discussed. This setup will be limited to the case of a domain between an attached shock and a straight line surface, but virtually any type of line motion is allowed. The extension to curved surfaces and detached shock waves is not significantly more complex, but is outside the scope of the current study.

Consider some stage in the solution of a line surface accelerating vertically through a horizontal supersonic flow, where the shock line has already become curved, as shown in figure 4.14. A zoomed view shows more clearly the distinction between the triangular field elements, and rectangular surface and shock elements. Note that the mesh elements are be set to grow along the surfaces by some factor to allow greater resolution near the tip. In this case a bias factor of 2.5 between the first and last cell sizes was used. The points along the boundaries have been interpolated from the previous time step to evenly spaced positions, as will be discussed. The mesh is then built inwards from the boundaries in the following way:

1. A set of lines are displaced from the shock and surface boundaries by local normal boundary vectors, so that rectangular elements, required by the boundary procedures may be formed. Each of these rectangular elements are also subdivided to create additional field elements required to cover these regions.
2. Straight lines are drawn between corresponding points on the displaced boundary lines so that triangular field elements may be built between them.
3. These lines are then divided vertically into segments of side length approximately equal to the corresponding boundary element size. Adjacent lines are then triangulated along these divisions.

This procedure ensures good quality elements and allows full control over element size and growth factors. It is also quite efficient and is performed very rapidly compared to the solution time of each time step, even for fine meshes. This is crucial since the mesh must be rebuilt after each time step.

Once the mesh is built, the field, surface and shock methods are applied to all the elements in the domain to produce scattered solution points. The tip point

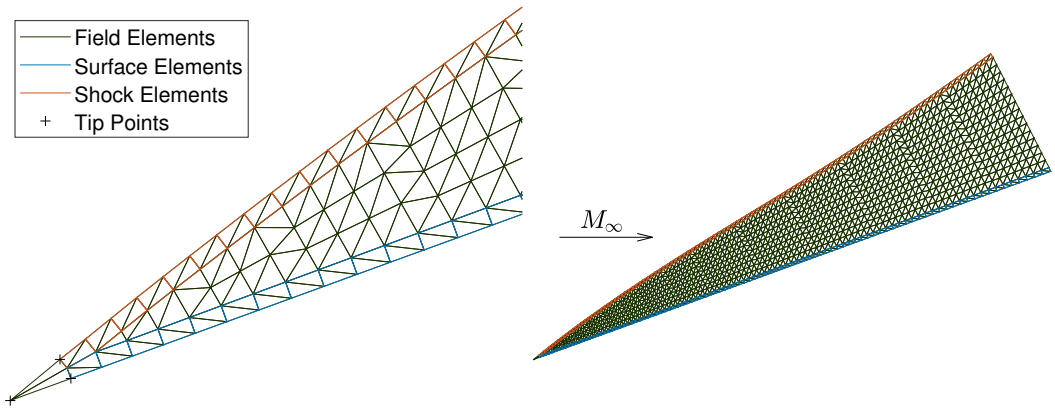
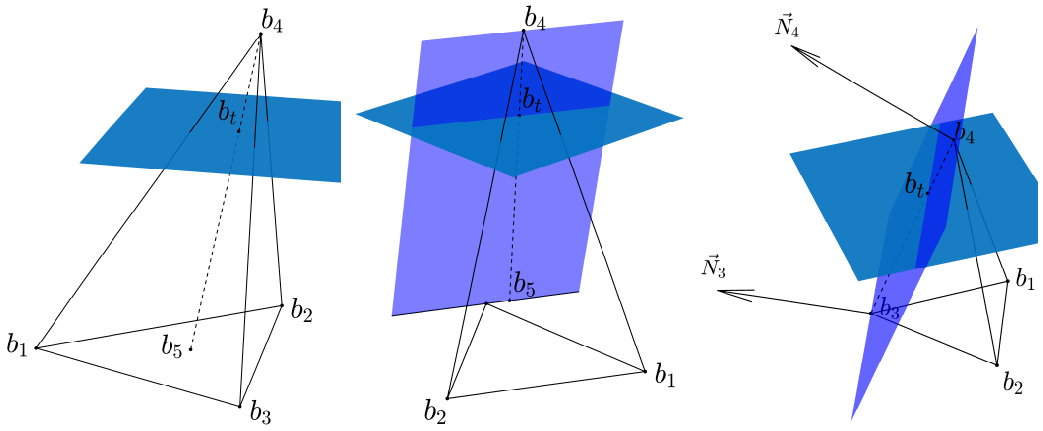


Figure 4.14: Method of characteristics mesh

boundary properties are calculated using the relative tip shock theory, described in section 3.3.5, which applies the oblique shock relations to the relative upstream flow conditions experienced by the moving tip.

The time step of each element depends on the cell dimensions, and local flow properties (they are obtained implicitly from the intersection of local characteristic surfaces) - so they are independent. Therefore, they must be interpolated to a common time plane. The global time step is taken as some factor of the minimum time step from all elements: $\Delta t_{global} = C \cdot \min(\Delta t_{domain})$, where C is defined as a global Courant number. Interpolation to the common time frame is then performed for all elements with $\Delta t > \Delta t_{global}$, as illustrated in figure 4.15. For field and surface cells, the intermediate point b_t is taken along the streamline; for shock cells, the intermediate shock point is taken along the line between the base shock point and solution point. Field and shock normals are interpolated linearly onto this plane.



(a) Field (b) Surface (c) Shock

Figure 4.15: Time plane interpolation

The scattered solution points, all at a common time frame, are shown in figure 4.16, over the current mesh. The surface and shock solution points appear to still lie on the previous boundaries - due to the scale. Zoomed views show the displacement of a surface and shock point upwards as the line accelerates.

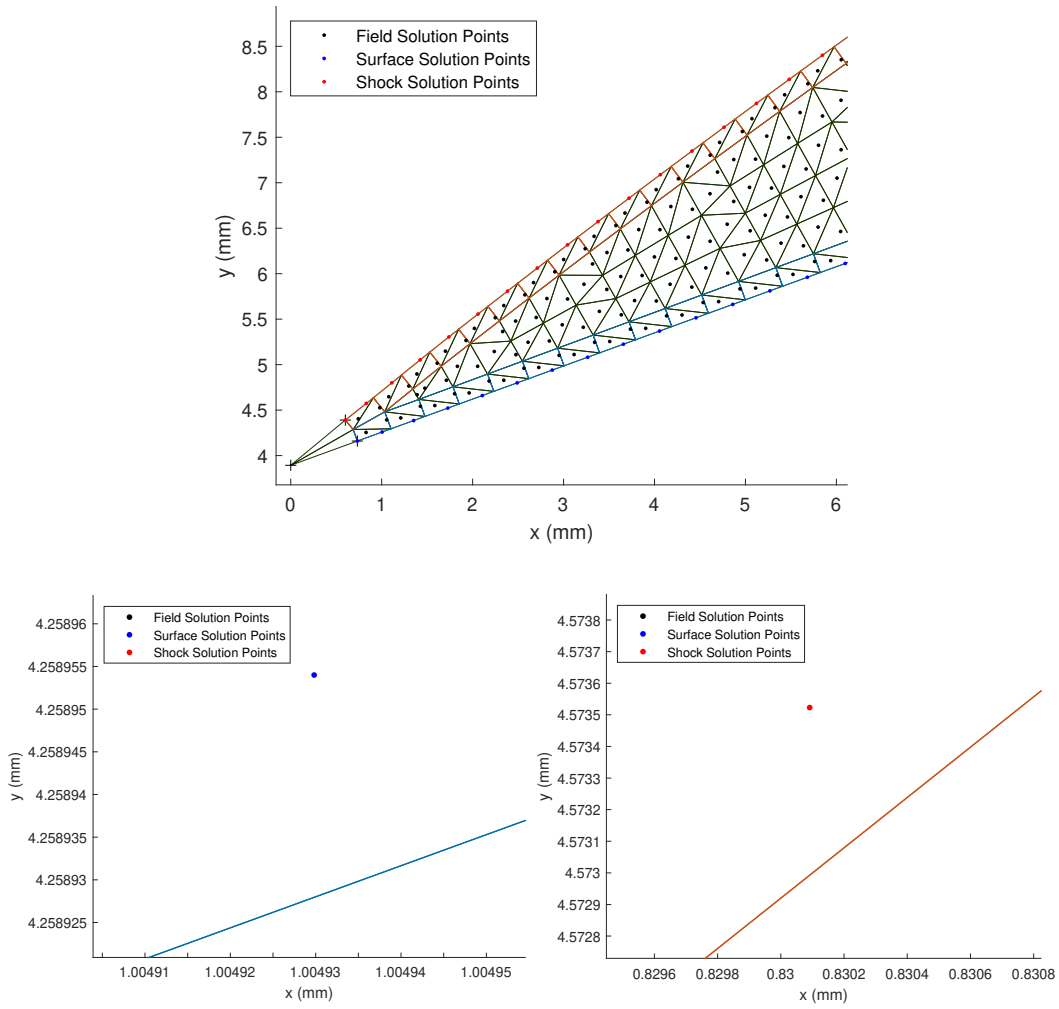


Figure 4.16: Scattered solution points

Once the new solution points are obtained, a new mesh must be built from the new boundary lines. This requires evenly distributed points on the new boundaries which are obtained in the following way:

1. Consider the scattered shock points. The distances between consecutive points may be numerically summed so that these positions may be parameterised in terms of curve length: A set of points (x_n, y_n) with corresponding curve lengths s_n will be available ($s = 0$ corresponds to the first shock point), and the line gradients at each of these points $\vec{u}_n$ are known - obtained by rotating the two-dimensional shock normals $\vec{n}_n$ 90° clock wise.

2. Now, cubic splines which match the shock points to the curve lengths are determined (a similar procedure was used in section 4.7.2) - such that the line gradients at each point are simultaneously matched. Cubic splines are used because they have exactly the number of degrees of freedom required to simultaneously match the shock location and gradient on either side of a shock segment.

3. Any point along the new curved shock line may now be obtained from the splines in terms of arbitrarily chosen curve lengths. i.e. $\vec{r}_{shock} = f(curvelength)$. A uniformly distributed curve length vector may be used to obtain the distributed points via the spline functions. The two dimensional normals of these shock points are obtained by rotating the corresponding spline gradients $\vec{u}$ 90° counter clock wise; while the time components of the space-time shock normal (φ) are interpolated linearly between the scattered solution points.

A similar process is performed for the surface points, such that the curve length distributions of the surface and shock line match. In this case, the surface points always lie on a straight line, so the curve length function f is linear. The surface flow properties u, v, p, T are interpolated linearly. The new mesh can now be built as described previously.

The final step is to interpolate the scattered solution data onto the new mesh field points in the domain. This is done using an inbuilt linear interpolation function in Matlab, which creates a Delaunay triangulation from the scattered points to interpolate to the new mesh points. This completes one time step. The process is then repeated to integrate the domain through time over the desired interval. Note that the use of linear interpolations may limit the accuracy of the scheme, but are used at present for simplicity. Future schemes should consider higher order interpolations. Additionally, since the flow is supersonic, it would be more appropriate to apply an upwind interpolation scheme - but since this code does not need to implicitly capture shock waves, this is not critical at present.

To initialise the domain, the oblique shock relations are applied to the initial surface angle for the given upstream Mach number, to obtain flow properties behind the shock. These properties are applied to all cells in the domain. The shock angle is used to construct the shock line (initially straight).

The exit boundary is not handled explicitly, as solution points just convect out of the domain (for supersonic flow) and are used to interpolate to the new mesh. However, since the time step of the domain is usually smaller than that of the large

cells near the end of the domain, interpolating the end cell solution points back to the global domain time plane may result in these points not exiting the domain. This means that the interpolation procedures must extrapolate to the new grid - which, it was found, may cause spurious flow gradients to propagate back into the domain, if not handled correctly. It was found that a nearest neighbor extrapolation produced relatively small errors and was used throughout for the exit boundary. Also, generally the domain was chosen to be somewhat longer than the domain of interest to avoid possible errors from this boundary.

Notice that except for updating the position of the tip, the surface motion is handled entirely by the surface function used by individual cells to find new intersection points - the new solution points at each surface cell are found intersection of the characteristic surfaces with the space-time evolution curve of the line surface. There is no need to explicitly update the surface cells in accordance with the line motion.

4.9 Validation and Performance

This code was used in the experimental investigation (section 3) to simulate rapid rotations of oblique shock wave domains. Although the experimental study was unable to provide sufficient resolution to directly validate this code, a degree of validation was obtained by comparison with a commercial Finite Volume (FV) code (which has been validated in many previous studies for many flow phenomena) - described in section 5. By comparing shock wave curvature, surface pressure variations and pressure contours throughout the domain, it was demonstrated that these codes showed significant agreement on the scale of the phenomena being studied. Additionally, these codes were compared in a parametric study, section 6, involving transverse linear accelerations of an oblique shock domain. Once again, the CFD codes showed significant agreement. The experimental case involved longer timescales with relatively gentle motions compared to the parametric study with highly intense accelerations and shorter timescales (which would be difficult to generate experimentally). Therefore, the MoC code was checked against the commercial code for strong and relatively weak dynamic effects.

Furthermore, the results from this code were generally significantly smoother than the FV results; due primarily to the effectiveness of shock fitting vs capturing for these relatively simple shock bound flow fields. The shock fitting of the MoC scheme precisely locates the shock points, resulting in smooth shock lines which are easily

extracted for post processing. Whereas for the shock capturing FV scheme, specialised post processing techniques were required to extract the approximate location of the shock points, which are inevitably noisy (jagged) compared to fitted shocks. Smoothing can be applied to the extracted shock points to reduce noise, but there is always the potential issue of introducing non-physical features through the smoothing process.

Additionally, the MoC code was less computationally expensive. The shock fitting of the MoC scheme avoided the large cell counts which result from fine cell refinement near shock waves needed for the FV shock capturing scheme. Also, in the MoC scheme, only the domain between the shock wave and surface is simulated; whereas in the FV scheme, a relatively wide domain must be included outside of this region - further increasing the cell count. To illustrate, simulation times are shown in table 4.1 for each code, simulating the same wedge motion for the same flow time, with similar sized cells within the surface-shock bound domain. The MoC code required about 20% less computational time for this particular case. These computations were performed on an Intel i7-950, 3.07GHz, 4-core, 8-thread processor, with 12 GB of RAM. The FV scheme required fewer time steps since the stability of its implicit time stepping allowed for relatively large time steps sizes. As mentioned, the cell count is far greater for the FV code due to the fine cell refinements required for shock capturing.

Table 4.1: CFD performance comparison

		FV	MoC
Cell Count		27,072	2,650
Time Steps		5,580	12,381
Simulation Time	hrs	10.53	8.60

4.10 Conclusions and Recommendations

The two-dimensional unsteady Method of Characteristics, modified tetrahedral network developed by Sauerwein was modified and applied to cases of rotating and linearly accelerating attached shock domains. The particular modifications were as follows:

1. The solution flow state was factorised out of the finite differences used for the transverse derivatives. In the original method, an initial estimate for the solution state was used to estimate these derivatives - which converged to the

upon iteration of the procedure. This modification resulted in a more stable and robust solution which converged significantly faster.

2. In Sauerwein's method, shock states were given an extra, unrealistic degree of freedom. A first order numerical solution method was used to solve the compatibility equations for two of these parameters, and the third component was corrected at each step by enforcing a unit length for the shock normal. Whereas, in this method, the shock states were paramterised in a manner more consistent with their degrees of freedom, and Richmond's third order iteration scheme was used to solve the nonlinear compatibility equations in terms of shock state parameters, which resulted in a more stable and robust convergence compared to the previous method.

3. The solution point intersections for the surface points were calculated with improved accuracy by including the higher order surface derivatives in the non-linear solution procedure.

4. The novel application of the method to an attached shock region was achieved by applying a relative motion oblique shock analysis to calculate the tip boundary properties.

The code was applied to cases of rapidly rotating and linearly accelerating attached shock domains and checked against a commercial Finite Volume code - generally demonstrating strong agreement on the scale of the dynamic features observed in these test cases. Additionally, the results produced by this MoC code for these cases were significantly smoother and obtained with less computational expense than the FV code. However, the MoC code was setup for a very specific type of problem - attached shock wave domains with flat surfaces, under the assumption of inviscid, adiabatic flow. It also cannot, at present, handle embedded shock waves which might form in the domain under extreme surface accelerations. Whereas the commercial FV code is easily adapted to complex geometries and model equations.

The improved results compared to the FV code were largely due to the shock fitting approach of the MoC method. Therefore, it is recommended that a Finite Volume shock-fitting method, such as the method of Paciorri et al. [13], is applied to these attached shock cases for comparison. Additionally, such an approach could facilitate the inclusion of viscosity to consider the effect of the wedge surface boundary layer on the attached shock wave and general fluid domain under accelerating surface motions.

The finite differences applied in this method were potentially second order in space and time due to the iterative convergence of the solution, using intermediate flow states. However, the true accuracy is difficult to evaluate owing to the complex nature of the solution process, and is not currently known. This point was noted by Sauerwein [1]. It is recommended that other MoC networks be considered, such as the pentahedral network by Butler et al. [20], which does indeed achieve higher accuracy; though with its own added complications.

Finally, it is recommended that the MoC method an application described here be extended to curved surfaces and detached shock waves. In fact the method may be extended to three-dimensional unsteady cases, as described by Sauerwein [1; 21].

5 Finite Volume CFD Setup

This section describes a finite volume (FV) density based Euler model developed in Ansys Fluent V19.2, which was used to simulate experimental profiles and compare with the Method of Characteristics code, developed for this investigation. The model geometry specified here is specific to the Experimental investigation (section 3), in which rotational motions of an oblique wedge are studied. However, the model is additionally used for a parametric numerical study for transverse linear wedge accelerations, in section 6 - where the wedge geometry is modified for a wider wedge angle. The methods described here are commonly used in the compressible fluid dynamics research community, and have been validated for many flow phenomena. Therefore, theoretical aspects in this section are not described in as much detail as the Method of Characteristics. Further theoretical details can be found in the following references [14; 15].

A structured mesh domain was constructed for a two-dimensional wedge geometry with a 50 mm chord length and 12° tip angle, shown in figure 5.1, with statistics shown in table 5.1. The domain size was kept relatively small, since the flow is always supersonic for these cases, and spurious features do not easily propagate back into the domain.

Table 5.1: Mesh statistics

Cell Size	0.5 mm
Number of Elements	$16,650$
Minimum Quality	94%
Maximum Skewness	7×10^{-2}

This scheme employs shock capturing, which naturally resolves shock waves through upwind discretisation. However, in order to achieve sufficiently fine shock wave resolution, cells near shock waves are refined at each time step. Dynamic mesh refinement was applied based on pressure and density gradients at each time step, to a maximum of three levels, as shown in figure 5.2. Specifically, cells with a gradient

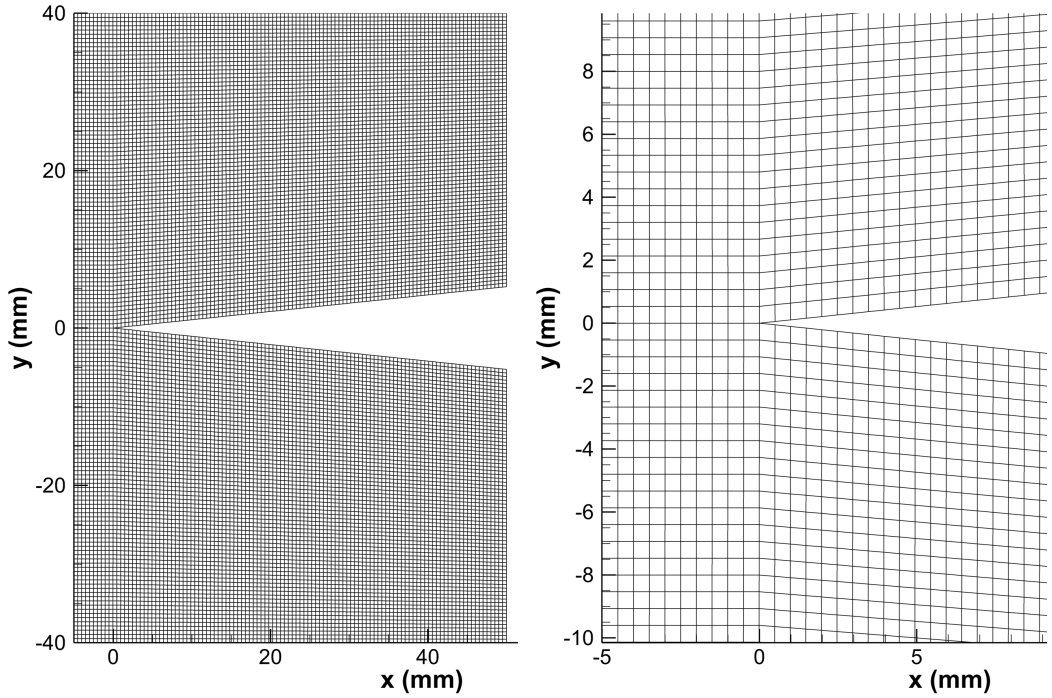


Figure 5.1: Finite volume mesh

magnitude above 70% of the maximum in the domain were marked for refinement, while those below 30% were marked for coarsening. The selections marked based on the pressure and density gradients are combined by a union operation. In this instance, a shock exists on the top surface and an expansion on the bottom due to the flow angle ($\approx -20°$).

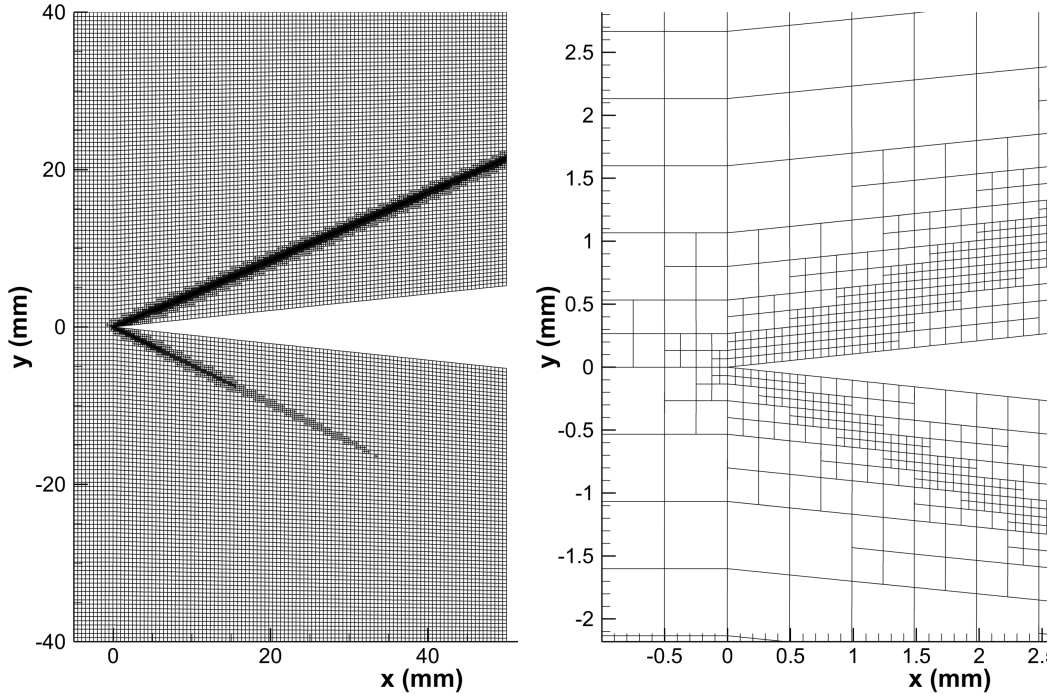


Figure 5.2: Dynamic adaption

5.1 Fluid Model

This is an Euler model, which ignores viscous terms and assumes the flow is adiabatic. The fluid (air) is modelled as an ideal gas with a specific heat ratio $k = 1.4$ and a gas constant $R_{air} = 287\ J.kg^{-1}.K^{-1}$.

5.2 Wedge Motion

The motion of the wedge was simulated by solving the equations in a non-inertial reference frame (see section 2.2). This allows arbitrary accelerating translations, rotations and curvilinear motions to be studied.

In Fluent, the Euler equations may be solved in a non-inertial reference frame which may independently translate with a velocity $\vec{V_t}$ with respect to the absolute reference frame, and rotate about its own origin with an angular velocity ω - both of which may vary arbitrarily in time. Accordingly, a relative frame velocity $\vec{U_r}$ relating the relative reference frame fluid velocity $\vec{V_r}$ and absolute reference frame fluid velocity $\vec{V}$ ($\vec{V_r} = \vec{V} - \vec{U_r}$) is defined in equation 5.1. Where $\vec{r}$ is the position vector in the relative reference frame, and the angular velocity vector $\vec{\omega}$ points in the z-direction (for a two-dimensional simulation in the $x - y$ plane). This transformation is used to transform the Euler equations.

Fluent has two formulations of the equations, absolute or relative: setting either the absolute or relative fluid velocity as the dependent variable in the momentum equation. Likewise the total energy density ρE is defined in the absolute or relative reference frame for the energy equation. For the density based solver, only the absolute formulation is available. The transformed equations with the absolute formulation are shown in equations 5.2-5.4 in matrix form, with velocities and the gradient operator defined as column vectors as shown in equation 5.5, and with the matrix transpose $\vec{V}^{\intercal}$ defined as usual. The total energy E and total enthalpy H are defined in equation 5.6. Note that the term $\rho\,\vec{\omega} \times \left(\vec{V} - \vec{V_t}\right)$ in the momentum equation is a source term representing both coriolis and centripetal acceleration. A translational velocity source term arises implicitly from the inclusion of the relative velocity vector $\vec{V_r}$ in the momentum equation. Likewise transnational and angular velocity source terms appear implicitly in the energy equation. These equations and the relevant theory are described in the Fluent 2020 R2 theory guide under the heading *Equations for a Moving Reference Frame*, which is also applicable to the

version 19.2 implementation. Unfortunately, this documentation is only available to licensed users.

Finally, the relative frame transnational and angular velocities may be set as constant or varied arbitrarily in time by a UDF. This non-inertial formulation allows a simple fixed mesh to be used for solving complex body motion problems - without the need for deforming meshes and excessively large domains.

$$\vec{U}_r = \vec{V}_t + \vec{\omega} \times \vec{r} \tag{5.1}$$

$$\frac{\partial \rho}{\partial t} + \left(\rho \vec{V}_r^{\intercal}\right) \bigtriangledown = 0 \tag{5.2}$$

$$\frac{\partial}{\partial t}\left(\rho \vec{V}\right) + \left(\rho \vec{V}\vec{V}_r^{\intercal}\right) \bigtriangledown + \rho \vec{\omega} \times \left(\vec{V} - \vec{V}_t\right) = - \bigtriangledown p \tag{5.3}$$

$$\frac{\partial}{\partial t}\left(\rho E\right) + \left(\rho \vec{V}_r^{\intercal} H + p \vec{U}_r^{\intercal}\right) \bigtriangledown = 0 \tag{5.4}$$

$$\vec{V} = \begin{bmatrix} u \\ v \end{bmatrix}, \ \bigtriangledown = \begin{bmatrix} \frac{\partial}{\partial x} \\ \frac{\partial}{\partial y} \end{bmatrix} \tag{5.5}$$

$$E = e + \frac{|\vec{V}|^2}{2}, \ H = E + \frac{p}{\rho} \tag{5.6}$$

5.3 Boundary Conditions

For all cases, a constant supersonic flow was created at the far-field (non-reflecting) boundary around the whole domain. This involves setting static pressure and temperature conditions along with the Mach number and flow direction. For a non-inertial frame case, there is no need to modify the boundary conditions so long as the frame is not rotating and the conditions are set as absolute (in the absolute reference frame). However, if the reference frame is rotating, it is necessary to update the flow direction at the boundary as the orientation of the domain changes with respect to the absolute reference frame - by trial and error, it was found that Fluent does not automatically perform this operation. This is achieved by dynamically updating the boundary flow direction with a UDF.

5.4 Solution Formulation and Methods

The coupled, conservation equations in integral form are discretised for this setup in a dual-time implicit formulation, which is second order in time. Dual time meaning that a pseudo time derivative is introduced to the equations, which when calculated to convergence in pseudo time, produces a time step in real time - with 2nd order accuracy in time step size. Implicit because the integration in pseudo time is performed implicitly (it depends on flow properties at future time steps). This implicit formulation results in a stable solution, even for large time steps (Courant Number > 1). Critically, it allows large time steps with respect to the CFL time step of the fine adapted cells near the shock wave - without this, the number of time steps required, and the computational time would be excessive.

The solver stores and computes flow variables at cell centres. Therefore, flow variables required at the cell faces, for the flux terms, must be interpolated/extrapolated. A third order MUSCL scheme was used for this, which combines a central difference and 2nd order upwind scheme. It provides improved resolution of shock discontinuities compared to the purely 2nd order upwind scheme, though it may produce over and undershoots, as its implementation in Fluent does not include a flux limiter. But this was found not to be a major issue.

The flux vectors were calculated using the AUSM+ scheme, which extrapolates convective and pressure fluxes based on local characteristic speeds and directions. This scheme provides accurate resolution of shock waves without oscillations.

5.5 Shock Extraction - Post Processing

In order to compare the shape of shock waves from the Finite Volume results with the Experimental and Method of Characteristics results, it was necessary to first extract points along the shock waves, since the this code employs shock capturing scheme and therefore does not store the precise location of shock wave boundaries. The process of extracting the shock curves will now be described. The processing was performed in Matlab, using after results were exported from Fluent. Consider the scattered data near an attached shock wave in figure 5.3. This shock is relatively straight, but this method is applicable to highly curved shock waves. The shock extraction process now proceeds as follows:

1. Points with a high pressure gradient magnitude were selected (in red): $\left|\left(\frac{\partial \rho}{\partial x}, \frac{\partial \rho}{\partial y}\right)\right| / max >$ 30%. This limit was set low so that even weak shocks could be captured.

2. A smooth curve is then fit through these points, using the method described in section 3.3.6.

3. Using this curve, and normal vectors along its length, a bounding box is created around the shock, as shown in figure 5.4. Within this box, a scattered linear interpolant was generated - which consists of a Deluanay triangulation built with the scattered points, used to interpolate linearly to query points as required. This is a built-in Malab function. Of course, the original mesh from Fluent could have been used, but it was simpler to use the built in method with scattered points.

4. Perpendicular line queries are then created across the interpolation region, as shown in figure 5.5a. The distance between each query point along these lines is chosen to be approximately 5% of the minimum adapted cell size. Finally, the positions of maximum pressure gradients across each of these lines are collected, as shown in figure 5.5b - these are the shock points.

These discrete shock points will inevitably include noise due to the imprecise location of shock points from shock capturing scheme.

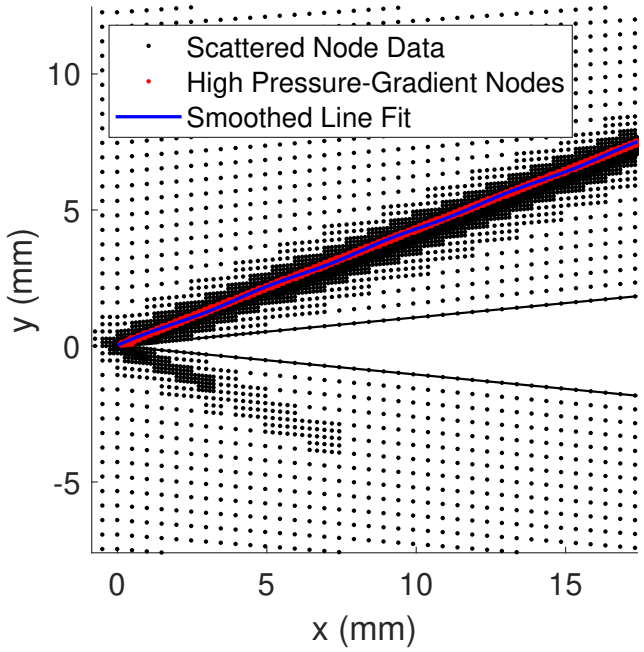


Figure 5.3: Finite volume shock capturing

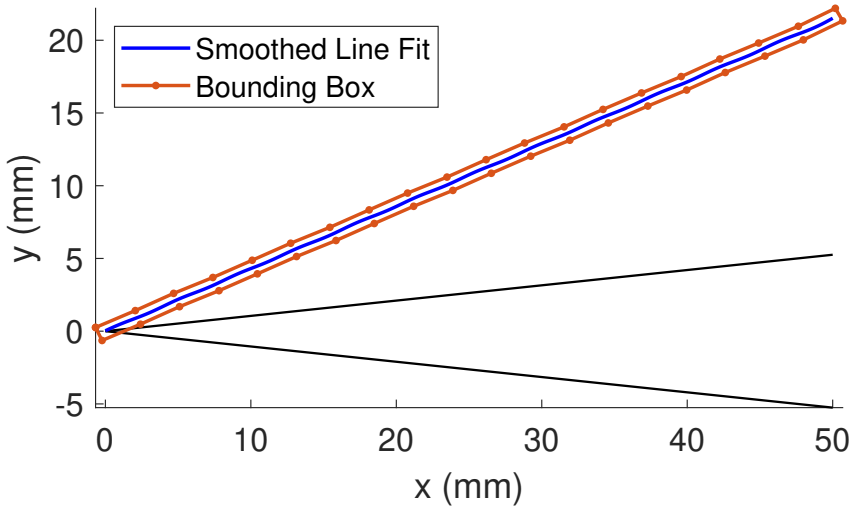
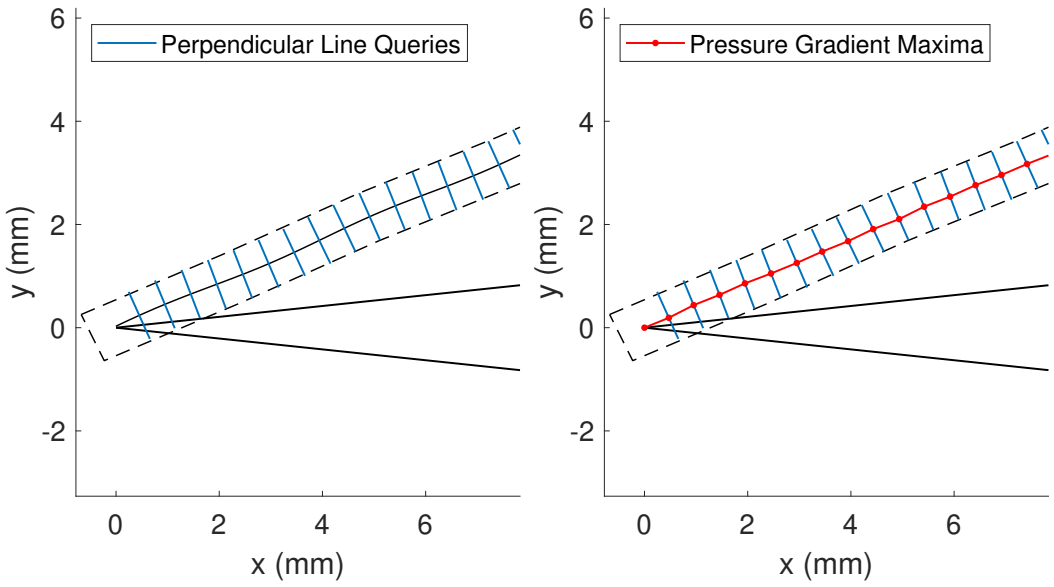


Figure 5.4: Bounding box



(a) Shock line queries

(b) Shock points

Figure 5.5: Shock point capturing

6 Linear Acceleration - Parametric CFD Study

A relatively simple linear acceleration case was selected for a parametric study to investigate transverse accelerations (perpendicular to the free stream airflow) of an attached oblique shock wave domain, and compare results between the Method of Characteristics (MoC) and Finite Volume (FV) codes described in sections 4 and 5 respectively. These cases are simultaneously used to check mesh independence.

The setup is a steady horizontal supersonic flow impinging on a wedge at an angle of incidence $\theta_s = 20^\circ$ to the flow (kept constant), while the wedge accelerates vertically. The problem is non-dimensionalised using terms from the unsteady Euler equations in a linearly accelerating (constant acceleration in one direction) non-inertial reference frame (as described section 2.2). The non-dimensional terms are the upstream Mach number $M_\infty = \frac{V_\infty}{a_\infty}$, linear acceleration parameter $Q = \frac{La_y}{V_\infty^2}$ (where a_y is the vertical acceleration) and the Strouhal number $S_t = \frac{V_\infty \mathcal{T}}{L}$. A length scale L is taken as the surface length ($50\ mm$) and a time scale $\mathcal{T}$ is defined by setting $S_t = 1$ for all cases, so that $\mathcal{T} = \frac{L}{V_\infty}$. This is the time taken for fluid to convect along the surface. All lengths and times will be scaled by the corresponding scales $\hat{x} = \frac{x}{L}, \hat{y} = \frac{y}{L}$, $\hat{t} = \frac{t}{\mathcal{T}}$. Additionally, the flow properties are normalised by the upstream conditions. In particular $\hat{p} = \frac{p}{p_\infty}$. Where the upstream static pressure and temperature are kept constant at $p_\infty = 10^5\ Pa$ and $T_\infty = 300\ K$ respectively.

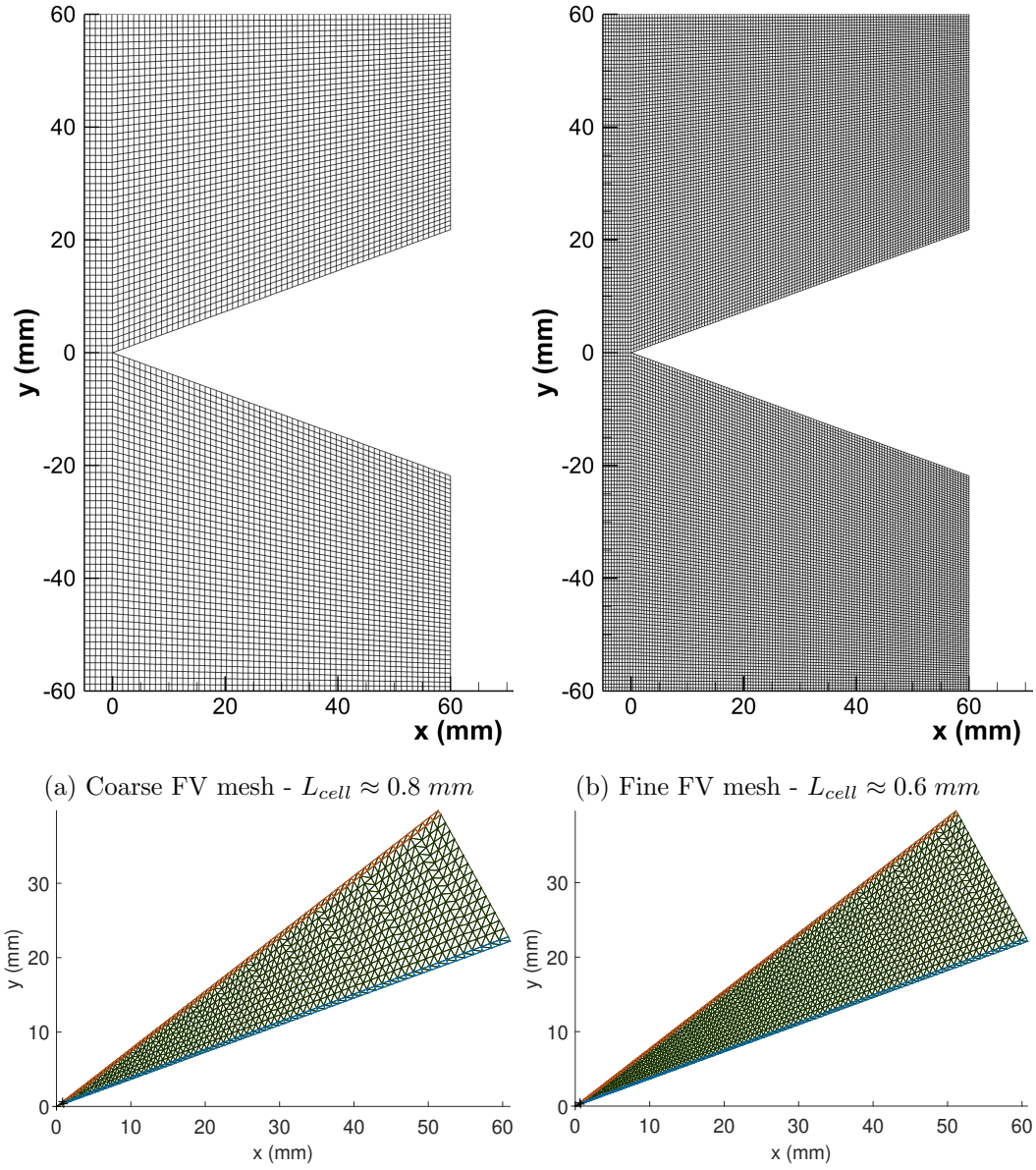
The meshes used in the CFD codes have a particular dimensional length scale. However, the solutions will be presented in non-dimensional terms and should be identical for dynamically similar cases. The finite volume mesh, in figure 6.1 is setup so that the half angle of the wedge is equal to the surface angle 20°. This allows the top and bottom surfaces to be used simultaneously to study positive and negative accelerations ($Q > 0$, $Q < 0$). The bottom surface solutions are reflected so that all results are presented for an upward facing wedge. Fine and coarse meshes are shown, which are used to test mesh Independence. For the FV

code, the vertical acceleration of the non-inertial reference frame is passed to the solver by a UDF which increases the translational frame velocity $\vec{V}_t$ (defined in section 5.2) linearly from rest according to: $\vec{V}_t = (0, a_y)\, t$. Note that the domain size is longer than the domain of consideration (surface length $L = 50mm$), to avoid potential spurious features from the outlet (particularly for the MoC code which uses a central interpolation scheme). Sample setup files for the Finite Volume code, linear acceleration case are available in the *Digital Appendix*.

The MoC, fine and coarse meshes are also shown. The MoC code solves the domain in the absolute reference frame, so the fluid domain will move up or downwards as the wedge accelerates. However, all comparisons are made in the relative frame, fixed to the wedge. Mesh metrics for the coarse and fine MoC and FV meshes are shown in table 6.1. The total cell counts after adaptive cell refinement are shown for the FV mesh. The time step size for the FV meshes were based on a Courant number slightly greater than 1, based on the original cell size - before adaption. The high stability of the implicit dual time stepping method for this code allowed large time steps compared to the CFL time step of the fine, adapted cells. Whereas, the MoC code demands a Courant number $C \leq 1$ for the smallest cell time step. However, since the MoC code does not require adaption for the shock wave, the time step sizes were not impractically small.

Table 6.1: Mesh metrics

		# Cells	# Cells (Adapted)	Time Step
FV	Coarse	6,432	15,324	10^{-7}
	Fine	17,760	38,822	10^{-7}
MoC	Coarse	1,575		9.74×10^{-8}
	Fine	2,680		7.38×10^{-8}



(a) Coarse FV mesh - $L_{cell} \approx 0.8\ mm$

(b) Fine FV mesh - $L_{cell} \approx 0.6\ mm$

(c) Coarse MoC mesh - $L_{cell} \approx 0.7\ mm$

(d) Fine MoC mesh - $L_{cell} \approx 0.5\ mm$

Figure 6.1: Finite Volume (FV) and Method of Characteristics (MoC) meshing

6.1 Mesh and Solver Independence

In order to compare the MoC and FV models and obtain mesh Independence, a set of cases were compared for positive and negative accelerations $|Q| = 0.2304$ ($|a_y| = 5 \times 10^6\ m/s^2$) and an upstream Mach number $M = 3$; the setup parameters are shown in table 6.2.

Table 6.2: Flow conditions

Mach Number M_∞		3
Static pressure P_∞		10^5 Pa
Static temperature T_∞		300 K
Surface Length L		50 mm
Time Scale $\mathcal{T}$		$4.80 \times 10^{-5}\ s$
Vertical Acceleration	Q	± 0.2304
	a_y	$\pm 5 \times 10^6\ m/s^2$

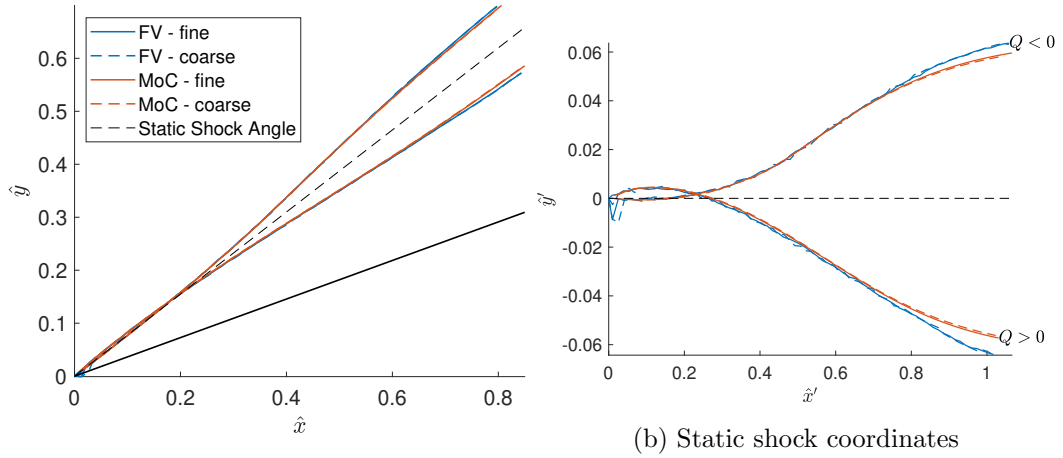
At time $\hat{t} = \frac{t}{\mathcal{T}} = 1$, solution shock lines are shown for positive and negative accelerations in figure 6.2. The shock lines are shown in the relative coordinate system (x, y-axis) and in a rotated coordinate system, aligned with the theoretical shock solution angle for a stationary wedge - which highlights deviations in the shock wave from the steady state solution. For this extreme acceleration, the shock is strongly curved. Accelerating upwards causes the shock to curve downwards, and visa versa - so that the shock effectively lags the motion of the tip. Immediately it should be clear that mesh independence is demonstrated for each code - the fine verses coarse mesh solutions are virtually indistinguishable. Additionally, the codes show good agreement with each other, demonstrating solver independence. There is however, some disagreement in the shock curvature towards the tail - which cannot be accounted for at this time.

These shock solutions have been superimposed to highlight and compare features, but in the absolute reference frame, the tails of these shock waves would align (rather than the tips) - since the surface would actually be moving up or downwards, and the tail portion of the shock is the last to receive the information of the surface disturbance.

Interestingly, the positive acceleration shock wave ($Q > 0$) starts inclined with respect to the stationary solution before curving downwards, and vise versa for ($Q < 0$). This is due to the relative velocity of the tip with respect to the upstream flow, as discussed in section 3.3.5 - the relative upstream conditions seen by the tip

(for $Q > 0$) are inclined at a steeper angle and at higher Mach number compared to the steady case; thus, the shock solution in the limit of the tip produces a steeper shock angle.

Generally, the MoC shock waves are significantly smoother - largely due to the shock fitting method - compared to the FV results, which uses shock capturing. Note the spurious deviation of the shock wave in the FV results near the tip - due to the imprecise position of the captured shock; although the post processing shock extraction method may also be to blame.

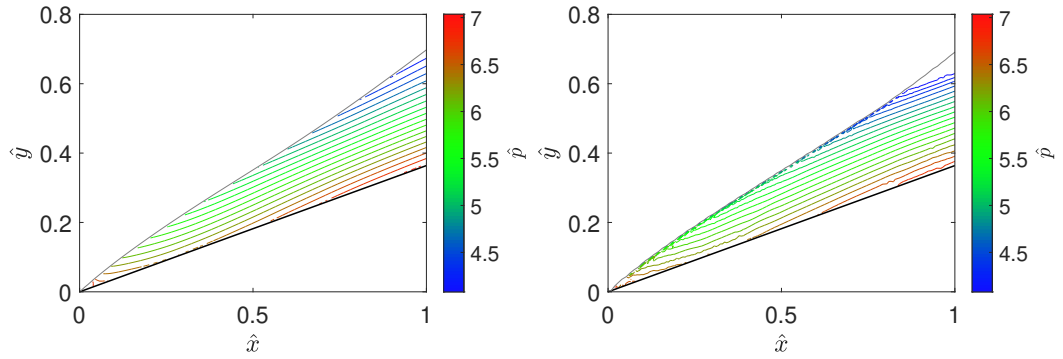


(a) Relative - wedge coordinates

(b) Static shock coordinates

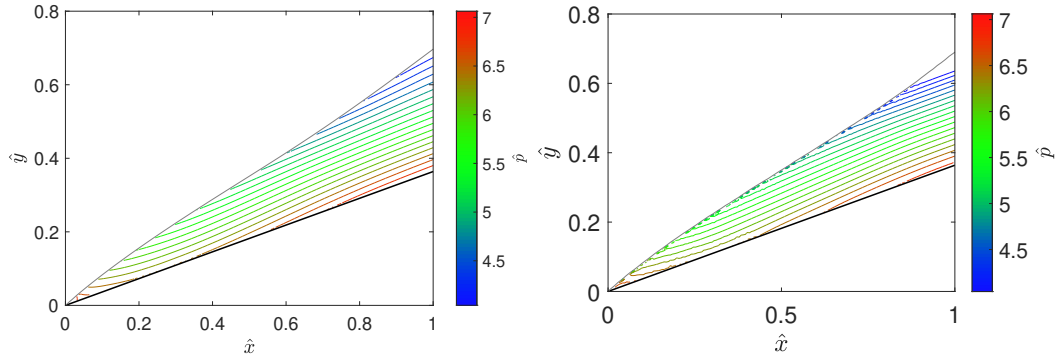
Figure 6.2: Captured shock independence

Pressure contours (normalised pressure $\hat{p} = \frac{p}{p_\infty}$) are shown comparing solvers, meshes and acceleration directions in figure 6.3. When the surface accelerates upwards, compression waves propagate into the flow, increasing pressure. These compression waves interact with the incident shock wave, causing it to curve. In the opposite sense ($Q < 0$), expansion waves propagate from the bottom surface. Once again mesh and solver independence is demonstrated.



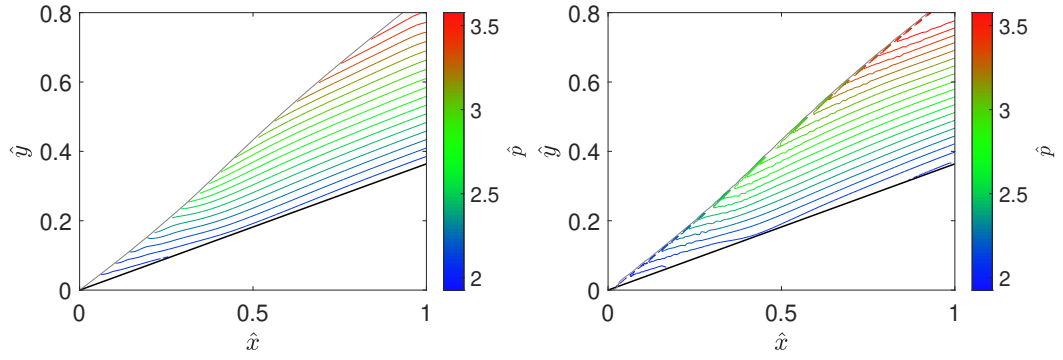
(a) MoC - coarse - $Q > 0$

(b) FV - coarse - $Q > 0$



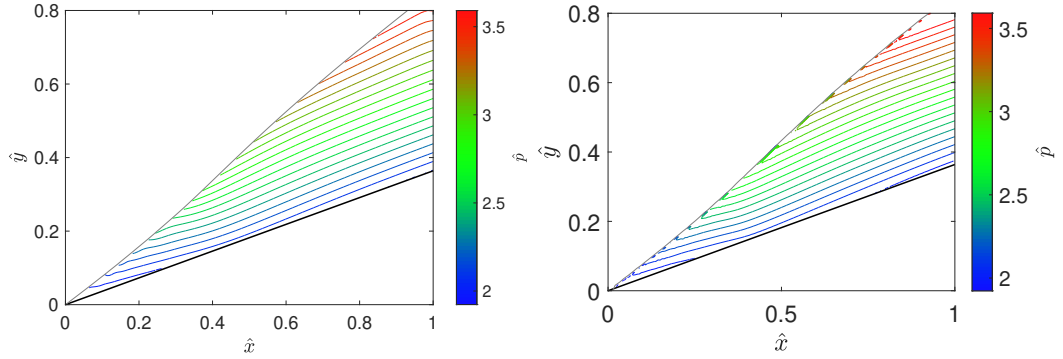
(c) MoC - fine - $Q > 0$

(d) FV - fine - $Q > 0$



(e) MoC - coarse - $Q < 0$

(f) FV - coarse - $Q < 0$



(g) MoC - fine - $Q < 0$

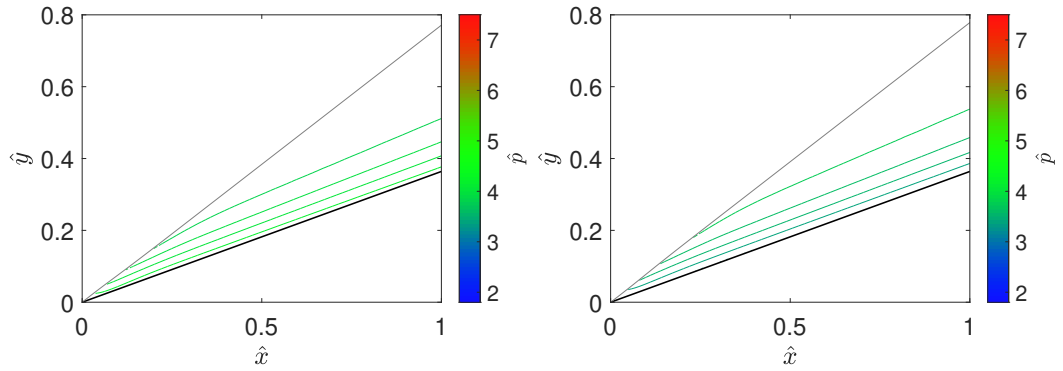
(h) FV - fine - $Q < 0$

Figure 6.3: Normalised pressure contours - CFD code comparison

6.2 Flow Field Evolution

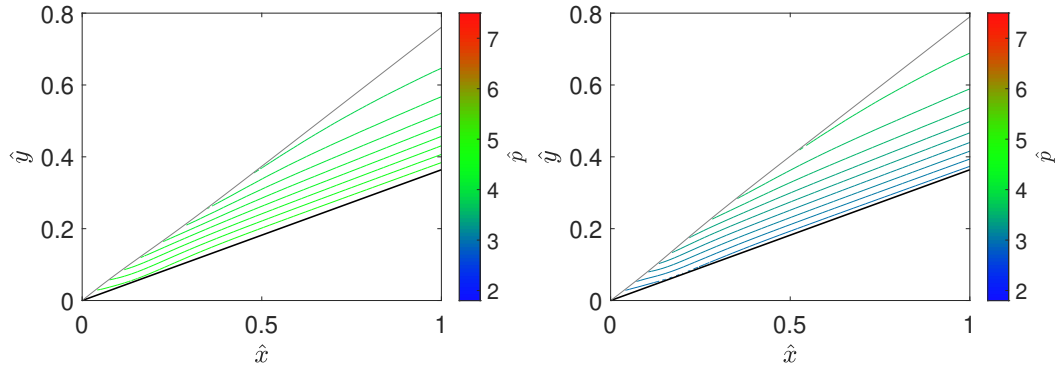
The evolution of the flow field for the same case, table 6.2, is shown in a series of pressure contours, from the MoC results, comparing positive and negative accelerations at corresponding times $\hat{t} = 0.2, 0.4, 0.6, 0.8$ in figure 6.4. These contours demonstrate more clearly the generation of compression ($Q > 0$) and expansion waves from the surface ($Q < 0$). Note how the contours become particularly curved near the tip, where the conditions become dominated by the limiting shock solution condition. Whereas, further from the tip, the contours appear parallel to the surface, indicating dominance of the transverse surface acceleration, which generates waves in this direction. This combined dependence on the tip effect, which is a function of relative velocity, and the surface pressure waves, which are a function of acceleration, is interesting, and may be worth studying in greater detail in future. Additionally, there is the interaction of the pressure waves with the entire shock boundary, which is expected to produce non-linear responses particularly for strong surface pressure waves.

The corresponding evolution of the shock curvature is demonstrated in figure 6.5, in the theory line coordinates. Starting from the static oblique shock solution ($\hat{y}' = 0$) at $\hat{t} = 0$, the shock curvature lags the motion of the tip as the delayed disturbances from the accelerating surface reach points further along the shock at later times. The apparent symmetry above and below the static shock line for opposite accelerations is somewhat trivial - it effectively represents the motion of the wedge in opposite directions, which is symmetrical. Therefore the movement of the shock tip is guaranteed to move by the same vertical displacement in opposite directions; while for both cases, the tail is still approximately in the original stationary shock position, as the surface disturbances only reach it shortly before $\hat{t} = 1$.



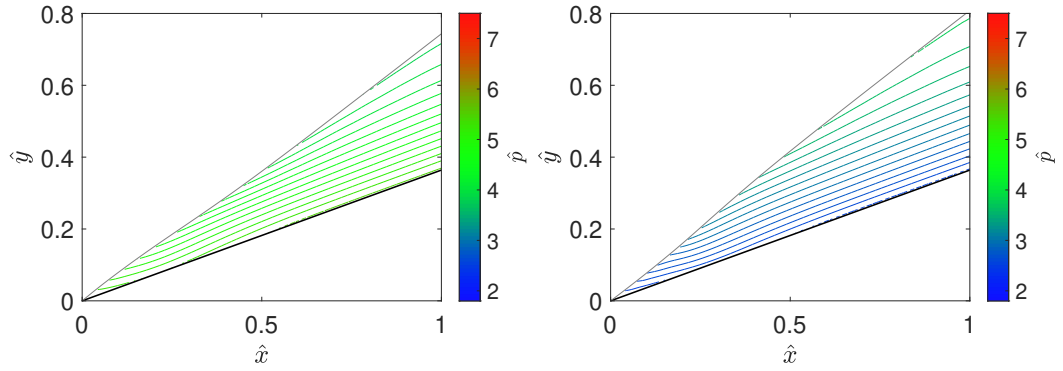
(a) $Q > 0$, $\hat{t} = 0.2$

(b) $Q < 0$, $\hat{t} = 0.2$



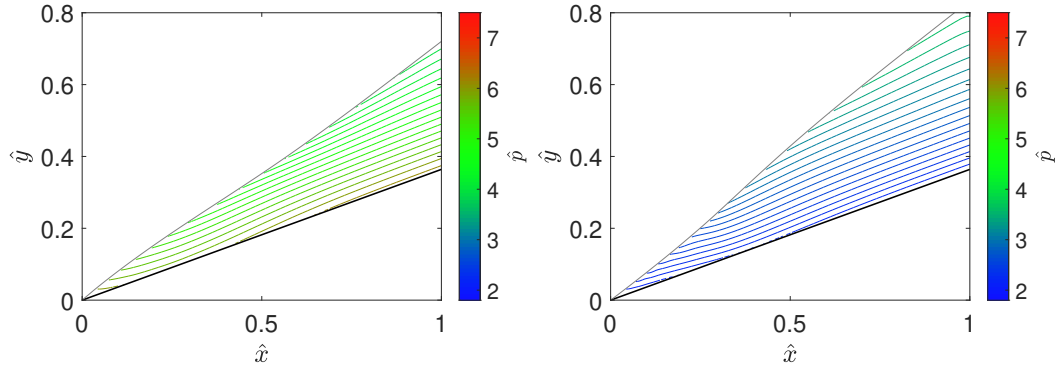
(c) $Q > 0$, $\hat{t} = 0.4$

(d) $Q < 0$, $\hat{t} = 0.4$



(e) $Q > 0$, $\hat{t} = 0.6$

(f) $Q < 0$, $\hat{t} = 0.6$



(g) $Q > 0$, $\hat{t} = 0.8$

(h) $Q < 0$, $\hat{t} = 0.8$

Figure 6.4: Evolving pressure contours

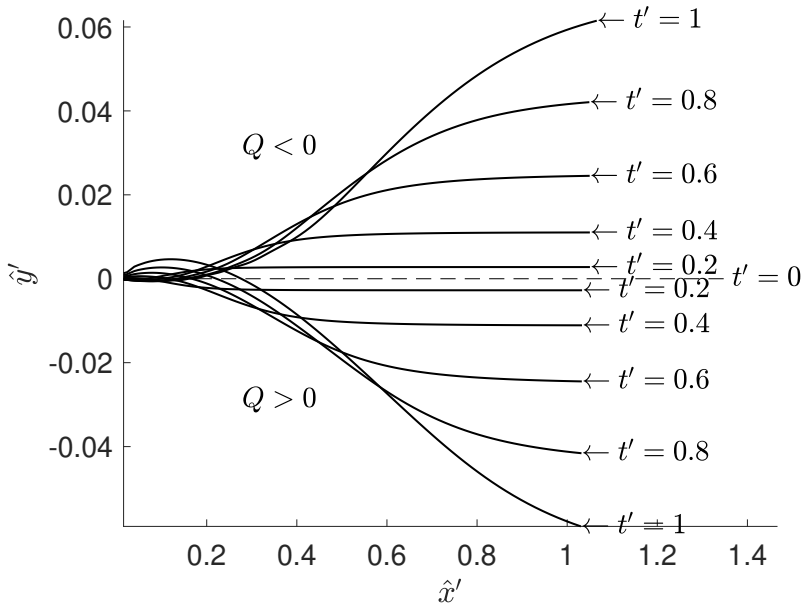
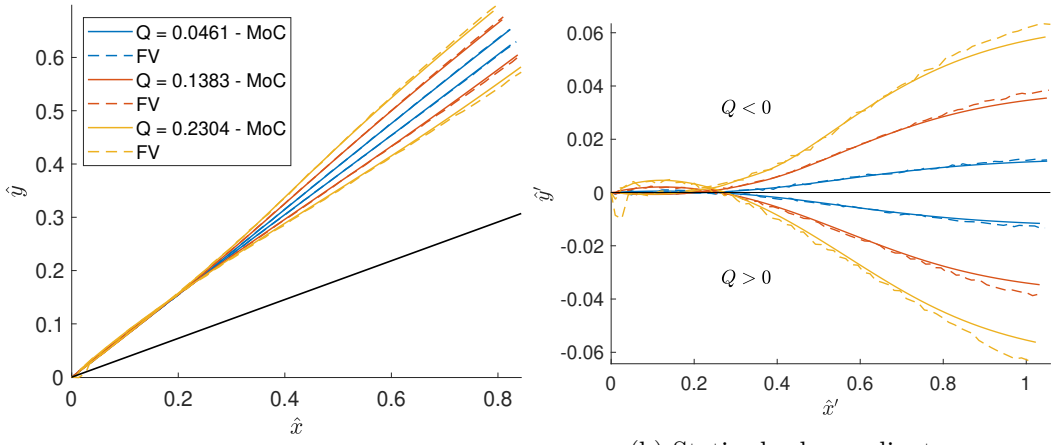


Figure 6.5: Evolution of shock curvature

6.3 Varying Acceleration

The effects of varying the time coordinate of the solution has been demonstrated. Now, a set of results at the same time ($\hat{t} = 1$), will be compared for a varying positive and negative accelerations, and then varying Mach number. To vary the acceleration parameter Q, only the vertical acceleration $a_y = \pm[1, 3, 5] \times 10^6\ m/s^2$ is varied, keeping all other parameters constant.

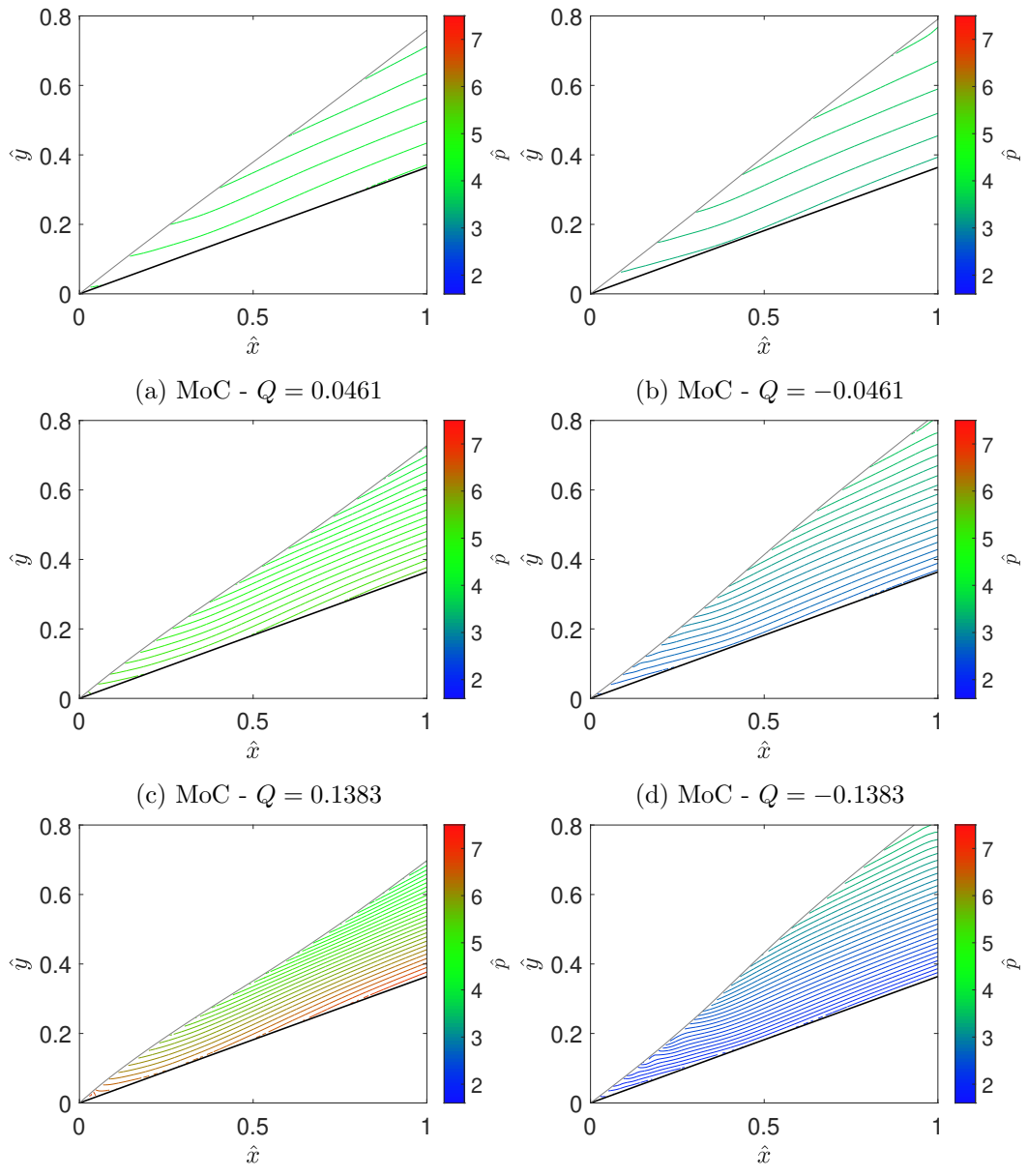
Consider the shock waves captured in figure 6.6. These results unsurprisingly demonstrate increasing shock curvature for increasing acceleration magnitude - as the shock wave curvature lags to a greater extent behind the more rapid movement of the wedge from its initial position. Once again the CFD codes show agreement; except for some deviation near the tails of the shock waves. Corresponding pressure contours are shown for the MoC results in figure 6.7. The contours clearly demonstrate the increasing strength of compression ($Q > 0$) and expansion ($Q < 0$) waves for increasing surface acceleration. However the overall shape of the pressure gradients does not appear to change significantly with increasing acceleration magnitude over this range.



(a) Relative - wedge coordinates

(b) Static shock coordinates

Figure 6.6: Varying acceleration



(a) MoC - $Q = 0.0461$

(b) MoC - $Q = -0.0461$

(c) MoC - $Q = 0.1383$

(d) MoC - $Q = -0.1383$

(e) MoC - $Q = 0.2304$

(f) MoC - $Q = -0.2304$

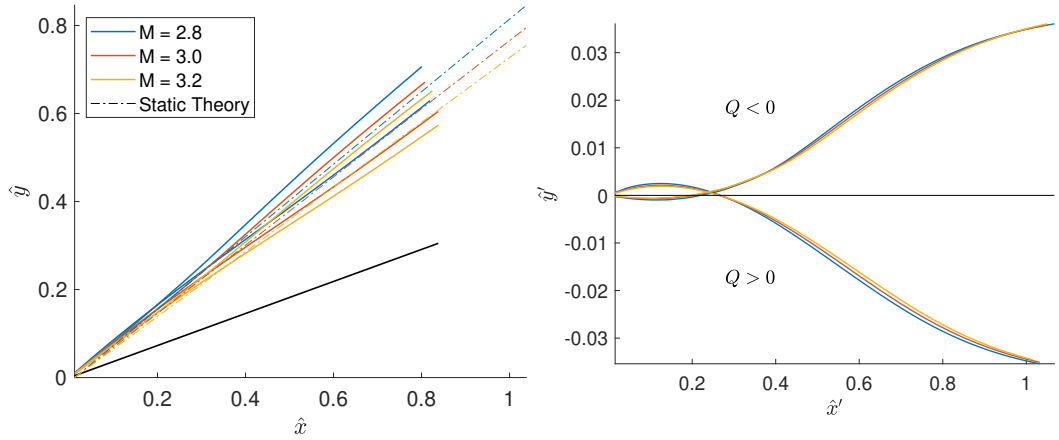
Figure 6.7: Pressure contours - varying acceleration

6.4 Varying Mach Number

Similarly, the effect of the Mach number on dynamic flow features caused by linear acceleration of an attached shock wave domain is examined by holding the other flow parameters constant and varying the Mach number. This is achieved by varying the upstream velocity V_∞. However, both the Mach number $M_\infty = \frac{V_\infty}{a_\infty}$ and the acceleration parameter $Q = \frac{La_y}{V_\infty^2}$ are dependent on the upstream velocity. Therefore, it is necessary to simultaneously vary a_y as V_∞ varies in order to keep Q constant while the Mach number is changed. Setting $Q = 0.2304$ and varying the Mach number $M = [2.8, 3.0, 3.2]$, the vertical accelerations are changed correspondingly $a_y = \pm[2.613, 3.000, 3.414] \times 10^6\ m/s^2$.

The resulting shock waves are shown in figure 6.8. In the horizontal axis, the shock waves are seen to rotate as their theory line angles change with Mach number. However, once again transforming all the shock waves to the theory line axis coordinates (where each shock is scaled by its own theory line), we see that there is almost no change in the shock wave shape for varying Mach numbers. Tentatively it might be said that the curvature is slightly weaker for higher Mach number shock waves in this range. However, it will be necessary to run a wider range of Mach numbers to state this with confidence.

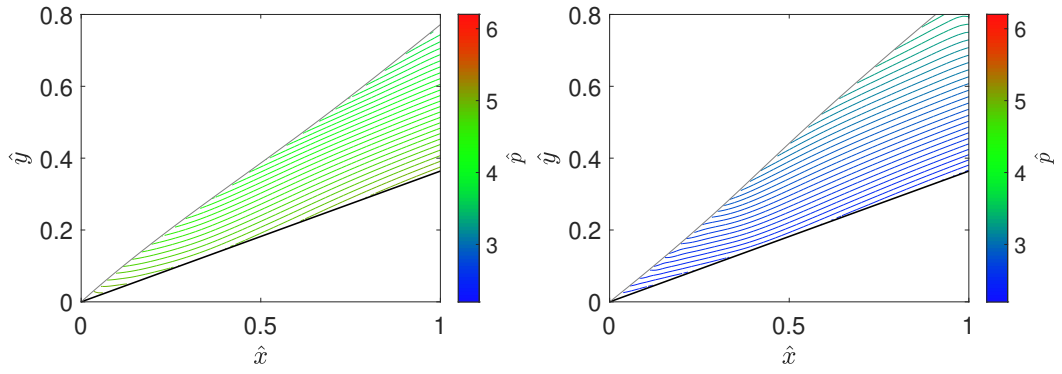
Corresponding normalised pressure contours are shown in figure 6.9. Increasing the Mach number unsurprisingly results in greater average pressures in the domain due to the higher pressures produced by the shock wave. However, the shape of the pressure contours appears to be virtually indistinguishable across the Mach numbers.



(a) Relative - wedge coordinates

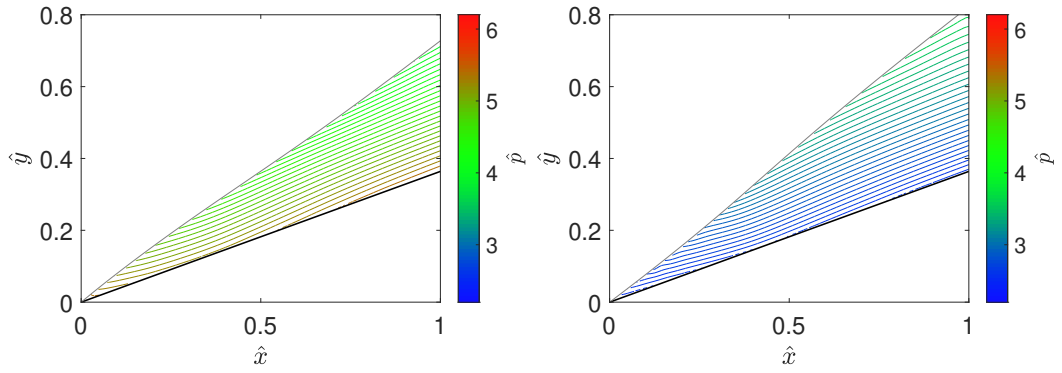
(b) Static shock coordinates

Figure 6.8: Varying Mach number



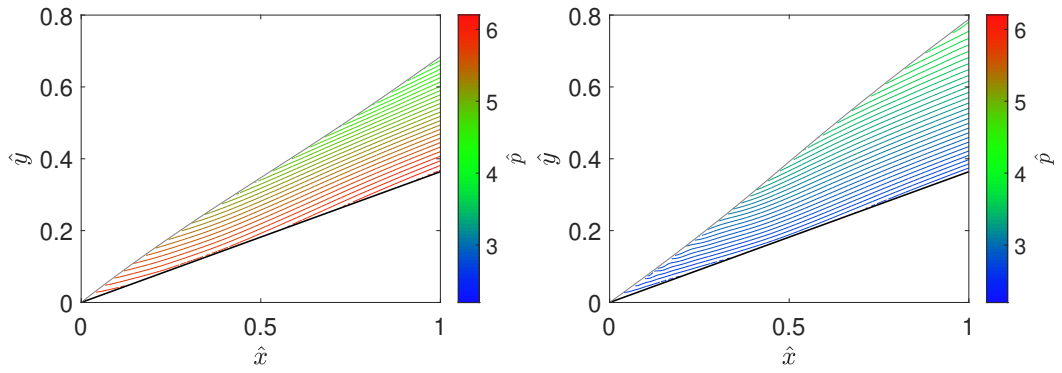
(a) MoC - $M = 2.8$, $Q > 0$

(b) MoC - $M = 2.8$, $Q < 0$



(c) MoC - $M = 3.0$, $Q > 0$

(d) MoC - $M = 3.0$, $Q < 0$



(e) MoC - $M = 3.2$, $Q > 0$

(f) MoC - $M = 3.2$, $Q < 0$

Figure 6.9: Pressure contours - varying Mach number

6.5 Conclusions and Recommendations

Simulations of intense transverse linear accelerations of an attached shock - oblique surface domain were completed over a range of accelerations and Mach numbers for the Method of Characteristics and Finite Volume codes. Results were non-dimensionalised so that they are applicable to all dynamically similar cases. With the following results:

- Significant shock wave curvature was observed, which increased with acceleration, but was insensitive to changes in Mach number, at least in the range tested. It was shown that the shock curvature effectively lags the motion of the surface due to the delayed propagation of pressure waves from the surface to points further along the shock wave.
- It was observed that the relative tip effects, which were a function of the wedge velocity, dominated the flow field in the limit of the tip boundary; while the transverse surface pressure waves, which are a function of surface acceleration, dominated the aft portion of the flow field. This resulted in an initial shock curvature opposite to the later curvature; as well as curvature of field pressure contours near the tip, which became parallel to the surface further along the domain.
- Mesh independence was achieved for both CFD codes and it was demonstrated that theMoC and FV codes showed significant agreement in terms of shock wave curvature and pressure distributions - thus providing some degree of validation of the MoC code for intense transverse linear acceleration cases. To fully validate the code for these cases, it would be necessary to compare the CFD results to experiment - which is not possible at this time.

Note the following recommendations:

- It is recommended that a wider range of Mach numbers be tested to better identify the effects of varying Mach numbers on dynamic shock wave curvature.
- Varying surface angles should be considered. Additionally, future work might include curved surfaces.
- Accelerations parallel to the flow direction should be considered, as well as more complex curviliear motions.

- Sufficiently intense accelerations should result in embedded shock waves inside the attached shock - oblique surface domain, which would be interesting to study.

References

[1] Sauerwein, H.: The Calculation of Two- and Three-Dimensional Inviscid Unsteady Flows by the Method of Characteristics. Tech. Rep., Office of Scientific Research United States Air Force, Cambridge, Massachusetts, 1964.

[2] Photos — F-35 Lightning II.
Available at: `https://www.f35.com/media/photos`

[3] Surujhal, D.: *No Title*. Ph.D. thesis, University of the Witwatersrand, Johannesburg, 2018.

[4] Hooseria, S.J.: *Three-Dimensional, Curved Shock Wave Interactions with Slender Bodies at Incidence*. Ph.D. thesis, The University of the Witwatersrand, 2015.

[5] Felthun, L.T. and Skews, B.W.: Dynamic shock wave reflection. *AIAA Journal*, vol. 42, no. 8, pp. 1633–1639, 2004. ISSN 00011452.

[6] Khotyanovsky, D.V., Kudryavtsev, A.N. and Ivanov, M.S.: Numerical study of transition between steady regular and Mach reflection caused by free-stream perturbations. In: *Proc. of 22nd Int. Symp. on Shock Waves (London, UK*, pp. 1261–1266. 1999.

[7] Anderson, J.D.: *Fundamentals of Aerodynamics*. McGraw-Hill Education, 2010. ISBN 9780073398105.
Available at: `https://books.google.co.za/books?id=xwY8PgAACAAJ`

[8] Naidoo, K. and Skews, B.W.: Dynamic effects on the transition between two-dimensional regular and Mach reflection of shock waves in an ideal, steady supersonic free stream. *Journal of Fluid Mechanics*, vol. 676, pp. 432–460, 2011. ISSN 00221120.

[9] Roohani, H. and Skews, B.W.: Unsteady aerodynamic effects experienced by aerofoils during acceleration and retardation. *Proceedings of the Institution*

of Mechanical Engineers, Part G: Journal of Aerospace Engineering, vol. 222, no. 5, pp. 631–636, 2008. ISSN 09544100.

[10] Gledhill, I.M., Forsberg, K., Eliasson, P., Baloyi, J. and Nordström, J.: Investigation of acceleration effects on missile aerodynamics using computational fluid dynamics. *Aerospace Science and Technology*, vol. 13, no. 4-5, pp. 197–203, 2009. ISSN 12709638.
Available at: `http://dx.doi.org/10.1016/j.ast.2009.04.008`

[11] Gledhill, I.M., Roohani, H., Forsberg, K., Eliasson, P., Skews, B.W. and Nordström, J.: Theoretical treatment of fluid flow for accelerating bodies. *Theoretical and Computational Fluid Dynamics*, vol. 30, no. 5, pp. 449–467, 2016. ISSN 14322250.

[12] Anderson, J.D.: *Modern compressible flow with historical perspective.* McGraw-Hill, 1982. ISBN 0070016542.

[13] Paciorri, R. and Bonfiglioli, A.: Numerical simulation of shock-shock interactions with an unstructured shock-fitting technique. In: *European Space Agency, (Special Publication) ESA SP*, vol. 659, pp. 1–8. 2009.

[14] Blazek, J.: *Computational Fluid Dynamics: Principles and Applications.* 1st edn. Elsevier Ltd, 2001. ISBN 9780128011720.

[15] Lomax, H., Pulliam, T.H. and Zingg, D.W.: *Fundamentals of Computational Fluid Dynamics.* Scientific Computation. Springer Berlin Heidelberg, Berlin, Heidelberg, 2001. ISBN 978-3-642-07484-4.
Available at: `http://link.springer.com/10.1007/978-3-662-04654-8`

[16] Thornhill, C.K.: The Numerical Method of Characteristics for Hyperbolic Problems in Three Independent Variables. Tech. Rep., Aeronautical Research Council, London, 1952.

[17] Sauer, R.: Dreidimensionale Probleme der Charakteristikentheorie partieller Differentialgleichungen. *ZAMM - Journal of Applied Mathematics and Mechanics / Zeitschrift für Angewandte Mathematik und Mechanik*, vol. 30, no. 11-12, pp. 347–356, 1950.
Available at: `https://onlinelibrary.wiley.com/doi/abs/10.1002/zamm.19503011004`

[18] Ferrari, C.: Interference Between Wing and Body at Supersonic Speeds-Analysis by the Method Characteristics. *Journal of the Aeronautical Sciences*, vol. 16, no. 7, pp. 411–434, 1949.
Available at: `https://doi.org/10.2514/8.11823`

[19] Holt, M.: The method of characteristics for steady supersonic rotational flow in three dimensions. *Journal of Fluid Mechanics*, vol. 1, no. 4, p. 409–423, 1956.

[20] Butler, D.S. and Lighthill, M.J.: The numerical solution of hyperbolic systems of partial differential equations in three independent variables. *Proceedings of the Royal Society of London. Series A. Mathematical and Physical Sciences*, vol. 255, no. 1281, pp. 232–252, 1960.
Available at: `https://royalsocietypublishing.org/doi/abs/10.1098/rspa.1960.0065`

[21] Sauerwein, H.: Numerical calculations of multidimensional and unsteady flows by the method of characteristics. *Journal of Computational Physics*, vol. 1, no. 3, pp. 406–432, 1967. ISSN 10902716.

[22] Courant, R., Friedrichs, K. and Lewy, H.: Über die partiellen Differenzengleichungen der mathematischen Physik. *Mathematische Annalen*, vol. 100, no. 1, pp. 32–74, 1928. ISSN 1432-1807.
Available at: `https://doi.org/10.1007/BF01448839`

[23] Rakich, J.V.: A method of characteristics for steady three-dimensional supersonic flow with application to inclined bodies of revolution. 1969.

[24] Delaney, R.A.: A second-order method of characteristics for two-dimensional unsteady flow with application to turbomachinery cascades. 1974.

[25] Settles, G.S.: *Schlieren and shadowgraph techniques: visualizing phenomena in transparent media*. Springer Science & Business Media, 2012.

[26] Skews, B.W.: Aspect ratio effects in wind tunnel studies of shock wave reflection transition. *Shock Waves*, vol. 7, no. 6, pp. 373–383, 1997. ISSN 1432-2153.
Available at: `https://doi.org/10.1007/s001930050092`

[27] Ku, H.H.: Notes on the use of propagation of error formulas. *Journal of Research of the National Bureau of Standards*, vol. 70, no. 4, 1966.

[28] Montgomery, D.C. and Runger, G.C.: *Applied statistics and probability for engineers*. John Wiley & Sons, 2010.

[29] Budynas, R.G. and Nisbett, J.K.: *Shigley's mechanical engineering design*. McGraw-Hill Education, 2020.

Appendix A Test Rig: Dynamic Modelling and Design

In this section, the approach to modelling the dynamics of the test rig, for the purposes of rotation rate predictions and stress analyses, is described; as well as the design process overview. Consider the detailed view of the driving linkage in figure A.1. The equations of motion may be written in terms of the wedge angle θ. The combined inertia of the drive head and piston are transformed to an equivalent angular inertia I_H based on the leg length R_2: $I_H = m_H R_2^2$. Where m_H is the combined mass. Likewise the horizontal drive arm inertia is transformed using R_1: $I_d = m_d R_1^2$. Finally, the angular inertia of the leg, wedge, and wedge arm are calculated by splitting them into simpler rectangular and triangular shapes and applying angular inertia equations for those shapes. Alternatively most CAD programs offer accurate inertia calculation. These inertia are summed to obtatain a final equivalent inertia $I_{eq} \approx 1.918 \times 10^{-3} kg.m^2$.

Likewise, the compression spring force becomes a moment about the leg pivot: $M_s = -k_s \left(L_0 + \theta R_2\right) R_2$, positive counter clock wise. Where L_0 is the initial spring compression length and $k_s \approx 180 kN/m$ is the combined spring stiffness.

The aerodynamic load on the wedge can be approximated by applying the oblique shock and expansion wave equations to determine the top and bottom surface pressure on the wedge and taking the normal surface forces at the center of each face. The corresponding moments are obtained using the perpendicular distance of the surface centers from the wedge pivot. This assumes that these pressures are constant over each surface - in reality, three-dimensional edge effects will cause the surface pressures to vary. The variation of wedge moment with respect to angle is shown in figure A.2 for a Mach 3 case. The variation is approximately linear, so the aerodynamic moment can be replaced by an equivalent angular spring with coefficient $\hat{k}_w \approx 3.56 N.m/rad$. However, note that this is a positive feedback element - it acts to rotate the wedge away from $\theta = 0$.

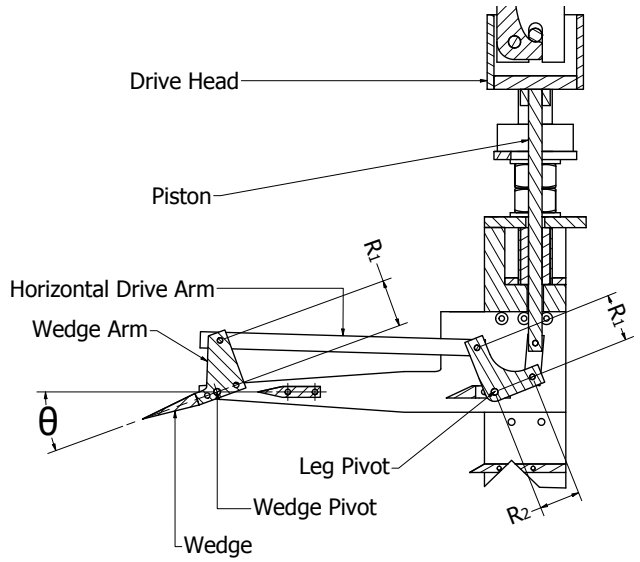


Figure A.1: Detailed Linkage View

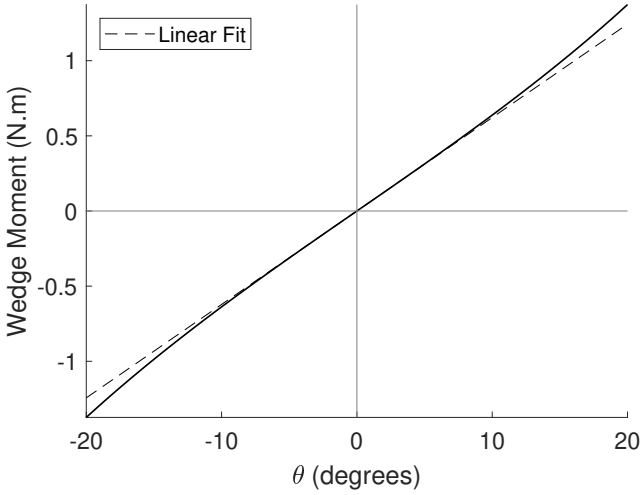


Figure A.2: Wedge Spring Moment Variation

Modelling of the rubber foam dampers is challenging due to its highly non-linear and strain-rate dependent elastic modulus. Ultimately, it was necessary to slowly build up the wedge rotation rate (before mounting the rig in the tunnel) with varying thicknesses of rubber foam to check the structural integrity of the rig. As an approximation, for design purposes, these were modelled as spring elements based on the elastic modulus E_f at 25% static compression. The spring moment coefficient of the foam is then given by $\hat{k}_f = -\frac{E_f A_f}{t_f} R_2^2$, where A_f and t_f are the area and thickness of the foam. In the model equation, this moment is activated by a Heaviside function $H(\theta - \theta_f)$ when the drive head reaches the foam dampers, at wedge angle $\theta = \theta_f$.

Finally, the model equation is by by equation A.1. This model can be solved by analytical methods on either side of the Heaviside activation; or a simple numerical solver can be applied to this single DoF ODE.

$$I_{eq}\frac{d^2\theta}{dt^2} = -k_s\left(L_0 + \theta R_2\right)R_2 + \hat{k}_w\theta - \hat{k}_f\theta H(\theta - \theta_f) \tag{A.1}$$

The primary design process aimed to satisfy the following conditions:

1. Maximise the angular velocity predicted by the dynamic model.
2. Simultaneously solve the spring design equations, which may be found in standard Engineering design texts such as Shigley's mechanical engineering design [29].
3. Determine forces between joints based on the solved linkage motion. Apply stress analyses to components to check for failure, with a relatively large safety factor ($n_s > 3$).

Appendix B Digital Appendix Contents

The contents of the digital appendix are available at the google drive link *Digital Appendix*(`https://drive.google.com/drive/folders/1WfEOD1lqs0MZ_vkzvSGPn6654SS0q8Yn?usp=sharing`)

The corresponding file structure is as follows, with folders in boldface:

- *Manufacturing-Drawings.pdf*
  -Full manufacturing drawings for the test rig
- **Experimental-Flow-Visualisation-Videos**:
  -High speed flow visualisation videos for each test in table 3.3. Note that these videos are inverted vertically due to the optical setup.
  Test 1.mp4
  .
  .
  Test 8.mp4
- **CFD**
  - **Finite-Volume**
    Journals, meshfiles, UDFs - all Fluent V19.2 runfiles
    * Linear-Acceleration-Setup
    * Matching-Experiment-Setup
  - **Method-of-Characteristics**
    Matlab (2019b) objects for the primary MoC procedures.